

# Investigations of nitrides, oxynitrides, borocarbonitrides and other materials

A Thesis Submitted for the Degree of

Doctor of Philosophy

*By*

Nitesh Kumar



Chemistry and Physics of Materials Unit  
Jawaharlal Nehru Centre for Advanced Scientific Research  
(A Deemed University)  
Bangalore, India.

**March 2014**



*Dedicated to my parents*



# *Declaration*

I hereby declare that the matter embodied in this thesis entitled *“Investigations of nitrides, oxynitrides, borocarbonitrides and other materials”* is the result of investigations carried out by me under the supervision of Prof. C. N. R. Rao, FRS and Prof. A. Sundaresan at the Chemistry and Physics of Materials Unit, Jawaharlal Nehru Centre for Advanced Scientific Research, Bangalore, India and that it has not been submitted elsewhere for the award of any degree or diploma.

In keeping with the general practice in reporting scientific observations, due acknowledgement has been made whenever the work described is based on the findings of other investigators.


---

(Nitesh Kumar)



# *Certificate*

I hereby certify that the matter embodied in this thesis entitled “*Investigations of nitrides, oxynitrides, borocarbonitrides and other materials*” has been carried out by Mr. Nitesh Kumar at the Chemistry and Physics of Materials Unit, Jawaharlal Nehru Centre for Advanced Scientific Research, Bangalore, India under my supervision and it has not been submitted elsewhere for the award of any degree or diploma.



---

(Prof. C. N. R. Rao)

**(Research Supervisor)**

---

(Prof. A. Sundaresan)

**(Research Supervisor)**





# *Acknowledgements*

I consider myself very fortunate to work under the joint guidance of **Prof. C. N. R. Rao** and **Prof. A. Sundaresan** in my Ph.D. Together they helped me in developing my perspective towards research and instilling in me an interest in solid state chemistry. They gave me enough freedom to pursue my imagination in various research problems while guiding me all along. Without their guidance and constant support my research would easily have gone wayward.

I sincerely thank my collaborators Prof U. V. Waghmare, Prof. Amparo Fuertes and Dr. Gerard Tobias for the successful completion of many joint projects and their invaluable discussions and timely guidance. I am grateful to Dr. A. Govindaraj for helping me in various experimental aspects during my Ph.D.

Most of my research problems would have been incomplete without the help of my co-workers - Dr. Kalyan Raidongia, Mr. Kota Moses, Dr. K. P. S. S. Hembram, Dr. Abhishek K. Mishra, Ms. Sharmila N. Shirodkar, Mr. Vinay I. Hegde, Ms. Urmimala Maitra, Ms. Jaysree Pan, Ms. N. Aysha, Ms. Stefania Sandoval, Dr. Judith Oró-Solé and Dr. Dinesh Jagadeesan.

I enjoyed attending courses provided by Prof. S. Balasubramanian, Prof. A. Sundaresan, Prof. S. M. Shivaprasad, Prof. N. Chandrabhas, Dr. T. K. Maji, Dr. Eswaramoorthy, Prof. K. S. Narayan, Prof. G. U. Kulkarni, Prof. S. K. Pati, Prof. Umesh V. Waghmare, Prof. S. Narasimhan, Dr. N. S. Vidhyadhiraja, Prof. S. Ranganathan (Materials Engineering, IISc) and Prof. T. N. Guru Row (SSCU, IISc) during my Master in Materials Science.

I highly appreciate technical help from Ms. N. R. Selvi (for FESEM), Mrs. T. Usha (for TEM), Mr. Vasu (for UV, PL, IR, TGA), Mr. Anil (for XRD) Mr Mahesh (for AFM) and Mr. Kishor (for XPS). Without their help, completion of various projects would not

have been possible. I thank Mrs. Shashi, Mrs. Sudha, Mr. Gowda and Mr. Victor for their help in various aspects.

Thanks to all my Int. PhD. batch mates with whom I started my life at this centre and whose cheerful company made these six years of life so memorable. I specially thank Soumik, Abhay and Urmimala for discussions on various aspects of Science and beyond. I also thank all my past and present lab mates: Dr. Vengadesh, Dr. Pranab, Dr. Shipra, Dr. Gomathi, Dr. Kalyan, Dr. Madhu, Dr. Matte, Dr. Sundarayya, Dr. Subrahmanyam, Moses, Urmimala, Dr. Naidu, Rana, Somnath, Chandan, Sunita, Ram Kumar, Sreedhara, Abhijit, Uttam, Gopal, Pramoda, Anand, Monali, Ajmala, Dr. Prasad, Dr. Vasu, Dr. Chitaiyah for fruitful interaction. I thank all my friends for the wonderful time and their help and support at various times during the past years.

Finally, I thank my parents for whom providing us the best education with the best of their capabilities has been the first priority. I am also indebted to my elder brother who has always been there like a guardian and friend to me. I dedicate this thesis to my  
parents.

# *Contents*

Declaration	iii
Certificate	v
Acknowledgements	vii
Contents	ix

## **A Brief introduction to nitrides and related materials** **1**

1. Introduction	1
2. Nitrogen sources for nitride materials	2
3. Types of nitride materials	
3.1 Metal nitrides	3
3.2 Oxynitrides	5
3.3 N-doped oxides	8
3.4 Boron nitride	9
3.5 Borocarbonitrides	12
3.6 N-doped graphene	13
4. Scope of this thesis	15
5. References	17

## **Part I Investigations of oxynitrides** **25**

### **Chapter I.1 Rare earth (La, Pr and Nd) vanadium oxynitrides: Synthesis, structure, magnetic and electrical properties**

Summary	27
1. Introduction	28
2. Scope of the present investigation	31
3. Experimental Section	31
4. Results and discussion	32
4.1 LaVO <sub>2.09</sub> N <sub>0.91</sub>	33

4.2	NdVO <sub>2</sub> N	39
4.3	PrVO <sub>2.24</sub> O <sub>0.76</sub>	41
4.4	Resistivity measurements	42
5.	Conclusions	43
6.	References	44
<b>Chapter I.2 Synthesis, structure and properties of rare earth niobium oxynitrides</b>		
	Summary	49
1.	Introduction	50
2.	Scope of the present investigation	51
3.	Experimental Section	51
4.	Results and discussion	51
5.	Conclusions	57
6.	References	59
<b>Chapter I.3 Photocatalytic hydrogen evolution by ATaO<sub>2</sub>N (A = Ca, Sr and Ba) synthesized by urea method</b>		
	Summary	61
1.	Introduction	62
2.	Scope of the present investigation	62
3.	Experimental Section	63
4.	Results and discussion	63
5.	Conclusions	68
6.	References	69
<b>Part II N and N, F-codoped oxides</b>		<b>71</b>
<b>Chapter II.1 Synthesis, photocatalysis and varied properties of nitrogen and fluorine co-substituted TiO<sub>2</sub> nanoparticles</b>		
	Summary	73
1.	Introduction	74
2.	Scope of the present investigations	75
3.	Experimental Section	76
4.	Results and discussion	77

4.1 Results from experiments	77
4.2 Important interpretations from first-principles calculations	87
5. Conclusions	90
6. References	92
<b>Chapter II.2 Ferroelectricity and other properties of nitrogen and fluorine co-substituted barium titanate</b>	
Summary	95
1. Introduction	96
2. Scope of the present investigation	96
3. Experimental Section	97
4. Results and discussion	97
5. Conclusions	103
6. References	104
<b>Part III Investigations of nitrides</b>	<b>107</b>
<b>Chapter III.1 Rock salt-type transition metal nitrides: Urea based synthesis and superconducting, magnetic &amp; photocatalytic properties</b>	
Summary	109
1. Introduction	110
2. Scope of the present investigation	111
3. Experimental Section	112
3.1 Synthesis of transition metal nitride nanoparticles	112
3.2 Characterization	112
4. Results and discussion	112
4.1 VN nanoparticles	112
4.2 NbN nanoparticles	115
4.3 CrN nanoparticles	118
4.4 Photocatalytic water splitting by TiN and VN nanoparticles	121
5. Conclusions	122
6. References	123
<b>Appendix A: Gas phase synthesis of CrN and Fe<sub>3</sub>N</b>	125

## **Chapter III.2 Synthesis and characterization of N-doped graphene**

Summary	127
1. Introduction	128
2. Scope of the present investigation	129
3. Experimental Section	129
3.1 Synthesis of GO	129
3.2 Synthesis of nitrogen doped graphene	130
3.2.1 Effect of temperature	130
3.2.2 Effect of duration of ammonolysis	130
3.2.3 Effect of flow rate of ammonia	131
3.3 Preparation of dispersion	131
3.4 Characterization	131
4. Results and discussion	131
5. Conclusions	142
6. References	143

## **Part IV Borocarbonitrides 141**

### **Chapter IV.1 Synthesis and gas adsorption studies of high surface area borocarbonitrides**

Summary	149
1. Introduction	150
2. Scope of the present investigation	152
3. Experimental Section	152
4. Results and discussion	153
5. Conclusions	162
6. References	163

### **Chapter IV.2 Gas phase synthesis of $BC_xN$ ( $x = 1-2$ ) and their characterization**

Summary	165
1. Introduction	166
2. Scope of the present investigation	166
3. Experimental Section	167
4. Results and discussion	168

5.	Conclusions	174
6.	References	165
<b>Part V Other studies</b>		<b>177</b>
<b>Chapter V.1 Temperature evolution of nickel sulphide phases: Their electrical and magnetic properties</b>		
	Summary	179
1.	Introduction	180
2.	Scope of the present investigation	182
3.	Experimental Section	183
	3.1 Synthesis of hexakis(thiourea)nickel(II) nitrate	183
	3.2 Synthesis of nickel sulphide particles	183
	3.3 Characterization	183
4.	Results and discussion	184
5.	Conclusions	196
6.	References	197
<b>Chapter V.2 Synthesis, electrical and magnetic properties of cobalt sulphide: CoS<sub>2</sub> and Co<sub>9</sub>S<sub>8</sub></b>		
	Summary	199
1.	Introduction	200
2.	Scope of the present investigation	202
3.	Experimental Section	202
	3.1 Synthesis of [Co(tu) <sub>4</sub> .(NO <sub>3</sub> ) <sub>2</sub> ]	202
	3.2 Synthesis of cobalt sulphide phases	202
	3.3 Characterization	203
4.	Results and discussion	203
5.	Conclusions	210
6.	References	211
<b>Chapter V.3 Investigation of ferromagnetism in MgO nanoparticles</b>		
	Summary	213
1.	Introduction	214

2.	Scope of the present investigation	214
3.	Experimental Section	215
4.	Results and discussion	216
	4.1 Undoped MgO nanoparticles	216
	4.2 Effect of Li-doping on MgO nanoparticles	221
5.	Conclusions	222
6.	References	223

#### **Chapter V.4 Room temperature ferromagnetism in thin-walled inorganic hollow spheres**

Summary		225
1.	Introduction	226
2.	Scope of the present investigation	226
3.	Experimental Section	227
	3.1 Materials	227
	3.2 Synthesis of carbon spheres	227
	3.3 Synthesis of ZnAl <sub>2</sub> O <sub>4</sub> hollow spheres	227
	3.4 Synthesis of GaN hollow spheres	228
	3.5 Synthesis of MgO hollow spheres	228
4.	Results and discussion	228
5.	Conclusions	233
6.	References	235



# **A brief introduction to nitrides and related materials**

## **1. Introduction**

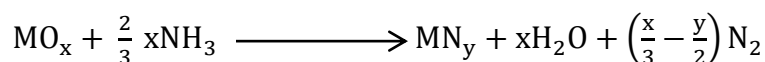
Nitrogen is the most abundant element in the earth's atmosphere constituting 78.09 % by volume. It is a colorless, odorless, tasteless and inert diatomic gas at standard conditions. Despite its abundance only few hundred nitrides are known compared to thousands of extensively studied and well characterized oxides. One of the reasons for this is the extremely high bond energy of  $N_2$  (941 kJ/mol) which is a possible decomposition product of nitrides explaining their low thermal stability. For the same reason  $N_2$  does not act as nitrating agent at temperatures below  $\sim 1300$  °C and ambient pressure. On the other hand, bond energy of  $O_2$  is comparatively small (499 kJ/mol). Hence, removal of  $N_2$  from  $Si_3N_4$  takes place at atmospheric pressure at about 1900 °C whereas  $SiO_2$  is thermally stable over 2000 °C without any loss of  $O_2$ . Moreover, the relatively very high energy of formation of the  $N^{3-}$  anion from atomic N (more than three times that of  $O^{2-}$  from O) is responsible for the reluctance of nitrogen to form ionic bonds except with the most electropositive of elements. These thermodynamic factors, therefore, explain both the rarity of nitrides and also their tendency to form unusual and often unique structure types.

Despite these difficulties there are many important and interesting nitrides and related materials known to solid state chemists. Group III nitrides represent an important group of direct band gap semiconductors constituting AlN, GaN and InN wherein the band gap spans from infrared to ultraviolet region (1.95-6.2 eV). They form a complete series of ternary alloys which, in principle, makes available any band gap within this range. Moreover, they also generate efficient luminescence and therefore used in commercially available high brightness visible light-emitting diodes (LEDs). Transition metal nitrides form an important class of materials known for their superior mechanical properties, for example extreme

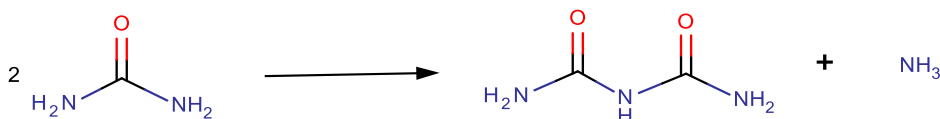
hardness, high melting, chemical stability *etc.* In addition, they also exhibit interesting electrical properties like superconductivity at low temperatures.

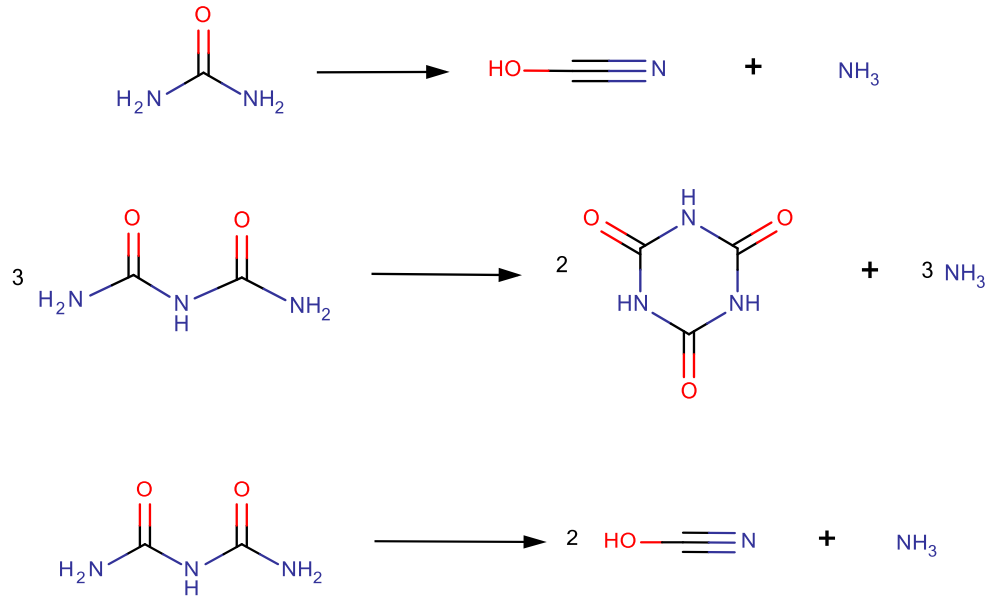
## 2. Nitrogen sources for nitride materials

Various nitrogen sources for the synthesis of nitrides and other related inorganic materials have been used among which ammonia (NH<sub>3</sub>) has been the most versatile one. NH<sub>3</sub> exists in the gaseous state at atmospheric pressure but can easily be liquefied (-33.3 °C) because of strong inter molecular hydrogen bonding. Nitridation to obtain metal nitrides and oxynitrides is carried out using starting materials like metal, metal oxide, amorphous oxide, metal chloride, metal sulphide *etc.* In the case of metal oxide as the starting material, the main driving force for the reaction with NH<sub>3</sub> is the formation of water and to a lesser extent the formation of binary or ternary nitrides. The general reaction can be represented as:



Because ammonolysis reaction often results in the reduction of metal ion, evolution of nitrogen gas is associated with this reaction. The formation of nitride in the above reaction depends on the thermodynamics of reaction and hence the choice of the initial precursor is very important. For this reason many starting materials other than oxides like metal, amorphous oxide, metal chloride, metal sulphide *etc.* have also been used. NH<sub>3</sub> is not stable at high temperature and dissociates into N<sub>2</sub> and H<sub>2</sub>. The process of dissociation starts just below 500 °C and increases on increasing the temperature.<sup>1</sup> Rather than doing ammonolysis by passing NH<sub>3</sub> directly, it can also be produced in situ by thermolysis of urea. On decomposition of urea, which starts at around 150 °C, a series of products are formed containing biuret, cyanic acid, cyanuric acid and ammonia.<sup>2</sup> The decomposition can be represented by the following chemical equations:





For the nitridation reaction, an excess amount of urea is normally mixed with the precursor and heated in the inert atmosphere above 500 °C. Nanoparticles of many nitrides, oxynitrides and nitrogen doped oxides are obtained by this method. Moreover, urea has also been used to dope nitrogen in graphene and for the synthesis of BN and  $B_xC_yN_z$ . Sodium amide ( $\text{NaNH}_2$ ) and lithium amide ( $\text{LiNH}_2$ ) also decompose to give rise to  $\text{NH}_3$  and have been used to obtain materials like TiN, TaN and  $\text{Ta}_3\text{N}_5$ .<sup>3-5</sup> Refractory nitrides (TiN, ZrN, HfN, NbN and TaN) have been prepared by using  $\text{Li}_3\text{N}$  and  $\text{NaN}_3$  as the nitrogen source starting from corresponding metal halides.<sup>6</sup>

### 3. Types of nitride materials

In this thesis we will consider two types of nitride materials: materials where nitrogen exist as  $\text{N}^{3-}$  and materials where nitrogen is bonded to the neighboring atoms with  $\text{sp}^2$  hybridized covalent bonds. In the first category we will consider metal nitrides focusing mainly on transition metal nitrides, oxynitrides and nitrogen-doped oxides. In the second category materials like boron nitride, borocarbonitride and N-doped graphene would be considered.

#### 3.1 Metal nitrides

Because of the difficulty of the formation of  $\text{N}^{3-}$ , there is a tendency for late transition metals to exhibit covalency in binary nitrides with low valence states. Even in the case of early

transition metals formation of nitrides below their highest oxidation states are often observed. For example, TiN is extremely stable and easy to form whereas  $Ti_3N_4$  is extremely difficult to synthesize and poorly characterized. In another example, many compositions of Group V elements with nitrogen are known, yet both  $V_3N_5$  and  $Nb_3N_5$  are not possible to make. As shown in Figure 1, many of the binary transition metal nitrides are interstitial compounds which can be thought as the eutectic mixture of metal atoms with varying quantities of nitrogen partially filling available sites. This is responsible for metallic properties like hardness, lustre, conductivity *etc.* for many of these binary nitrides as well as the existence of many nonstoichiometric nitrides. Some aspects of the transition metal nitrides are also discussed in the introduction of Part III of the thesis.

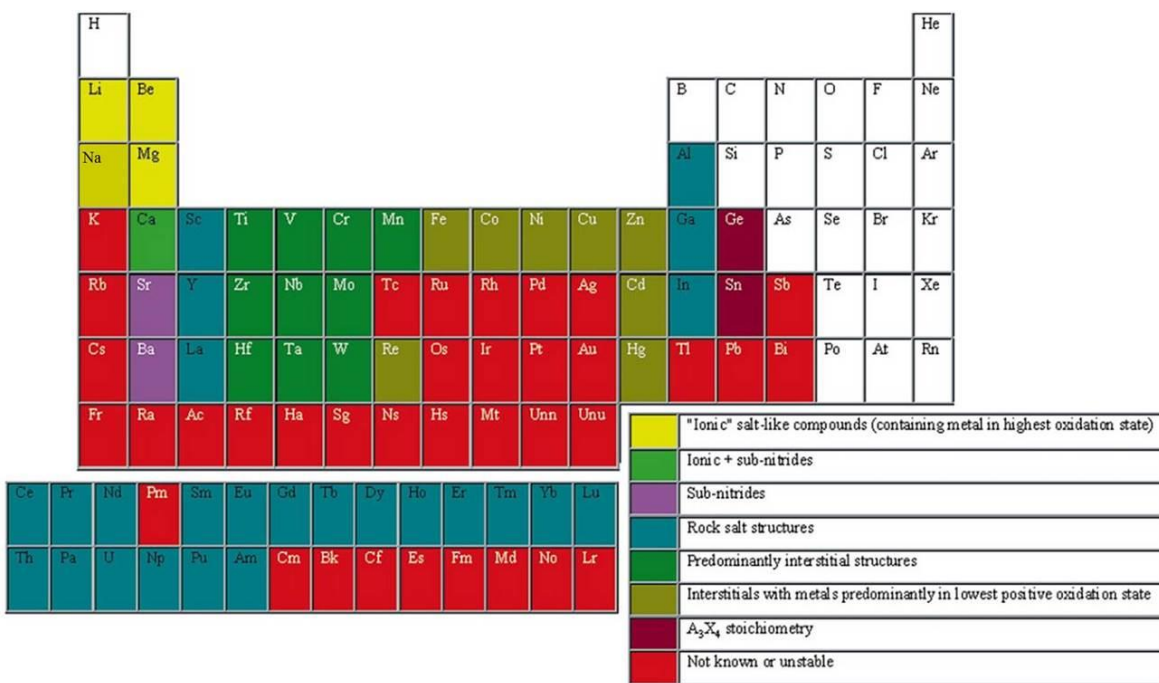


Figure 1 Broad structure types adopted by binary metal nitrides by element.<sup>7</sup> [reproduced from ref. 7 with permission]

The metallic nature of bonding is not the characteristic of only transition metal nitrides but also observed in several other binary nitrides. The most electropositive alkali metals are essentially ionic nitrides whereas the heavier, less electropositive alkaline earth metals preferentially form sub-nitrides. The expected stoichiometric compounds such as  $Ba_3N_2$  and  $Sr_3N_2$  could not be prepared whereas compositions such as  $Sr_2N$  and  $Ba_3N$  with reduced metal ions are well characterized in the literature.<sup>8-9</sup> In contrast, calcium forms both

stoichiometric  $\text{Ca}_3\text{N}_2$  and the sub-nitride  $\text{Ca}_2\text{N}$ .<sup>10-11</sup> Smaller alkaline earths Mg and Be show no evidence for low oxidation state compounds.

Recently, rare-earth nitrides (RENs) gained a lot of attention because one of the compounds of this group, GdN, has been predicted to be a magnetic narrow gap semiconductor<sup>12</sup> in the bulk form which is yet to be confirmed experimentally with some reports showing it to be a semimetal.<sup>13</sup> This would make it an excellent candidate for spintronic materials. Other members of this family have not been extensively studied. All of the RENs have the rare-earth atoms in a 3+ valence except for CeN which was claimed to be closer to 4+.<sup>14-15</sup> The magnetic properties of many of the RENs are not well known. NdN, GdN,<sup>16-19</sup> TbN,<sup>20-21</sup> DyN,<sup>21</sup> HoN<sup>21</sup> and SmN<sup>22</sup> are known to be ferromagnetic, while YbN<sup>23</sup> is reported to be antiferromagnetic. First half of the series with the exceptions of CeN, EuN, and NdN show semimetallic nature. CeN, and EuN are metallic, with strong perturbation of f level at  $E_F$  in EuN. NdN has a small band gap. The second half of the series shows semiconducting behavior.<sup>24</sup>

In 2004, Gregoryanz reported the synthesis of first noble metal nitride by synthesizing PtN at 45-50 GPa and temperature exceeding 2000 K.<sup>25</sup> It has a cubic zinc blend structure with a possible space group of  $F-43m$ . This novel compound exhibits extremely high value of bulk modulus comparable to super hard c-BN ( $K_0 = 372(\pm 5)$  and 379 GPa, respectively). At similar reaction conditions, Crowhurst *et al.* claimed to obtain the compound PtN<sub>2</sub> and suggested the structure to be of pyrite type using first-principles calculations.<sup>26</sup> They also reported the formation of IrN<sub>2</sub> at 47 GPa and 1600 K exhibiting much lower symmetry. Nearly at the same time, Young *et al.* synthesized IrN<sub>2</sub> and OsN<sub>2</sub> at 50 GPa and 2000 K.<sup>27</sup> IrN<sub>2</sub> exhibited the highest ever bulk modulus of  $K_0 = 428(12)$  GPa, higher than that of any previously synthesized material and only second to diamond ( $K_0 = 440$  GPa).

### **3.2 Oxynitrides**

Oxynitrides are the inorganic compounds wherein a stoichiometric amount or an order of the stoichiometric amount of nitrogen occupies oxygen sites. The basis of the formation of oxynitrides is the similar chemical, structural and electronic features of oxide and nitride ions. Due to comparable polarizability, electronegativity, coordination numbers and ionic

radii of nitride and oxide, they can coexist in many structure types known for oxides. Structures like perovskites,<sup>28</sup> spinels,<sup>29</sup> pyrochlores,<sup>30</sup> baddeleyites,<sup>31</sup> scheelites,<sup>32</sup> apatites,<sup>33</sup> *etc.* have been reported for oxynitrides in the literature with nitrogen non-stoichiometries in some cases. Oxidation state of the cations and thus the physical and electronic properties of oxynitrides can be varied by changing the N/O ratio for a constant cationic composition. Nitrogen being less electronegative than oxygen pushes the valence band towards the Fermi level without affecting the conduction band and hence decreases the optical band gap of the material. The metal–nitrogen bond is more covalent than the metal–oxygen bond because nitrogen is more polarizable than oxygen which thereby decreases the interelectronic repulsion and the energy of the d orbitals. Also, the higher electrical charge of nitride ion leads to a larger crystal field splitting in nitride compounds.

As discussed earlier, the most common method for the synthesis of perovskite oxynitrides is the treatment of a mixture of reactants or oxide precursors in NH<sub>3</sub> at high temperature. At temperatures where the reaction of oxides with ammonia becomes appreciable, NH<sub>3</sub> dissociates into N<sub>2</sub> and H<sub>2</sub>. The rate of dissociation can be suppressed by flowing ammonia at high rates. The presence of H<sub>2</sub> because of the dissociation of ammonia may lead to reduction of the cations and in some cases it competes with the formation of the oxynitride. Oxynitrides can be obtained by ammonolysis of either a mixture of reactants, a crystalline oxide or a reactive oxide precursor. ATaO<sub>2</sub>N and ANbO<sub>2</sub>N (A = Ca, Sr and Ba) are prepared by ammonolysis of a mixture of ACO<sub>3</sub> and Ta/Nb<sub>2</sub>O<sub>5</sub> at high temperature. Materials like LaTiO<sub>2</sub>N and LaTaON<sub>2</sub> have been prepared from crystalline La<sub>2</sub>Ti<sub>2</sub>O<sub>7</sub> and LaTaO<sub>4</sub> respectively in the ammonolysis conditions at high temperature. The kinetics of ammonolysis from these crystalline oxides are often slow and can be improved by selecting highly reactive amorphous oxide precursors. The use of such precursors also helps to bring down the ammonolysis temperatures. Clarke *et al.* showed that although LaTiO<sub>2</sub>N could be made from crystalline La<sub>2</sub>Ti<sub>2</sub>O<sub>7</sub>, for more electropositive Zr, the synthesis of LaZrO<sub>2</sub>N required X-ray amorphous oxide precursor.<sup>34</sup> For some oxynitrides like Na<sub>x</sub>La<sub>1-x</sub>TaO<sub>1+2x</sub>N<sub>2-2x</sub>,<sup>35</sup> BaTa<sub>1-x</sub>Zr<sub>x</sub>O<sub>2+x</sub>N<sub>1-x</sub><sup>36</sup> *etc.* for which crystalline oxide precursors are not available due to overall cationic charge considerations, the use of X-ray amorphous oxide precursors is the necessity.

One of the important structural aspects of oxynitrides is the anion ordering. There can be two extreme cases for anion ordering where there can be complete ordering of anions or there can exist a complete disorder in anions. TaON and Si<sub>2</sub>ON<sub>2</sub> are examples of oxynitrides with completely ordered nitrogen and oxygen. Wurtzite-type (GaN)<sub>1-x</sub>(ZnO)<sub>x</sub> (x = 0.12) is an example of completely disordered oxynitride. However, only few oxynitrides fall into either of these categories and most have intermediate anion order with local clustering or extended correlations that may give rise to nonrandom site occupancies in the averaged crystal structure. Neutron scattering is a powerful tool for determining such orders, as there is good contrast between the nuclear scattering lengths of oxygen (5.83 fm) and nitrogen (9.36 fm). For example, in the case of SrTaO<sub>2</sub>N and also in SrNbO<sub>2</sub>N there exist a zigzag MN chains within two-dimensional layers of the SrMO<sub>2</sub>N perovskites. Extensive treatment of anion ordering can be found in recent papers by Attfield *et al.*<sup>28, 37-38</sup>

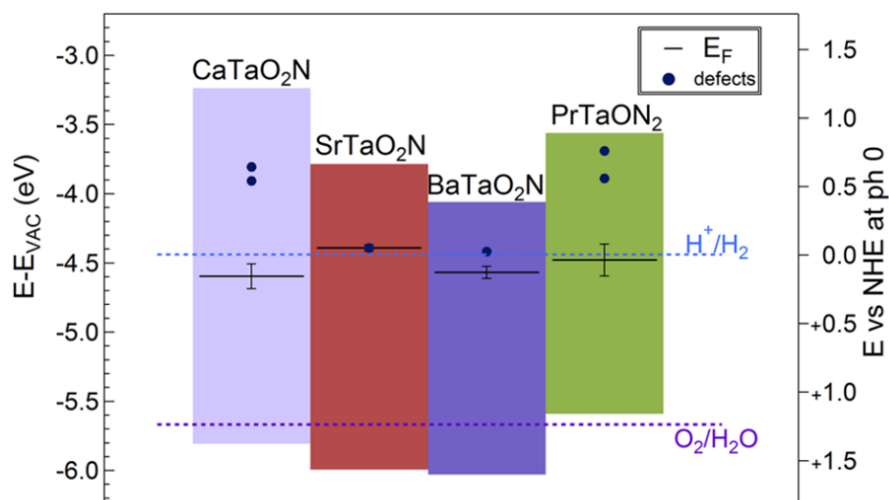


**Figure 2 Energy-level diagrams of tantalum oxynitrides showing EC and EV as well as band gap (colored) and defect levels (•)<sup>39</sup> [reproduced from ref. 39 with permission]**

Perovskite oxynitrides of Ta<sup>5+</sup>, Nb<sup>5+</sup> and Ti<sup>4+</sup> and alkaline earth or rare earth metals show bright colours with band gaps ranging from 1.8 to 3 eV<sup>40</sup> and hence find applications as non-toxic inorganic pigments. The band gap can be tuned by changing the N/O ratio that takes place for charge compensation in the substitution of cations with different oxidation states, for example, Ca<sub>1-x</sub>La<sub>x</sub>TaO<sub>2-x</sub>N<sub>1+x</sub><sup>41</sup> where the color changes from yellow for x = 0 (band gap

2.75 eV) to red for  $x = 1$  (1.9 eV),  $\text{SrTi}_{1-x}\text{Nb}_x\text{O}_{3-x}\text{N}_x$ , with band gaps from 3.24 eV for  $x = 0.05$  to 1.82 eV for  $x = 0.95$ ,<sup>42</sup> and  $\text{La}_{1-x}\text{A}_x\text{TiO}_{2+x}\text{N}_{1-x}$  (A = Sr, Ba).<sup>43</sup> Recently, oxynitrides have been studied for their photocatalytic water splitting activities because of their suitable valence and conduction bands positioning and band gaps in the visible region.<sup>39</sup>

$\text{ATaO}_2\text{N}$  (A = Ca, Sr and Ba),  $\text{ANbO}_2\text{N}$  (A = Ca, Sr and Ba),  $\text{LaTiO}_2\text{N}$ , TaON,  $(\text{GaN})_{1-x}(\text{ZnO})_x$  etc. have been used as visible light catalysts for water splitting reaction. Siritanaratkul *et al.* studied photocatalytic activities of various niobium oxynitrides and concluded that  $\text{CaNbO}_2\text{N}$ , with a band gap of 2.0 eV was capable of producing  $\text{H}_2$  and  $\text{O}_2$  from aqueous solutions of electron donors and acceptors, respectively, even under irradiation at wavelengths  $> 560$  nm.<sup>44</sup> Maeda *et al.* demonstrated  $\text{SrNbO}_2\text{N}$ , an n-type semiconductor with a band gap smaller than 2.0 eV, can function as a photoanode for water splitting even without application of an external bias.<sup>45</sup>

### 3.3 N-doped Oxides

Small amount of nitrogen substituted in the oxygen site can change the electronic properties of oxides. Among all the oxide materials, doping of nitrogen in  $\text{TiO}_2$  has been studied in most detail. Being biologically and chemically inert, stable to corrosion, non-toxic and relatively cheap,  $\text{TiO}_2$  is considered to be the most suitable for environmental applications and has been widely employed to promote photocatalytic degradation of harmful organic compounds.<sup>46</sup> The main drawback of  $\text{TiO}_2$  for photocatalysis is that its band gap is rather large, 3.0 – 3.2 eV, and thus only a small portion of the solar spectrum is absorbed in the UV region ( $\lambda < 380$  nm). Hence, large effort has been made to prepare doped- $\text{TiO}_2$  with the absorption edge shifted towards the visible light region, as this would result in a tremendous improvement of photocatalytic efficiency. Because of the low photocatalytic activity and photostability of various transition metal (TM)-doped  $\text{TiO}_2$  systems, nitrogen doping has proved to be the most suitable method to tune the band gap for visible light absorption. Doping of nitrogen in  $\text{TiO}_2$  has been carried out mostly for the catalytically more active anatase (3.2 eV) form. The doping is accompanied by the appearance of well localized isolated N 2p states above the O 2p valence band thus reducing the overall band gap of anatase. Details of



the synthesis and photocatalytic properties of N-TiO<sub>2</sub> are included in the introduction of Chapter II.1.

To the lesser extent, N-doping has been studied for some other oxide systems. Zinc oxide (ZnO) is a wide band gap semiconductor (3.37 eV). It exhibits n-type conductivity originating from the incorporation of hydrogen atoms within the ZnO host lattice to give rise to a large amount of shallow donor levels.<sup>47</sup> Obtaining a stable p-type ZnO remains a great challenge, and the fabrication of reliable p-type thin films is a bottleneck, which imposes a barrier for its commercial use in ZnO-based optoelectronic devices. Chavillon *et al.* showed that the combination of a high zinc vacancy concentration with insertion of nitrogen and coexistence of oxide and peroxide groups led to the stabilization of positive charge carriers.<sup>48</sup> They prepared the material by decomposing zinc peroxide (ZnO<sub>2</sub>) at temperatures lower than 350 °C in NH<sub>3</sub> atmosphere. Mapa *et al.* prepared Zn<sub>1+δ</sub>O<sub>0.85</sub>N<sub>0.15</sub> by heating equimolar mixture of Zn(NO<sub>3</sub>)<sub>2</sub>·6H<sub>2</sub>O and urea which could absorb visible light with the onset at 600 nm.<sup>49</sup> Such material with significant absorption in visible range can be used for various photocatalytic activities. Bhirud *et al.* showed excellent hydrogen evolution activity (3957 μmolh<sup>-1</sup>) in visible light by using N-doped ZnO as catalyst.<sup>50</sup> Yang *et al.* prepared vertically aligned N-ZnO nanowires and demonstrated photoelectrochemical hydrogen evolution in visible light with an overall hydrogen generation efficiency of 0.15%.<sup>51</sup> Recently, there have some progress on the synthesis and photocatalytic properties of CeO<sub>2</sub> nanoparticles. Mao *et al.*<sup>52</sup> used N-CeO<sub>2</sub> nanoparticles for visible light degradation of methylene blue whereas, Fuertes and co-workers<sup>53</sup> used them for visible light acetaldehyde decomposition. Similarly, N-doped Ta<sub>2</sub>O<sub>5</sub>,<sup>54</sup> SrTiO<sub>3</sub><sup>55</sup> *etc.* have also been reported to exhibit visible light catalytic activity.

### **3.4 Boron nitride**

Boron nitride (BN) is the lightest among all group V-III compounds and draws similarity with graphite and diamond in terms of number of electrons between the neighboring atoms. h-BN (hexagonal-BN) is counterpart of graphite with sp<sup>2</sup> hybridization in the constituent atoms whereas c-BN (cubic-BN) can be related to diamond with sp<sup>3</sup> hybridized three dimensional network of B and N. h-BN consists of layers of hexagonal BN networks with

lattice constants ( $a = 2.504 \text{ \AA}$ ,  $c = 6.661 \text{ \AA}$ ) comparable to those of graphite ( $a = 2.458 \text{ \AA}$ ,  $c = 6.696 \text{ \AA}$ ). These h-BN layers are arranged on top of each other with an interlayer separation of  $3.331 \text{ \AA}$  in AA'AA'.... sequence, such that B atoms in one layer are bonded to N atoms in the adjacent layer by electrostatic interaction.

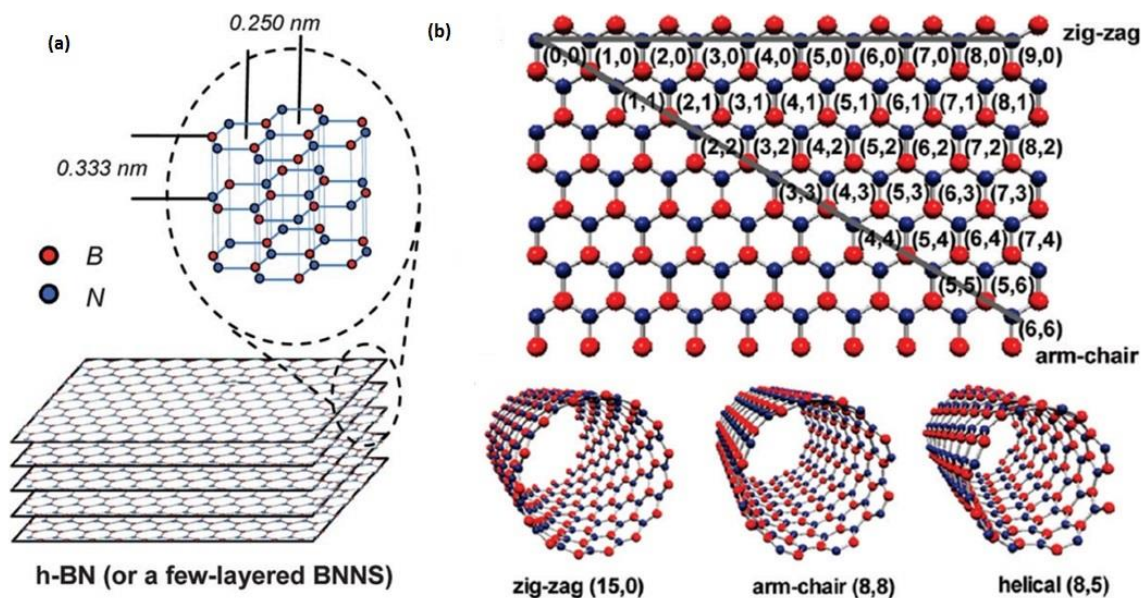


**Figure 3 (a) Structural basis of BN,<sup>56</sup> (b) Plane BN sheet with possible wrapping fashions and the corresponding (n,m) indices, also including ball and stick structural models of three types of single-walled BNNTs made of a wrapped BN layer: zig-zag (15,0), arm-chair (8,8), and a helical (8,5) tube.<sup>57</sup> [reproduced from ref. 56 and 57 with permission]**

The most important difference between h-BN and graphite is the strong ionic character of the B–N bond related to the significant difference in electronegativity of nitrogen and boron. According to Bader analysis there is a transfer of 2.19 electrons from boron to nitrogen and this ionic character leads to a large band gap opening.<sup>58</sup> Hence, in contrast to graphene where two bands cross each other at Fermi energy to exhibit semimetallic property, single layer of h-BN is insulating with a theoretical band gap of 4.5 eV.<sup>59</sup> Interesting electronic and mechanical properties of carbon nanotubes arose interest in the research of other nanotubes. Boron nitride nanotubes were first envisaged theoretically in 1994<sup>60-61</sup> followed by its experimental realization shortly after in 1995 by Chopra *et al.*<sup>62</sup> However, the electronic properties and hence the band gap of BNNTs do not depend on their radii and helicities unlike in the case of carbon nanotubes.<sup>63</sup>

Despite the negligible electrical conductivity, BN sheets have excellent thermal conductivities. The lattice thermal conductivity ( $\kappa_L$ ) of single-layer BN is found to be considerably larger than that of bulk BN, with room temperature values as high as  $600 \text{ Wm}^{-1}\text{K}^{-1}$ , one of the highest among non-carbon-based materials. These values are yet smaller than single-layer graphene ( $\kappa_L = 1500\text{-}2500 \text{ Wm}^{-1}\text{K}^{-1}$ ) because of stronger phonon-phonon scattering in single-layer BN.<sup>64</sup> BN exhibits excellent mechanical properties. Theoretically, layered h-BN possess a Young's modulus ranging from 0.198 to 0.328 TPa.<sup>65</sup> The bulk modulus of BN is found to be 160 Pa-m which is lesser than that of graphene (202 Pa-m). According to Golberg *et al.* for chemically exfoliated BNNSs, bending moduli increase with decreasing sheet thickness and achieves the theoretical value of 31.2 GPa for sheets with thickness less than 50 nm.<sup>66</sup> BNNTs are one of the stiffest insulating nanofibres as their Young's modulus ( $Y = 1.1\text{-}1.3 \text{ TPa}$ ) is close to that of CNTs ( $Y = 1.3\text{-}1.8 \text{ TPa}$ ). They are even more resistant to failure than CNTs, according to some recent experiments.<sup>67</sup> In addition to the excellent mechanical properties, BN exhibits high stability towards thermal oxidation compared to carbon nanostructures. Li *et al.* have studied the stability of monolayer, bilayer and trilayer BN sheets towards oxidation and found that monolayer BN remained unchanged till  $700 \text{ }^\circ\text{C}$  after which it started getting oxidized.<sup>68</sup> Oxidation for bilayer and trilayer BN started at slightly higher temperatures. However, monolayer graphene sheet started reacting with  $\text{O}_2$  at  $250 \text{ }^\circ\text{C}$ . Thin films of BN have been used for coating applications because of their high thermal stability. Recently, Liu *et al.* coated 5 nm thick layer of BN on Ni sheet and found that such a material was stable under a low oxygen partial pressure at a temperature as high as  $1100 \text{ }^\circ\text{C}$ .<sup>69</sup> Similarly, BN coated Cu, stainless steel and graphene sheets were also stable in oxygen at high temperatures. Thermal stability towards oxidation of multiwalled BNNTs also was found to be higher than the corresponding MWCNTs. Oxidation of BNNTs started only at  $800\text{-}850 \text{ }^\circ\text{C}$  whereas MWCNTs started getting oxidized at  $400 \text{ }^\circ\text{C}$  with the completion of oxidation at  $700 \text{ }^\circ\text{C}$ .<sup>70</sup> Insulating layered BN with graphene-like honeycomb structure and difference of only 1.7 % in the lattice constant compared to graphene makes it ideal to be used as substrate in high quality graphene growth.<sup>71-74</sup> Very weak interaction between BN and graphene layers is very important for this structure to be used in device applications.<sup>71</sup>

### 3.5 Borocarbonitrides

Graphene being a two dimensional gapless material with high charge carrier mobility has managed to realize many applications like field effect transistors, supercapacitors, sensors, water splitting catalysts *etc.* On the other hand, boron nitride (BN) which also has the two dimensional arrangements of boron and nitrogen behave like an insulator with a band gap of 4.7 eV. The main factor which is responsible for this stark difference is the polar B-N bond where the lone pair of electrons on p orbital is localized. On the other hand unpaired electron on p orbital in carbon in the case of graphene is delocalized throughout the layer. A hybrid material,  $B_xC_yN_z$ , which can be thought as a combination of both graphene and boron nitride has recently attracted much attention. This material which is also called borocarbonitride, is intermediate to graphene and boron nitride not only in terms of structure but also when electronic properties are considered. Figure 4 shows different ways in which graphene and BN components can be arranged to obtain borocarbonitrides with different properties. Metal

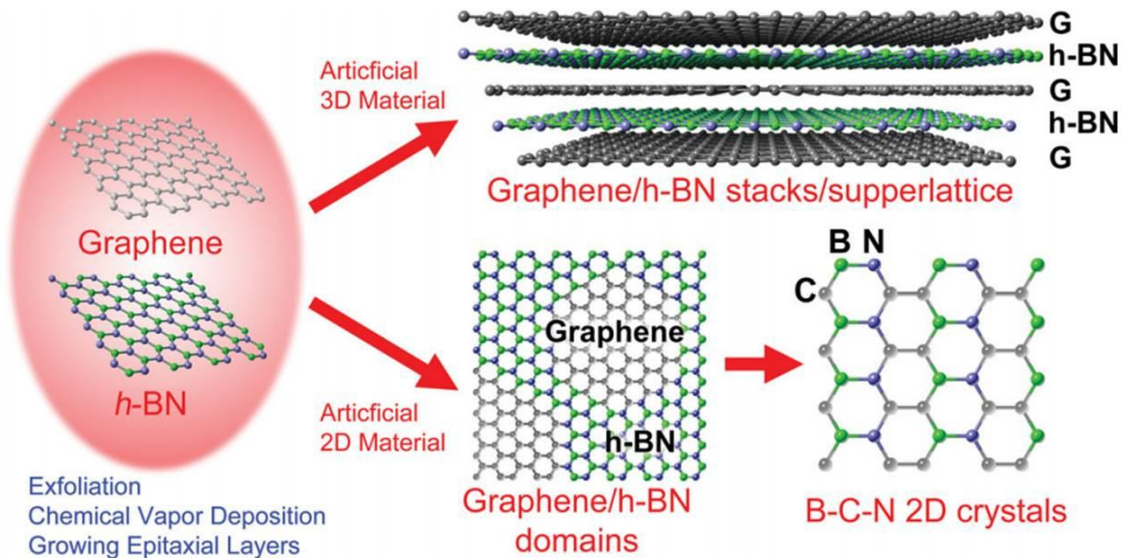


**Figure 4 Schematics of possible approaches for artificial B-N-C layers. Exfoliation, chemical vapor deposition, and epitaxial growth are three common methods to synthesize carbon- and BN-based atomic layered structures such as graphene and h-BN. The B-N-C layers could be constructed vertically for G/h-BN stacks/supperlattice, or in-plane for G/h-BN domains and finally B-C-N 2D crystals with a controllable stoichiometry.<sup>75</sup> [reproduced from ref. 75 with permission]**

to insulator transition has been observed in CVD grown  $B_xC_yN_z$  with high carbon contents where the presence of BN and graphene domains is predicted.<sup>76</sup> High thermal stability (combustion) in  $B_xC_yN_z$  would be expected when boron, carbon and nitrogen are randomly arranged avoiding N-N and B-B bonds. The same has been observed in  $B_xC_yN_z$  obtained by gas phase synthesis.<sup>77</sup> Layers of graphene and BN can be stacked on top of each other by methods like CVD and liquid phase exfoliation. Gao *et al.* artificially stacked graphene and BN by liquid phase exfoliation method which exhibited interesting electrical, mechanical, and optical properties different from their starting parent layers.<sup>78</sup>

Like other layered materials for example carbon nanotubes, nanotubes of borocarbonitrides are also studied for their structural and electronic properties. Both single-walled and multi-walled  $B_xC_yN_z$  have been considered for this purpose. There are many methods to obtain  $B_xC_yN_z$  nanotubes the most studied being chemical vapor deposition (CVD). Nanoparticles of transition metals are used as catalyst for the synthesis of nanotubes of  $B_xC_yN_z$  by the pyrolysis of single precursor containing boron, carbon and nitrogen atoms or a combination of two or three precursors. For example, nanotubes of the composition  $BC_2N$  were obtained by the pyrolysis of  $CH_3CN.BCl_3$  at 950-1000 °C using cobalt nanopowder as catalyst.<sup>79</sup> Wang *et al.* grew multiwalled carbon-rich  $B_xC_yN_z$  nanotubes on MgO supported Fe-Mo bimetallic catalyst by employing  $CH_4$ ,  $B_2H_6$  and ethylene diamine as reactant gases.<sup>80</sup> In a work by Kim *et al.*, it was demonstrated that different structure variants of multiwalled borocarbonitride nanotubes could be obtained in the CVD conditions just by changing C/B ratio.<sup>81</sup> When C:B is 1:1, BN nanotubes with outer layer of C were obtained while at higher value of C:B ratio (2:1), the entire product was carbon doped BN nanotubes. At low concentration of carbon (1:2), a mixture of carbon and BN nanotubes was obtained. Nanosheets of  $B_xC_yN_z$  also have been prepared by CVD technique by many workers.<sup>82-83</sup>

### **3.6 N-doped graphene**

Graphene, a single layer of  $sp^2$ -bonded carbon atoms, has many exotic properties like ambipolar electric field effect,<sup>84</sup> high mobility of charge carriers ( $2 \times 10^5 \text{ cm}^2/\text{V s}$ ),<sup>85-86</sup> anomalous quantum Hall effect,<sup>87-89</sup> massless relativistic carriers<sup>88</sup> *etc.* These properties make graphene a potential candidate for applications in electronics, sensors, batteries, supercapacitors, and catalysts.<sup>90-95</sup> It has been found that most of the as-made graphene FETs

are p-type because of the adsorbates like physisorbed oxygen molecules and/or moisture. In order to get high noise immunity and low static power consumption, graphene-based integrated circuits with complement FETs containing both n-type and p-type devices are required. According to recent theoretical predictions, in-plane substitution of nitrogen in carbon sites can modulate the electronic properties of graphene to an n-type semiconductor with a result of electron and hole transport features being asymmetric relative to the Dirac point.<sup>96</sup> This has been confirmed by many experimental studies lately.<sup>97-98</sup>

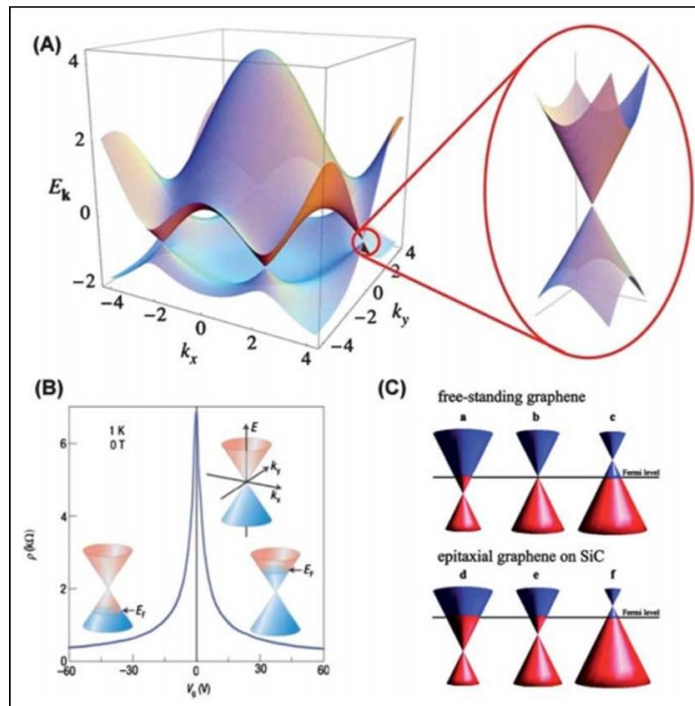


**Figure 5 (A) Left: the band structure of graphene in the honeycomb lattice with zoom-in of the energy bands close to one of the Dirac points, (B) Ambipolar electric field effect in single-layer graphene, (C) A schematic diagram of the position of the Dirac point and the Fermi level as a function of doping. The upper panel is n-type doped, pristine and p-type doped free standing graphene (a to c). The lower panel is n-type doped, pristine and p-type doped epitaxial graphene grown on silicon carbide (SiC) (d to f).<sup>99</sup> [reproduced from ref. 99 with permission]**

Fundamentally, nitrogen doped graphene can be obtained in two ways: direct synthesis and post treatment. Post treatment has the disadvantage of inclusion of nitrogen at the surface only whereas the direct synthesis has potential to provide homogenous distribution of nitrogen throughout the material. Chemical vapor deposition (CVD), arc discharge and solvothermal synthesis are some methods for the direct synthesis of N-graphene. In CVD method, N-graphene is grown in the presence of a catalyst (Cu, Ni *etc.*) from gaseous carbon

containing reactants like methane, ethylene, acetylene *etc.* and ammonia at high temperature.<sup>98, 100-101</sup> Alternatively, N-graphene can also be prepared by decomposing nitrogen containing liquid organic precursors like acetonitrile and pyridine at high temperature.<sup>102-103</sup> Deng *et al.* synthesized N-graphene solvothermally by the reaction of lithium nitride with tetrachloromethane at 250 °C. Nitrogen content as high as 16.4 % could be achieved by this method.<sup>104</sup> Rao *et al.*<sup>105-106</sup> employed arc discharge method to successfully obtained N-graphene in the presence of pyridine vapor or NH<sub>3</sub>. The N-graphene synthesized with nanodiamond as the carbon source showed higher nitrogen content than that synthesized from graphite. In post treatment approach, graphene or graphene oxide is treated with ammonia or the nitrogen containing compounds at high temperature. Treatment of graphene in ammonia atmosphere at high temperature gives rise to N-doping in low concentrations. Only 1.1 at. % N-doping could be achieved by Guo *et al.*<sup>107</sup> at 1100 °C whereas, Geng *et al.*<sup>108</sup> obtained doping concentration of 2.8 at. % at 800 - 900 °C. Later it was realized that lattice defects played important role in N-doping. Guo *et al.*,<sup>107</sup> in order to get N-graphene, irradiated pristine graphene with N<sup>+</sup> followed by annealing in NH<sub>3</sub>. Purpose of the N<sup>+</sup> irradiation was to introduce lattice defects. Interestingly, no N-doping was observed when graphene was annealed in NH<sub>3</sub> without prior N<sup>+</sup> irradiation. Reduced graphene oxide and graphene oxide which consist of large concentrations of defects have recently been used for highly doped N-graphene by many workers. Li *et al.*<sup>97</sup> carried out ammonolysis of graphene oxide at different temperatures to obtain varied amount of N-doping with maximum doping concentration (5 at. %) at 500 °C. Graphene oxide can also be treated with nitrogen containing compounds like urea or melamine at high temperature or in microwave conditions for N-doping.<sup>109-111</sup> N-doped graphene has been used in various applications like field effect transistors (FETs),<sup>98, 103, 112</sup> oxygen reduction catalysis in fuel cells,<sup>100-101, 113</sup> supercapacitors,<sup>114-117</sup> Li-ion battery<sup>102, 118-119</sup> *etc.*

#### **4. Scope of this thesis**

This thesis deals with the following studies:

**Part I**      Investigations of oxynitrides

**Part II**     N and N, F-codoped oxides

**Part III**    Investigations of nitrides

**Part IV**    Borocarbonitrides

**Part V**    Other studies



## 5. References

1. E. P. Perman and G. A. S. Atkinson, *Proc. R. Soc. Lond.* **1904**, *74*, 110-117.
2. A. M. Wynne, *J. Chem. Educ.* **1987**, *64*, 180.
3. X. Feng, Y.-J. Bai, B. Lü, C.-G. Wang, Y.-X. Qi, Y.-X. Liu, G.-L. Geng and Li, *Inorg. Chem.* **2004**, *43*, 3558-3560.
4. Y. Huang, Y. Gu, M. Zheng, Z. Xu, W. Zeng and Y. Liu, *Mater. Lett.* **2007**, *61*, 1056-1059.
5. I. P. Parkin and A. T. Rowley, *Adv. Mater.* **1994**, *6*, 780-782.
6. E. G. Gillan and R. B. Kaner, *Inorg. Chem.* **1994**, *33*, 5693-5700.
7. D. H. Gregory, *J. Chem. Soc., Dalton Trans.* **1999**, 259-270.
8. N. E. Brese and M. O'Keeffe, *J. Solid State Chem.* **1990**, *87*, 134-140.
9. U. Steinbrenner and A. Simon, *Z. Anorg. Allg. Chem.* **1998**, *624*, 228-232.
10. Y. Laurent, J. Lang and M.-T. Le Bihan, *Acta Crystallogr. Sect. B: Struct. Crystal. Crystal Chem.* **1968**, *24*, 494-499.
11. E. Keve and A. Skapski, *Inorg. Chem.* **1968**, *7*, 1757-1761.
12. W. R. Lambrecht, *Phys. Rev. B* **2000**, *62*, 13538.
13. C.-g. Duan, R. F. Sabiryanov, J. Liu, W. N. Mei, P. A. Dowben and J. R. Hardy, *Phys. Rev. Lett.* **2005**, *94*, 237201.
14. A. Svane, Z. Szotek, W. M. Temmerman and H. Winter, *Solid State Commun.* **1997**, *102*, 473-477.
15. G. A. Landrum, R. Dronskowski, R. Niewa and F. J. DiSalvo, *Chem. Eur. J.* **1999**, *5*, 515-522.
16. P. Wachter and E. Kaldis, *Solid State Commun.* **1980**, *34*, 241-244.
17. D. Li, Y. Haga, H. Shida and T. Suzuki, *Physica B: Condensed Matter* **1994**, *199*, 631-633.
18. H. Yamada, T. Fukawa, T. Muro, Y. Tanaka, S. Imada, S. Suga, D.-X. Li and T. Suzuki, *J. Phys. Soc. Jpn.* **1996**, *65*, 1000-1004.
19. D. X. Li, Y. Haga, H. Shida, T. Suzuki, Y. S. Kwon and G. Kido, *J. Phys.: Condens. Matter* **1997**, *9*, 10777.
20. J. M. Jakobsen, G. K. H. Madsen, J. E. Jørgensen, J. Staun Olsen and L. Gerward, *Solid State Commun.* **2002**, *121*, 447-452.

21. T. A. Yamamoto, T. Nakagawa, K. Sako, T. Arakawa and H. Nitani, *J. Alloys Compd.* **2004**, 376, 17-22.
22. C. Meyer, B. J. Ruck, J. Zhong, S. Granville, A. R. H. Preston, G. V. M. Williams and H. J. Trodahl, *Phys. Rev. B* **2008**, 78, 174406.
23. D. X. Li, A. Oyamada, K. Hashi, Y. Haga, T. Matsumura, H. Shida, T. Suzuki, T. Kasuya, A. Dönni and F. Hulliger, *J. Magn. Magn. Mater.* **1995**, 140–144, Part 2, 1169-1170.
24. P. Larson, W. R. L. Lambrecht, A. Chantis and M. van Schilfgaarde, *Phys. Rev. B* **2007**, 75, 045114.
25. E. Gregoryanz, C. Sanloup, M. Somayazulu, J. Badro, G. Fiquet, H.-K. Mao and R. J. Hemley, *Nature Mater.* **2004**, 3, 294-297.
26. J. C. Crowhurst, A. F. Goncharov, B. Sadigh, C. L. Evans, P. G. Morrall, J. L. Ferreira and A. J. Nelson, *Science* **2006**, 311, 1275-1278.
27. A. F. Young, C. Sanloup, E. Gregoryanz, S. Scandolo, R. J. Hemley and H.-k. Mao, *Phys. Rev. Lett.* **2006**, 96, 155501.
28. M. Yang, J. Oró-Solé, J. A. Rodgers, A. B. Jorge, A. Fuertes and J. P. Attfield, *Nat. Chem.* **2010**, 3, 47-52.
29. J. Grins, P.-O. Käll and G. Svensson, *J. Solid State Chem.* **1995**, 117, 48-54.
30. G. M. Veith, M. Greenblatt, M. Croft and J. B. Goodenough, *Mater. Res. Bull.* **2001**, 36, 1521-1530.
31. D. Armytage and B. E. F. Fender, *Acta Crystallogr., Sect. B: Struct. Crystallogr. Cryst. Chem.* **1974**, 30, 809-812.
32. F. Cheviré, F. Tessier and R. Marchand, *Mater. Res. Bull.* **2004**, 39, 1091-1101.
33. J. Guyader, F. F. Grekov, R. Marchand and J. Lang, *Rev Chim Miner* **1978**, 15, 431-438.
34. S. J. Clarke, B. P. Guinot, C. W. Michie, M. J. C. Calmont and M. J. Rosseinsky, *Chem. Mater.* **2001**, 14, 288-294.
35. K. Ueda, H. Kato, M. Kobayashi, M. Hara and M. Kakihana, *J. Mater. Chem. A* **2013**, 1, 3667-3674.
36. T. Matoba, K. Maeda and K. Domen, *Chem.–Eur. J.* **2011**, 17, 14731-14735.
37. J. P. Attfield, *Crystal Growth & Design* **2013**, 13, 4623-4629.

38. J. Oró-Solé, L. Clark, W. Bonin, J. P. Attfield and A. Fuertes, *Chem. Commun.* **2013**, 49, 2430-2432.
39. S. Balaz, S. H. Porter, P. M. Woodward and L. J. Brillson, *Chem. Mater.* **2013**, 25, 3337-3343.
40. Y.-I. Kim and P. M. Woodward, *J. Solid State Chem.* **2007**, 180, 3224-3233.
41. M. Jansen and H. P. Letschert, *Nature* **2000**, 404, 980-982.
42. A. Maegli, S. Yoon, E. Otal, L. Karvonen, P. Mandaliev and A. Weidenkaff, *J. Solid State Chem.* **2011**, 184, 929-936.
43. F. Cheviré, F. Tessier and R. Marchand, *Eur. J. Inorg. Chem.* **2006**, 2006, 1223-1230.
44. B. Siritanaratkul, K. Maeda, T. Hisatomi and K. Domen, *ChemSusChem* **2011**, 4, 74-78.
45. K. Maeda, M. Higashi, B. Siritanaratkul, R. Abe and K. Domen, *J. Am. Chem. Soc.* **2011**, 133, 12334-12337.
46. M. R. Hoffmann, S. T. Martin, W. Choi and D. W. Bahnemann, *Chem. Rev.* **1995**, 95, 69-96.
47. C. G. Van de Walle, *Phys. Rev. Lett.* **2000**, 85, 1012.
48. B. Chavillon, L. Cario, A. Renaud, F. Tessier, F. Cheviré, M. Boujtita, Y. Pellegrin, E. Blart, A. Smeigh, L. Hammarström, F. Odobel and S. Jobic, *J. Am. Chem. Soc.* **2011**, 134, 464-470.
49. M. Mapa and C. S. Gopinath, *Chem. Mater.* **2008**, 21, 351-359.
50. A. P. Bhirud, S. D. Sathaye, R. P. Waichal, L. K. Nikam and B. B. Kale, *Green Chemistry* **2012**, 14, 2790-2798.
51. X. Yang, A. Wolcott, G. Wang, A. Sobo, R. C. Fitzmorris, F. Qian, J. Z. Zhang and Y. Li, *Nano Lett.* **2009**, 9, 2331-2336.
52. C. Mao, Y. Zhao, X. Qiu, J. Zhu and C. Burda, *Phys. Chem. Chem. Phys.* **2008**, 10, 5633-5638.
53. A. B. Jorge, Y. Sakatani, C. Boissiere, C. Laberty-Roberts, G. Sauthier, J. Fraxedas, C. Sanchez and A. Fuertes, *J. Mater. Chem.* **2012**, 22, 3220-3226.
54. T. M. Suzuki, T. Nakamura, S. Saeki, Y. Matsuoka, H. Tanaka, K. Yano, T. Kajino and T. Morikawa, *J. Mater. Chem.* **2012**, 22, 24584-24590.

55. F. Zou, Z. Jiang, X. Qin, Y. Zhao, L. Jiang, J. Zhi, T. Xiao and P. P. Edwards, *Chem. Commun.* **2012**, 48, 8514-8516.
56. Y. Lin and J. W. Connell, *Nanoscale* **2012**, 4, 6908-6939.
57. D. Golberg, Y. Bando, Y. Huang, T. Terao, M. Mitome, C. Tang and C. Zhi, *ACS Nano* **2010**, 4, 2979-2993.
58. X. Jiang, J. Zhao and R. Ahuja, *J. Phys.: Condens. Matter* **2013**, 25, 122204.
59. Y.-H. Kim, K. J. Chang and S. G. Louie, *Phys. Rev. B* **2001**, 63, 205408.
60. A. Rubio, J. L. Corkill and M. L. Cohen, *Phys. Rev. B* **1994**, 49, 5081.
61. X. Blase, A. Rubio, S. G. Louie and M. L. Cohen, *Europhys. Lett.* **1994**, 28, 335.
62. N. G. Chopra, R. J. Luyken, K. Cherrey, V. H. Crespi, M. L. Cohen, S. G. Louie and A. Zettl, *Science* **1995**, 269, 966-967.
63. X. Blase, A. Rubio, S. G. Louie and M. L. Cohen, *Phys. Rev. B* **1995**, 51, 6868-6875.
64. L. Lindsay and D. A. Broido, *Phys. Rev. B* **2011**, 84, 155421.
65. L. Boldrin, F. Scarpa, R. Chowdhury and S. Adhikari, *Nanotechnology* **2011**, 22, 505702.
66. C. Li, Y. Bando, C. Zhi, Y. Huang and D. Golberg, *Nanotechnology* **2009**, 20, 385707.
67. R. Arenal, M.-S. Wang, Z. Xu, A. Loiseau and D. Golberg, *Nanotechnology* **2011**, 22, 265704.
68. L. H. Li, J. Cervenka, K. Watanabe, T. Taniguchi and Y. Chen, *ACS Nano* **2014**.
69. Z. Liu, Y. Gong, W. Zhou, L. Ma, J. Yu, J. C. Idrobo, J. Jung, A. H. MacDonald, R. Vajtai and J. Lou, *Nat. Commun.* **2013**, 4.
70. Y. Chen, J. Zou, S. J. Campbell and G. Le Caer, *Appl. Phys. Lett.* **2004**, 84, 2430-2432.
71. M. Bokdam, P. A. Khomyakov, G. Brocks, Z. Zhong and P. J. Kelly, *Nano Lett.* **2011**, 11, 4631-4635.
72. N. Kharche and S. K. Nayak, *Nano Lett.* **2011**, 11, 5274-5278.
73. L. Britnell, R. V. Gorbachev, R. Jalil, B. D. Belle, F. Schedin, A. Mishchenko, T. Georgiou, M. I. Katsnelson, L. Eaves and S. V. Morozov, *Science* **2012**, 335, 947-950.

74. R. Quhe, J. Zheng, G. Luo, Q. Liu, R. Qin, J. Zhou, D. Yu, S. Nagase, W.-N. Mei and Z. Gao, *NPG Asia Mater.* **2012**, *4*, e6.
75. L. Song, Z. Liu, A. L. M. Reddy, N. T. Narayanan, J. Taha-Tijerina, J. Peng, G. Gao, J. Lou, R. Vajtai and P. M. Ajayan, *Adv. Mater.* **2012**, *24*, 4878-4895.
76. L. Song, L. Balicas, D. J. Mowbray, R. B. Capaz, K. Storr, L. Ci, D. Jariwala, S. Kurth, S. G. Louie, A. Rubio and P. M. Ajayan, *Phys. Rev. B* **2012**, *86*, 075429.
77. N. Kumar, K. Raidongia, A. K. Mishra, U. V. Waghmare, A. Sundaresan and C. N. R. Rao, *J. Solid State Chem.* **2011**, *184*, 2902-2908.
78. G. Gao, W. Gao, E. Cannuccia, J. Taha-Tijerina, L. Balicas, A. Mathkar, T. N. Narayanan, Z. Liu, B. K. Gupta, J. Peng, Y. Yin, A. Rubio and P. M. Ajayan, *Nano Lett.* **2012**, *12*, 3518-3525.
79. M. Terrones, A. M. Benito, C. Manteca-Diego, W. K. Hsu, O. I. Osman, J. P. Hare, D. G. Reid, H. Terrones, A. K. Cheetham, K. Prassides, H. W. Kroto and D. R. M. Walton, *Chem. Phys. Lett.* **1996**, *257*, 576-582.
80. W. L. Wang, X. D. Bai, K. H. Liu, Z. Xu, D. Golberg, Y. Bando and E. G. Wang, *J. Am. Chem. Soc.* **2006**, *128*, 6530-6531.
81. S. Y. Kim, J. Park, H. C. Choi, J. P. Ahn, J. Q. Hou and H. S. Kang, *J. Am. Chem. Soc.* **2007**, *129*, 1705-1716.
82. L. Ci, L. Song, C. Jin, D. Jariwala, D. Wu, Y. Li, A. Srivastava, Z. F. Wang, K. Storr and L. Balicas, *Nat. Mater.* **2010**, *9*, 430-435.
83. M. Kawaguchi, T. Kawashima and T. Nakajima, *Chem. Mater.* **1996**, *8*, 1197-1201.
84. K. S. Novoselov, A. K. Geim, S. V. Morozov, D. Jiang, Y. Zhang, S. V. Dubonos, I. V. Grigorieva and A. A. Firsov, *Science* **2004**, *306*, 666-669.
85. X. Du, I. Skachko, A. Barker and E. Y. Andrei, *Nat. Nanotech.* **2008**, *3*, 491-495.
86. K. I. Bolotin, K. J. Sikes, Z. Jiang, M. Klima, G. Fudenberg, J. Hone, P. Kim and H. L. Stormer, *Solid State Commun.* **2008**, *146*, 351-355.
87. Y. Zhang, Y.-W. Tan, H. L. Stormer and P. Kim, *Nature* **2005**, *438*, 201-204.
88. K. S. A. Novoselov, A. K. Geim, S. V. Morozov, D. Jiang, M. I. Katsnelson, I. V. Grigorieva, S. V. Dubonos and A. A. Firsov, *Nature* **2005**, *438*, 197-200.
89. K. S. Novoselov, E. McCann, S. V. Morozov, V. I. Fal'ko, M. I. Katsnelson, U. Zeitler, D. Jiang, F. Schedin and A. K. Geim, *Nature Physics* **2006**, *2*, 177-180.

90. A. K. Geim and K. S. Novoselov, *Nat. Mater.* **2007**, *6*, 183-191.
91. K. Zhang, L. L. Zhang, X. Zhao and J. Wu, *Chem. Mater.* **2010**, *22*, 1392-1401.
92. M. J. Allen, V. C. Tung and R. B. Kaner, *Chem. Rev.* **2009**, *110*, 132-145.
93. A. V. Murugan, T. Muraliganth and A. Manthiram, *Chem. Mater.* **2009**, *21*, 5004-5006.
94. S. Stankovich, D. A. Dikin, G. H. Dommett, K. M. Kohlhaas, E. J. Zimney, E. A. Stach, R. D. Piner, S. T. Nguyen and R. S. Ruoff, *Nature* **2006**, *442*, 282-286.
95. Y.-M. Lin, C. Dimitrakopoulos, K. A. Jenkins, D. B. Farmer, H.-Y. Chiu, A. Grill and P. Avouris, *Science* **2010**, *327*, 662-662.
96. A. Lherbier, X. Blase, Y.-M. Niquet, F. Triozon and S. Roche, *Phys. Rev. Lett.* **2008**, *101*, 036808.
97. X. Li, H. Wang, J. T. Robinson, H. Sanchez, G. Diankov and H. Dai, *J. Am. Chem. Soc.* **2009**, *131*, 15939-15944.
98. D. Wei, Y. Liu, Y. Wang, H. Zhang, L. Huang and G. Yu, *Nano Lett.* **2009**, *9*, 1752-1758.
99. H. Liu, Y. Liu and D. Zhu, *J. Mater. Chem.* **2011**, *21*, 3335-3345.
100. Z. Luo, S. Lim, Z. Tian, J. Shang, L. Lai, B. MacDonald, C. Fu, Z. Shen, T. Yu and J. Lin, *J. Mater. Chem.* **2011**, *21*, 8038-8044.
101. L. Qu, Y. Liu, J.-B. Baek and L. Dai, *ACS Nano* **2010**, *4*, 1321-1326.
102. A. L. M. Reddy, A. Srivastava, S. R. Gowda, H. Gullapalli, M. Dubey and P. M. Ajayan, *ACS Nano* **2010**, *4*, 6337-6342.
103. Z. Jin, J. Yao, C. Kittrell and J. M. Tour, *ACS Nano* **2011**, *5*, 4112-4117.
104. D. Deng, X. Pan, L. Yu, Y. Cui, Y. Jiang, J. Qi, W.-X. Li, Q. Fu, X. Ma, Q. Xue, G. Sun and X. Bao, *Chem. Mater.* **2011**, *23*, 1188-1193.
105. L. S. Panchakarla, K. S. Subrahmanyam, S. K. Saha, A. Govindaraj, H. R. Krishnamurthy, U. V. Waghmare and C. N. R. Rao, *Adv. Mater.* **2009**, *21*, 4726-4730.
106. A. Ghosh, D. J. Late, L. Panchakarla, A. Govindaraj and C. Rao, *J. Exp. Nanosci.* **2009**, *4*, 313-322.
107. B. Guo, Q. Liu, E. Chen, H. Zhu, L. Fang and J. R. Gong, *Nano Lett.* **2010**, *10*, 4975-4980.

108. D. Geng, Y. Chen, Y. Chen, Y. Li, R. Li, X. Sun, S. Ye and S. Knights, *Energy Environ. Sci.* **2011**, *4*, 760-764.
109. Z.-H. Sheng, L. Shao, J.-J. Chen, W.-J. Bao, F.-B. Wang and X.-H. Xia, *ACS Nano* **2011**, *5*, 4350-4358.
110. Z. Lin, G. Waller, Y. Liu, M. Liu and C.-P. Wong, *Adv. Energy Mater.* **2012**, *2*, 884-888.
111. K. Gopalakrishnan, A. Govindaraj and C. N. R. Rao, *J. Mater. Chem. A* **2013**, *1*, 7563-7565.
112. C. Zhang, L. Fu, N. Liu, M. Liu, Y. Wang and Z. Liu, *Adv. Mater.* **2011**, *23*, 1020-1024.
113. Y. Shao, S. Zhang, M. H. Engelhard, G. Li, G. Shao, Y. Wang, J. Liu, I. A. Aksay and Y. Lin, *J. Mater. Chem.* **2010**, *20*, 7491-7496.
114. H. M. Jeong, J. W. Lee, W. H. Shin, Y. J. Choi, H. J. Shin, J. K. Kang and J. W. Choi, *Nano Lett.* **2011**, *11*, 2472-2477.
115. B. Jiang, C. Tian, L. Wang, L. Sun, C. Chen, X. Nong, Y. Qiao and H. Fu, *Appl. Surf. Sci.* **2012**, *258*, 3438-3443.
116. Y. Qiu, X. Zhang and S. Yang, *Phys. Chem. Chem. Phys.* **2011**, *13*, 12554-12558.
117. L. Sun, L. Wang, C. Tian, T. Tan, Y. Xie, K. Shi, M. Li and H. Fu, *RSC Adv.* **2012**, *2*, 4498-4506.
118. Z.-S. Wu, W. Ren, L. Xu, F. Li and H.-M. Cheng, *ACS Nano* **2011**, *5*, 5463-5471.
119. H. Wang, C. Zhang, Z. Liu, L. Wang, P. Han, H. Xu, K. Zhang, S. Dong, J. Yao and G. Cui, *J. Mater. Chem.* **2011**, *21*, 5430-5434.





*Part I*  
*Investigations*  
*of oxynitrides*

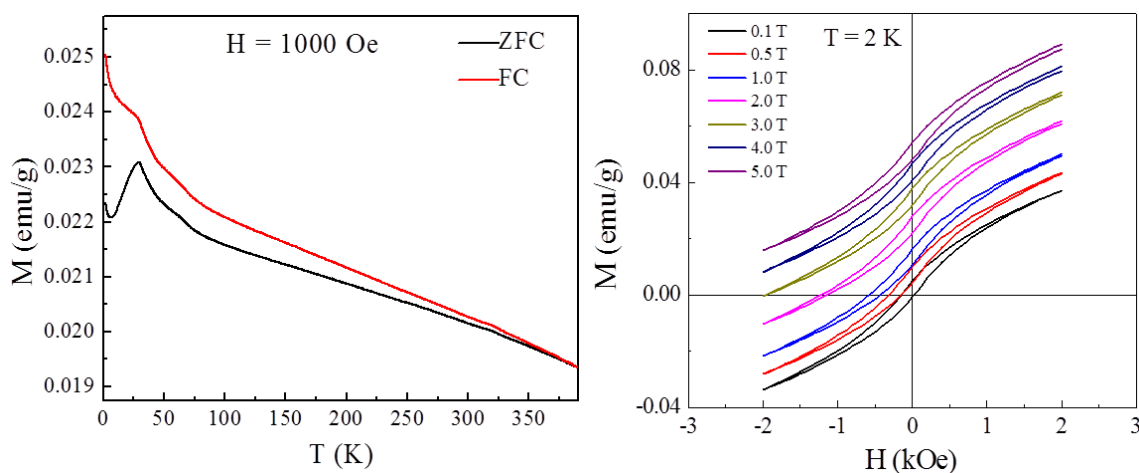


# Chapter I.1

## Rare earth (La, Pr and Nd) vanadium oxynitrides: Synthesis, structure, magnetic and electrical properties\*

### Summary

The vanadium oxynitride perovskites  $\text{LaVO}_{3-x}\text{N}_x$  ( $0 \leq x \leq 0.9$ ),  $\text{NdVO}_{3-x}\text{N}_x$  ( $0 \leq x \leq 1$ ) and the new praseodymium analogues  $\text{PrVO}_{3-x}\text{N}_x$  ( $0 \leq x \leq 0.76$ ) have been prepared by treatment of  $\text{RVO}_4$  oxides ( $\text{R} = \text{La, Pr and Nd}$ ) in flowing  $\text{NH}_3$  gas. Variable temperature neutron diffraction studies show that  $\text{NdVO}_2\text{N}$  and  $\text{PrVO}_{2.24}\text{O}_{0.76}$  have orthorhombic  $Pbnm$  symmetry between 3.5 and 300 K, but  $\text{LaVO}_{2.11}\text{N}_{0.89}$  undergoes a broad  $Pbnm$  and  $R-3c$  structural transition over this temperature range.  $\text{LaVO}_{3-x}\text{N}_x$  shows divergence between ZFC and FC magnetizations with a peak at 29 K which is confirmed to be due to spin-glass transition by AC magnetic susceptibility measurements. Magnetization of  $\text{NdVO}_2\text{N}$  can be explained by the combination of paramagnetic spins of  $\text{Nd}^{3+}$ , temperature independent Pauli paramagnetic  $\text{V}^{4+}$  and a small amount of  $\text{V}^{3+}$  impurity. The main feature in the otherwise weak ferromagnetic  $\text{PrVO}_{2.24}\text{N}_{0.76}$  is a sudden drop in ZFC magnetization near 10 K which is possibly due to the re-entrant spin-glass transition at this temperature. All the three materials show semiconducting behavior.



\* A paper based on these studies has appeared in *J. Mater. Chem. C*, 2014

## 1. Introduction

Narrow 3d bands and strong Coulomb correlations in first-row transition metal oxides impart interesting electronic and magnetic properties. Single-valent transition metal oxides with perovskite structures have localized or itinerant electrons depending on the strength of 180° M-O-M interaction relative to the on-site Coulomb energy ( $U_{eff}$ ).<sup>1-2</sup> Itinerant electron behavior is observed where M-O-M interactions are dominant over  $U_{eff}$ . Such conditions are found in 3d<sup>1</sup> configurations of V<sup>4+</sup>. For example, SrVO<sub>3</sub> and CaVO<sub>3</sub> (V-3d<sup>1</sup>) are correlated metals (itinerant electron systems) whereas LaVO<sub>3</sub> and YVO<sub>3</sub> (V-3d<sup>2</sup>) are insulators (localized electron systems).<sup>3-6</sup> Complete solid solutions of perovskite La<sub>1-x</sub>Ca<sub>x</sub>VO<sub>3</sub>, Y<sub>1-x</sub>Ca<sub>x</sub>VO<sub>3</sub> and La<sub>1-x</sub>Sr<sub>x</sub>VO<sub>3</sub> are investigated where the intermediate compositions show metal to insulator transition.<sup>6-8</sup> SrVO<sub>3</sub> and CaVO<sub>3</sub> exhibit temperature independent Pauli paramagnetism whereas long-range antiferromagnetic interactions are observed in RVO<sub>3</sub> (R = rare earth). Magnetic behaviors of RVO<sub>3</sub> are investigated in detail with fascinating properties like anomalous diamagnetism in LaVO<sub>3</sub> and YVO<sub>3</sub>, orbital quantum fluctuations in PrVO<sub>3</sub> etc.<sup>9-11</sup>

Playing with A site substitution is not the only way to change the structural and electronic properties of such perovskites. The other strategy can be the anion substitution (especially nitride or fluoride ion) in non-stoichiometric or stoichiometric fashion. The first method, for example doping nitrogen in SrTiO<sub>3</sub>, imparts significant variation in electronic properties in terms of the position of valence band which eventually controls the optical properties of the material.<sup>12</sup> Substitution of such kind is discussed in detail in Part II of the thesis. On the other hand, the substitution of the stoichiometric fashion includes oxyfluorides and oxynitrides. Oxynitrides are of much importance because of their interesting optical properties and their applications as pigments, dielectrics, photocatalysts, colossal magnetoresistive materials etc.<sup>13-19</sup> Recently, by employing neutron diffraction technique, deeper insight of the structure of oxynitrides could be gained by studying the ordering of oxide and nitride ions in the lattice.<sup>20-21</sup> The study of such anion ordering is possible because of the very different neutron scattering lengths of oxygen (5.83 fm) and nitrogen (9.36 fm).

Compound	Precursors and reaction temperature	Study	References
BaTaO <sub>2</sub> N	Sol-gel derived amorphous Ba <sub>2</sub> Ta <sub>2</sub> O <sub>7</sub> , BaCO <sub>3</sub> + Ta <sub>2</sub> O <sub>5</sub> (950-1000 °C), BaO + TaON (1500 °C)	Structure, dielectric properties, photocatalysis of water splitting <i>etc</i>	17, 22-29
SrTaO <sub>2</sub> N	Sol-gel derived amorphous Sr <sub>2</sub> Ta <sub>2</sub> O <sub>7</sub> , flux grown crystalline Sr <sub>2</sub> Ta <sub>2</sub> O <sub>7</sub> , SrCO <sub>3</sub> + Ta <sub>2</sub> O <sub>5</sub> (950-1000 °C), SrO + TaON (1500 °C)	Structure, dielectric properties, photocatalysis of water splitting <i>etc</i>	17, 20, 22, 25, 27, 29-31
CaTaO <sub>2</sub> N	Sol-gel derived amorphous Ca <sub>2</sub> Ta <sub>2</sub> O <sub>7</sub> , CaCO <sub>3</sub> + Ta <sub>2</sub> O <sub>5</sub> (950-1000 °C)	Structure, dielectric properties, photocatalysis of water splitting <i>etc</i>	17, 22, 25, 27, 31
Ba <sub>1-x</sub> Sr <sub>x</sub> TaO <sub>2</sub> N	BaTaO <sub>2</sub> N + SrTaO <sub>2</sub> N (950 °C)	Structure solution by neutron diffraction	32
BaNbO <sub>2</sub> N	Sol-gel derived amorphous Ba <sub>2</sub> Nb <sub>2</sub> O <sub>7</sub> , (950-1000 °C)	Neutron diffraction study, photocatalysis of water splitting <i>etc</i>	22-23, 26, 33
SrNbO <sub>2</sub> N	Sol-gel derived amorphous Sr <sub>2</sub> Nb <sub>2</sub> O <sub>7</sub> , SrCO <sub>3</sub> + Nb <sub>2</sub> O <sub>5</sub> (950-1000 °C)	Structure, Photocatalysis of water splitting <i>etc</i>	20, 22, 34-35
CaNbO <sub>2</sub> N	Sol-gel derived amorphous Ca <sub>2</sub> Nb <sub>2</sub> O <sub>7</sub> , CaCO <sub>3</sub> + Nb <sub>2</sub> O <sub>5</sub> (950-1000 °C)	Synthesis, photocatalysis of water splitting <i>etc</i>	22, 33
LaTaO <sub>2</sub> N	Sol-gel derived amorphous LaTaO <sub>4</sub> , crystalline LaTaO <sub>4</sub> (850-950 °C)	Structure analysis by XRD and neutron diffraction	31
LnTaO <sub>2</sub> N (Ln= Nd, Sm, Gd, Eu)	Sol-gel derived amorphous LnTaO <sub>4</sub> , crystalline LnTaO <sub>4</sub> (950 °C)	Synthesis and structure	36-37
Ca <sub>1-x</sub> La <sub>x</sub> TaO <sub>2-x</sub> N <sub>1+x</sub> (0.05 < x < 1)	CaCO <sub>3</sub> , La <sub>2</sub> O <sub>3</sub> , Ta <sub>2</sub> O <sub>5</sub> aq (850 °C)	Pigment characteristics	15

Compound	Precursors and reaction temperature	Study	References
$A_{0.5}La_{0.5}TaO_{1.5}N_{1.5}$ (A = Ca, Sr, Ba)	Amorphous oxide precursor (1000 °C)	Structure analysis by XRD and neutron diffraction	38
$Na_xLa_{1-x}TaO_{1+2x}N_{2-2x}$	Amorphous oxide precursor (1000 °C)	Water oxidation study	39
$LaNbON_2$	Amorphous $LaNbO_4$ with flux (950 °C)	Structure and optical properties	40
$LnNbON_2$ (Ln = Pr, Nd)	$LnNbO_4$ (950 °C)	Structure and magnetic properties	41
$EuNbO_2N$	$EuNbO_4$ , 950 °C	Magnetocapacitance	42
$LaVO_{2-x}N_x$ (0 < x < 0.9)	Monazite $LaVO_4$ (650-850 °C)	Magnetic, electrical and thermal transport properties	43
$NdVO_2N$	$NdVO_4$ (700 °C)	Structure and magnetic properties	44
$LaTiO_2N$	Amorphous and crystalline $La_2Ti_2O_7$ (850-950 °C), mixed oxide precursor with NaCl flux (900 °C)	Structure analysis by XRD and neutron diffraction, photocatalytic water splitting	45-47
$NdTiO_2N$	$Nd_2Ti_2O_7$ (950 °C)	Structure analysis by XRD and neutron diffraction	45
$LaZrO_2N$	Amorphous $La_2Zr_2O_7$ (950 °C)	Structure analysis by XRD and neutron diffraction	45
$RZrO_2N$ (R = Pr, Nd and Sm)	$R_2O_3$ and $Zr_2ON_2$ (1200-1500 °C, 2-3 GPa)	Structure analysis by XRD and neutron diffraction	48
$SrMoO_2N$	$SrMoO_4$ (800 °C)	Magnetic, electrical and thermal transport	49
$SrMoO_{2.5}N_{0.5}$	$SrMoO_4$ (800 °C)	Structure and magnetic properties	50
$SrMoO_{2.6}N_{0.4}$	$SrMoO_4$ (750 °C)	Structure and magnetic and electrical properties	51
$CaMoO_{1.7}N_{1.3}$	$CaMoO_4$ (800 °C)	Structure analysis by XRD and neutron diffraction	52
$SrWO_2N$	$SrWO_4$ (900 °C)	Structure and magnetic properties	50
$SrWO_{1.63}N_{1.37}$	$SrWO_4$ (900 °C)	Structure analysis by XRD and neutron diffraction	53

Compound	Precursors and reaction temperature	Study	References
$\text{Ca}_x\text{Sr}_{1-x}\text{WO}_2\text{N}$ ( $x = 0, 0.25, 0.5$ and $1$ )	$\text{Ca}_x\text{Sr}_{1-x}\text{WO}_4$ ( $900^\circ\text{C}$ )	Structure, optical and electronic properties	54
$\text{LaWO}_x\text{N}_{3-x}$ ( $x = 0.6-0.8$ )	$\text{La}_2\text{W}_2\text{O}_9$ ( $700-900^\circ\text{C}$ )	Electrical conductivity and thermoelectric power	55
$\text{LaWO}_{0.6}\text{N}_{2.4}$	$\text{La}_2\text{W}_2\text{O}_9$	Structure analysis by neutron diffraction	56
$\text{EuWO}_{1.58}\text{N}_{1.42}$	$\text{Eu}_2\text{W}_2\text{O}_9$ ( $800^\circ\text{C}$ )	Structure and magnetic properties	57
$\text{EuWO}_{1+x}\text{N}_{2-x}$ ( $0.16 \leq x \leq 0.46$ )	$\text{Eu}_2\text{W}_2\text{O}_9$ ( $600-850^\circ\text{C}$ )	Colossal magnetoresistance	58

Oxynitrides of different structures are known among which compounds with perovskite-type structure are studied in most detail. Table above enlists oxynitrides with perovskite structure along with their synthesis methods.

## 2. Scope of the present investigation

Oxynitrides of first row transition metals with finite number of d electrons are very rare. Formation of such oxynitrides would be highly desirable because of their interesting magnetic and electrical properties. Recently, a double perovskite,  $\text{Sr}_2\text{FeMoO}_5\text{N}$ ,<sup>59</sup> has been reported with iron in the highest oxidation state ( $\text{Fe}^{4+}$ ). In this respect,  $\text{RVO}_2\text{N}$  would be an exciting candidate because of V-3d<sup>1</sup> configuration. Unlike inclusion of alkaline earth metal in the rare earth site in  $\text{RVO}_3$ , this is an alternate to achieve V-3d<sup>1</sup> configuration. Merchand *et al.* prepared  $\text{LaVO}_{3-x}\text{N}_x$  ( $1 \leq x \leq 0.9$ ) but were unable to observe any metal to insulator transition as in the case of cation-doped  $\text{RVO}_3$ . Here, in addition to  $\text{LaVO}_{3-x}\text{N}_x$ , we have prepared  $\text{PrVO}_{2.24}\text{N}_{0.76}$  and  $\text{NdVO}_2\text{N}$  and investigated their structural, electrical transport and magnetic properties.

## 3. Experimental section

The oxynitrides  $\text{LaVO}_{3-x}\text{N}_x$ ,  $\text{PrVO}_{3-x}\text{N}_x$  and  $\text{NdVO}_{3-x}\text{N}_x$  were prepared by treatment of  $\text{LaVO}_4$ ,  $\text{PrVO}_4$  and  $\text{NdVO}_4$  under  $\text{NH}_3(\text{g})$  between  $650$  and  $800^\circ\text{C}$ . The oxide precursors were prepared by treatment of pellets containing stoichiometric amounts of  $\text{La}_2\text{O}_3$  (Aldrich,

99.9 %), Pr<sub>6</sub>O<sub>11</sub> (Aldrich, 99.9 %) or Nd<sub>2</sub>O<sub>3</sub> (Aldrich, 99.9 %) and V<sub>2</sub>O<sub>5</sub> (Aldrich, 99.9 %) at 900 °C for 15 hours. The rare earth oxides were previously treated at 900 °C for 12 hours. LaVO<sub>4</sub> (monazite) and NdVO<sub>4</sub> (zircon) were prepared in air whereas PrVO<sub>4</sub> (zircon) was prepared in Ar in order to prevent the oxidation of Pr<sup>3+</sup>. Ammonia flow rates were between 180 and 600 cm<sup>3</sup>/minute and the treatment times varied between 20 and 250 hours, with slow cooling to room temperature in ammonia and with intermediate regrinding.

X-ray diffraction data were collected either on a Siemens D5000 or a Rigaku diffractometer using Cu K $\alpha$  radiation ( $\lambda = 1.5418 \text{ \AA}$ ). Rietveld refinements from X-ray diffraction data were performed using the program *Fullprof*.<sup>60</sup> Temperature dependent powder neutron diffraction data were collected on the D2B powder diffractometer at the high flux neutron reactor of the Institut Laue-Langevin, France. Nitrogen contents were determined by combustion analysis using a Thermo Fisher Scientific instrument.

DC magnetization was carried out in SQUID VSM (Quantum Design, USA). AC magnetic susceptibility and resistivity were measured in a Physical Property Measurement System (Quantum Design, USA). Resistivity measurements were carried out on sintered pellets using four probe technique in Physical Property Measurement System (Quantum Design, USA).

#### 4. Results and discussion

Synthesis of RVO<sub>3-x</sub>N<sub>x</sub> requires several rounds of ammonolysis of RVO<sub>4</sub>. After first few rounds, RVO<sub>4</sub> transforms to corresponding RVO<sub>3</sub> with negligible amount of nitrogen as confirmed from XRD, elemental analysis and magnetic properties. In this process, V<sup>4+</sup> reduces to V<sup>3+</sup>. On further ammonolysis, oxygen atoms in RVO<sub>3</sub> start getting replaced by nitrogen atoms to give rise to RVO<sub>3-x</sub>N<sub>x</sub> which is accompanied by the oxidation of V<sup>3+</sup> into V<sup>4+</sup>. Such oxidation of metal ions is very rare in the synthesis of oxynitrides considering the reducing conditions of ammonolysis reaction. Here, nitridation which is an oxidation process competes with reduction. Reduction reaction can be minimized by carrying out the ammonolysis reaction at temperatures as low as possible. Retuerto *et al.* synthesized Sr<sub>2</sub>FeMoO<sub>5</sub>N at 650 °C by ammonolysis reaction of oxide precursor.<sup>59</sup>



#### 4.1 LaVO<sub>2.09</sub>N<sub>0.91</sub>

LaVO<sub>2.09</sub>N<sub>0.91</sub> is prepared by the ammonolysis of LaVO<sub>4</sub> at 750 °C. LaVO<sub>4</sub> has a monoclinic unit cell with monazite-type structure. The other crystal type which is also a metastable phase has zirconite-type tetragonal structure. Marchand *et al.* observed that zirconite-LaVO<sub>4</sub> does not yield in high nitrogen containing oxynitride. Except LaVO<sub>4</sub>, all other RVO<sub>4</sub> (R = rare earth) crystallize only in zirconite-type tetragonal structure. XRD patterns of RVO<sub>4</sub> (R = La, Pr and Nd) are shown in Figure 1. Like RVO<sub>3</sub>, oxynitrides with formula RVO<sub>3-x</sub>N<sub>x</sub> also crystallize in GdFeO<sub>3</sub> type orthorhombic perovskite structure. XRD patterns along with the Le Bail fittings of LaVO<sub>2.09</sub>N<sub>0.91</sub>, PrVO<sub>2.24</sub>N<sub>0.76</sub> and NdVO<sub>2</sub>N are shown in Figure 2. Interestingly, XRD pattern of LaVO<sub>2.09</sub>N<sub>0.91</sub> could not be fitted by a model containing only *Pbnm* phase.

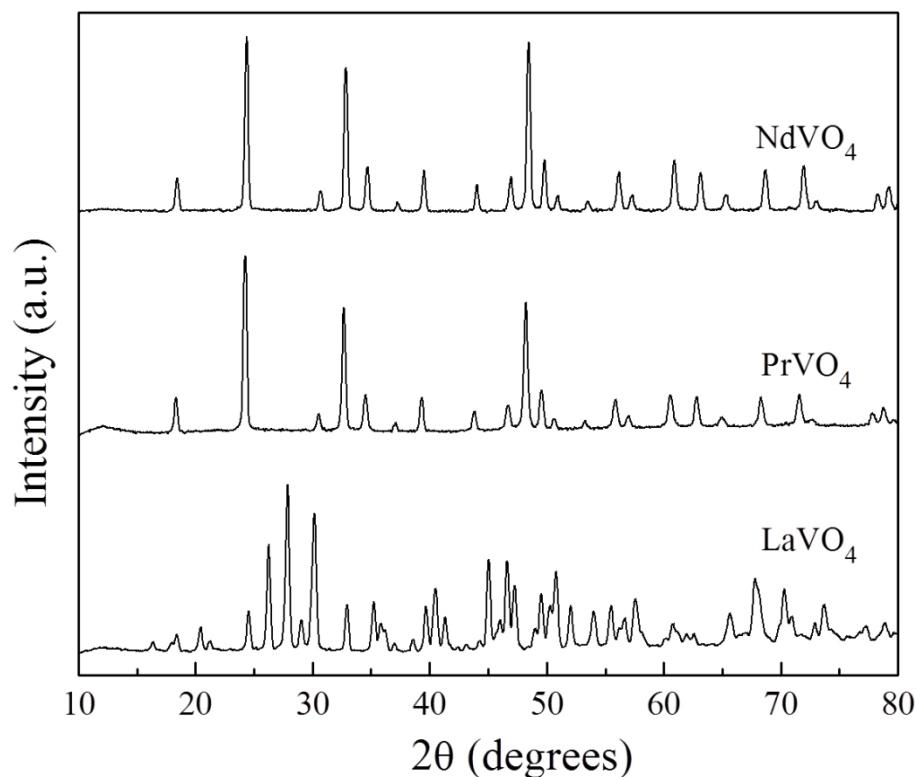


**Figure 1** XRD patterns of RVO<sub>4</sub> (R = La, Pr and Nd)

When in addition to *Pbnm*, *R-3c* is included in the model, the fitting improves significantly as can be seen in the Figure 3.  $\chi^2$  value for the fitting with a model containing both *Pbnm* and *R-3c* phases is 1.91 while it is 4.03 when the model considers only *Pbnm* phase. By neutron diffraction we have shown that LaVO<sub>2.09</sub>N<sub>0.91</sub> undergoes a structural phase transition from a

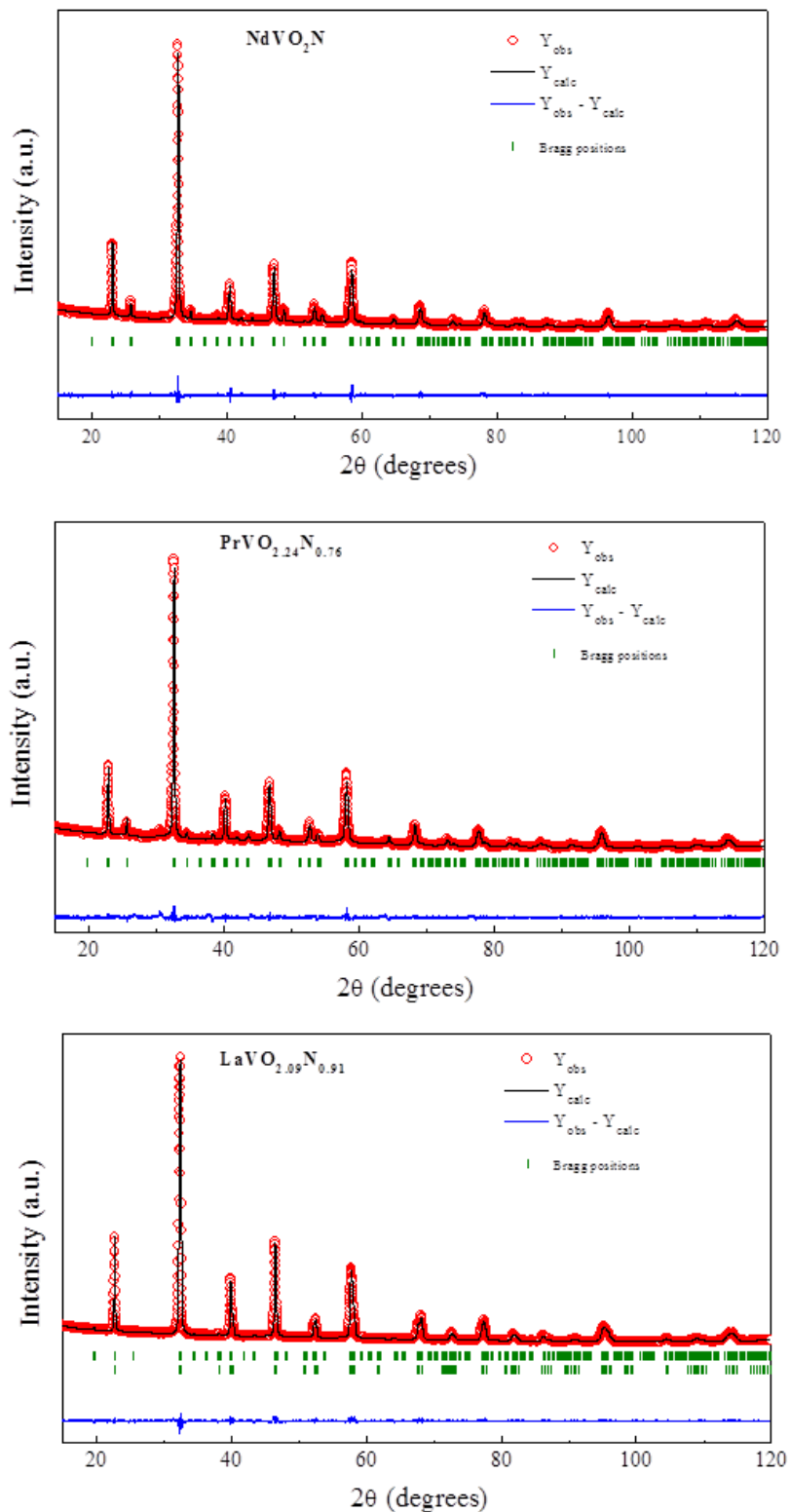


Figure 2 XRD patterns of  $LaVO_{2.09}N_{0.91}$ ,  $PrVO_{2.24}N_{0.76}$  and  $NdVO_2N$  along with Le Bail fitting

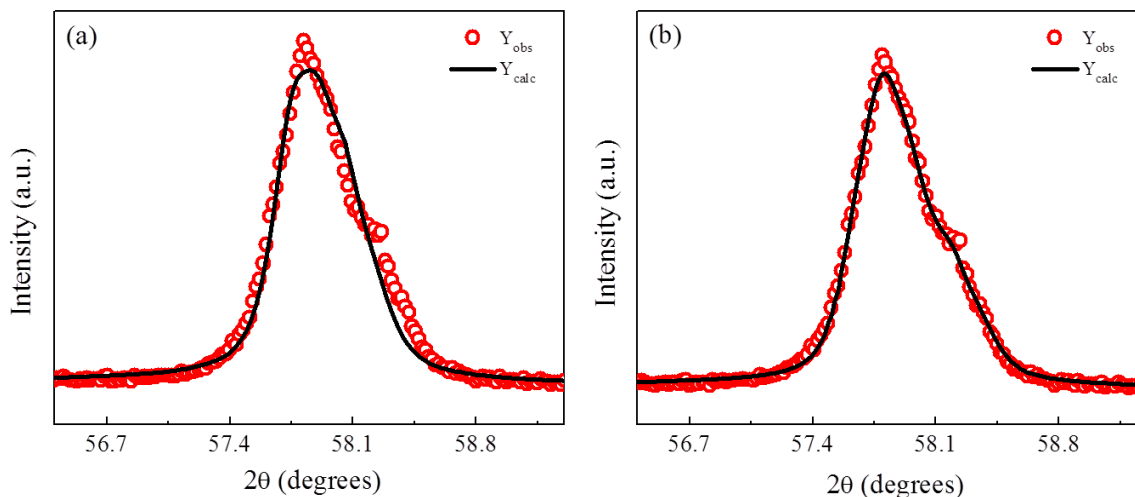


Figure 3 Le Bail fitting of  $\text{LaVO}_{2.09}\text{N}_{0.91}$  with a model containing (a) orthorhombic phase and (b) both orthorhombic and monoclinic phases

Table 1 Cell parameters of oxynitrides phases.

Compound	Cell parameters (Å)			Cell volume (Å) <sup>3</sup>
	a	b	c	
$\text{LaVO}_{2.09}\text{N}_{0.91}$ ( <i>Pbnm</i> )	5.5382(3)	5.5098(6)	7.7765(7)	237.294(34)
$\text{LaVO}_{2.09}\text{N}_{0.91}$ ( <i>R-3c</i> )	5.5344(2)	5.5344(2)	13.4274(5)	356.175(20)
$\text{PrVO}_{2.24}\text{N}_{0.76}$ ( <i>Pbnm</i> )	5.4876(2)	5.5201(3)	7.7576(4)	234.995(19)
$\text{NdVO}_2\text{N}$ ( <i>Pbnm</i> )	5.4677(1)	5.5049(2)	7.7347(2)	232.808(11)

low temperature orthorhombic (*Pbnm*) phase to a high temperature rhombohedral (*R-3c*) phase with both the phases co-existing at 3.5 and 300 K. The proportions of phases (orthorhombic to rhombohedral), are found to be 82:18 and 19:81 at 3.5 and 300 K respectively. The transition from low temperature *Pbnm* to high temperature *R-3c* phases is quite common in rare earth-based oxide perovskites, for example  $\text{LaAlO}_3$ ,  $\text{LaFeO}_3$ ,  $\text{La}_{1-x}\text{Sr}_x\text{VO}_3$  (for  $0.23 < x < 0.40$ )<sup>61</sup> and some doped  $\text{RMnO}_3$  phases.<sup>62</sup> However, the transition has not previously been reported in an oxynitride system. There is no group-subgroup relation between *Pbnm* and *R-3c* so the transition is first order and phase coexistence is often observed. For  $\text{LaVO}_{2.11}\text{N}_{0.89}$  the transition is centred at  $\sim 200$  K but both phases are observed

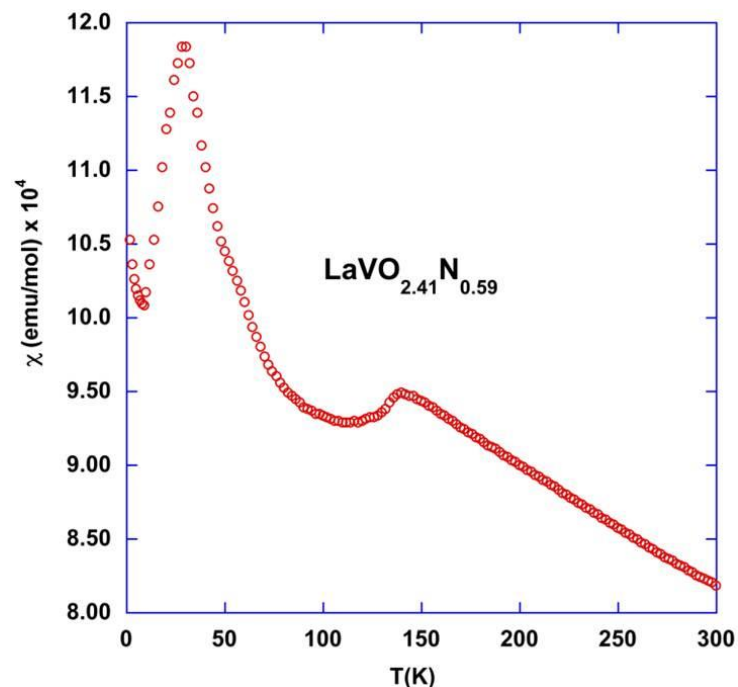


Figure 4 FC magnetization of  $\text{LaVO}_{2.41}\text{N}_{0.59}$  at 1T field

between 3.5 and 300 K. Table 1 shows cell parameters of orthorhombic and monoclinic phases of  $\text{LaVO}_{2.09}\text{N}_{0.91}$  as well as of  $\text{PrVO}_{2.24}\text{N}_{0.76}$  and  $\text{NdVO}_2\text{N}$ . Marchand *et al.* reported that with increasing N content (decreasing  $\text{V}^{3+}$  content), the antiferromagnetic (AFM) transition gradually disappears and there is no magnetic anomaly for  $\text{LaVO}_{2.1}\text{N}_{0.9}$  down to liquid nitrogen temperature.<sup>43</sup> We have investigated two samples with

compositions  $\text{LaVO}_{2.41}\text{N}_{0.59}$  and  $\text{LaVO}_{2.09}\text{N}_{0.91}$ .  $\text{LaVO}_{2.41}\text{N}_{0.59}$  shows a magnetic anomaly at 140 K which coincides with the Néel temperature of  $\text{LaVO}_3$  and a low temperature peak at 29 K (Figure 4). For  $\text{LaVO}_{2.09}\text{N}_{0.91}$ , the 140 K anomaly disappears but the low temperature peak remains, showing that it is characteristic of the oxynitride. It can be seen that the magnetization shows a divergence between ZFC and FC magnetizations right from 390 K indicating a blocking temperature above 390 K. Similar divergence is found between ZFC and FC magnetizations in  $\text{La}_{0.4}\text{Ca}_{0.6}\text{VO}_3$  and could be attributed to the lattice defects.<sup>63</sup> Such lattice defects especially oxygen vacancy is expected in our oxynitride systems considering the highly reducing reaction conditions. Absence of paramagnetic character as well as other effects as implications of these lattice defects will be discussed later in this chapter.

In order to understand the origin of the low temperature (29 K) peak, we have studied  $\text{LaVO}_{2.09}\text{N}_{0.91}$  in detail. Figure 5 shows the zero field cooled (ZFC) and field cooled (FC) magnetization of  $\text{LaVO}_{2.09}\text{N}_{0.91}$  at 1 kOe. The peak at 29 K and the divergence between ZFC and FC measurements below this temperature hints toward a spin glass state. The large divergence above 29 K in ZFC and FC magnetizations which is attributed to lattice defects results in ferromagnetic hysteresis loop at room temperature. Figure 6(a) shows magnetic

hysteresis loops at 2 and 300 K. Hysteresis at 2 K is because of the combination of effects of spin glass state as well as the lattice defects while at 300 K only lattice defects play role. Coercive fields ( $H_C$ ) at 2 and 300 K are 82 and 40 Oe respectively as shown in Figure 6(b).

Recently, DC magnetization measurements have been used to probe ageing effects of the spin glasses.<sup>64-66</sup> In order to observe a memory effect below the spin freezing transition ( $T_f = 29$  K), the sample was cooled in zero field (ZFC) from room temperature to a temperature below  $T_f$  followed by waiting at that particular temperature ( $T_w$ ) for 6000 s. This allows the

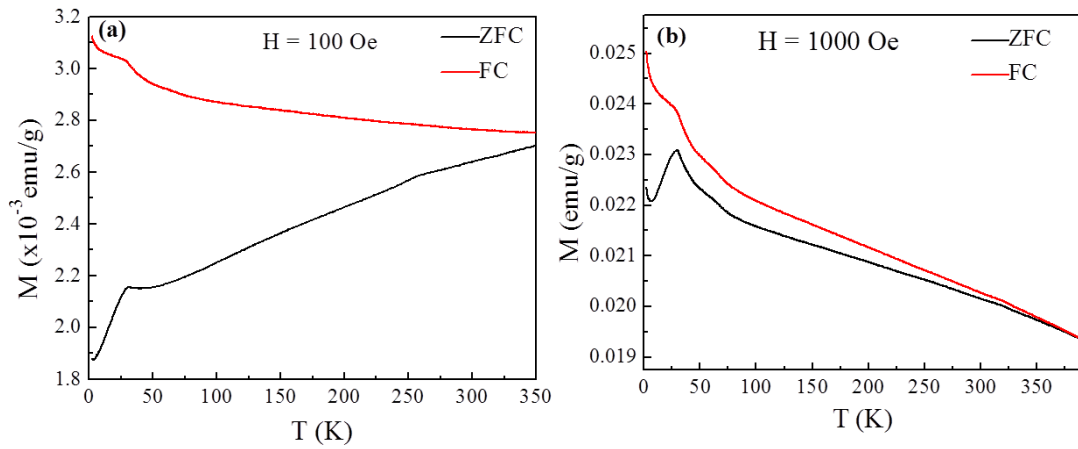


Figure 5 ZFC and FC magnetization of  $\text{LaVO}_{2.09}\text{N}_{0.91}$  at (a) 100 Oe and 1000 Oe

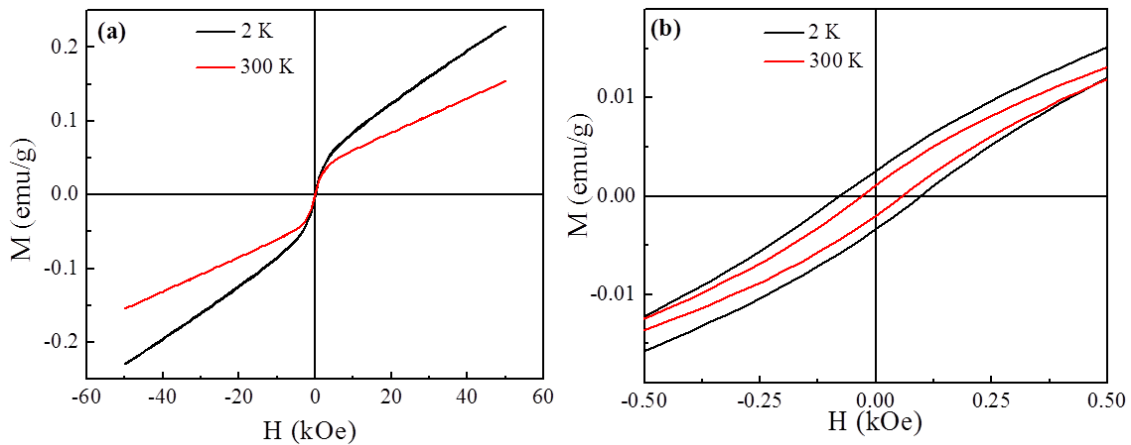
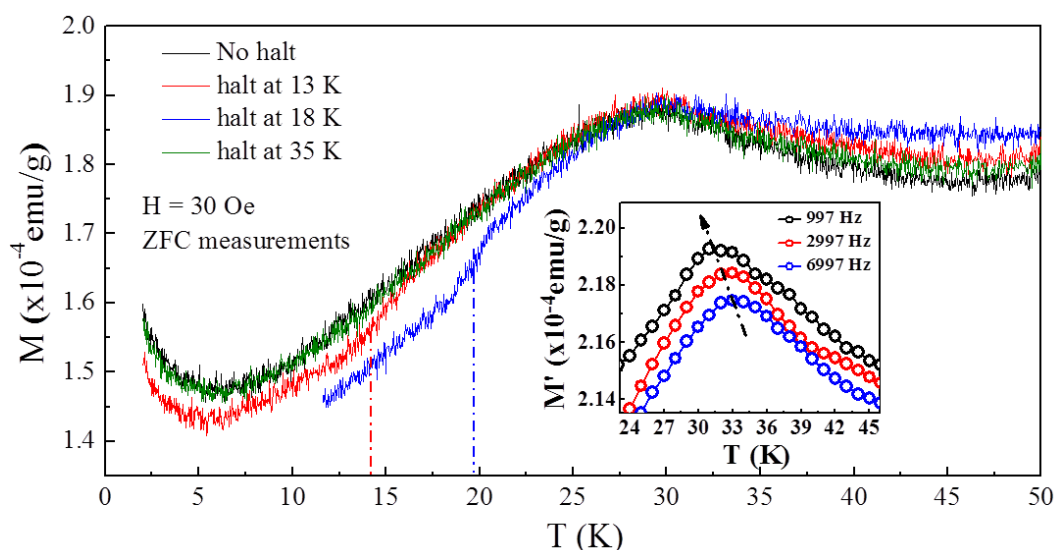


Figure 6 (a) Magnetic hysteresis of  $\text{LaVO}_{2.09}\text{N}_{0.91}$  at 2 and 300 K, (b) enlarged view near the origin

sample to age through equilibration. The sample was then cooled to 2 K and the magnetization was measured while warming the sample under an applied field of 30 Oe. The importance of keeping the applied field to a small value is to monitor the magnetization

behaviour without perturbing the system magnetically. A deviation in the magnetization is observed at  $T_W$  (for  $T_W = 18$  K and 13 K) as shown in Figure 7, but no deviation is observed when  $T_W (= 35$  K) is above  $T_f$ . In addition, an observed frequency dependence of the 29 K peak in AC susceptibility measurements (inset of Figure 7) confirms that it corresponds to a spin-glass transition. The presence of a spin glass (SG) phase in the  $\text{LaVO}_{2.09}\text{N}_{0.91}$  sample is further demonstrated by measuring the magnetization at 2 K as a function of field while cooling. A systematic shift of the loop in the positive magnetization direction is observed (Figure 8(a)) with the increase in the cooling field. Such behaviour is expected in a material



**Figure 7 Memory effect in  $\text{LaVO}_{2.09}\text{N}_{0.91}$  with halts at different temperatures. Inset shows the AC magnetic susceptibility at different frequencies**

which contains interfaces between SG and the AFM components because of the pinning of the SG spins at the interface by the AFM spins.<sup>67</sup> The shift disappears above 29 K as shown in Figure 8(b). Our  $\text{LaVO}_{2.1}\text{N}_{0.9}$  with majority of  $\text{V}^{4+}$  is similar to another perovskite system like  $\text{SrVO}_3$  with completely  $\text{V}^{4+}$ . In  $\text{SrVO}_3$ ,  $3d^1$  electron is not localized and show temperature independent Pauli paramagnetism.<sup>68</sup> The similar effect is observed in  $\text{LaVO}_{2.09}\text{N}_{0.91}$  where the magnetization do not vary much ( $\sim 20\%$  in 29-390 K interval) after the antiferromagnetic transition because this region is dominated by Pauli paramagnetism of  $\text{V}^{4+}$ . The little drop in the magnetization can be explained on the basis of paramagnetic contribution from  $\text{V}^{3+}$ .

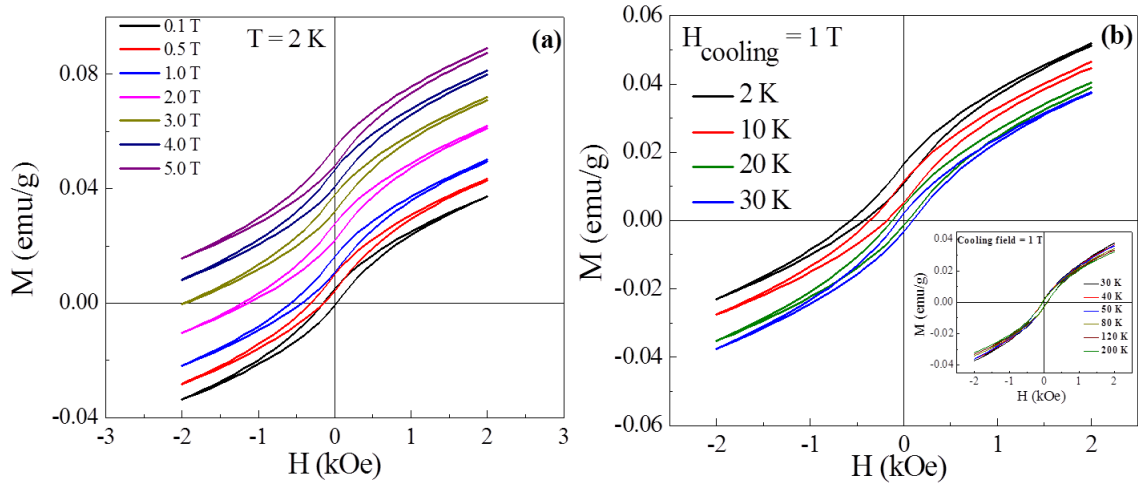


**Figure 8(a) Effect of cooling field on hysteresis loops at 2 K, (b) effect of temperature on the hysteresis loops below spin-glass temperature with inset showing the effect above spin glass temperature in  $\text{LaVO}_{2.09}\text{N}_{0.91}$**

## 4.2 $\text{NdVO}_2\text{N}$

In contrast to the earlier report of  $\text{NdVO}_2\text{N}^{69}$  which shows no spin ordering down to 2 K (measured at 1 T field), we observe a magnetic transition near 136 K (Figure 9(a)) when measured at low magnetic field (200 Oe). This indicates the presence of small amount of  $\text{V}^{3+}$  in the system. Hence, we have avoided temperature below 150 K to fit Curie-Weiss law. To accommodate the Pauli paramagnetic behavior of  $\text{V}^{4+}$ , we used the following equation between 150 and 300 K (Figure 9(b)):

$$\chi^{-1} = \frac{C}{T - \theta} - \chi_0^{-1}$$

The value of C (Curie constant) is found to be 1.56 K-mol-Oe/emu which gives an effective paramagnetic moment of 3.53 B.M. comparable to the ideal Nd  $4f^3$  paramagnetic moment (3.62 B.M.).  $\theta$  (Weiss constant) is found to be -43.98 K indicating the antiferromagnetic interaction in the system. Comparatively smaller value of Pauli paramagnetic moment ( $6.38 \times 10^{-4}$  emu/mol-Oe) is obtained than the previous report. Finite value of coercivity at 2 K (Figure 10) is also indicative of the presence of small amount of  $\text{V}^{3+}$  in this material.

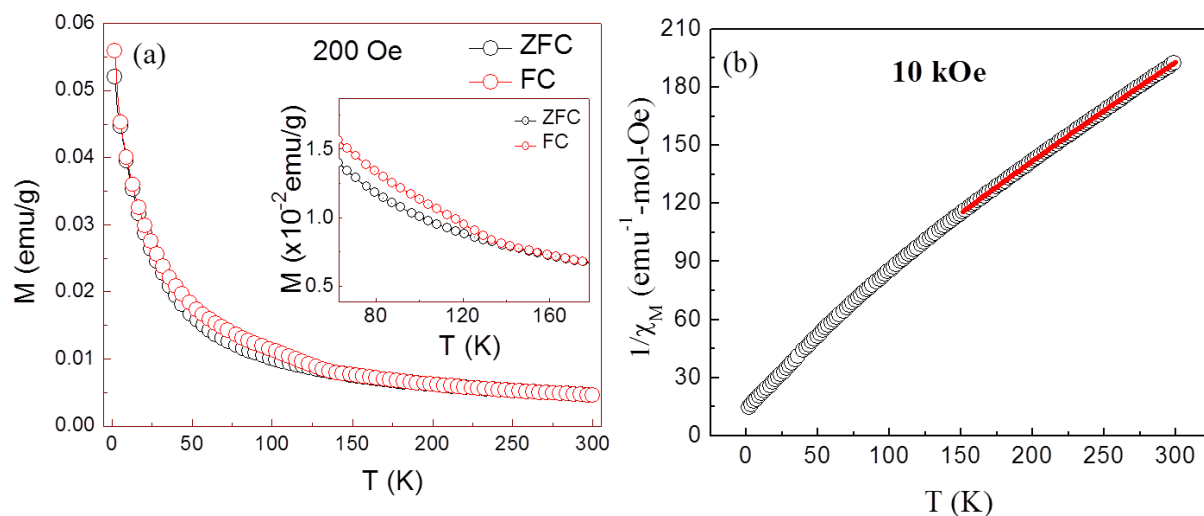


Figure 9(a) ZFC and FC magnetization of  $\text{NdVO}_2\text{N}$  at 200 Oe with inset showing the enlarged view near the magnetic transition, (b) Curie-Weiss law fitting of FC magnetization at 10 kOe

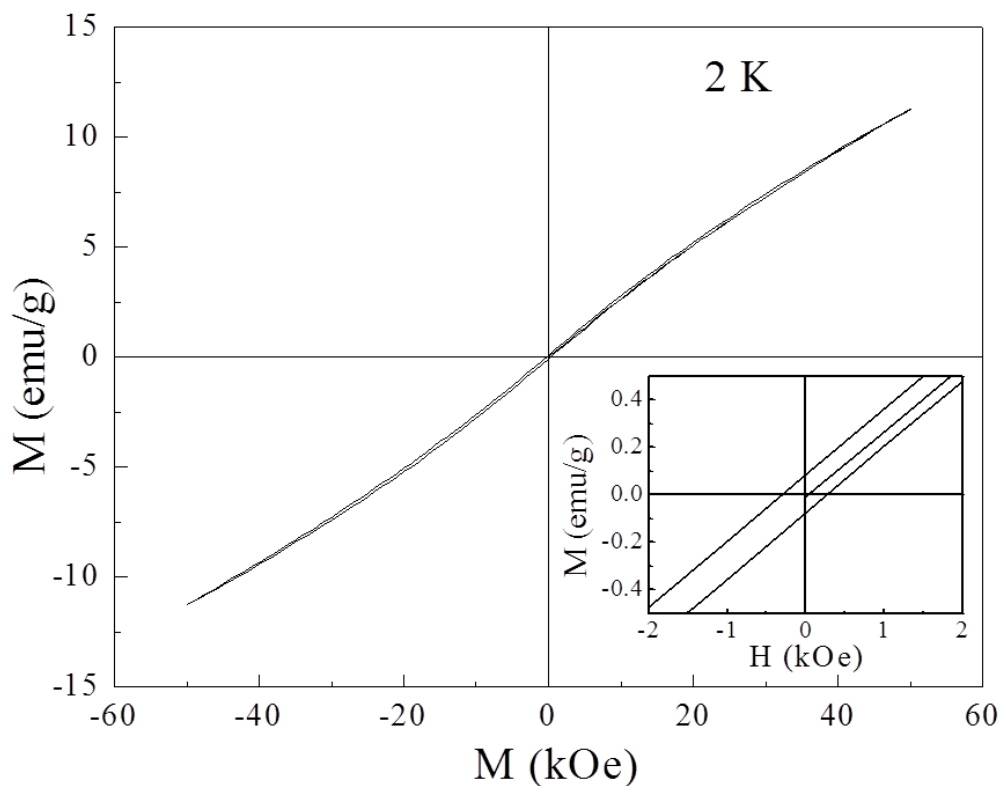
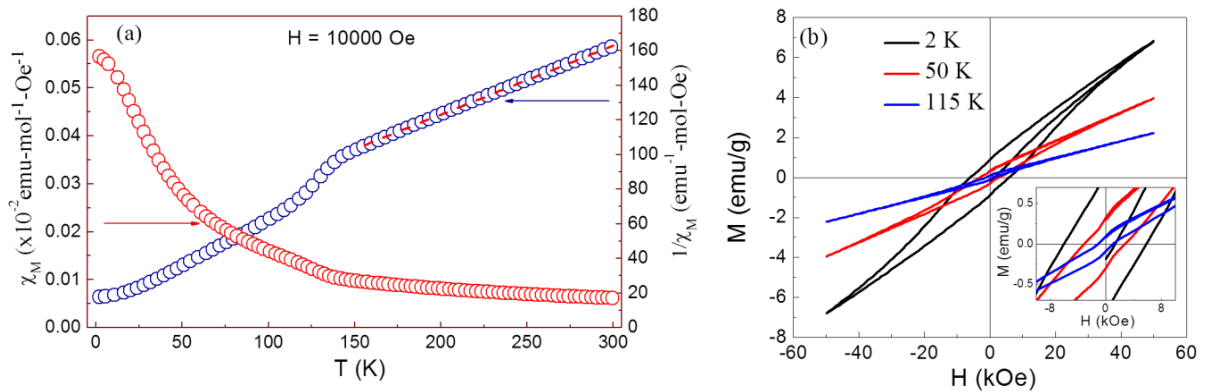


Figure 10 Magnetization as a function of field at 2 K for  $\text{NdVO}_2\text{N}$



### 4.3 PrVO<sub>2.24</sub>N<sub>0.76</sub>

The parent compound, PrVO<sub>3</sub>, shows antiferromagnetic spin ordering of V<sup>3+</sup> electrons at 132 K.<sup>70</sup> In the present case of PrVO<sub>2.24</sub>N<sub>0.76</sub>, we observe a similar anomaly at 134 K (Figure 11(a)). The magnetization above this temperature is fitted with the same equation as in the case of NdVO<sub>2</sub>N. The value of C is found to be 2.14 K-mol-Oe/emu which gives the effective paramagnetic moment of 4.13 B.M. Considering the ideal Pr<sup>3+</sup> and V<sup>3+</sup> paramagnetic moments to be 3.58 and 2.83 B.M. respectively, the effective paramagnetic moment should be  $\sqrt{(3.58)^2 + 0.24 * (2.83)^2} = 3.84$  B.M. which is slightly less than the observed value. The factor 0.24 is according to the formula where one unit contains 0.24 V<sup>3+</sup>. Pauli paramagnetic moment of  $5.78 \times 10^{-4}$  emu/mol-Oe is found from the fitting. Figure 11(b) shows hysteresis loops at different temperatures. At 2 K, high values of coercive field ( $H_C = 5.9$  kOe) and remanent magnetization ( $M_R = 0.9$  emu/g) are obtained which can be attributed to the canted arrangement of V<sup>3+</sup> antiferromagnetic spins. Values of  $H_C$  and  $M_R$  decrease with increasing temperature.



**Figure 11 (a) FC magnetization and Curie-Weiss law fitting for PrVO<sub>2.24</sub>N<sub>0.76</sub> at 10 kOe (b) Magnetization at different temperatures with inset showing the enlarged view near the origin**

We observe a sudden fall in the ZFC magnetization at 11 K measured under different applied magnetic fields (Figure 12 (a)). This is similar to a spin-glass transition. In order to confirm it, we carried out DC magnetization relaxation measurements at 2 K. For this, we cool the sample in the zero field condition till 2 K and apply 1000 Oe field at that temperature. The value of moment is then measured with respect to time where a strong relaxation in the magnetization is seen. The curve can be fitted with the equation,  $M(t) = -1 + 2t^\gamma$ , with  $\gamma =$

0.004 signifying a high degree of relaxation (Inset of Figure 12 (b)). In contrast, we do not see any relaxation in FC measurements.

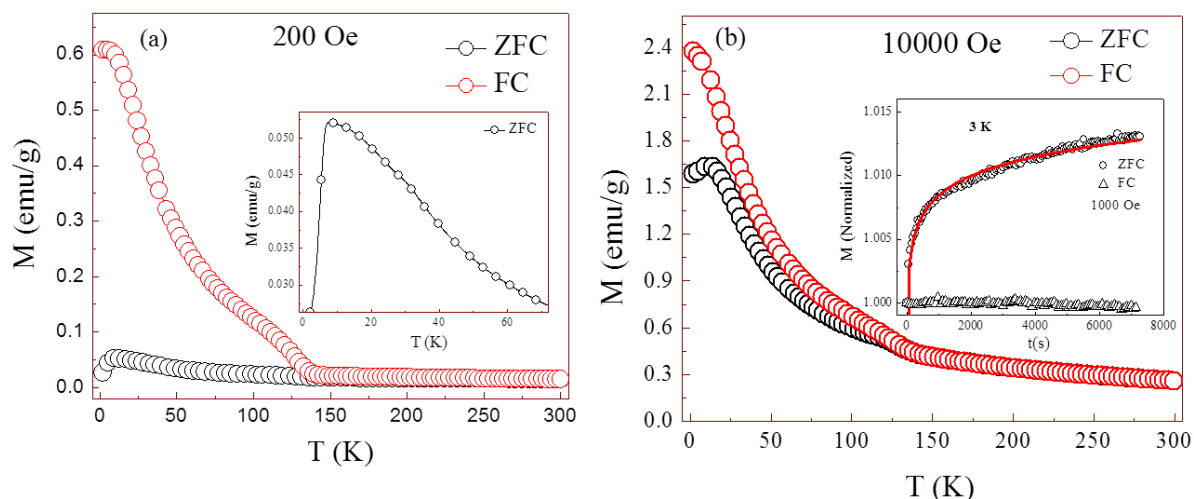


**Figure 12 (a) ZFC-FC magnetizations at 200 Oe with inset showing the ZFC magnetization at low temperature. (b) ZFC-FC magnetizations at 10000 Oe with inset showing the DC relaxation data at 2 K**

#### 4.4 Resistivity measurements

Resistivity-temperature data measured on ceramic pellets are shown in Figure 13. All the samples show narrow bandgap semiconducting behaviour with fitted activation energies of 59, 106 and 125 meV for  $\text{LaVO}_{2.09}\text{N}_{0.91}$ ,  $\text{PrVO}_{2.24}\text{N}_{0.76}$  and  $\text{NdVO}_2\text{N}$  respectively at room

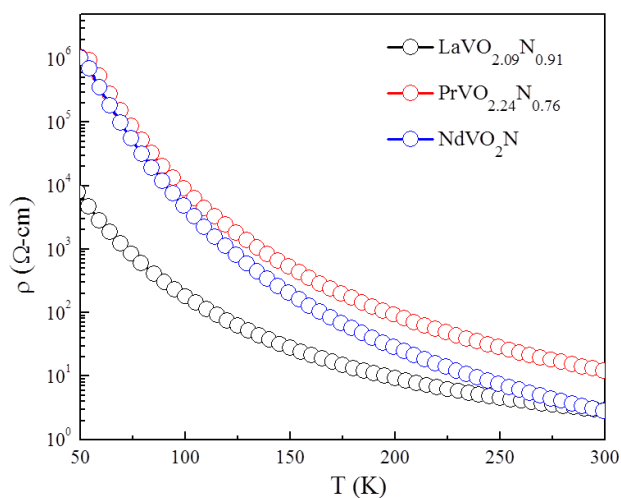


**Figure 13 Resistivity of  $\text{LaVO}_{2.09}\text{N}_{0.91}$ ,  $\text{PrVO}_{2.24}\text{N}_{0.76}$  and  $\text{NdVO}_2\text{N}$  with respect to temperature.**

temperature. This semiconducting behaviour is not consistent with the Pauli paramagnetism observed in the magnetic susceptibility measurements for the Pr and Nd materials, and may reflect resistive grain boundaries between intrinsically conducting particles. Non-ohmic conductivity in ceramic oxynitride pellets was found in a study of  $\text{EuWO}_{2-x}\text{N}_{1+x}$ .<sup>71</sup> The change in electronic properties because of more covalent nitrogen compared to oxygen can also not be ruled out.

## 5. Conclusions

The vanadium oxynitrides perovskites  $\text{LaVO}_{3-x}\text{N}_x$  ( $0 \leq x \leq 0.9$ ),  $\text{NdVO}_2\text{N}$  ( $0 \leq x \leq 1$ ) and the new praseodymium analogues  $\text{PrVO}_{2.24}\text{N}_{0.76}$  have been prepared by treatment of  $\text{RVO}_4$  oxides (R = La, Pr and Nd) in flowing  $\text{NH}_3$  gas. The ammonolysis reaction is concomitant with the reduction of  $\text{V}^{5+}$  in the  $\text{RVO}_4$  precursors to give  $\text{V}^{3+}$  in  $\text{RVO}_3$  perovskites that are progressively nitrated and show different proportions of  $\text{V}^{4+}/\text{V}^{3+}$ . Variable temperature neutron diffraction studies show that  $\text{NdVO}_2\text{N}$  and  $\text{PrVO}_{2.24}\text{O}_{0.76}$  have orthorhombic *Pbnm* symmetry between 3.5 and 300 K, but  $\text{LaVO}_{2.11}\text{N}_{0.89}$  undergoes a broad *Pbnm* and *R-3c* structural transition over this temperature range.  $\text{LaVO}_{2.09}\text{N}_{0.91}$  shows divergence between ZFC and FC magnetizations with a peak at 29 K which is confirmed to be due to spin-glass transition by ac magnetic susceptibility measurements. Magnetization of  $\text{NdVO}_2\text{N}$  can be explained by the combination of paramagnetic spins of  $\text{Nd}^{3+}$ , temperature independent Pauli paramagnetic  $\text{V}^{4+}$  and a small amount of  $\text{V}^{3+}$  impurity. The main feature in the otherwise weak ferromagnetic  $\text{PrVO}_{2.24}\text{N}_{0.76}$  is a sudden drop in ZFC magnetization near 10 K which is possibly due to the re-entrant spin-glass transition at this temperature. All the three materials show semiconducting behavior.

## 6. References

1. J. B. Goodenough, *Prog. Solid State Chem.* 1971, 5, 145-399.
2. J. B. Goodenough, Localized-itinerant electronic transitions in perovskites. In *Recent Developments in High Temperature Superconductivity*, Springer: 1996; pp 37-60.
3. M. Onoda, H. Ohta and H. Nagasawa, *Solid State Commun.* 1991, 79, 281-285.
4. P. Dougier, J. C. C. Fan and J. B. Goodenough, *J. Solid State Chem.* 1975, 14, 247-59.
5. K. Morikawa, T. Mizokawa, K. Kobayashi, A. Fujimori, H. Eisaki, S. Uchida, F. Iga and Y. Nishihara, *Phys. Rev. B* 1995, 52, 13711.
6. H. C. Nguyen and J. B. Goodenough, *Phys. Rev. B* 1995, 52, 8776.
7. A. V. Mahajan, D. C. Johnston, D. R. Torgeson and F. Borsa, *Phys. Rev. B* 1992, 46, 10973.
8. J. B. Goodenough and J.-S. Zhou, Transport properties. In *Localized to Itinerant Electronic Transition in Perovskite Oxides*, Springer: 2001; pp 17-113.
9. H. C. Nguyen and J. B. Goodenough, *Phys. Rev. B* 1995, 52, 324.
10. L. D. Tung, M. R. Lees, G. Balakrishnan and D. M. Paul, *Phys. Rev. B* 2007, 75, 104404.
11. L. D. Tung, *Phys. Rev. B* 2005, 72, 054414.
12. Y. Y. Mi, S. J. Wang, J. W. Chai, J. S. Pan, C. H. A. Huan, Y. P. Feng and C. K. Ong, *Appl. Phys. Lett.* 2006, 89, 231922-231922-3.
13. R. J. Xie, *J. Am. Ceram. Soc.* 2013, 96, 665-687.
14. A. Fuertes, *J. Mater. Chem.* 2012, 22, 3293-3299.
15. M. Jansen and H. P. Letschert, *Nature* 2000, 404, 980-982.
16. Y.-I. Kim, P. M. Woodward, K. Z. Baba-Kishi and C. W. Tai, *Chem. Mater.* 2004, 16, 1267-1276.
17. M. Higashi, R. Abe, T. Takata and K. Domen, *Chem. Mater.* 2009, 21, 1543-1549.
18. K. Maeda, M. Higashi, B. Siritanaratkul, R. Abe and K. Domen, *J. Am. Chem. Soc.* 2011, 133, 12334-12337.
19. M. Yang, J. Oró-Solé, A. Kusmartseva, A. Fuertes and J. P. Attfield, *J. Am. Chem. Soc.* 2010, 132, 4822-4829.

20. M. Yang, J. Oró-Solé, J. A. Rodgers, A. B. Jorge, A. Fuertes and J. P. Attfield, *Nat. Chem.* 2010, 3, 47-52.
21. J. P. Attfield, *Crystal Growth & Design* 2013, 13, 4623-4629.
22. R. Marchand, F. Pors and Y. Laurent, *REV. INT. HAUTES TEMP. REFRACT. Rev. Int. Hautes Temp. Refract.* 1986, 23, 11.
23. F. Pors, R. Marchand, Y. Laurent, P. Bacher and G. Roult, *Mater. Res. Bull.* 1988, 23, 1447-1450.
24. X. Gouin, R. Marchand, Y. Laurent and F. Gervais, *Solid State Commun.* 1995, 93, 857-859.
25. M. Higashi, R. Abe, K. Teramura, T. Takata, B. Ohtani and K. Domen, *Chem. Phys. Lett.* 2008, 452, 120-123.
26. Y.-I. Kim, *Ceram. Int.* 2012, 38, 2609-2612.
27. Y.-I. Kim, P. M. Woodward, K. Z. Baba-Kishi and C. W. Tai, *Chem. Mater.* 2004, 16, 1267-1276.
28. K. Page, M. W. Stoltzfus, Y.-I. Kim, T. Proffen, P. M. Woodward, A. K. Cheetham and R. Seshadri, *Chem. Mater.* 2007, 19, 4037-4042.
29. S. J. Clarke, K. A. Hardstone, C. W. Michie and M. J. Rosseinsky, *Chem. Mater.* 2002, 14, 2664-2669.
30. Y. Mizuno, H. Wagata, K. Yubuta, N. Zettsu, S. Oishi and K. Teshima, *CrystEngComm* 2013, 15, 8133-8138.
31. E. Günther, R. Hagenmayer and M. Jansen, *Z. Anorg. Allg. Chem.* 2000, 626, 1519-1525.
32. F. Pors, P. Bacher, R. Marchand, Y. Laurent and G. Roult, *Revue internationale des hautes températures et des réfractaires* 1987, 24, 239-246.
33. B. Siritanaratkul, K. Maeda, T. Hisatomi and K. Domen, *ChemSusChem* 2011, 4, 74-78.
34. A. Rachel, S. G. Ebbinghaus, M. Güngerich, P. J. Klar, J. Hanss, A. Weidenkaff and A. Reller, *Thermochim. Acta* 2005, 438, 134-143.
35. G. Tobías, D. Beltrán-Porter, O. I. Lebedev, G. Van Tendeloo, J. Rodríguez-Carvajal and A. Fuertes, *Inorg. Chem.* 2004, 43, 8010-8017.
36. F. Pors, R. Marchand and Y. Laurent, *J. Solid State Chem.* 1993, 107, 39-42.

37. P. Maillard, F. Tessier, E. Orhan, F. Cheviré and R. Marchand, *Chem. Mater.* 2004, *17*, 152-156.
38. M. Weller and J. Rooke, *Solid State Phenom.* 2003, *90*, 417-422.
39. K. Ueda, H. Kato, M. Kobayashi, M. Hara and M. Kakihana, *J. Mater. Chem. A* 2013, *1*, 3667-3674.
40. D. Logvinovich, Stefan G. Ebbinghaus, A. Reller, I. Marozau, D. Ferri and A. Weidenkaff, *Z. Anorg. Allg. Chem.* 2010, *636*, 905-912.
41. N. Kumar, A. Sundaresan and C. N. R. Rao, *Mater. Res. Bull.* 2011, *46*, 2021-2024.
42. A. B. n. Jorge, J. Oró-Solé, A. M. Bea, N. Mufti, T. T. M. Palstra, J. A. Rodgers, J. P. Attfield and A. Fuertes, *J. Am. Chem. Soc.* 2008, *130*, 12572-12573.
43. P. Antoine, R. Assabaa, P. L'Haridon, R. Marchand, Y. Laurent, C. Michel and B. Raveau, *Mater. Sci. Eng., B* 1989, *5*, 43-46.
44. J. Oro-Sole, L. Clark, W. Bonin, J. P. Attfield and A. Fuertes, *Chem. Commun.* 2013, *49*, 2430-2432.
45. S. J. Clarke, B. P. Guinot, C. W. Michie, M. J. C. Calmont and M. J. Rosseinsky, *Chem. Mater.* 2001, *14*, 288-294.
46. M. Yashima, M. Saito, H. Nakano, T. Takata, K. Ogisu and K. Domen, *Chem. Commun.* 2010, *46*, 4704-4706.
47. A. Kasahara, K. Nukumizu, T. Takata, J. N. Kondo, M. Hara, H. Kobayashi and K. Domen, *Journal of Physical Chemistry B* 2002, *107*, 791-797.
48. M. Yang, J. A. Rodgers, L. C. Middler, J. Oró-Solé, A. B. n. Jorge, A. Fuertes and J. P. Attfield, *Inorg. Chem.* 2009, *48*, 11498-11500.
49. D. Logvinovich, J. Hejtmánek, K. Knizek, M. Marysko, N. Homazava, P. Tomes, R. Aguiar, S. G. Ebbinghaus, A. Reller and A. Weidenkaff, *J. Appl. Phys.* 2009, *105*, 023522-023522-6.
50. I. D. Fawcett, K. V. Ramanujachary and M. Greenblatt, *Mater. Res. Bull.* 1997, *32*, 1565-1570.
51. G. Liu, X. Zhao and H. A. Eick, *J. Alloys Compd.* 1992, *187*, 145-156.
52. D. Logvinovich, M. H. Aguirre, J. Hejtmánek, R. Aguiar, S. G. Ebbinghaus, A. Reller and A. Weidenkaff, *J. Solid State Chem.* 2008, *181*, 2243-2249.
53. M. T. Weller and S. J. Skinner, *Int. J. Inorg. Mater.* 2000, *2*, 463-467.

54. M. Yashima, U. Fumi, H. Nakano, K. Omoto and J. R. Hester, *Journal of Physical Chemistry C* 2013, *117*, 18529-18539.
55. P. Antoine, R. Marchand, Y. Laurent, C. Michel and B. Raveau, *Mater. Res. Bull.* 1988, *23*, 953-957.
56. P. Bacher, P. Antoine, R. Marchand, P. L'Haridon, Y. Laurent and G. Roult, *J. Solid State Chem.* 1988, *77*, 67-71.
57. R. Pastrana-Fábregas, J. Isasi-Marín, C. Cascales and R. Sáez-Puche, *J. Solid State Chem.* 2007, *180*, 92-97.
58. M. Yang, J. Oró-Solé, A. Kusmartseva, A. Fuertes and J. P. Attfield, *J. Am. Chem. Soc.* 2010, *132*, 4822-4829.
59. M. Retuerto, C. De la Calle, M. J. Martínez-Lope, F. Porcher, K. Krezhov, N. Menendez and J. A. Alonso, *J. Solid State Chem.* 2012, *185*, 18-24.
60. J. Rodríguez-Carvajal, *Physica B* 1993, *192*, 55-69.
61. P. Dougier and P. Hagenmuller, *J. Solid State Chem.* 1975, *15*, 158-166.
62. J. P. Attfield, *Int. J. Inorg. Mater.* 2001, *3*, 1147-1152.
63. H. C. Nguyen and J. B. Goodenough, *Phys. Rev. B* 1995, *52*, 8776-8787.
64. R. Mathieu, P. Jönsson, D. N. H. Nam and P. Nordblad, *Phys. Rev. B* 2001, *63*, 092401.
65. R. Mathieu, M. Hudl and P. Nordblad, *Europhys. Lett.* 2010, *90*, 67003.
66. P. E. Jönsson, R. Mathieu, P. Nordblad, H. Yoshino, H. A. Katori and A. Ito, *Phys. Rev. B* 2004, *70*, 174402.
67. E. Passamani, C. Larica, C. Marques, A. Takeuchi, J. Proveti and E. Favre-Nicolin, *J. Magn. Magn. Mater.* 2007, *314*, 21-29.
68. M. Onoda, H. Ohta and H. Nagasawa, *Solid State Commun.* 1991, *79*, 281-285.
69. J. Oró-Solé, L. Clark, W. Bonin, J. P. Attfield and A. Fuertes, *Chem. Commun.* 2013, *49*, 2430-2432.
70. L. Tung, *Phys. Rev. B* 2005, *72*, 054414.
71. A. Kusmartseva, M. Yang, J. Oró-Solé, A. Bea, A. Fuertes and J. P. Attfield, *Appl. Phys. Lett.* 2009, *95*, 022110-022110-3.



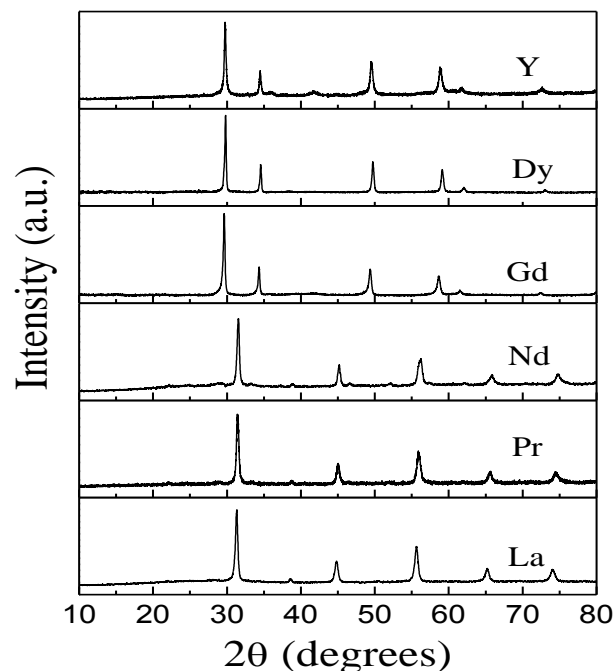


## Chapter I.2

### Synthesis, structure and properties of rare earth niobium oxynitrides\*

#### Summary

Ammonolysis of rare earth niobates of the type  $\text{LnNbO}_4$  ( $\text{Ln} = \text{Y}, \text{La}, \text{Pr}, \text{Nd}, \text{Gd}, \text{Dy}$ ) yields to oxynitrides of different structures. When  $\text{Ln} = \text{La}, \text{Nd}$  and  $\text{Pr}$ , the structure is that of an orthorhombic perovskite of the general formula  $\text{LnNbON}_2$ . As the size of the rare earth decreases, the oxynitride has a nitrogen-deficient defect fluorite ( $\text{Ln} = \text{Pr}, \text{Nd}, \text{Gd}$ ), or pyrochlore ( $\text{Ln} = \text{Y}$ ) structure. The IR spectra of the oxynitrides and the corresponding oxides are significantly different. Thermogravimetric analysis suggests the formation of an intermediate phase wherein the  $\text{N}_2$  molecule is attached to the oxide lattice above  $400^\circ\text{C}$  and decomposes to give the oxide on heating in an oxygen atmosphere. Raman spectra of the intermediate phases show evidence for the  $\text{N}\equiv\text{N}$  stretching vibration. Gadolinium niobium oxynitride is found to be paramagnetic.



\*A paper based on this work has appeared in *Mater. Res. Bull.*, **2011**.

## 1. Introduction

Studies of ternary oxynitrides have mainly been focused on compounds with perovskite-type structure. Very few other structure-types like scheelite,<sup>1-2</sup>  $\text{K}_2\text{NiF}_4$ <sup>3</sup> etc. are known for oxynitride materials. Ternary oxynitrides with all these different types of structures do not form a large pool of compounds mainly because of difficulties in preparation and thermal instability. There is however, some progress in this area in recent years.<sup>4</sup> Partial replacement of stoichiometric amount of oxygen by nitrogen not only modifies the electronic properties by narrowing down the band gap from ultraviolet to visible region but also brings about structural changes. Thus,  $\text{CaTaO}_2\text{N}$ ,  $\text{LaTaON}_2$  and the solid solutions  $\text{Ca}_{(1-x)}\text{La}_x\text{TaO}_{(2-x)}\text{N}_{(1+x)}$  exhibit excellent yellow, red and colours in between respectively with high dielectric properties.<sup>5</sup> These materials are potential replacements for cadmium-based toxic pigments. In order to satisfy charge balance requirements, structural transformations occur in oxynitride compared to the parent oxides. For example, ammonolysis in the presence of flowing ammonia changes the pyrochlore structure of  $\text{Nd}_2\text{Ti}_2\text{O}_7$  to that of the perovskite  $\text{NdTiO}_2\text{N}$ .<sup>6</sup> Scheelite type  $\text{SrWO}_4$  changes to cubic  $\text{SrWO}_2\text{N}$  perovskite.<sup>7</sup> Recently the magnetic properties of some oxynitrides have been studied: e.g.  $\text{EuNbO}_2\text{N}$  and  $\text{EuWO}_2\text{N}$  are ferromagnetic and exhibit magnetoresistance.<sup>8</sup>

Very few niobium based oxynitrides are known among which alkaline earth metal niobium oxynitrides are the most popular ones. These compounds are mainly investigated for their superior photocatalytic activities and dielectric properties. Domen and co-workers have explored  $\text{CaNbO}_2\text{N}$ ,  $\text{SrNbO}_2\text{N}$  and  $\text{BaNbO}_2\text{N}$  as hydrogen and oxygen evolution catalysts.<sup>9-10</sup> Woodward *et al.* investigated the dielectric permittivity and electrical resistivity of  $\text{BaNbO}_2\text{N}$  and found that electrical resistivity was 7 orders less than the corresponding tantalum oxynitride with metallic temperature dependence.<sup>11</sup> This was explained by the presence of small amount of  $\text{Nb}^{4+}$  because of highly reducing atmosphere. Fuertes *et al.* observed large magnetoresistance in  $\text{EuNbO}_2\text{N}$ . They explained magnetoresistance on the basis of coupling of carrier  $\text{Nb}^{4+}$  spins with the localized  $\text{Eu}^{2+}$  spins analogous to the manganites.<sup>8</sup> Magnetocapacitance was explained by extrinsic effects. Gerard *et al.* demonstrated the synthesis of two compounds in the niobium based Ruddlesden-Popper series,  $(\text{SrO})(\text{SrNb}_{2-x}\text{N}_x)_n$  with  $n = 1$  and  $n = 2$ . Finite magnetic moments in these materials again confirmed a

mixed Nb<sup>5+</sup>/Nb<sup>4+</sup> system.<sup>12</sup> Recently, SrNbO<sub>2</sub>N was considered to study anion doping in perovskite oxynitrides. It provides evidence of well-defined anion ordering with disordered cis -M-N- chains confined to chains within the three dimensional perovskite structure.<sup>13</sup>

## 2. Scope of the present investigation

Maillard *et al.*<sup>14</sup> studied ammonolysis of rare earth tantalates, LnTaO<sub>4</sub> (Ln = rare earth and Y) and found structural dependence of the oxynitride on the size of rare earth ion. Larger rare earth ions form nitrogen-rich oxynitrides of perovskite structure of the type LnTaON<sub>2</sub>. With decrease in size of the rare earth ion, the oxynitride tends to form the nitrogen-deficient pyrochlore structure as in Ln<sub>2</sub>Ta<sub>2</sub>O<sub>5</sub>N<sub>2</sub> or the defect fluorite structure. While LaNbON<sub>2</sub> has been studied, the structural evolution of oxynitrides with respect to the size of rare earth in the niobate system has not been investigated.<sup>15</sup> We have carried out ammonolysis of oxides of the formula LnNbO<sub>4</sub> (Ln = Y, La, Pr, Nd, Gd, Dy) and studied the structures and properties of the resulting oxynitrides.

## 3. Experimental section

The parent oxides of LnNbO<sub>4</sub> were prepared by grinding stoichiometric amounts of Ln<sub>2</sub>O<sub>3</sub> (except Pr<sub>6</sub>O<sub>11</sub>) and Nb<sub>2</sub>O<sub>5</sub> followed by heating in air at 1200 °C for 12 h. Rare earth oxides were preheated at 900 °C for 10 h before use. Ammonolysis of the powder oxide precursors were carried out by heating them in ammonia flow of ~ 250 mL/min at 950 °C for 16 h. Powder X-ray diffraction (XRD) patterns were recorded with a Bruker D8 X-ray diffractometer with Cu K $\alpha$  radiation. Thermal gravimetric analysis (TGA) was carried out in Mettler Toledo Star system. Infrared spectra were recorded with a Bruker IFS 66v/S spectrometer. Raman spectra were recorded with a LabRAM HR with a 633 nm line from a HeNe laser. Magnetic measurements were carried out with the VSM option of Physical Property Measurement System (Quantum Design, USA).

## 4. Results and discussion

Rare earth niobates of the formula LnNbO<sub>4</sub> (Ln = rare earth or Y) crystallize in the monoclinic fergusonite structure. The cell parameters decrease as the size of the Ln ion decreases. XRD patterns of these oxides are shown in Figure 1. Reaction of LnNbO<sub>4</sub> with

ammonia at 950 °C results in partial or no ammonolysis when the flow rate of NH<sub>3</sub> is slow. This is due to the fact that water vapor forms during ammonolysis, and remains above the

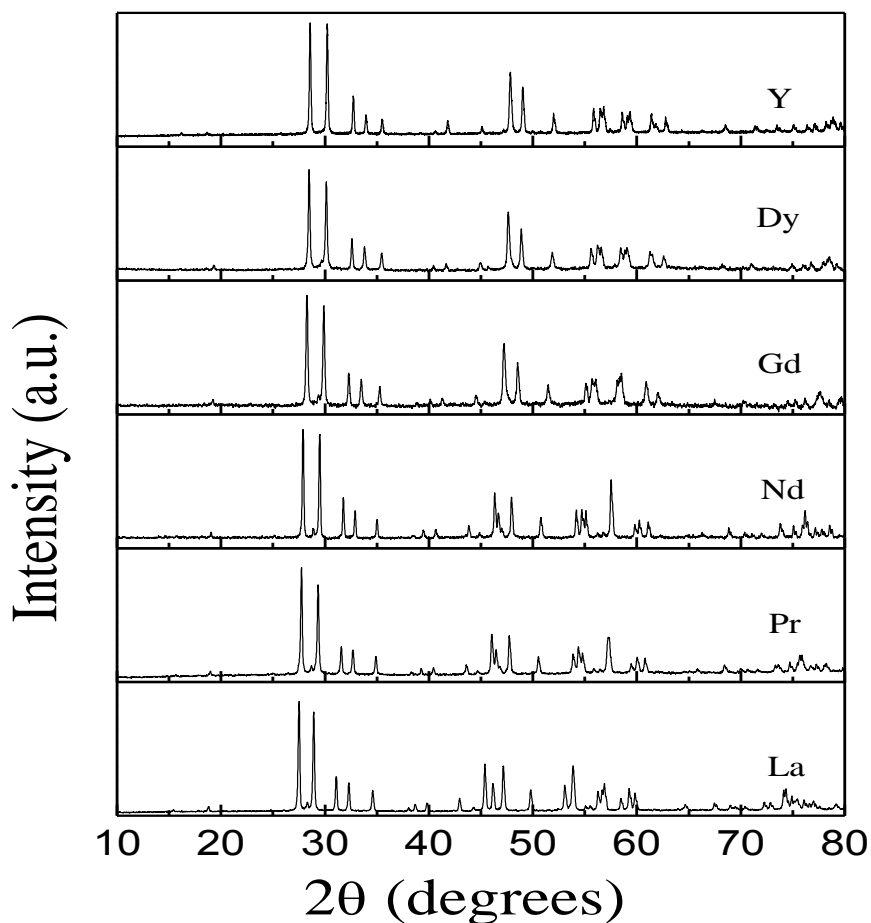


Figure 1 XRD patterns of LnNbO<sub>4</sub> (Ln = rare earths and Y)

oxide sample. For proper ammonolysis to occur, the vapor should be removed by a fast flow of NH<sub>3</sub>. Another important factor is the dissociation of NH<sub>3</sub> above 500 °C. Fast flow of NH<sub>3</sub> ensures that the sample is least exposed to N<sub>2</sub> and H<sub>2</sub> which are the products of the NH<sub>3</sub> dissociation. Complete ammonolysis of niobate results in the formation of an oxynitride; the structure of each depends on the size of the rare earth ion. In Figure 2, powder XRD patterns of the oxynitrides show that the larger rare earth ions, La<sup>3+</sup>, Pr<sup>3+</sup>, and Nd<sup>3+</sup> form oxynitrides with orthorhombic perovskite structure (space group *Pnma*); Gd and Dy form nitrogen-deficient oxynitrides, GdNb(O,N,□)<sub>4</sub>, with a cubic defect fluorite structure. Yttrium forms a nitrogen-deficient cubic pyrochlore of the formula Y<sub>2</sub>Nb<sub>2</sub>O<sub>5</sub>N<sub>2</sub>. The only difference between the defect fluorite structure and the cubic pyrochlore structure is the presence of a reflection

corresponding to the (311) plane at  $2\theta = 28^\circ$ . This results in the doubling of the cell parameter. The inset in Figure 2 shows the presence of the (311) reflection in the XRD

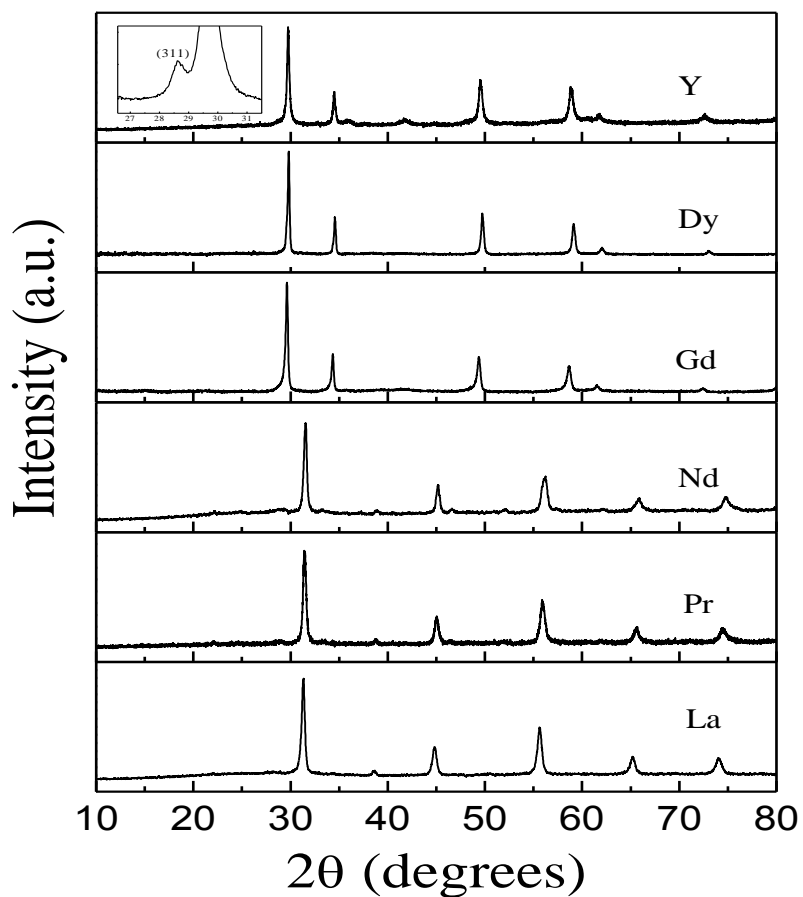
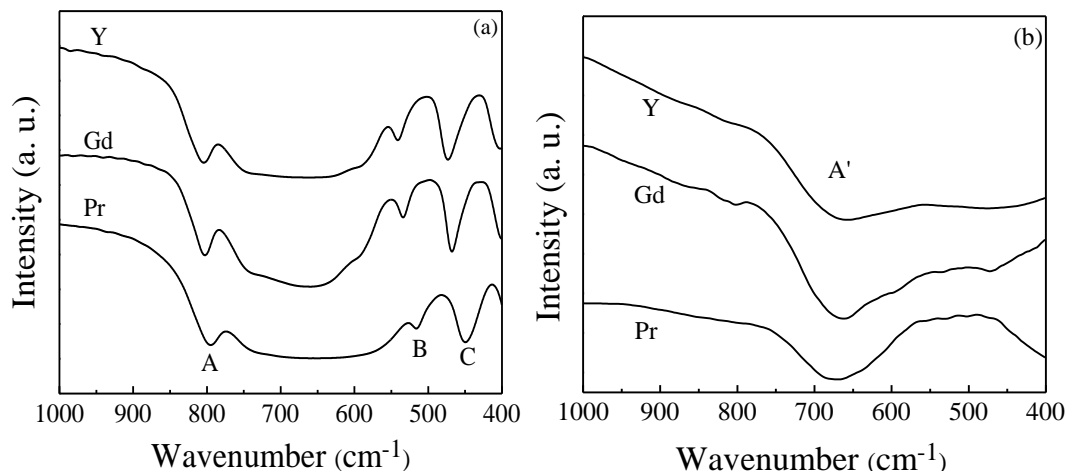


Figure 2 XRD patterns of oxynitrides. Inset shows the peak corresponding to (311) reflection in  $Y_2Nb_2O_5N_2$

Table 1 Structural parameters of rare earth oxynitrides

Ln	Structure	Space group	Cell parameters (Å)		
			a	b	c
La	Perovskite	<i>Pmna</i>	5.7288	8.1006	5.5707
Nd	Perovskite	<i>Pmna</i>	5.6953	8.0595	5.6933
Pr	Perovskite	<i>Pmna</i>	5.6771	8.0124	5.7011
Gd	Defect fluorite	<i>Fm-3m</i>	10.4377		
Dy	Defect fluorite	<i>Fm-3m</i>	10.3433		
Y	Pyrochlore	<i>Fm-3m</i>	10.2528		

pattern of the oxynitride of yttrium. The appearance of this reflection is due to the existence of cationic ordering between Y and Nb ions.<sup>14</sup> The cell parameters as well as the corresponding space groups of the various oxynitrides synthesized by us are listed in Table 1.



**Figure 3 IR spectra of (a) oxides of Pr, Gd and Y and (b) corresponding oxynitrides**

In Figure 3(a), the IR spectra of the LnNbO<sub>4</sub> are similar to those of the oxynitrides of fergusonite structure.<sup>16</sup> Characteristic bands occur around 800, 520 and 450 cm<sup>-1</sup> with designation A, B and C, respectively. The first band (800 cm<sup>-1</sup>) is related to the metal-oxygen stretching while those at 520 and 450 cm<sup>-1</sup> correspond to the Nb-O-Nb bending modes. In Figure 3(b), the infrared spectra of the oxynitrides are completely different from those of the corresponding oxides and there is only one prominent band in the 600-700 cm<sup>-1</sup> region. The IR frequency of the A, B and C bands of LnNbO<sub>4</sub> increases as the size of the rare earth ion decreases. The frequency of the A' band of the oxynitrides in the 600-700 cm<sup>-1</sup> region, however, decreases with decreasing size of the rare earth ion.

Figure 4 shows TGA curves of LaNbON<sub>2</sub>, GdNb(O,N,□)<sub>4</sub> and Y<sub>2</sub>Nb<sub>2</sub>O<sub>5</sub>N<sub>2</sub> which are representative of the three structure types. TGA was carried out in an oxygen atmosphere at a heating rate of 10 °C/min. LaNbON<sub>2</sub> is stable up to 300 °C, above which there is a sudden increase in mass. This is considered to be due to the formation of a N<sub>2</sub>-oxide complex.<sup>17</sup> The calculated weight gain, in the transformation of LaNbON<sub>2</sub> to the intermediate state, N<sub>2</sub>-oxide complex, corresponds to the composition LaNbO<sub>3</sub>.N<sub>2</sub>. This intermediate state is stable

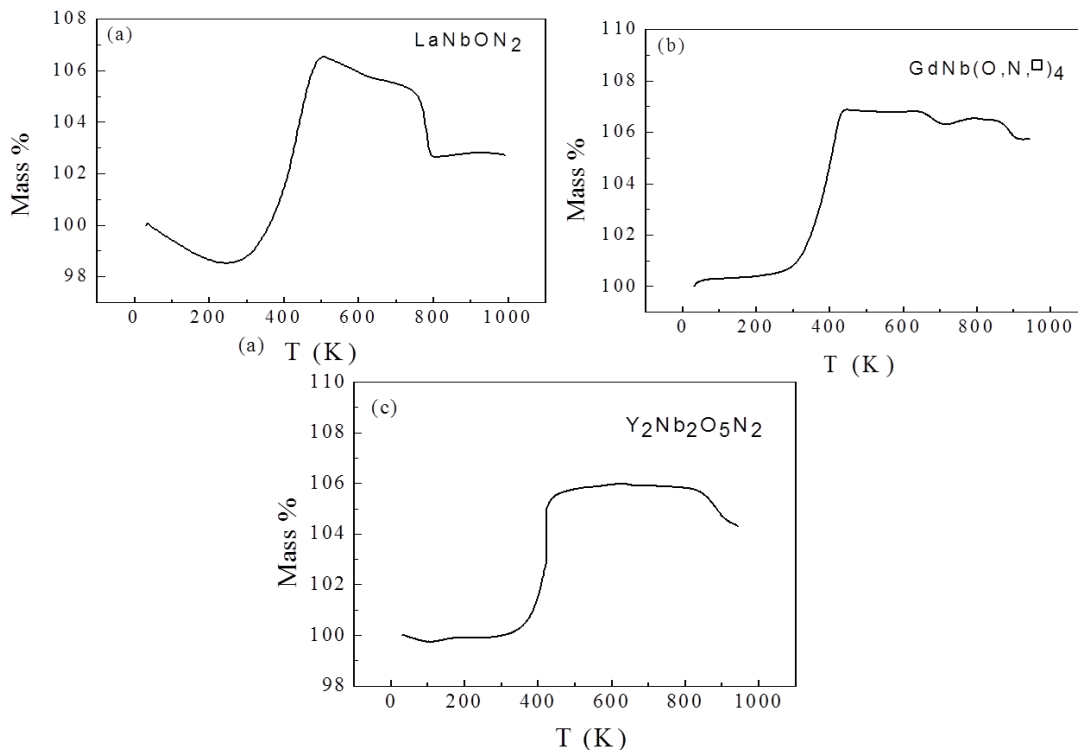


**Figure 4 TGA of oxynitrides of (a) La, (b) Gd and (c) Y**

up to  $\sim 800$  °C; above this temperature the TGA curve shows a weight loss due to the formation of  $\text{LaNbO}_4$  from  $\text{LaNbO}_3 \cdot \text{N}_2$ . The TGA plots of  $\text{GdNb}(\text{O}, \text{N}, \square)_4$  and  $\text{Y}_2\text{Nb}_2\text{O}_5\text{N}_2$  also show evidence of the presence of the intermediate  $\text{N}_2$ -oxide phase. In the case of  $\text{Y}_2\text{Nb}_2\text{O}_5\text{N}_2$ , this complex is stable up to  $\sim 850$  °C (Figure 4(c)).

The nitrogen species in the oxynitrides were characterized by X-ray photon spectroscopy (XPS). A shift in the N 1s band from  $\sim 397$  eV due to nitride ion to  $\sim 402$  eV due to  $\text{N}_2$  is expected for the intermediate phase ( $\text{LaNbO}_3 \cdot \text{N}_2$ ) of the oxynitrides.<sup>17</sup> XPS spectra of the as-prepared  $\text{LaNbON}_2$  as well as of the intermediate phase obtained by heating  $\text{LaNbON}_2$  at 530 °C for 30 h in an oxygen atmosphere were recorded. The starting oxynitride shows the N 1s band at  $\sim 397$  eV due to the nitride ion (Figure 5). The intermediate phase in the sample heated to 530 °C shows a feature at  $\sim 402$  eV (inset of Figure 5) due to the presence of  $\text{N}_2$  attached to the crystal lattice of the oxide.

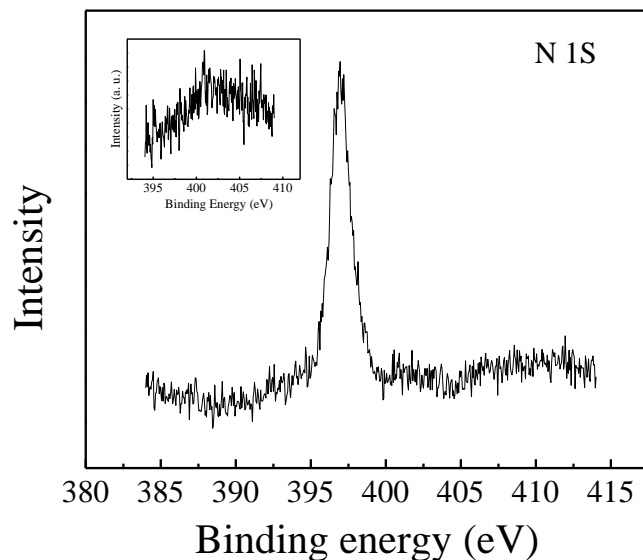


Figure 5 XPS spectrum of N 1s level of  $\text{LaNbON}_2$ . Inset shows the spectrum of N 1s level of the intermediate phase.

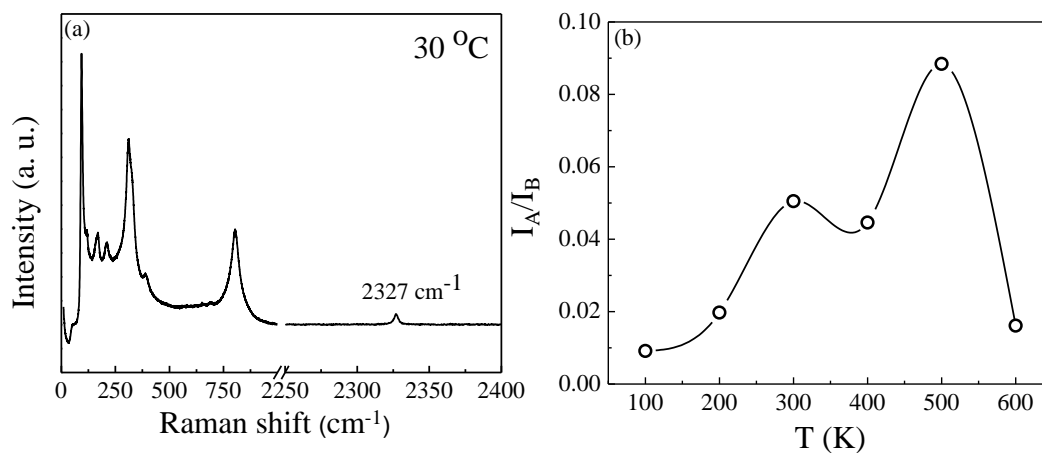
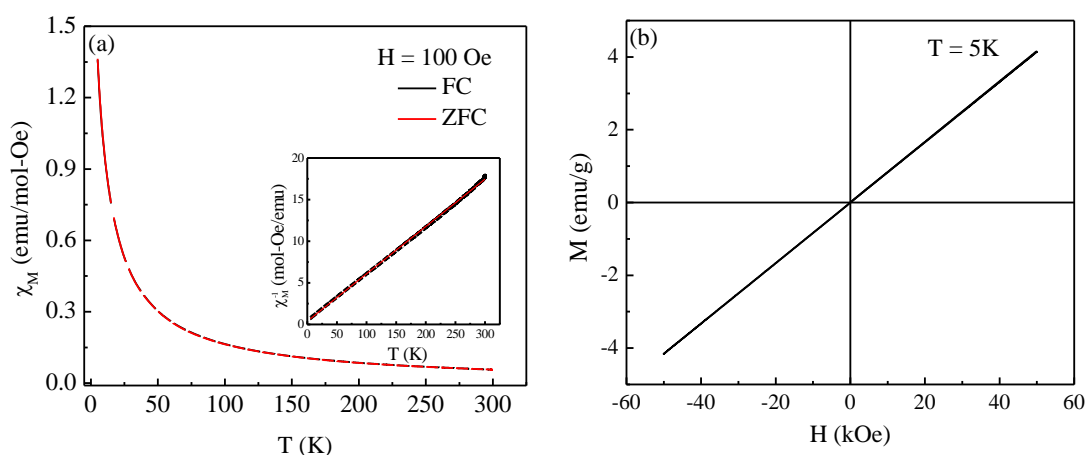


Figure 6 (a) Raman spectrum of  $\text{LaNbON}_2$  at room temperature and (b) Temperature dependence of the intensity ratio of the band at  $2327\text{ cm}^{-1}$  with respect to the band at  $94\text{ cm}^{-1}$

In Figure 6(a), the Raman spectrum of  $\text{LaNbON}_2$  at room temperature has a feature at  $2327\text{ cm}^{-1}$ , corresponding to the  $\text{N}\equiv\text{N}$  bond stretching. The ratio of the intensity of this band relative to the band at  $94\text{ cm}^{-1}$  is plotted as a function of temperature in Figure 6(b). The ratio increases with the increase in temperature up to  $500\text{ }^\circ\text{C}$  and decreases thereafter. The presence of the  $\text{N}\equiv\text{N}$  bond stretching at room temperature can be attributed to the local heating due to the high intensity laser beam. But as the temperature increases, the relative



intensity of the band increases. After 500 °C the local temperature of the sample might cross the decomposition temperature of the intermediate phase giving rise to a decrease in the intensity. The nature of the intermediate state is not yet fully understood. XPS analysis carried out by us and also by other workers rule out the presence of  $N^{3-}$ . In contrast to our Raman spectroscopic observation of the presence of  $N\equiv N$  stretching, Gendre *et al*<sup>17</sup> predict this intermediate to be of the type  $M-N=N-M$  as also found in organometallics. No direct evidence of such intermediate has been provided by them and is solely based on the compatibility of N-N and M-N bonds in the oxide lattice.



**Figure 7 (a) ZFC and FC data for the oxynitride of Gd with Inset showing the Curie-Weiss plot; (b) isothermal magnetization at 5 K**

Figure 7(a) shows the magnetization versus temperature behavior of  $GdNb(O,N,\square)_4$ . In the inset of Figure 7(a), the plot of  $1/\chi$  versus temperature could be fit to the Curie-Weiss law with  $\theta \sim 0$  K over the entire range of temperature, which is attributed to no magnetic interaction in the compound. The calculated magnetic moment corresponds to the paramagnetic state of  $Gd^{3+}$ . The isothermal magnetization data at 5 K (Figure 7(b)) reveals a typical linear behaviour of a paramagnetic compound. These observations rule out the reduction of niobium from its  $Nb^{5+}$  state as observed in some niobium oxynitrides earlier.<sup>18</sup>

## 5. Conclusions

In conclusion, rare earth oxynitrides were synthesized from the corresponding niobates of the general formula  $LnNbO_4$  ( $Ln = Y, La, Pr, Nd, Gd$  and  $Dy$ ). The larger rare earth ions ( $La, Pr$  and  $Nd$ ) form the perovskite structure, but as the size of the rare earth decreases nitrogen-

deficient oxynitrides (Ln = Gd, Dy) with defect perovskite or pyrochlore structures (Ln = Y) are favoured. The oxynitrides are stable in oxygen up to ~ 400 °C. Above this temperature an intermediate complex,  $\text{LnNbO}_3\text{N}_2$  with  $\text{N}_2$  attached to the oxide lattice is formed. The Raman spectra show a band corresponding to  $\text{N}\equiv\text{N}$  stretching. The intensity of this band increases with the increase in temperature. The gadolinium niobium oxynitride shows paramagnetic behaviour till the lowest measured temperature (5 K).

## 6. References

1. P. L'Haridon, R. Pastuszak and Y. Laurent, *J. Solid State Chem.* 1982, *43*, 29-32.
2. F. Cheviré, F. Tessier and R. Marchand, *Mater. Res. Bull.* 2004, *39*, 1091-1101.
3. S. J. Clarke, K. A. Hardstone, C. W. Michie and M. J. Rosseinsky, *Chem. Mater.* 2002, *14*, 2664-2669.
4. A. Fuertes, *Dalton Trans.* 2010, *39*, 5942-5948.
5. M. Jansen and H. P. Letschert, *Nature* 2000, *404*, 980-982.
6. S. J. Clarke, B. P. Guinot, C. W. Michie, M. J. C. Calmont and M. J. Rosseinsky, *Chem. Mater.* 2002, *14*, 288-294.
7. I. D. Fawcett, K. V. Ramanujachary and M. Greenblatt, *Mater. Res. Bull.* 1997, *32*, 1565-1570.
8. M. Yang, J. Oró-Solé, A. Kusmartseva, A. Fuertes and J. P. Attfield, *J. Am. Chem. Soc.* 2010, *132*, 4822-4829.
9. B. Siritanaratkul, K. Maeda, T. Hisatomi and K. Domen, *ChemSusChem* 2011, *4*, 74-78.
10. K. Maeda, M. Higashi, B. Siritanaratkul, R. Abe and K. Domen, *J. Am. Chem. Soc.* 2011, *133*, 12334-12337.
11. Y.-I. Kim, P. M. Woodward, K. Z. Baba-Kishi and C. W. Tai, *Chem. Mater.* 2004, *16*, 1267-1276.
12. G. Tobías, D. Beltrán-Porter, O. I. Lebedev, G. Van Tendeloo, J. Rodríguez-Carvajal and A. Fuertes, *Inorg. Chem.* 2004, *43*, 8010-8017.
13. M. Yang, J. Oró-Solé, J. A. Rodgers, A. B. Jorge, A. Fuertes and J. P. Attfield, *Nat. Chem.* 2010, *3*, 47-52.
14. P. Maillard, F. Tessier, E. Orhan, F. Cheviré and R. Marchand, *Chem. Mater.* 2005, *17*, 152-156.
15. D. Logvinovich, S. G. Ebbinghaus, A. Reller, I. Marozau, D. Ferri and A. Weidenkaff, *Z. Anorg. Allg. Chem.* 2010, *636*, 905-912.
16. A. Hristea, E.-J. Popovici, L. Muresan, M. Stefan, R. Grecu, A. Johansson and M. Boman, *J. Alloys Compd.* 2009, *471*, 524-529.
17. L. Le Gendre, R. Marchand and Y. Laurent, *J. Eur. Ceram. Soc.* 1997, *17*, 1813-1818.

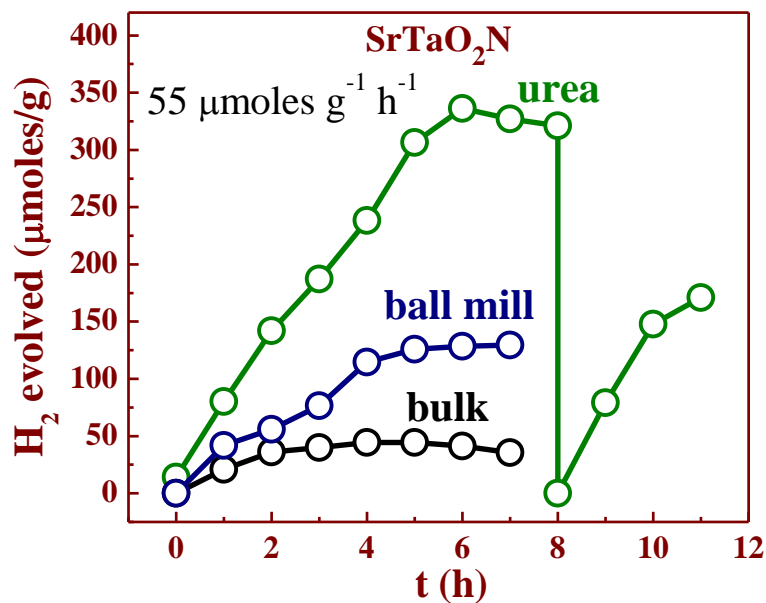
18. A. B. n. Jorge, J. Oró-Solé, A. M. Bea, N. Mufti, T. T. M. Palstra, J. A. Rodgers, J. P. Attfield and A. Fuertes, *J. Am. Chem. Soc.* 2008, *130*, 12572-12573.

## Chapter I.3

### Photocatalytic hydrogen evolution by ATaO<sub>2</sub>N (A = Ca, Sr and Ba) synthesized by urea method

#### Summary

We prepared nanoparticles of ATaO<sub>2</sub>N (A = Ca, Sr and Ba) with urea as the nitrogen source. ATaO<sub>2</sub>N crystallize in perovskite structure. All the three compounds absorb in the visible region and known to have the bottom of the conduction band edge more negative than the reduction potential of water, hence, good candidates for hydrogen evolution catalysis. We observe significant hydrogen evolution in these materials without the use of any cocatalyst.



## 1. Introduction

Photocatalytic water splitting to  $H_2$  and  $O_2$  by semiconducting materials is a broad area of research where the study of oxide materials forms a large part of it. Main disadvantage of using oxide material is that most of them absorb only in the ultra-violet region of the solar spectrum. Huge amount of effort has also been put in engineering the band structure of these oxide materials. On the other hand most of the nitride materials show overlap of bands to result in metallic behavior or very narrow gap. Oxynitrides which contain both oxide and nitride ions in stoichiometric amount have electronic properties intermediate of the two. Many of the oxynitrides absorb light in the visible region and hence been used as pigments. Jansen *et al.* demonstrated the possibility of tuning the color of pigment in the perovskite-type  $Ca_{1-x}La_xTaO_{2-x}N_{1+x}$  system.<sup>1</sup> Several other oxynitrides have been used as water splitting catalyst. Siritanaratkul *et al.* studied photocatalytic activity of  $ANbO_2N$  ( $A = Ca, Sr$  and  $Ba$ ) and  $LaNbON_2$  for water reduction and found that only  $CaNbO_2N$  is active when methanol as a sacrificial agent and Pt as a co-catalyst were used.<sup>2</sup> Higashi *et al.* used Pt-coated  $ATaO_2N$  ( $A = Ca, Sr$  and  $Ba$ ) as hydrogen evolution catalyst with methanol or  $I^-$  as an electron donor.<sup>3</sup>

The most commonly used method to synthesize oxynitride is the ammonolysis of crystalline oxide precursors at high temperatures. For example,  $LaNbON_2$  is prepared from crystalline  $LaNbO_4$  at 950 °C. Synthesis of oxynitrides from amorphous oxide precursors is also extensively used. The advantage of this method is that it requires less temperature and/or ammonolysis time for synthesis. Clarke *et al.* prepared  $LaTiO_2N$  from crystalline  $La_2Ti_2O_7$  but  $LaZrO_2N$  could not be obtained from rather unreactive  $La_2Zr_2O_7$  and was synthesized from amorphous oxide precursor.<sup>4</sup>

## 2. Scope of the present investigation

Gomathi *et al.* showed that nanoparticles of  $ATaO_2N$  ( $A = Ca, Sr$  and  $Ba$ ) and some other perovskite oxynitrides could be prepared by using urea as a nitrogen source.<sup>5</sup> Here, we show that  $ATaO_2N$  ( $A = Ca, Sr$  and  $Ba$ ) nanoparticles obtained from this method can be used as hydrogen evolution catalyst without any co-catalyst. We also compare the activity of these nanoparticles with the bulk oxynitrides prepared by conventional ammonolysis method.

### 3. Experimental section

For the synthesis of  $ATaO_2N$  ( $A = Ca, Sr$  and  $Ba$ ), stoichiometric amount of  $ACO_3$  and  $Ta_2O_5$  were mixed with excess of urea (10 times by weight of  $ACO_3 + Ta_2O_5$ ). The mixture was heated at  $950\text{ }^\circ\text{C}$  in nitrogen atmosphere for 2 h. Corresponding bulk materials were prepared by mixing stoichiometric amount of  $ACO_3$  and  $Ta_2O_5$  followed by heating in ammonia at  $950\text{ }^\circ\text{C}$  for 12 h at a flow rate of  $\sim 600\text{ mL/min}$ . The obtained powder was ground and subjected to same ammonolysis conditions for two more cycles. X-ray diffraction patterns were recorded in Rigaku-99 diffractometer using  $Cu\ K\alpha$  radiation. UV-visible spectra were recorded in Perkin Elmer Lambda 900 UV/Vis/NIR spectrometer in the diffuse reflectance mode.

Photocatalytic  $H_2$  evolution experiments were carried out in a stoppered Quartz vessel. 400 W Xe lamp (Newport) fitted with 12 cm path length of water filter for removal of IR radiation and a 400 nm cut off filter to block the UV light was used to irradiate the vessel. Photoreduction of  $H_2O$  into  $H_2$  was carried out in aqueous solution containing 0.1M  $Na_2SO_4$  and 0.1 M  $Na_2S$ . 2 mg of the catalyst was dispersed in 50 mL water by ultrasonication and the vessel was later purged with  $N_2$  to remove all the gases before irradiation. The evolved gases were analyzed by gas chromatography using Perkin Elmer Clarus 580 GC. 1 mL of the evolved gases was injected manually after every 1 h for analysis.

### 4. Results and discussion

Unlike other conventional methods, urea based synthesis of oxynitrides result in nanoparticles.<sup>5</sup> Figure 1 shows XRD patterns of  $CaTaO_2N$ ,  $SrTaO_2N$  and  $BaTaO_2N$  nanoparticles. All the three oxynitrides have perovskite type structure.  $CaTaO_2N$  crystallizes in orthorhombic structure (space group,  $Pnma$ ),  $SrTaO_2N$  is tetragonal (space group,  $I4/mcm$ ) while  $BaTaO_2N$  forms cubic perovskite (space group,  $Pm3m$ ) structure. Using Scherrer's formula we obtain the crystallite size of  $CaTaO_2N$ ,  $SrTaO_2N$  and  $BaTaO_2N$  to be 29, 24 and 49 nm respectively.

Figure 2 shows the XRD patterns of  $SrTaO_2N$  obtained from urea method ( $SrTaO_2N$ -urea) and high temperature ammonolysis method ( $SrTaO_2N$ -bulk). We have ball-

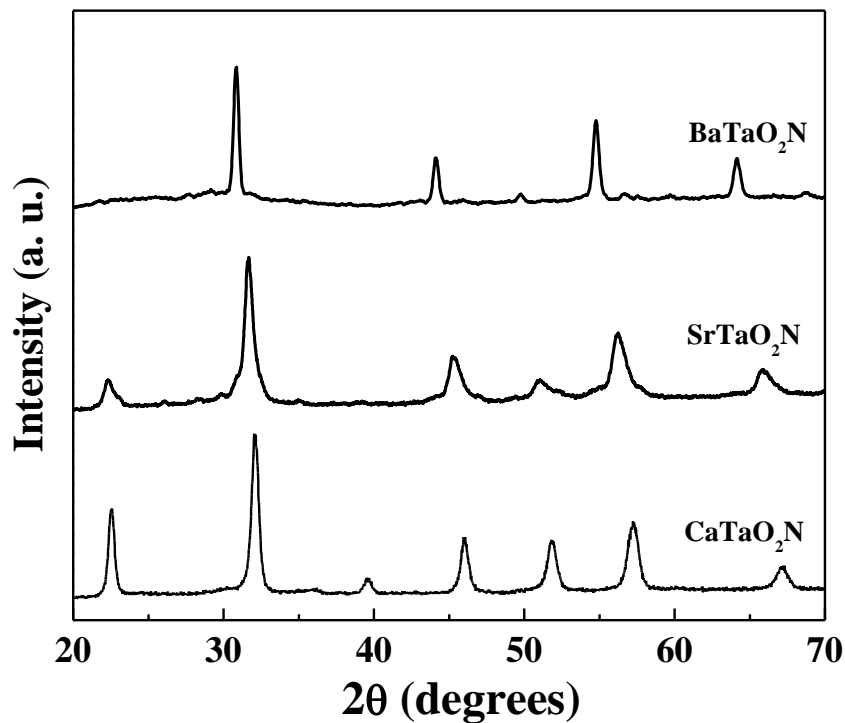


Figure 1 XRD patterns of  $CaTaO_2N$ ,  $SrTaO_2N$  and  $BaTaO_2N$

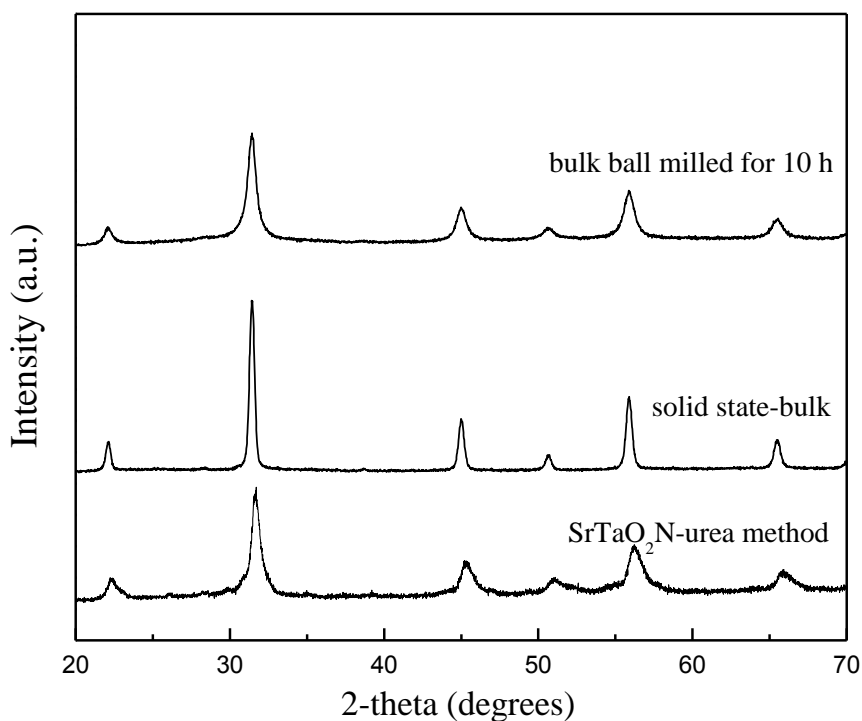
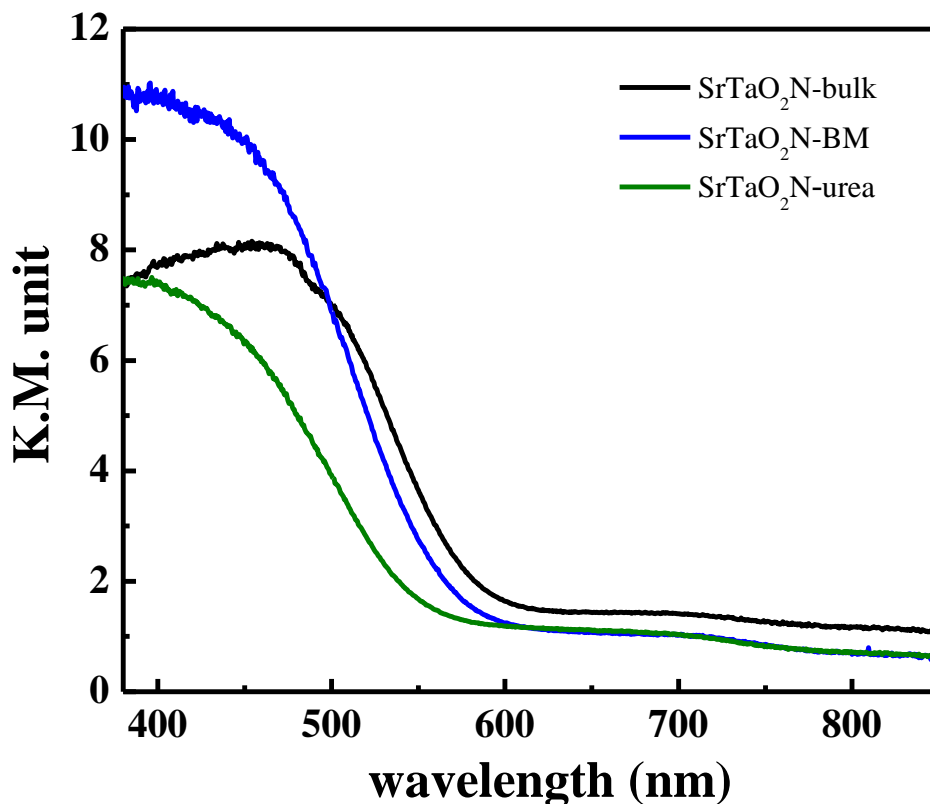


Figure 2 XRD patterns of  $SrTaO_2N$  prepared by urea method, high temperature ammonolysis method and ball milled  $SrTaO_2N$  obtained from high temperature ammonolysis method



milled the bulk  $\text{SrTaO}_2\text{N}$  for 10 hours to obtain smaller particles of crystalline  $\text{SrTaO}_2\text{N}$  ( $\text{SrTaO}_2\text{N}$ -BM). Reflections in the XRD patterns for bulk  $\text{SrTaO}_2\text{N}$  is quite sharp signifying the bulk nature of the sample. On ball milling we can clearly observe significant broadening of the reflections because of the decrease in the particle size.



**Figure 3 UV-Vis spectra of  $\text{SrTaO}_2\text{N}$  prepared by urea method, high temperature ammonolysis method and ball milled  $\text{SrTaO}_2\text{N}$  obtained from high temperature ammonolysis method**

Figure 3 shows the UV-Vis spectra of three  $\text{SrTaO}_2\text{N}$  samples carried out in diffuse reflectance mode. The absorbance is converted into Kubelka-Munk unit. The calculated band gaps from the respective band edge positions are 2.25, 2.12 and 2.08 eV for  $\text{SrTaO}_2\text{N}$ -urea,  $\text{SrTaO}_2\text{N}$ -bulk and  $\text{SrTaO}_2\text{N}$ -BM respectively. The larger value of the band gap is because of the nitrogen deficiency in our nanoparticles samples prepared by urea method. This can be expected because unlike the bulk synthesis where ammonia flows continuously, urea decomposes at low temperatures and might not be able to supply enough ammonia (in-situ). Moreover, the urea based synthesis is one step reaction whereas in the bulk synthesis we carry out three cycles of ammonolysis. The slightly higher value of band gap in ball milled

sample compared to the bulk sample is due to the loss of some nitrogen content because of the mechanical heating while milling.

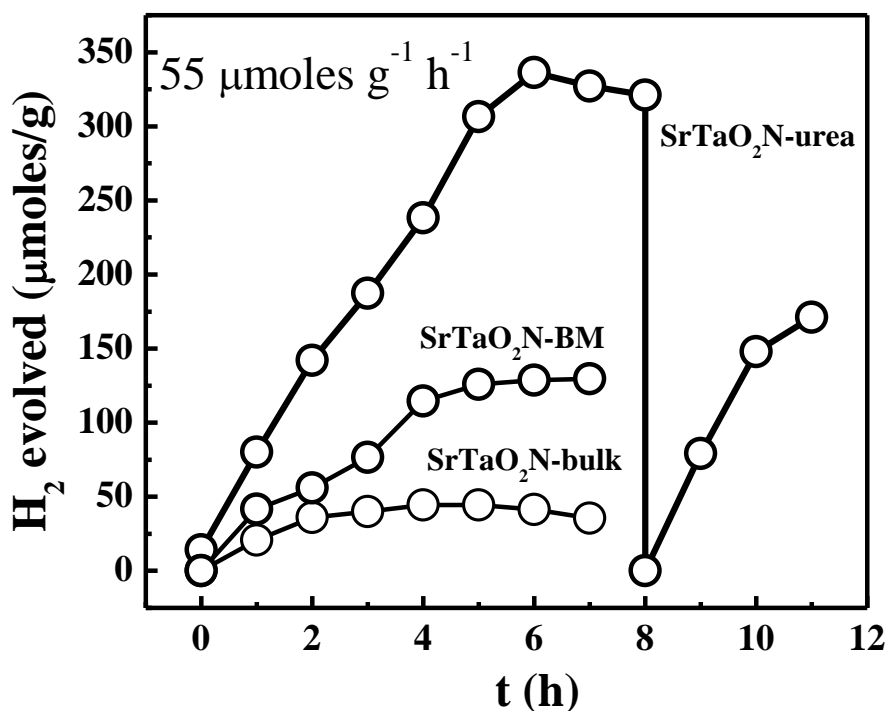


Figure 4 H<sub>2</sub> evolution with time for SrTaO<sub>2</sub>N-urea, SrTaO<sub>2</sub>N-bulk, SrTaO<sub>2</sub>N-BM under visible light ( $\lambda > 400$ )

Recently, Woodward and coworkers showed using a combination of spectroscopic techniques that the bottom of the conduction band in CaTaO<sub>2</sub>N, SrTaO<sub>2</sub>N and BaTaO<sub>2</sub>N is more negative than the water reduction potential.<sup>6</sup> According to this study, SrTaO<sub>2</sub>N should be a good material for the photocatalysis of hydrogen evolution from water reduction. We have tested all the three SrTaO<sub>2</sub>N samples as catalysts for hydrogen evolution (Figure 4). We do not use any co-catalyst for this reaction. Na<sub>2</sub>S + Na<sub>2</sub>SO<sub>3</sub> is used as sacrificial agent in the aqueous medium which donate electrons to the valence band of SrTaO<sub>2</sub>N where holes are created during photo excitation by visible light ( $\lambda > 400$  nm). This reduces the probability of electron-hole recombination process thus favors the reduction of water at the conduction band of SrTaO<sub>2</sub>N. We observe that our SrTaO<sub>2</sub>N-urea sample is the most active catalyst with overall H<sub>2</sub> evolution of 325 μmole per gram of the catalyst at a rate of 55 μmoles/g/h. SrTaO<sub>2</sub>N-bulk and SrTaO<sub>2</sub>N-BM show overall H<sub>2</sub> evolution of 38 and 140 μmole per gram

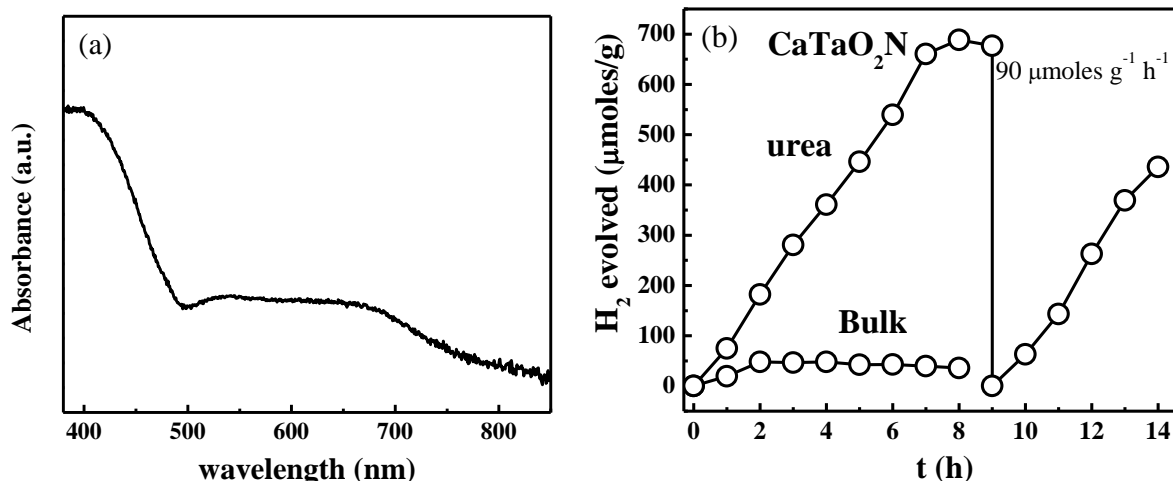


Figure 5 (a) UV-Vis spectra of CaTaO<sub>2</sub>N-urea and (b) H<sub>2</sub> evolution with time for CaTaO<sub>2</sub>N-urea and CaTaO<sub>2</sub>N-bulk

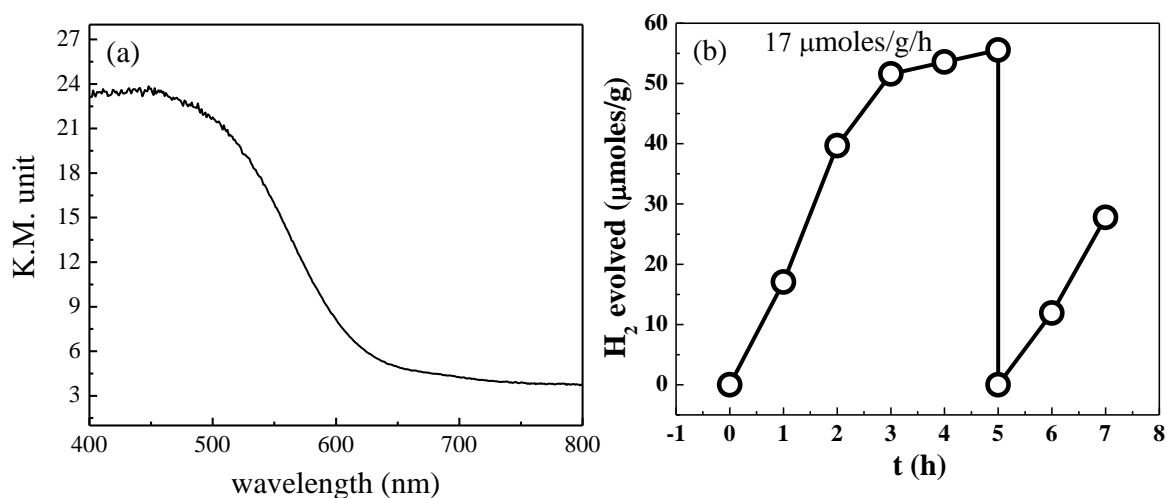


Figure 6 (a) UV-Vis spectra and (b) H<sub>2</sub> evolution with time of BaTaO<sub>2</sub>N-urea

respectively. High activity of SrTaO<sub>2</sub>N-urea sample can be attributed to the high surface area compared to SrTaO<sub>2</sub>N-bulk. The surface area of the SrTaO<sub>2</sub>N-bulk is increased by ball milling and we see an enhancement of activity in SrTaO<sub>2</sub>N-BM compared to SrTaO<sub>2</sub>N-bulk. To the best of our knowledge, this is the first report of H<sub>2</sub> evolution catalysis by ATaO<sub>2</sub>N (A = Ca, Sr and Ba) without the use of any cocatalyst. Figure 5(a) shows the UV-Vis spectrum of CaTaO<sub>2</sub>N nanoparticles prepared by urea method with a band gap of 2.50 eV which is slightly more than the bulk CTaO<sub>2</sub>N (2.40 eV). Hydrogen evolution of CaTaO<sub>2</sub>N-urea is shown in Figure 5(b). It shows an overall H<sub>2</sub> evolution of 698 μmoles/g with a rate of 90

μmoles/g/h. The corresponding bulk material shows relatively small activity with overall evolution of only 50 μmoles/g. In Figure 6(a) we show the UV-Vis spectrum of BaTaO<sub>2</sub>N nanoparticles with a band gap of 1.94 eV. H<sub>2</sub> evolution activity of BaTaO<sub>2</sub>N is the least (overall H<sub>2</sub> evolution = 56 μmoles/g ) compared to the other nanoparticles systems prepared by urea method despite the lowest band gap (Figure 6(b)). This is probably due to the relatively larger size (49 nm, compared to 29 and 24 nm for CaTaO<sub>2</sub>N and SrTaO<sub>2</sub>N respectively) of BaTaO<sub>2</sub>N nanoparticles.

## **5. Conclusions**

We prepared nanoparticles of ATaO<sub>2</sub>N (A = Ca, Sr and Ba) by urea method. They absorb visible light with band gap 2.50, 2.25 and 1.94 eV for CaTaO<sub>2</sub>N, SrTaO<sub>2</sub>N and BaTaO<sub>2</sub>N respectively. The larger value of band gap compared to their bulk counterpart is because of nitrogen deficiency in the nanoparticles. These samples were tested for H<sub>2</sub> evolution catalysis in the visible light and found to be active without the use of any cocatalyst. Despite of the lowest band gap among all, BaTaO<sub>2</sub>N shows the least activity due to the larger particle size.

## 6. References

1. M. Jansen and H. P. Lescourt, *Nature* 2000, 404, 980-982.
2. B. Siritanaratkul, K. Maeda, T. Hisatomi and K. Domen, *ChemSusChem* 2011, 4, 74-78.
3. M. Higashi, R. Abe, T. Takata and K. Domen, *Chem. Mater.* 2009, 21, 1543-1549.
4. S. J. Clarke, B. P. Guinot, C. W. Michie, M. J. Calmont and M. J. Rosseinsky, *Chem. Mater.* 2002, 14, 288-294.
5. A. Gomathi, S. Reshma and C. N. R. Rao, *J. Solid State Chem.* 2009, 182, 72-76.
6. S. Balaz, S. H. Porter, P. M. Woodward and L. J. Brillson, *Chem. Mater.* 2013, 25, 3337-3343.



## *Part II*

# *N and N, F-codoped Oxides*



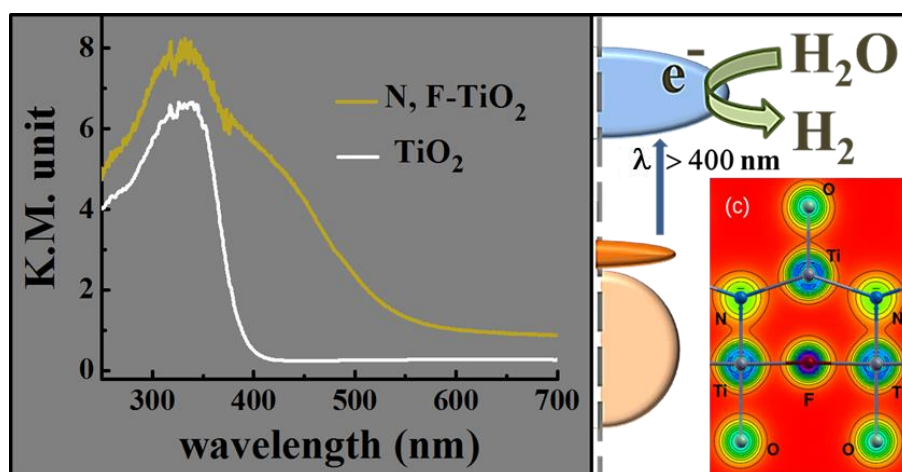


## Chapter II.1

### Synthesis, photocatalysis and varied properties of nitrogen and fluorine co-substituted TiO<sub>2</sub> nanoparticles\*

#### Summary

TiO<sub>2</sub> (anatase) co-doped with nitrogen and fluorine, synthesized by a simple solid state route, using urea and ammonium fluoride as sources of nitrogen and fluorine respectively as well as by decomposition of (NH<sub>4</sub>)<sub>2</sub>TiF<sub>6</sub> for comparison, have been characterized by various techniques. XPS analysis shows the composition to be TiO<sub>1.7</sub>N<sub>0.18</sub>F<sub>0.12</sub> for urea based method (N, F-TiO<sub>2</sub>-urea) and TiO<sub>1.9</sub>N<sub>0.04</sub>F<sub>0.06</sub> for complex decomposition method (N, F-TiO<sub>2</sub>-complex). Both the materials are defect-free as revealed by photoluminescence spectroscopy. Thus, N, F-TiO<sub>2</sub>-urea exhibits smaller defect-induced magnetization compared to the nitrogen-doped sample. Co-substitution of N and F is accompanied with an enhancement of the absorption of light in the visible region giving rise to yellow color with a band gap of ~ 2.2 eV in case of N, F-TiO<sub>2</sub>-urea. It exhibits enhanced photocatalytic activity and also significant hydrogen evolution (400 μmoles/g) on interaction with visible light in the absence of any co-catalyst which is much higher compared to N, F-TiO<sub>2</sub>-complex and N-TiO<sub>2</sub>.



\* A paper based on this work has appeared in *Inorg. Chem.*, 2013

## 1. Introduction

TiO<sub>2</sub> is one of the most studied binary transition metal oxide which finds applications in heterogeneous catalysis as a photocatalyst for degradation of organic pollutants and production of hydrogen, in solar cells for generation of electricity, as gas sensors, as pigment in paints and cosmetics, as corrosion protective coating, in ceramics for its high dielectric constant, in electrical devices such as varistors.<sup>1-10</sup> At ambient conditions, it is found in three different structures: anatase (tetragonal), rutile (tetragonal) and brookite (orthorhombic). TiO<sub>6</sub> octahedra in rutile are slightly distorted. It is thermodynamically the most stable among the three phases which remains stable at most temperatures and pressures up to 60 kbar. In anatase, TiO<sub>6</sub> octahedra are more distorted than in rutile. It is mostly stable in the nanocrystalline form and transforms to the rutile phase on increasing the size. Brookite crystallizes in the orthorhombic structure. It is the least dense of all and has been rarely studied for the above mentioned applications. However, highly faceted nanocrystals of brookite has been shown to be an excellent catalyst towards the photodegradation of organic contaminants.<sup>11</sup>

Increasing energy demands and rapid consumption of fossil fuels has motivated a great deal of research on materials capable of producing hydrogen by reduction of water. Among them, TiO<sub>2</sub> has been an important material because of its band structure, high chemical and photostabilities, as well as abundance and nontoxicity. A limitation, however, is that the visible region of the solar spectrum cannot be used with TiO<sub>2</sub>. Considerable amount of work has been carried out in order to extend the absorption of TiO<sub>2</sub> to the visible region. Metal ion doping in TiO<sub>2</sub> is one of the ways to narrow down the band gap. The decrease in the band gap is not sufficient to enhance the photocatalytic activity of TiO<sub>2</sub>. Choi *et al.* doped many metal ions in quantum sized (2-4 nm) anatase particles among which Fe<sup>3+</sup>, Mo<sup>5+</sup>, Ru<sup>3+</sup>, Os<sup>3+</sup>, Re<sup>5+</sup>, V<sup>4+</sup> and Rh<sup>3+</sup> (0.1-0.5 atomic %) showed increase in the photoreactivity for both oxidation and reduction on the other hand a decrease was observed for Co<sup>3+</sup> and Al<sup>3+</sup>.<sup>12</sup> p-type doping is obtained by dissolving lower valent metal ions (Cr<sup>3+</sup>, Al<sup>3+</sup>, Ga<sup>3+</sup>, Ba<sup>2+</sup>, Ln<sup>3+</sup> *etc.*) compared to Ti<sup>4+</sup> in TiO<sub>2</sub> lattice while higher valent metal ions (Nb<sup>5+</sup>, Ta<sup>5+</sup>, Sb<sup>5+</sup> *etc.*) provide n-type doping. Using ab initio calculations, Karvinen *et al.* showed that Ti<sup>3+</sup>, V<sup>3+</sup>,

Cr<sup>3+</sup>, Mn<sup>3+</sup> and Fe<sup>3+</sup> doping narrow the band-gap significantly in case of anatase whereas there is no effect in the rutile system.<sup>13</sup>

Anion doping in TiO<sub>2</sub> is also studied by many workers with nitrogen doping being the most versatile one.<sup>14-17</sup> Effect of nitrogen doping on the electronic properties of TiO<sub>2</sub> has been investigated extensively in the literature.<sup>18-21</sup> Asahi *et al.* performed spin restricted LDA calculations of nitrogen doped anatase and concluded that the band narrowing was due to mixing of N and O 2*p* states in the valence band.<sup>18</sup> Latter studies demonstrated that upon doping, nitrogen forms localized band just above the valence band edge in order to narrow the band gap of anatase.<sup>22-23</sup> Due to the band narrowing, N-doped TiO<sub>2</sub> can now absorb visible light unlike pristine TiO<sub>2</sub>. This led to many studies on the visible light induced photocatalytic activity using N-TiO<sub>2</sub>.<sup>24-27</sup> Hashimoto and coworkers<sup>26</sup> have studied the decomposition of gaseous 2-propanol by N-TiO<sub>2</sub> with visible light. A disadvantage of nitrogen doping is that it creates oxygen vacancies which increase the electron-hole recombination rate. In contrast to the N-doping, fluorine doping in TiO<sub>2</sub> does not change the band gap because the p orbitals of fluorine are lower in energy than those of the less electronegative oxygen atoms. However, the strong electron withdrawing ability of ≡Ti-F groups present on the surface of fluorine-doped TiO<sub>2</sub> makes the recombination of photogenerated electrons and holes difficult allowing this material to be used as a better photocatalyst in the ultraviolet region than undoped TiO<sub>2</sub>.<sup>17, 28-29</sup>

## 2. Scope of the present investigation

In order to achieve photocatalytic activity in the visible region, yet maintaining the defect-free crystal structure, co-doping of TiO<sub>2</sub> by nitrogen and a transition metal<sup>30-31</sup> as well as with nitrogen and fluorine has been attempted.<sup>32-37</sup> It is to be noted that one N atom and one F atom are equivalent to two oxygen atoms and such co-substitution would not create oxygen vacancies and other defects. Wang *et al.*<sup>33</sup> examined the synergistic effect of N and F co-doping on the electronic structure of TiO<sub>2</sub> and its photocatalytic activity, while Liu *et al.*<sup>36</sup> studied water splitting by N, F co-doped TiO<sub>2</sub> prepared hydrothermally starting from bulk TiN. The contents of N and F in the studies reported in the literature are relatively small. We considered it important to synthesize TiO<sub>2</sub> (anatase) with fairly high contents of N and F and study its properties. Towards this end, we have used urea instead of ammonia, ammonium

halides or melamine as the nitrogen source.<sup>26, 38-41</sup> Urea is known to be an effective and cheap source of nitrogen for the synthesis of nitrides, oxynitrides and N-doped oxides.<sup>42-45</sup> Starting with TiO<sub>2</sub> nanoparticles and using urea as the nitrogen source and NH<sub>4</sub>F as the fluorine source, we have obtained N, F co-doped TiO<sub>2</sub> with relatively high percentages of both the dopants. We have investigated the optical, magnetic and photocatalytic properties of N, F-TiO<sub>2</sub> in some detail. In order to understand the electronic structure and properties of N, F-TiO<sub>2</sub>, we have carried out detailed first-principles calculations.

### 3. Experimental section

TiO<sub>2</sub> nanoparticles were prepared by sol-gel method. In a typical synthesis,<sup>46</sup> 2 g Pluronic P 123 was dissolved in 50 mL, 1M NaCl aqueous solution. To this solution, 10 mL titanium isopropoxide was added slowly and stirred at room temperature for 10 h. The white precipitate was centrifuged and washed several times with distilled water and ethanol. The product was dried at 80 °C for 10 h. The obtained powder was then heated in oxygen at 400 °C for 2 h. The TiO<sub>2</sub> powder so obtained was ground with excess of urea and NH<sub>4</sub>F (10 times each by weight). The mixture was heated in nitrogen at 500 °C for 2 h to obtain yellow N, F co-doped TiO<sub>2</sub> powder (N, F-TiO<sub>2</sub>-urea). For comparison, the starting TiO<sub>2</sub> was heated under similar conditions. To dope only nitrogen (N-TiO<sub>2</sub>-urea), the undoped TiO<sub>2</sub> was mixed with urea (10 times by weight) and heated at 500 °C for 1 h in nitrogen atmosphere. N-doped TiO<sub>2</sub> was also prepared by heating the starting TiO<sub>2</sub> powder at 800 °C for 5h in ammonia. The product was heated in air at 450 °C for 30 minutes to obtain light yellow N-doped TiO<sub>2</sub> powder. N, F co-doped TiO<sub>2</sub> (N, F-TiO<sub>2</sub>-complex) was also prepared by decomposing (NH<sub>4</sub>)<sub>2</sub>TiF<sub>6</sub> in air at 550 °C for 1 h according to a reported procedure.<sup>47</sup>

X-ray diffraction patterns were recorded in Bruker D8 Discover Diffractometer and Rigaku-99 diffractometer using Cu K $\alpha$  radiation. In order to obtain cell parameters of doped and undoped TiO<sub>2</sub> powders, Le Bail fitting was carried out using *Fullprof* software.<sup>48</sup> X-ray photoelectron (XP) spectra were recorded in an Omicron Nanotechnology Spectrometer with the Mg K $\alpha$  as X-ray source. Transmission electron microscopy studies were carried out in JEOL JEM 3010, fitted with Gatan CCD camera operating at an accelerating voltage of 300 kV. UV-visible spectra were recorded in Perkin Elmer Lambda 900 UV/Vis/NIR

spectrometer in the diffuse reflectance mode. Photoluminescence spectra were recorded in Flurolog-3 spectrophotometer from Horiba Jobin Yvon. Magnetic measurements were carried out in SQUID VSM (Quantum Design, USA).

In the dye degradation studies, 4 mg catalyst was added to 10 mL of 30  $\mu$ M methyl orange (MO) aqueous solution in a cylindrical quartz vessel and the mixture sonicated for 15 min followed by stirring for 30 min in dark. The vessel was irradiated with the visible light by exposing it to a 400 W Xe lamp (Newport) fitted with 12 cm path length of water filter for removal of IR radiation along with a 400 nm cut-off filter. 1 mL of the mixture was taken out at an interval of 20 min for 2 h for recording UV-Vis spectra in order to get the concentration of MO. Before taking the UV-Vis spectra, the catalyst dispersed in the mixture was centrifuged out to avoid scattering.

Photocatalytic H<sub>2</sub> evolution experiments were carried out in a stoppered Quartz vessel. 400 W Xe lamp (Newport) fitted with 12 cm path length of water filter for removal of IR radiation and a 400 nm cut off filter to block the UV light was used to irradiate the vessel. Photoreduction of H<sub>2</sub>O into H<sub>2</sub> was carried out in aqueous solution containing 0.1M Na<sub>2</sub>SO<sub>4</sub> and 0.1 M Na<sub>2</sub>S. 2 mg of the catalyst was dispersed in 50 mL water by ultrasonication and the vessel was later purged with N<sub>2</sub> to remove all the gases before irradiation. The evolved gases were analyzed by gas chromatography using Perkin Elmer Clarus 580 GC. 1 mL of the evolved gases was injected manually after every 1 h for analysis.

## **4. Results and discussion**

### **4.1 Results from experiments**

The white product of the sol-gel synthesis is amorphous and has some carbon content even after several washing because of the use of excess surfactant. In order to remove it and to make the sample crystalline, the amorphous powder was heated at 500 °C for 2 h. The product obtained contains pure anatase form of TiO<sub>2</sub>. At higher temperatures, thermodynamically more stable rutile phase is known to form. Direct ammonolysis of this anatase powder at temperature 500 °C failed to provide N-doped TiO<sub>2</sub> which was evident

from the grey color of the product as confirmed from elemental analysis. The grey color could be due to the oxygen vacancy at the surface of the anatase particles. At 600 °C we

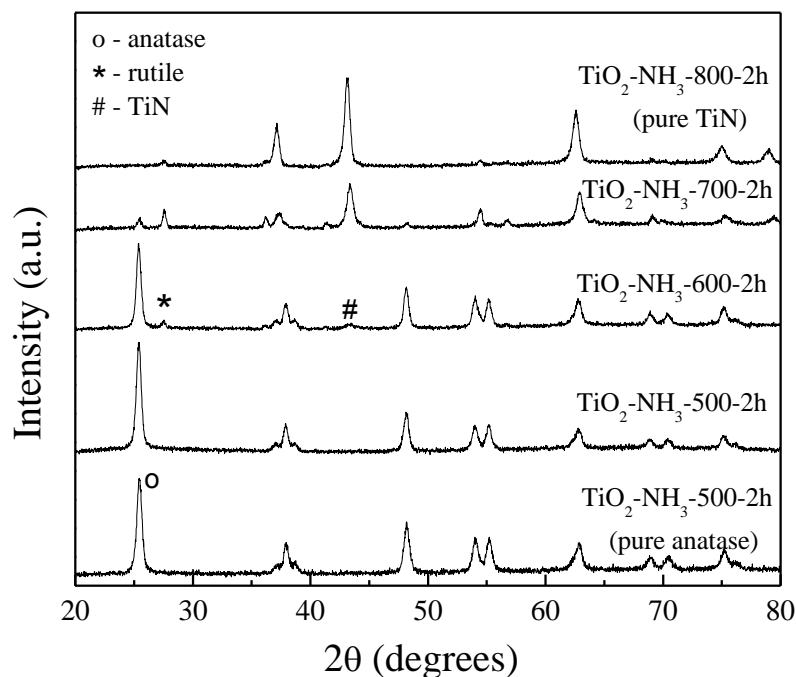


Figure 1 XRD patterns of TiO<sub>2</sub> nanoparticles heated at different temperatures in ammonia

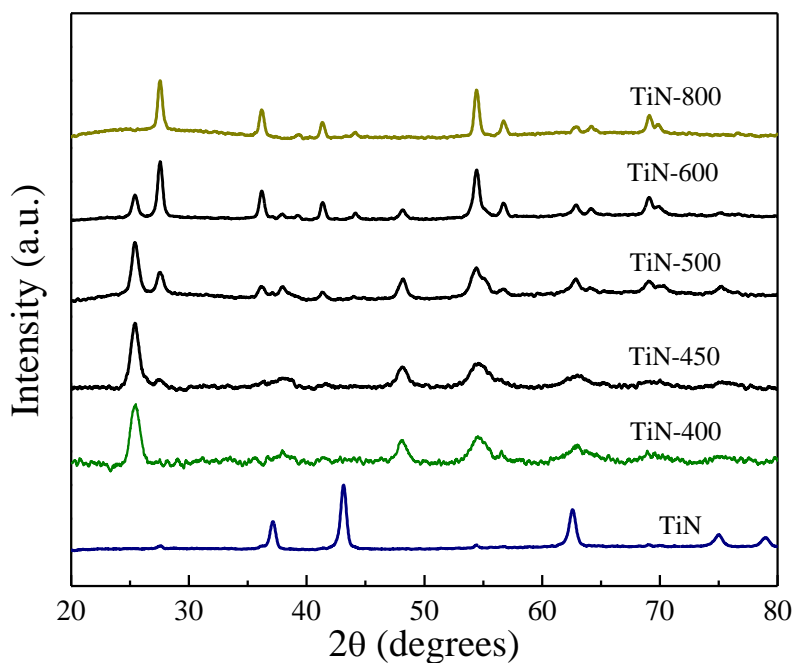


Figure 2 XRD patterns of TiN and the materials obtained after heating TiN in air at different temperatures

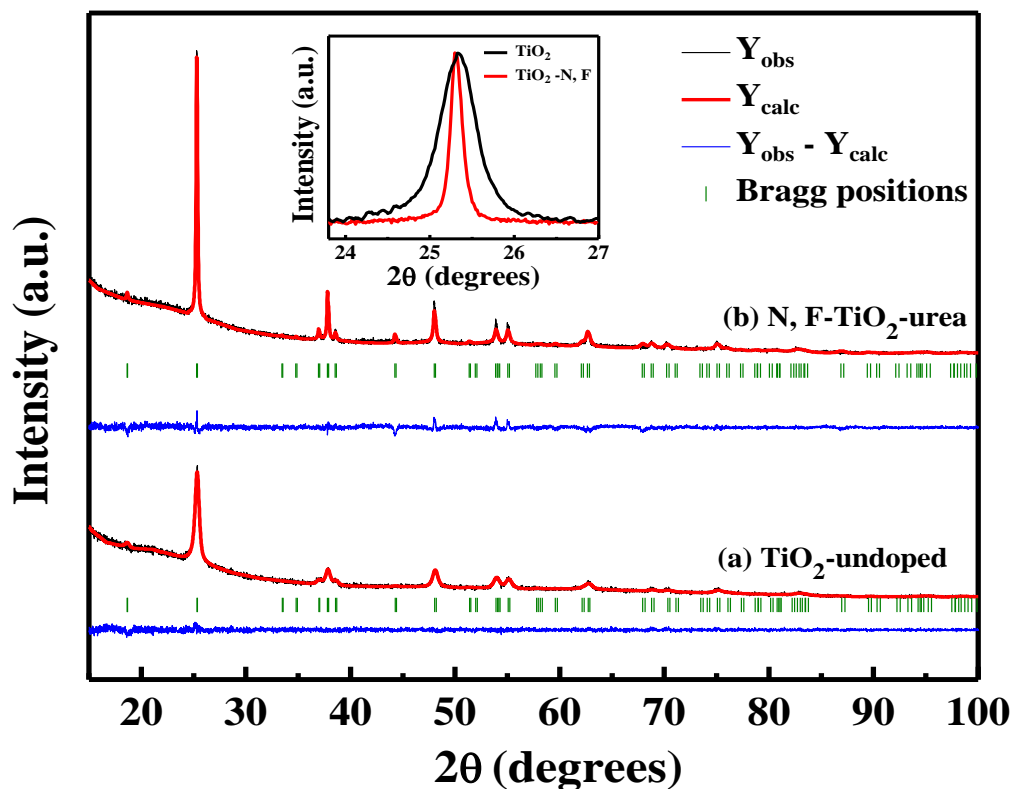
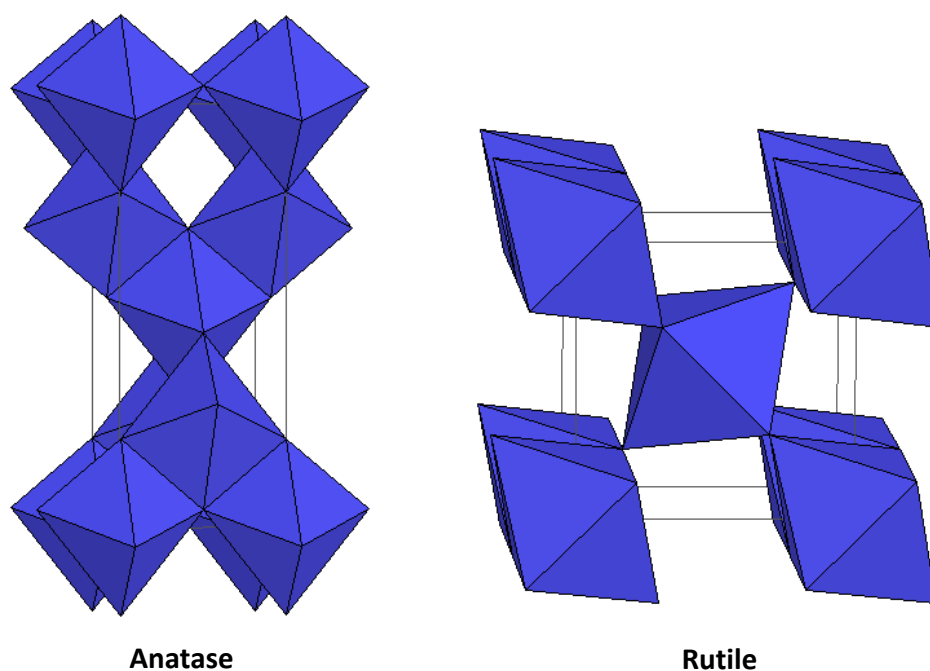


Figure 3 XRD patterns of (a) undoped-TiO<sub>2</sub> and (b) N, F-TiO<sub>2</sub>-urea. Inset shows magnified view of the (101) reflections

observe the appearance of small amount of rutile phase (Figure 1) and an indication of the formation of TiN. At 700 °C, the major phase is TiN with small amounts of anatase and rutile while at 800 °C the phase pure TiN is obtained. Another approach to achieve nitrogen doping is to oxidize TiN hydrothermally or high temperature treatment in air. Until now this method has been utilize to obtain only the rutile phase of the N-doped TiO<sub>2</sub>.<sup>36, 49-50</sup> Here, we show that if TiN is heated in air at low temperature for short durations it is possible to obtain anatase phase of N-doped TiO<sub>2</sub>. Figure 2 shows the pure anatase phase which is prepared by heating TiN at a temperature 400 °C in air. The powder obtained is light yellow in color which fades away as the temperature is increased. At higher temperatures rutile phase is more stable and at 800 °C a pale yellow colored pure rutile phase is obtained. We also varied the treatment time at 800 °C but the rutile phase was the only phase at this temperature even for a treatment time as low as 5 minutes. Apart from ammonia we also carried out a reaction of undoped TiO<sub>2</sub> with excess of urea in nitrogen atmosphere at 500 °C but like ammonia treatment, we obtained a grey powder which was again probably a surface reduced TiO<sub>2</sub>. In

addition to urea when we add excess of ammonium fluoride as a fluorine source, we obtain a dark yellow powder (N, F-TiO<sub>2</sub>-urea). Figure 3 shows the XRD patterns of undoped-TiO<sub>2</sub> and N, F-TiO<sub>2</sub>-urea, both of which crystallize in the anatase structure with the tetragonal space group  $P4_2/mnm$ , without any trace of the rutile phase. The cell parameters obtained by fitting the XRD patterns for the undoped-TiO<sub>2</sub> and N, F-TiO<sub>2</sub>-urea are  $a = 3.783(1) \text{ \AA}$ ,  $c = 9.509(3) \text{ \AA}$  and  $a = 3.788(1) \text{ \AA}$ ,  $c = 9.513(3) \text{ \AA}$  respectively. The XRD pattern of N, F-TiO<sub>2</sub>-urea exhibits sharper reflections (see inset of Figure 3 showing the (101) reflections). The crystallite sizes from the Scherrer's formula are 16 and 51 nm for undoped-TiO<sub>2</sub> and N, F-TiO<sub>2</sub>-urea samples respectively. The anatase structure can be visualized by arrays of TiO<sub>6</sub> octahedra with four edges of each octahedron shared with the neighboring octahedron. On the other hand rutile can be imagined as infinite columns of edge shared octahedral while each edge-shared oxygen is corner-shared with an adjacent infinite chain.



**Figure 4 Crystal structure of anatase and rutile**

Figure 5 shows the core-level X-ray photoelectron spectra (XPS) in the N 1s and F 1s regions of N, F-TiO<sub>2</sub>-urea. Nitrogen doped TiO<sub>2</sub> has been well characterized by XPS in terms of nature of N atoms at the surface and inside the crystal. The N 1s spectrum in Figure 5(a) can be deconvoluted into three peaks centred around 396.9, 398.4 and 401.0 eV. The signal at the lowest binding energy is ascribed to the nitrogen atom directly bonded to Ti<sup>5+</sup> and the signal



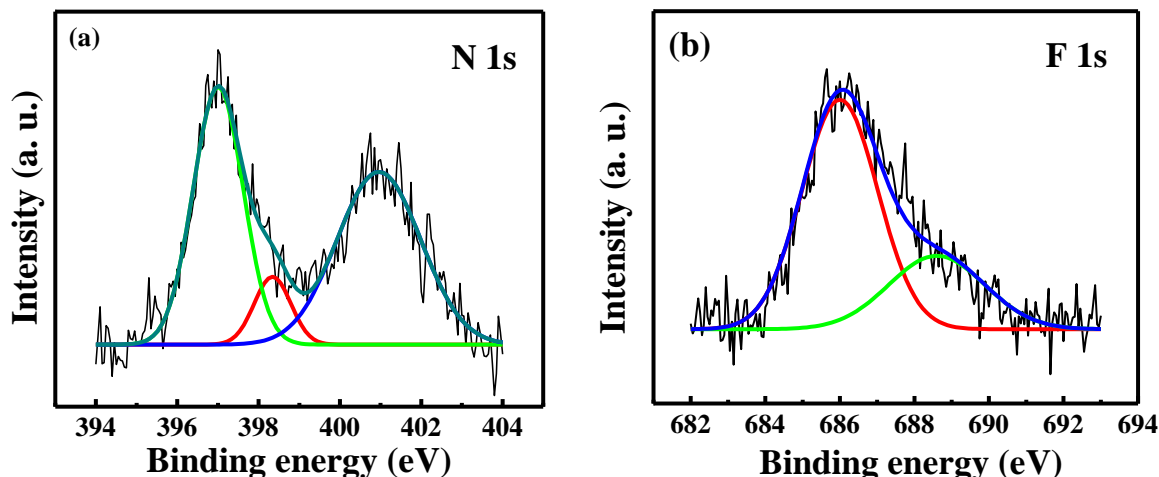


**Figure 5** Core-level XP spectra in the (a) N 1s and (b) F 1s regions of N, F-TiO<sub>2</sub>-urea

around 398.4 eV to interstitial nitrogen atoms.<sup>52</sup> Surface adsorbed nitrogen mostly present as NH gives rise to a peak at 401 eV.<sup>32</sup> The core-level spectrum of fluorine in Figure 5(b) can be deconvoluted into peaks centered around 686.0 and 688.6 eV. The more intense peak at 686.0 eV has been attributed to the formation of species such as TiOF<sub>2</sub> at the surface of the particles.<sup>32</sup> The peak at the higher binding energy (688.6 eV) is due to the substitution of fluorine in the oxygen site of TiO<sub>2</sub>.<sup>32, 36, 52</sup> Taking the capture cross sections into account, the composition of the co-substituted compound by taking only the signals at 396.9 and 688.6 eV for nitrogen and fluorine respectively works out to be TiO<sub>1.7</sub>N<sub>0.18</sub>F<sub>0.12</sub>. If we take both 396.9 and 398.4 eV signals of N 1s and both the 686 and 688.6 eV signals of F 1s into consideration, the composition turns out to be TiO<sub>1.47</sub>N<sub>0.28</sub>F<sub>0.25</sub>. Decomposing (NH<sub>4</sub>)<sub>2</sub>TiF<sub>6</sub> in air results in a moderate amount of nitrogen and fluorine co-doping with a composition TiO<sub>1.9</sub>N<sub>0.04</sub>F<sub>0.06</sub>. The TiO<sub>2</sub> sample doped only with nitrogen (obtained from TiN) has the composition TiO<sub>0.97</sub>N<sub>0.03</sub> as determined by XPS.

FESEM images of undoped, N-doped (from TiN) and N, F-codoped (urea and complex method) samples are shown in Figure 6. An average size of 15-20 nm with some extent of agglomeration among the particles can be observed. N-doped TiO<sub>2</sub> exhibits more agglomeration along with an increase in the average particle size (Figure 6(b)). This is expected because the TiN used for the synthesis was obtained by the ammonolysis of undoped TiO<sub>2</sub> at high temperature (800 °C). It is surprising to note that under the similar thermal conditions used for undoped TiO<sub>2</sub>, codoping of N and F enhances the crystal growth

significantly to result in big particles with sharp edges (Figure 6(c) and (d)). Figure 7 shows TEM images of undoped-TiO<sub>2</sub> and N, F-TiO<sub>2</sub>-urea samples. The average size of the undoped-TiO<sub>2</sub> is found to be ~ 15 nm as shown in Figure 7(a). On co-substitution of nitrogen and fluorine, the crystallite size grows considerably as shown in Figure 7(b). These observations are consistent with the XRD results. Inset of Figures 7(a) and (b) shows HREM images revealing the (101) lattice fringes which indicates the single crystalline nature of the particles.

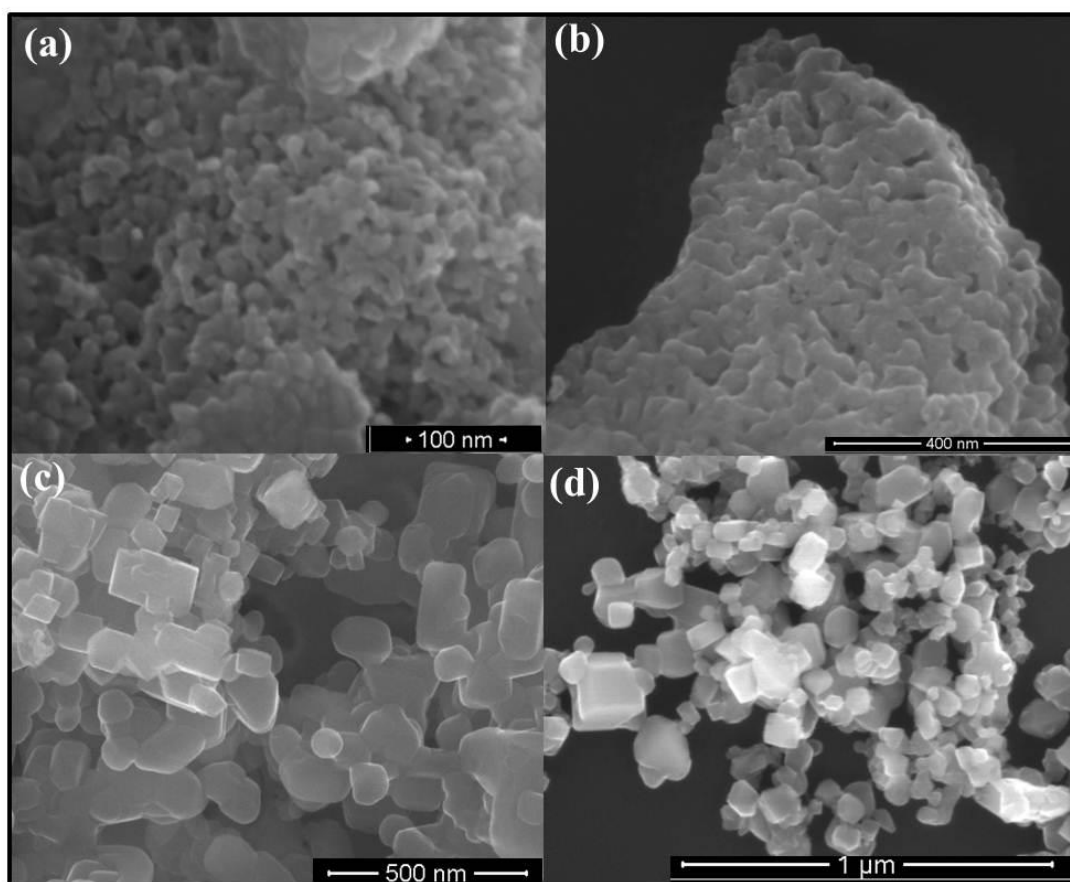


**Figure 6 FESEM images of (a) undoped-TiO<sub>2</sub> nanoparticles, (b) N-doped TiO<sub>2</sub> obtained from TiN, (c) N, F-TiO<sub>2</sub> from urea method and (d) N, F-TiO<sub>2</sub> from complex method**

In Figure 8(a), we show the UV-visible spectra of undoped-TiO<sub>2</sub>, N-doped TiO<sub>2</sub>, N, F-TiO<sub>2</sub>-urea and N, F-TiO<sub>2</sub>-complex. The band edge in the undoped-TiO<sub>2</sub> is observed at 393 nm (3.15 eV), consistent with the indirect band gap of anatase. Substitution with nitrogen causes only a small change in the spectrum with a weak broad feature around 450 nm. On co-

substituting with both nitrogen and fluorine by urea and ammonium fluoride, the white powder turns dark yellow (Figure 8(a)). The absorption extends to the visible region with

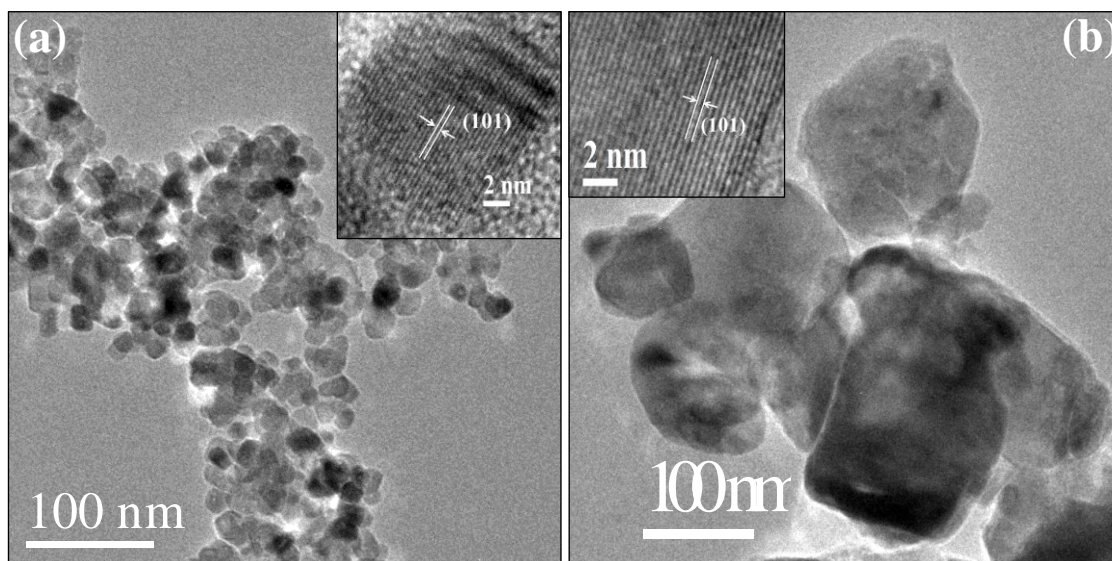


Figure 7 TEM images of (a) undoped-TiO<sub>2</sub> and (b) N, F-TiO<sub>2</sub>-urea. Inset shows the HREM images

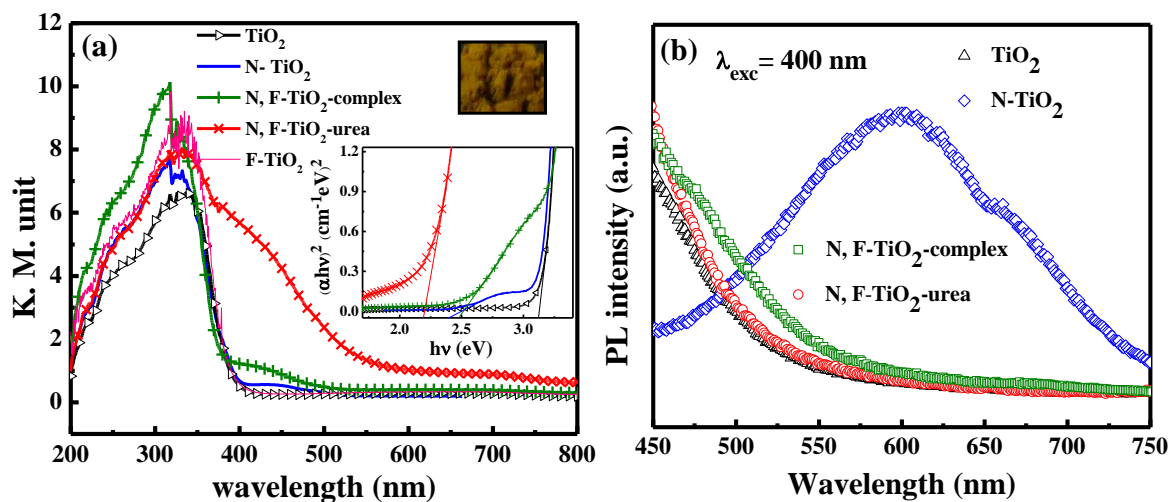


Figure 8 (a) UV-Visible and (b) PL spectra of undoped-TiO<sub>2</sub>, N-doped TiO<sub>2</sub>, N, F-TiO<sub>2</sub>-complex and N, F-TiO<sub>2</sub>-urea. Insets in (a) show the color of N, F-TiO<sub>2</sub>-urea and the Tauc plot for all doped and undoped samples

the band edge at 563 nm (2.2 eV). The band edge in the case of N, F-TiO<sub>2</sub>-complex is found to be 496 nm (2.5 eV). The inset of Figure 8(a) shows Tauc's plot for all the four samples. Band-gap estimations are carried out using this plot. The absorption in the visible region in

N, F-TiO<sub>2</sub>-urea is significantly high compared to the earlier reports of TiO<sub>2</sub>.<sup>26, 33, 40</sup> This can be attributed to the high content of N and F in the sample prepared by us. It should be noted that when TiO<sub>2</sub> is heated in the urea alone, there is almost no substitution of nitrogen causing no change in the color and the band edge position. Presence of F appears to help in increasing the extent of N doping. We have also shown the UV-visible spectrum of F-TiO<sub>2</sub> which shows no detectable change in the band edge position compared to undoped-TiO<sub>2</sub>.

Photoluminescence (PL) spectroscopy is a useful technique to study defects in oxides. PL spectra at an excitation wavelength of 400 nm of undoped-TiO<sub>2</sub>, N-TiO<sub>2</sub>, N, F-TiO<sub>2</sub>-urea and N, F-TiO<sub>2</sub>-complex are shown in Figure 8(b). A broad emission band centred around 600 nm can be clearly seen in N-TiO<sub>2</sub>. The presence of this band is attributed to the oxygen vacancies.<sup>53-54</sup> The absence of defect band in co-doped TiO<sub>2</sub> is expected because co-doping of nitrogen and fluorine in the oxygen site maintains the charge balance in the oxide.

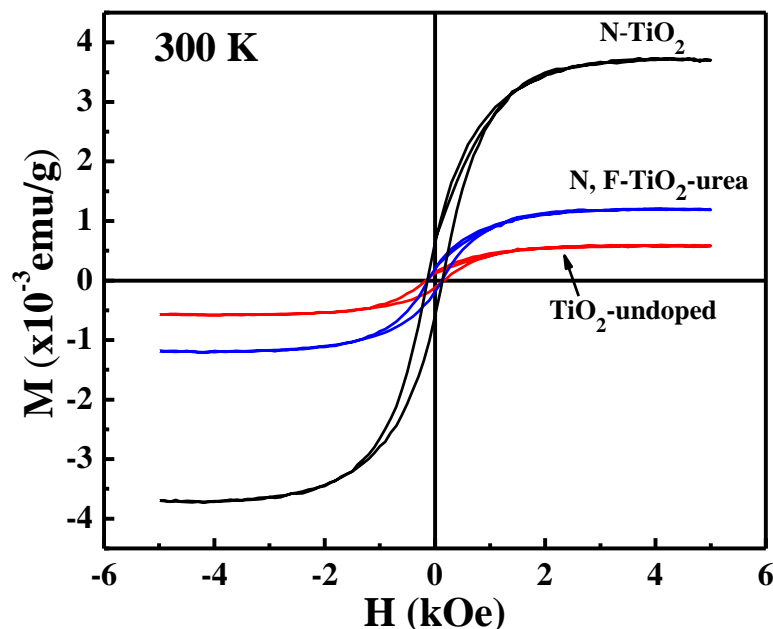
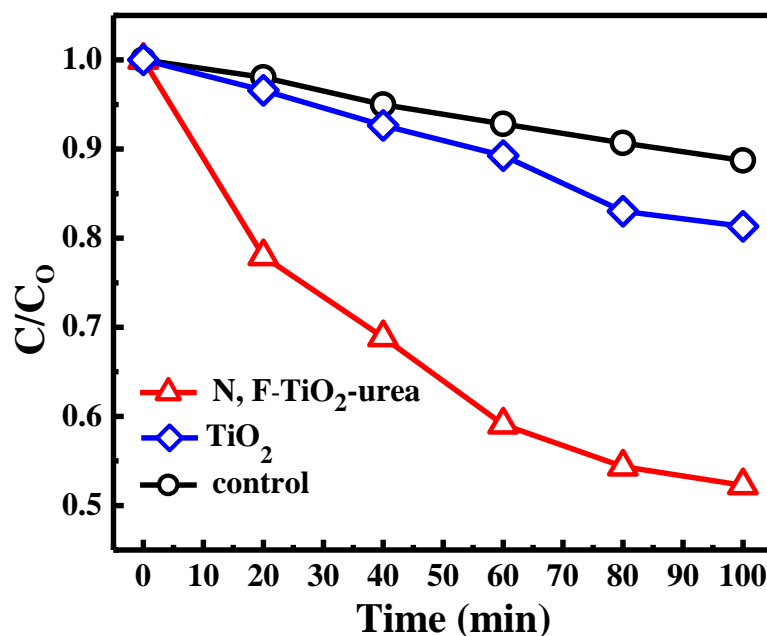


Figure 9 Magnetic hysteresis of undoped-TiO<sub>2</sub>, N-doped TiO<sub>2</sub> and N, F-TiO<sub>2</sub>-urea at room temperature

It has been established recently that room temperature ferromagnetism is a universal feature of otherwise non-magnetic inorganic nanoparticles.<sup>55-56</sup> The origin of the ferromagnetism is attributed to the presence of defects such as cation or anion vacancies in the nanoparticles. Figure 9 shows the room temperature magnetization data of undoped and doped TiO<sub>2</sub>

samples. We observe room temperature ferromagnetic hysteresis in both undoped and doped TiO<sub>2</sub> nanoparticles, but the saturation magnetization ( $M_S$ ) of N-doped TiO<sub>2</sub> is the highest with a value of  $3.7 \times 10^{-3}$  emu/g. This observation is consistent with the PL results, which show a broad oxygen defect related band in the case of N-doped TiO<sub>2</sub>. For undoped-TiO<sub>2</sub> and N, F-TiO<sub>2</sub>-urea, where we do not observe any PL defect band, the values of  $M_S$  are  $0.6 \times 10^{-3}$  and  $1.2 \times 10^{-3}$  emu/g respectively. These values are smaller than the value exhibited by N-doped TiO<sub>2</sub> ( $3.7 \times 10^{-3}$  emu/g).

Dye degradation capability is employed as a measure of the photocatalytic activity of a material. We have studied the degradation of methyl orange (MO) to establish the



**Figure 10** Degradation of methyl orange by undoped-TiO<sub>2</sub> and N, F-TiO<sub>2</sub>-urea on visible light irradiation (> 400 nm) along with control

photocatalytic activity of undoped-TiO<sub>2</sub> and N, F-TiO<sub>2</sub>-urea. MO is photostable in the absence of the catalyst unlike methylene blue which shows appreciable degradation in light without any catalyst. When exposed to light with wavelength > 400 nm, MO degrades with a much faster rate in the presence of N, F-TiO<sub>2</sub>-urea as compared to the undoped-TiO<sub>2</sub> as shown in Figure 10. Visible light MO degradation activity in N, F-TiO<sub>2</sub>-urea is attributed to the high visible light absorption in the material. The mechanism of degradation of MO in the presence of TiO<sub>2</sub> is mainly due to the hole oxidation process at higher concentration of MO,

while at the lower concentrations of MO, hydroxyl radicals (OH<sup>·</sup>) are more effective.<sup>57</sup> Results of control experiments with the dye irradiated under visible light (without any catalyst) are also included in Figure 10.

TiO<sub>2</sub> has been used to produce hydrogen by reducing water, since the minimum of the conduction band is more negative than water reduction potential. TiO<sub>2</sub> has, however, the disadvantage of having a high band gap which limits its use in the visible range of the solar spectrum. Nitrogen doping alone is capable of pushing the valance band towards higher energy to narrow the band gap but co-doping with nitrogen and fluorine maintains the charge balance in the system, resulting in eliminating defects or lowering the defect concentration

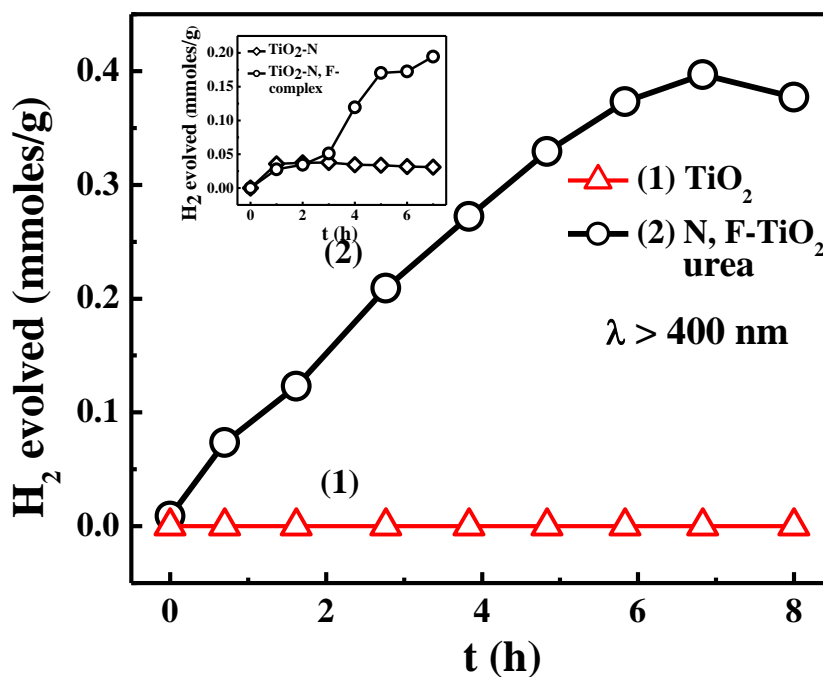


**Figure 11** Hydrogen evolution with respect to time on irradiation with visible light (> 400 nm) for undoped-TiO<sub>2</sub> and N, F-TiO<sub>2</sub>-urea. Inset shows the data for N-doped TiO<sub>2</sub> and N, F-TiO<sub>2</sub>-complex

and a substantial decrease in the band gap. Figure 11 shows the evolution of hydrogen with time for undoped-TiO<sub>2</sub> as well as N, F-TiO<sub>2</sub>-urea in visible light ( $\lambda > 400$  nm). N, F-TiO<sub>2</sub>-urea shows a maximum hydrogen evolution of 400  $\mu$ moles/g of the catalyst with a rate of  $\sim 60$   $\mu$ moles/g/h without the loading of any noble metal or other co-catalyst. To the best of our knowledge, this value of H<sub>2</sub> evolution is highest reported so far under visible light illumination for TiO<sub>2</sub> without any co-catalyst. Under similar conditions, undoped-TiO<sub>2</sub> and

P-25 do not show any H<sub>2</sub> evolution. The inset of Figure 11 shows the H<sub>2</sub> evolution of N-doped TiO<sub>2</sub> and N, F-TiO<sub>2</sub>-complex samples. N-doped TiO<sub>2</sub> shows H<sub>2</sub> evolution of 37 μmoles/g, much lesser than that of N, F-TiO<sub>2</sub>-urea. Defect sites are known to act as recombination centers for photogenerated electrons and holes.<sup>58</sup> As already discussed, PL emission of N-doped TiO<sub>2</sub> shows broad band due to oxygen vacancy, thus lesser yield of H<sub>2</sub> in N-TiO<sub>2</sub> can be attributed to the faster recombination of electron-hole at the defect sites. Li *et al.*<sup>59</sup> also found photocatalytic activity of TiO<sub>2</sub> decreased with increase in defect related PL emission. The N, F-TiO<sub>2</sub>-complex shows relatively higher value of H<sub>2</sub> evolution (180 μmoles/g) compared to N-TiO<sub>2</sub> but yet smaller than N, F-TiO<sub>2</sub>-urea, the latter having a higher N and F content and greater absorption in the visible region.

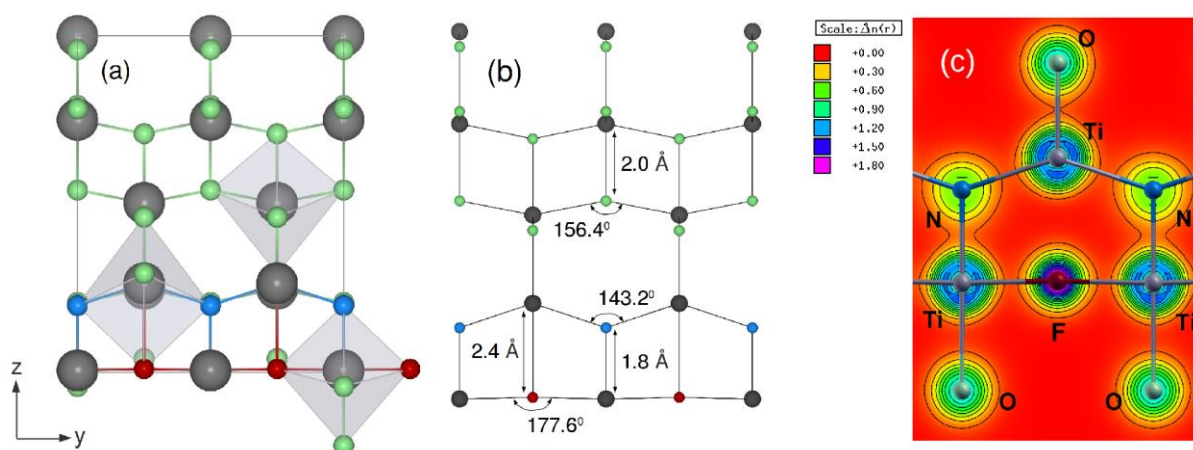


**Figure 12 Structure of N, F-TiO<sub>2</sub> showing (a) Ti in three differently coordinated octahedral environments, (b) the local distortions caused by nitrogen and fluorine co-substitution, and (c) contours of electronic charge density on the (100) plane (Ti = grey, O = green, N = blue, F = maroon)**

## 4.2 Important interpretations from first-principles calculations

First-principles calculations carried out by Prof. Waghmare and co-workers have provided important insight of the local structure and electronic properties of N, F-codoped TiO<sub>2</sub>. They observe significant local structural distortions in N, F-TiO<sub>2</sub> induced at the sites of substitutions (Figure 12(a)). The Ti-N bond length along the *c*-axis is 1.82 Å while the length of the Ti-F bond is 2.40 Å. Notably, these are 7.5% shorter and 22.3% longer respectively, relative to the Ti-O bonds (1.96 Å) in bulk TiO<sub>2</sub>. The changes in the bond lengths of Ti-N

and Ti-F bonds along the *ab*-plane are somewhat less dramatic and are about 3.7% and -1.5% respectively leading to smaller Ti-N-Ti (143.2°) and larger Ti-F-Ti (177.6°) bond angles, in comparison with Ti-O-Ti bond angles in bulk TiO<sub>2</sub> (156.4°) (Figure 12(b)). These structural changes suggest that the behavior of nitrogen and fluorine is like negative and positive charges respectively in N, F-TiO<sub>2</sub>. These local distortions are more pronounced in N, F-TiO<sub>2</sub> than in F-TiO<sub>2</sub> and N-TiO<sub>2</sub>, indicating that nitrogen and fluorine co-substitution reinforces the effects of their substitution individually and gives greater stability.

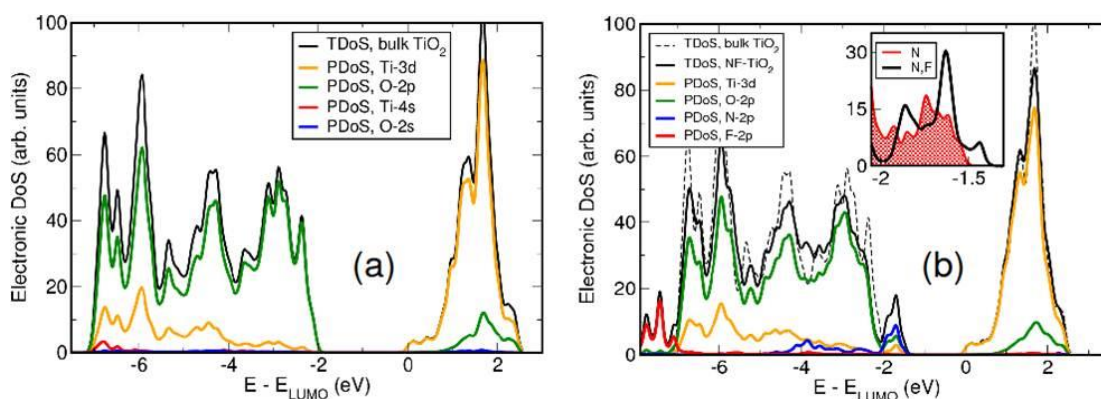


**Figure 13** Density of electronic states projected onto atomic orbitals in (a) bulk, undoped TiO<sub>2</sub>, and (b) N, F-co-substituted TiO<sub>2</sub>. The inset in (b) is a comparison between the total density of electronic states (at the top of the valence band) of N-TiO<sub>2</sub> and N, F-TiO<sub>2</sub>, clearly showing the enhancement in the sub-band due to fluorine co-substitution.

LDA calculations predict an indirect band gap of 2.06 eV for bulk TiO<sub>2</sub>. N, F-TiO<sub>2</sub> has an isolated occupied band split weakly from the rest of the valence bands, leading to a *direct* and considerably reduced gap of 1.48 eV. From the hybrid exchange functional calculations on a 2x2x1 mesh of Bloch vectors, they estimate the correction to the band gaps (in order to address the underestimation of band gaps compared to the experimental findings) and add it to LDA estimates obtained using a much finer mesh of k-vectors. Thus, the corrected band gaps of pure TiO<sub>2</sub> (3.92 eV) and N, F-TiO<sub>2</sub> (3.06 eV) are slightly overestimated in comparison with the experimentally measured values (3.20 eV and 2.28 eV, respectively), but they succeed in capturing more accurately the change in the band gap upon nitrogen and fluorine co-substitution. This reduction in the electronic band gap is essential and partially responsible for the improved photocatalytic activity of TiO<sub>2</sub> after co-substitution with nitrogen and fluorine.



In bulk TiO<sub>2</sub>, the valence band is constituted primarily of O 2*p* orbitals with a little mixing with the Ti 3*d* states while the lowest energy conduction bands are predominantly Ti 3*d* in character (Figure 13(a)). The uppermost valence bands are most affected by N, F substitution, with the N 2*p* derived states arising as a sub-band with a bandwidth of about 0.6 eV, at the top of the valence band (with weaker contributions from the Ti 3*d* and the O 2*p* derived states), thereby effectively reducing the band gap (Figure 13(b)). Analysis of the density of electronic states of N-TiO<sub>2</sub>, F-TiO<sub>2</sub> and N, F-TiO<sub>2</sub> reveals that (a) *p* states of the strongly electronegative fluorine atoms are deep-lying in energy (~6 eV lower than the valence band maximum while those of the less electronegative nitrogen are concentrated at the top of the valence band. (b) Formation of the sub-band of *p* states of the nitrogen atoms (in N, F-TiO<sub>2</sub>) at the top of the valence band is greatly enhanced by the fluorine co-substitution. The lowest energy conduction bands are essentially unaffected by N, F co-substitution and retain their Ti 3*d* character.

Effect of nitrogen and fluorine co-substitution on the nature of interaction of water with (001) and (101) surfaces of TiO<sub>2</sub> has also been studied. Strength of water molecules to adsorb on these surfaces increases significantly upon co-substitution with nitrogen and fluorine, reflected in the increase in adsorption energies: from ~1.6 eV to ~3.6 eV for the (001) surface, and from ~0.7 eV to ~2.0 eV for the (101) surface. Moreover, in the case of (001) surface of N, F-TiO<sub>2</sub>, there is formation of an intermediate complex, characterized by a weakened bond (3.11 Å) between an oxygen (fluorine) atom and the Ti(5c) atom involved in the adsorptive interaction. As a result, this activated oxygen (fluorine) forms a bond (1.04 Å) with a hydrogen atom of the water molecule (Figure 14). The O-H bond lengths of the strained water molecule are 0.97 Å and 1.44 Å, the latter hydrogen being bonded to the activated oxygen (fluorine) atom. This is the intermediate state preempting the dissociation of the water molecule.

For (101) surface too, structural changes contribute towards enhanced catalytic activity: a water molecule relaxes to a position favoring bonding interaction between its hydrogen atoms and two neighboring oxygen (fluorine) atoms on the surface (with O-H bond lengths of 1.69 Å and 1.82 Å). The corresponding O-H bond lengths of the strained water molecule are 1.02 Å and 1.00 Å (in contrast with 0.97 Å for an isolated molecule), making it relatively

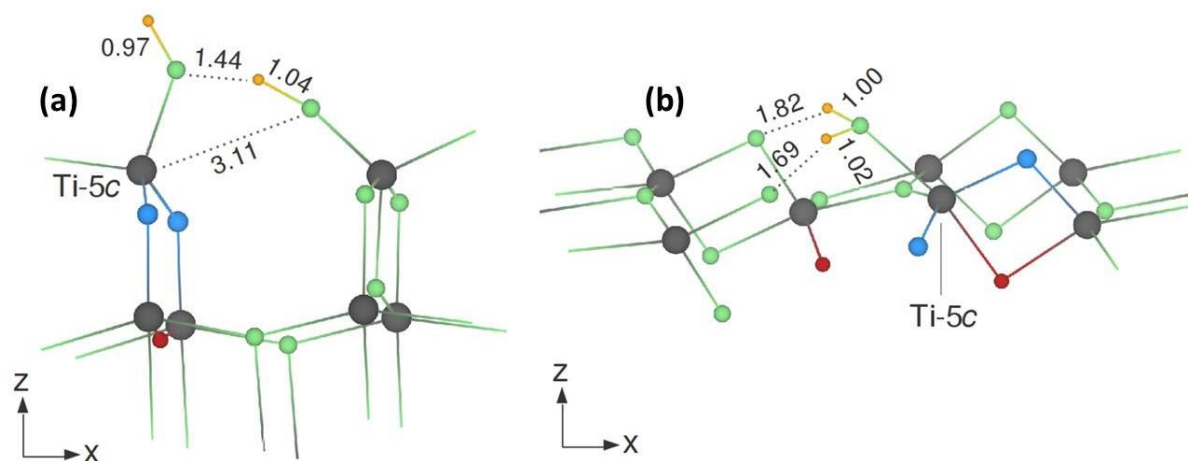


**Figure 14** Interaction of a water molecule with the (a) (001) surface, and (b) (101) surface of N, F-TiO<sub>2</sub>. (All bond lengths shown are in angstrom. Ti = grey, O = green, N = blue, F = maroon, H = orange).

easier to photolyse. The chemical origin of these structural changes lies in the relatively stronger bond between the Ti(5c) atom and a nitrogen atom substituted at the neighboring site, leading to weakening of the Ti(5c)-O(F) bond. The latter is broken with ease and the oxygen (fluorine) atom bonds with a hydrogen atom of the water molecule. Thus, a weaker Ti(5c)-O(F) bond and the associated structural changes contribute towards relatively enhanced water dissociation capabilities of N, F-TiO<sub>2</sub>. Secondly, the sub-band due to N-2p derived states at the top of the valence band, further pronounced by fluorine co-substitution, facilitates absorption of a photon and subsequent electron transfer to a water molecule, thereby increasing the ease with which water is split into hydrogen and oxygen. These factors, combined with the reduced electronic band gap, result in the enhancement of the photocatalytic activity of TiO<sub>2</sub> upon co-substitution with nitrogen and fluorine.

## 5. Conclusions

A simple route to synthesize the anatase phase of N, F-TiO<sub>2</sub> using urea and ammonium fluoride as nitrogen and fluorine sources respectively has been described. The composition of this phase is found to be TiO<sub>1.7</sub>N<sub>0.18</sub>F<sub>0.12</sub>. A lower saturation magnetization of the N, F-TiO<sub>2</sub>-urea sample compared to nitrogen-doped TiO<sub>2</sub> is attributed to the absence of oxygen vacancies as revealed from photoluminescence spectroscopy. A significant reduction in the

band gap on co-substitution with nitrogen and fluorine, accompanied by the yellow coloration is observed. Significant hydrogen evolution (400  $\mu\text{mol/g}$ ) from water is observed with N, F-TiO<sub>2</sub>-urea on visible light irradiation, due to the enhanced visible light absorption. First-principles calculations show that co-substitution of oxygen with nitrogen and fluorine is preferred over their individual substitution in TiO<sub>2</sub>, with nitrogen and fluorine preferably occupying nearest neighbor sites. The *p*-orbitals of nitrogen are most effective in altering the electronic structure of TiO<sub>2</sub>, giving rise to a sub-band at the top of the valence band, the effect being enhanced by the presence of fluorine. LDA calculations underestimate the band gap and the associated changes and provide a clear picture of the structural and electronic changes caused in TiO<sub>2</sub> due to the co-substitution by nitrogen and fluorine. Calculations on water adsorption on the (001) surface on N, F-TiO<sub>2</sub> show that the strong Ti-N bond weakens the bond between that Ti and the neighboring anion, facilitating the formation of a hydrogen bond between that anion and a hydrogen of the adsorbed water molecule, easing the dissociation of water and thereby increasing the photocatalytic activity of N, F-TiO<sub>2</sub>.

## 6. References

1. A. Fujishima and K. Honda, *Nature* **1972**, 238, 37-38.
2. I. K. Konstantinou and T. A. Albanis, *Appl. Catal. B-Environ.* **2004**, 49, 1-14.
3. R. Wang, K. Hashimoto, A. Fujishima, M. Chikuni, E. Kojima, A. Kitamura, M. Shimohigoshi and T. Watanabe, *Nature* **1997**, 388, 431-432.
4. M. Grätzel, *Nature* **2001**, 414, 338-344.
5. M. Grätzel, *J Photoch. Photobio C* **2003**, 4, 145-153.
6. I.-D. Kim, A. Rothschild, B. H. Lee, D. Y. Kim, S. M. Jo and H. L. Tuller, *Nano Lett.* **2006**, 6, 2009-2013.
7. S. El-Sherbiny, F. Morsy, M. Samir and O. A. Fouad, *Appl. Nanosci.* **2013**, 1-9.
8. Q. Li, G. Luo and J. Feng, *Electroanalysis* **2001**, 13, 359-363.
9. G. X. Shen, Y. C. Chen and C. J. Lin, *Thin Solid Films* **2005**, 489, 130-136.
10. M. F. Yan and W. W. Rhodes, *Appl. Phys. Lett.* **1982**, 40, 536-537.
11. H. Lin, L. Li, M. Zhao, X. Huang, X. Chen, G. Li and R. Yu, *J. Am. Chem. Soc.* **2012**, 134, 8328-8331.
12. W. Choi, A. Termin and M. R. Hoffmann, *J. Phys. Chem.* **1994**, 98, 13669-13679.
13. S. Karvinen, P. Hirva and T. A. Pakkanen, *J. Mol. Struct.- Thermochem* **2003**, 626, 271-277.
14. V. Likodimos, C. Han, M. Pelaez, A. G. Kontos, G. Liu, D. Zhu, S. Liao, A. A. de la Cruz, K. O'Shea, P. S. M. Dunlop, J. A. Byrne, D. D. Dionysiou and P. Falaras, *Ind. Eng. Chem. Res.* **2013**, 52, 13957-13964.
15. H. Wang and J. P. Lewis, *J. Phys.: Condens. Matter* **2006**, 18, 421.
16. A. M. Czoska, S. Livraghi, M. Chiesa, E. Giamello, S. Agnoli, G. Granozzi, E. Finazzi, C. D. Valentin and G. Pacchioni, *J. Phys. Chem. C* **2008**, 112, 8951-8956.
17. J. Yu, Q. Xiang, J. Ran and S. Mann, *CrystEngComm* **2010**, 12, 872-879.
18. R. Asahi, T. Morikawa, T. Ohwaki, K. Aoki and Y. Taga, *science* **2001**, 293, 269-271.
19. T. Lindgren, J. M. Mwabora, E. Avendaño, J. Jonsson, A. Hoel, C.-G. Granqvist and S.-E. Lindquist, *J. Phys. Chem. B* **2003**, 107, 5709-5716.
20. S. Sakthivel and H. Kisch, *ChemPhysChem* **2003**, 4, 487-490.

21. H. Irie, Y. Watanabe and K. Hashimoto, *J. Phys. Chem. B* **2003**, *107*, 5483-5486.
22. C. Di Valentin, G. Pacchioni and A. Selloni, *Phys. Rev. B* **2004**, *70*, 085116.
23. M. Batzill, E. H. Morales and U. Diebold, *Phys. Rev. Lett.* **2006**, *96*, 026103.
24. W. Balcerski, S. Y. Ryu and M. R. Hoffmann, *J. Phys. Chem. C* **2007**, *111*, 15357-15362.
25. M. Sathish, B. Viswanathan, R. P. Viswanath and C. S. Gopinath, *Chem. Mater.* **2005**, *17*, 6349-6353.
26. H. Irie, Y. Watanabe and K. Hashimoto, *J. Phys. Chem. B* **2003**, *107*, 5483-5486.
27. T. L. Thompson and J. T. Yates, *Chem. Rev.* **2006**, *106*, 4428-4453.
28. J. H. Pan, Z. Cai, Y. Yu and X. S. Zhao, *J. Mater. Chem.* **2011**, *21*, 11430-11438.
29. J. Yu, W. Wang, B. Cheng and B.-L. Su, *J. Phys. Chem. C* **2009**, *113*, 6743-6750.
30. S. Hoang, S. Guo and C. B. Mullins, *J. Phys. Chem. C* **2012**, *116*, 23283-23290.
31. Q. Meng, T. Wang, E. Liu, X. Ma, Q. Ge and J. Gong, *Phys. Chem. Chem. Phys.* **2013**.
32. D. Li, H. Haneda, S. Hishita and N. Ohashi, *Chem. Mater.* **2005**, *17*, 2588-2595.
33. Q. Wang, C. Chen, W. Ma, H. Zhu and J. Zhao, *Chem. - Eur. J.* **2009**, *15*, 4765-4769.
34. D. Chen, Z. Jiang, J. Geng, J. Zhu and D. Yang, *J. Nanopart. Res.* **2009**, *11*, 303-313.
35. H. A. Seibel Ii, P. Karen, T. R. Wagner and P. M. Woodward, *J. Mater. Chem.* **2009**, *19*, 471-477.
36. G. Liu, H. G. Yang, X. Wang, L. Cheng, J. Pan, G. Q. Lu and H.-M. Cheng, *J. Amer. Chem. Soc.* **2009**, *131*, 12868-12869.
37. K. Maeda, Y. Shimodaira, B. Lee, K. Teramura, D. Lu, H. Kobayashi and K. Domen, *J. Phys. Chem. C* **2007**, *111*, 18264-18270.
38. R. Niewa and F. J. DiSalvo, *Chem. Mater.* **1998**, *10*, 2733-2752.
39. A. Fuertes, *Dalton Trans.* **2010**, *39*, 5942-5948.
40. J. Zhang, Y. Wu, M. Xing, S. A. K. Leghari and S. Sajjad, *Energy Environ. Sci.* **2010**, *3*, 715-726.
41. H. Zhao, M. Lei, X. Chen and W. Tang, *J. Mater. Chem.* **2006**, *16*, 4407-4412.
42. A. Gomathi, A. Sundaresan and C. N. R. Rao, *J. Solid State Chem.* **2007**, *180*, 291-295.
43. A. Gomathi, S. Reshma and C. N. R. Rao, *J. Solid State Chem.* **2009**, *182*, 72-76.

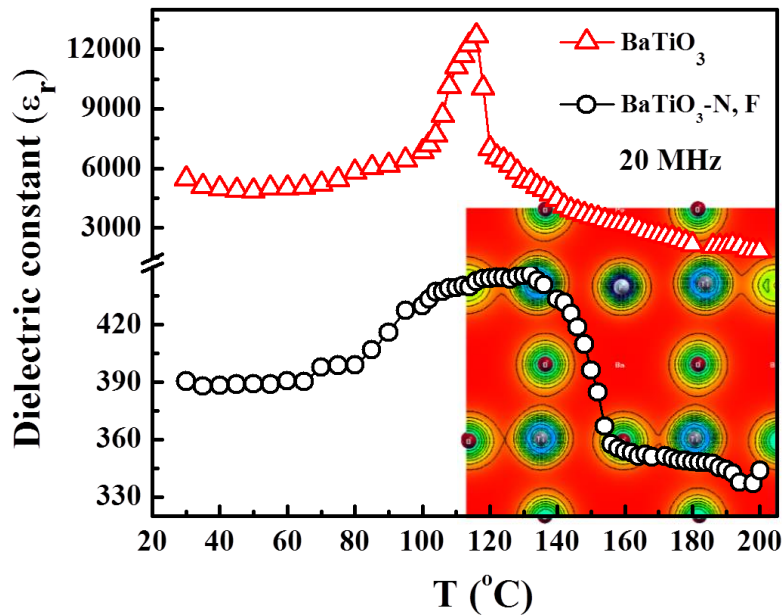
44. C. Giordano, C. Erpen, W. Yao and M. Antonietti, *Nano Lett.* **2008**, *8*, 4659-4663.
45. C. Giordano, C. Erpen, W. Yao, B. Milke and M. Antonietti, *Chem. Mater.* **2009**, *21*, 5136-5144.
46. S. Han, S.-H. Choi, S.-S. Kim, M. Cho, B. Jang, D.-Y. Kim, J. Yoon and T. Hyeon, *Small* **2005**, *1*, 812-816.
47. H. A. Seibel Ii, P. Karen, T. R. Wagner and P. M. Woodward, *J. Mater. Chem.* **2009**, *19*, 471-477.
48. J. Rodríguez-Carvajal, *Physica B* **1993**, *192*, 55-69.
49. S. Livraghi, M. R. Chierotti, E. Giamello, G. Magnacca, M. C. Paganini, G. Cappelletti and C. L. Bianchi, *J. Phys. Chem. C* **2008**, *112*, 17244-17252.
50. I. N. Martyanov, S. Uma, S. Rodrigues and K. J. Klabunde, *Chem. Commun.* **2004**, 2476-2477.
51. N. C. Saha and H. G. Tompkins, *J. Appl. Phys.* **1992**, *72*, 3072-3079.
52. W. Guosheng, W. Jiali, N. Samantha and C. Aicheng, *Nanotechnology* **2010**, *21*, 085701.
53. X. Li, C. Gao, J. Wang, B. Lu, W. Chen, J. Song, S. Zhang, Z. Zhang, X. Pan and E. Xie, *J. Power Sources* **2012**, *214*, 244-250.
54. Z. Wu, F. Dong, W. Zhao and S. Guo, *J. Hazard. Mater.* **2008**, *157*, 57-63.
55. A. Sundaresan, R. Bhargavi, N. Rangarajan, U. Siddesh and C. N. R. Rao, *Phys. Rev. B* **2006**, *74*, 161306.
56. A. Sundaresan and C. N. R. Rao, *Nano Today* **2009**, *4*, 96-106.
57. L. Yu, J. Xi, M.-D. Li, H. T. Chan, T. Su, D. L. Phillips and W. K. Chan, *Phys. Chem. Chem. Phys.* **2012**, *14*, 3589-3595.
58. A. Kudo and Y. Miseki, *Chem. Soc. Rev.* **2009**, *38*, 253-278.
59. X. Z. Li, F. B. Li, C. L. Yang and W. K. Ge, *J. Photochem. Photobio. A* **2001**, *141*, 209-217.

## Chapter II.2

### Ferroelectricity and other properties of nitrogen and fluorine co-substituted barium titanate\*

#### Summary

BaTiO<sub>3</sub>, with both nitrogen and fluorine substituted for oxygen, has been prepared and the properties of the doped material with the composition BaTiO<sub>2.8</sub>N<sub>0.1</sub>F<sub>0.1</sub> have been studied. The color of the sample changes to light green on doping accompanying a broad visible absorption band with the edge at 2.5 eV. The first order ferroelectric transition changes to a broad transition on doping along with a decrease in the dielectric constant. Ferroelectricity persists even on substitution of nitrogen and fluorine in BaTiO<sub>3</sub>. Calculated Born charges clearly reveal a strong disparity in the interaction of N, O and F. Disorder in these hetero *ferro-active* anions leads to a relaxor-like diffuse phase transition and reduction in polarization. First-principles calculations also suggests also suggests that the reduction in the band-gap of BaTiO<sub>3</sub> by 0.65 eV on co-doping.



\* A paper based on this work has appeared in *J. Phys. Condens. Matter*, **2013**

## 1. Introduction

Effect of cation substitution on the properties of metal oxides has been investigated in great detail whereas the study of anion-substituted metal oxides is scarce in the literature. There have been reports of substitution of nitrogen and fluorine in semiconductors like  $\text{TiO}_2$  and  $\text{ZnO}$ .<sup>1-8</sup> Motivation behind such substitution has been to engineer the band structure of the semiconductors, mainly to narrow the band gap in order to achieve absorption of light in the visible range. There are reports of nitrogen-induced magnetization in semiconducting oxides like  $\text{TiO}_2$ ,  $\text{ZnO}$  and  $\text{SnO}_2$  etc.<sup>9-10</sup> N-doped  $\text{BaTiO}_3$  has been prepared by Muller *et al.*<sup>11</sup> Their work is focused mainly on understanding the nature of defect sites created and effect of thermal stability upon doping. Tan *et al.* prepared N-doped bulk  $\text{BaTiO}_3$  and observed defect induced ferromagnetism compared to diamagnetic undoped  $\text{BaTiO}_3$ .<sup>12</sup>  $\text{BaTiO}_3$  has the perovskite structure with a tetragonal ferroelectric phase at the room temperature. It is extensively used in ceramic capacitors, sensors and memory devices. It transforms to the cubic paraelectric phase at 120 °C. Several modifications have been tried with the substitution at cationic sites in order to modify the dielectric properties. The most common dopants are Nb<sup>13-14</sup>, Sn<sup>15-16</sup>, Sr<sup>17</sup>, La<sup>18-20</sup>, Zr<sup>21</sup>, Ce<sup>22-24</sup>, Ca<sup>25</sup> and Y<sup>26-27</sup>.

## 2. Scope of the present investigation

To the best of our knowledge, there is no report of effect of anion substitution on the ferroelectricity of the material. We were interested in exploring the effect of anion substitution on ferroelectricity in an oxide material. For this purpose, we have chosen  $\text{BaTiO}_3$ , which is the most studied ferroelectric material. We have substituted both nitrogen and fluorine in  $\text{BaTiO}_3$  to investigate its effect on various properties, ferroelectricity in particular. Co-substitution of N and F for oxygen is based on the fact that one N and one F are equivalent to two oxygen atoms. Besides carrying out experimental studies involving optical, dielectric and ferroelectric measurements, we have carried out detailed first-principles theoretical calculations to demonstrate how interesting properties arise even at a low concentration of the substitution.



### 3. Experimental section

Pure BaTiO<sub>3</sub> as well as N, F co-doped BaTiO<sub>3</sub> were prepared by the solid state method. In a typical synthesis of BaTiO<sub>3</sub>, stoichiometric amount of BaCO<sub>3</sub> and TiO<sub>2</sub> were ground and heated at 950 °C for 15 h. In order to prepare N, F co-doped BaTiO<sub>3</sub>, stoichiometric amount of BaCO<sub>3</sub>, BaF<sub>2</sub> and TiO<sub>2</sub> were ground together and heated in flowing ammonia with a flow rate of ~ 200 mL/min at 950 °C for 15 h. For dielectric and ferroelectric measurements, a dense cylindrical pellet of BaTiO<sub>3</sub> and N, F-BaTiO<sub>3</sub> were sintered at 950 °C in air and ammonia flow respectively. Powder X-ray diffraction (XRD) patterns were recorded with a Bruker D8 Discover diffractometer. To obtain the cell parameters of doped and undoped BaTiO<sub>3</sub>, Le Bail fitting was carried out on the overnight collected XRD data using the *FullProf* programme. X-ray photoelectron spectra (XPS) were recorded in an Omicron Nanotechnology Spectrometer with Mg K $\alpha$  as the x-ray source. UV-Vis spectra were collected in a Perkin Elmer Lambda 900 UV/Vis/NIR spectrometer in the diffuse reflectance mode. Ferroelectric measurements were carried out on sintered pellets using a Radiant Technologies Precision Workstation. Dielectric properties were measured in an Impedance Analyzer (Agilent 4294A).

First-principles calculations were carried out by Waghmare *et al.* using the Quantum Espresso<sup>28</sup> implementation of the density functional theory (DFT) to study N and F co-doped BaTiO<sub>3</sub>, with a local density approximation (LDA) as parameterized in the Perdew-Zunger<sup>29</sup> functional for the exchange correlation energy. Energy cutoffs of 30 Ry and 180 Ry were used to truncate the plane wave basis in representation of the Kohn-Sham wavefunctions and density respectively.

### 4. Results and discussion

The XP spectra of N, F co-doped BaTiO<sub>3</sub> in Figure 1 show the N 1s and F 1s signals around 401 and 685.8 eV respectively. Taking the capture cross section into account, the composition of the doped sample is estimated to be BaTiO<sub>2.8</sub>N<sub>0.1</sub>F<sub>0.1</sub>. The inset of the Figure 1(b) shows the Ti 2p spectrum which rules out the presence of Ti<sup>3+</sup>. The absence of Ti<sup>3+</sup> minimizes the presence of oxygen vacancies in the N, F-doped sample. When we try to dope only nitrogen by heating a mixture of BaCO<sub>3</sub> and TiO<sub>2</sub> in ammonia in we obtain a grey

powder devoid of any nitrogen. The presence of small amount of BaF<sub>2</sub> in the reaction mixture increases the amount of nitrogen in the final product.

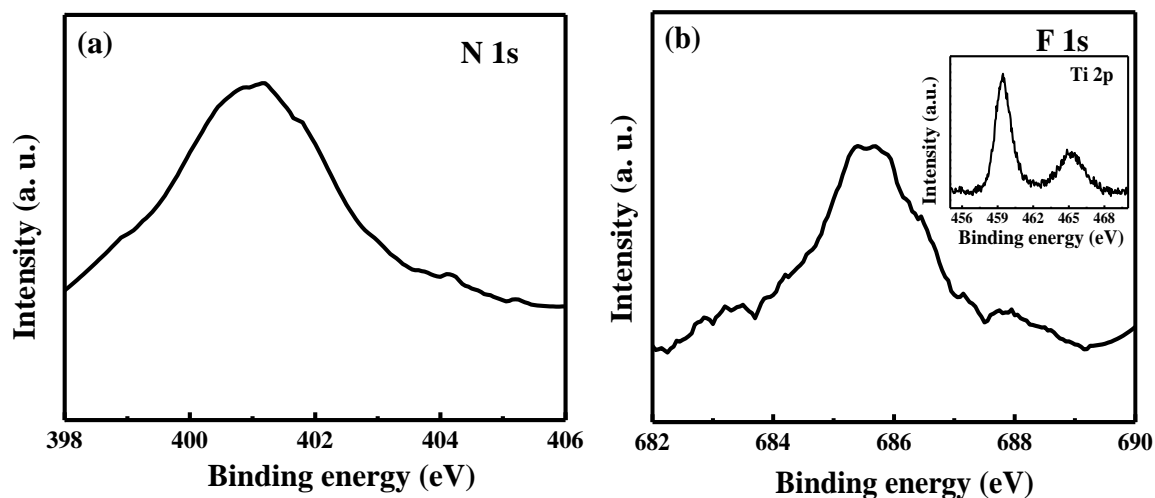


**Figure 1** XP core level spectra of (a) N and (b) F of N, F doped BaTiO<sub>3</sub>

Figure 2 shows XRD patterns of undoped as well as N, F co-doped BaTiO<sub>3</sub>. Both these materials crystallize in the *P4mm* tetragonal space group. The cell parameters of pure BaTiO<sub>3</sub> are  $a = 3.997(4)$  Å and  $c = 4.030(3)$  Å. The XRD pattern of the N, F co-doped sample does not show the presence of any impurity phase and the cell parameters are  $a = 4.000(5)$  and  $c = 4.024(2)$  Å. The calculated  $c/a$  ratios for the undoped and doped samples are 1.008 and 1.006 respectively, suggesting that N, F co-doping in the oxygen site makes the crystal slightly less tetragonal. This is revealed in the inset of Figure 2, where the (112) and (211) reflections of the undoped and doped samples are given together. The reflections are well-separated in pure BaTiO<sub>3</sub> compared to the doped sample. As we know that it is not possible to distinguish nitrogen, oxygen and fluorine from X-ray diffraction it is very difficult to gain insight about various structural parameters. Here, first-principles calculations prove to be a very important tool. It predicts that the lowest energy structure would be one with N-Ti-F in the linear arrangement with distance between N and F being 3.98 Å. The local structural distortions involve formation of short Ti-N bonds (1.83 Å) and long Ti-F bonds (2.15 Å). The Ti-O bond-length in the cubic structure is average of the two, 2 Å.

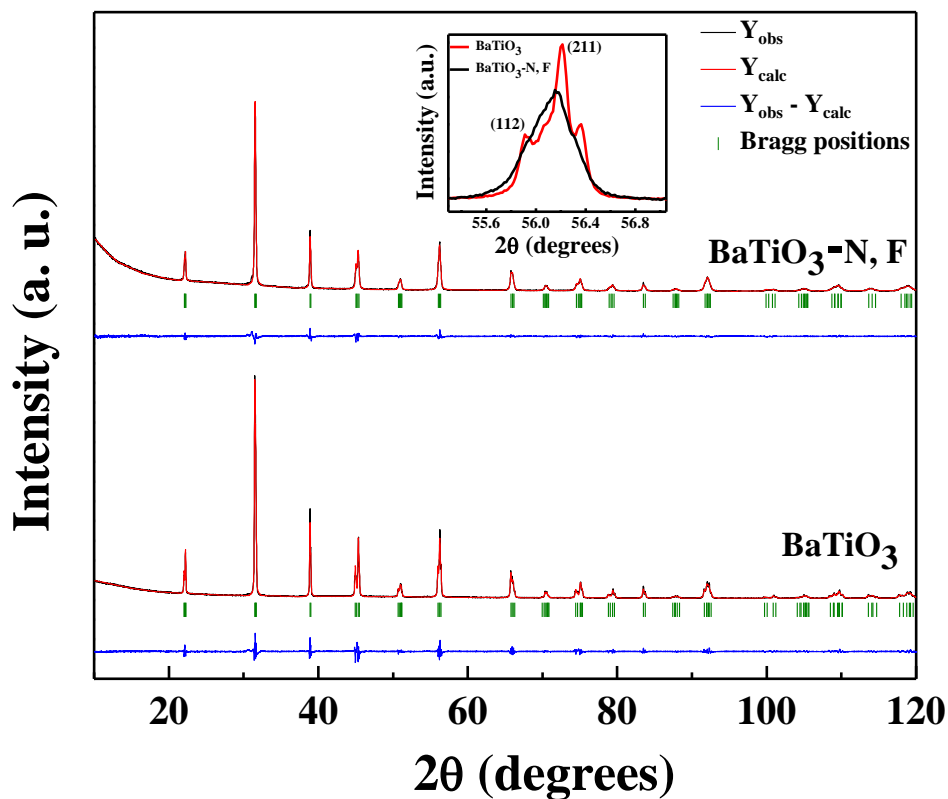


Figure 2 XRD patterns of undoped and N, F co-doped BaTiO<sub>3</sub>. Inset shows the enlarged version of (112) and (211) reflections

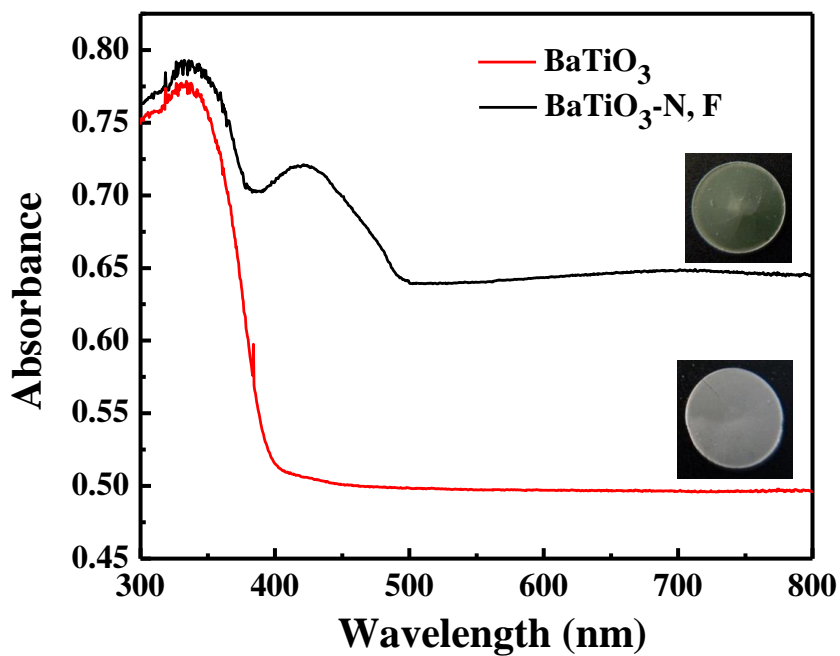
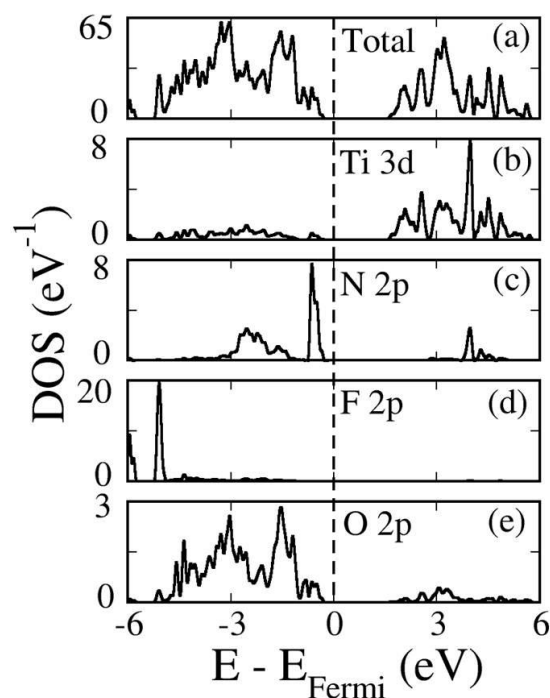


Figure 3 UV-Vis spectra of undoped and N, F co-doped BaTiO<sub>3</sub> with inset showing the colors of the powders

Figure 3 shows the UV-Vis spectra of undoped and N, F co-doped BaTiO<sub>3</sub> samples. The band gap of the samples can be calculated from the band edge positions. For the undoped sample, band gap is 3.15 eV. On co-substitution of N and F, the sample turns light green (see inset in Figure 3). A new absorption band in the visible region extending to 2.5 eV emerges in the doped sample.

Extension of the absorption edge in the visible region is well known in N, F-cosubstituted TiO<sub>2</sub> and ZnO.<sup>3, 8</sup> First-principles calculations predict direct band gap of 2.64 eV in the N, F-cosubstituted BaTiO<sub>3</sub> in contrast to the indirect gap of 3.31 eV in the undoped-BaTiO<sub>3</sub>. The top-most valence band is almost isolated from the rest. This is also supported from the experimental fact that rather than getting a continuous band edge we observe a clear maximum in the visible region giving rise to two edges. The top of the valence band has a strong contribution from the 2p states of N. Bands associated with the 2p orbitals of F are deep in energy (-5 eV) at the bottom of the valence band, consistent that with the completely filled shell and the ionic character (Figure 4).



**Figure 4** Total electronic density of states of F and N doped BaTiO<sub>3</sub>. Partial electronic density of states of (b) Ti 3d, (c) N 2p, (d) F 2p, (e) O 2p

Figure 5 shows ferroelectric hysteresis loops of the undoped and N, F co-doped BaTiO<sub>3</sub> samples. Ferroelectricity persists even on co-substitution of nitrogen and fluorine in BaTiO<sub>3</sub>. The coercivity and saturation polarization of the doped samples are 18.4 kV/cm and 2.6 μC/cm<sup>2</sup> respectively at 1 kHz and 300 K. The corresponding values for the undoped sample are 12.3 kV/cm and 6.2 μC/cm<sup>2</sup> respectively. The low polarization value of the undoped sample is because of the low sintering

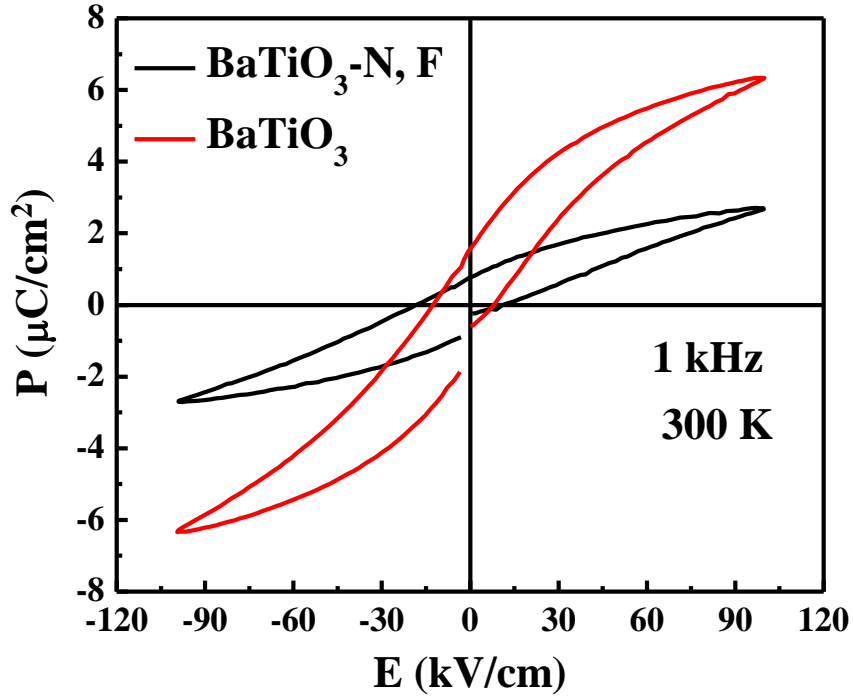
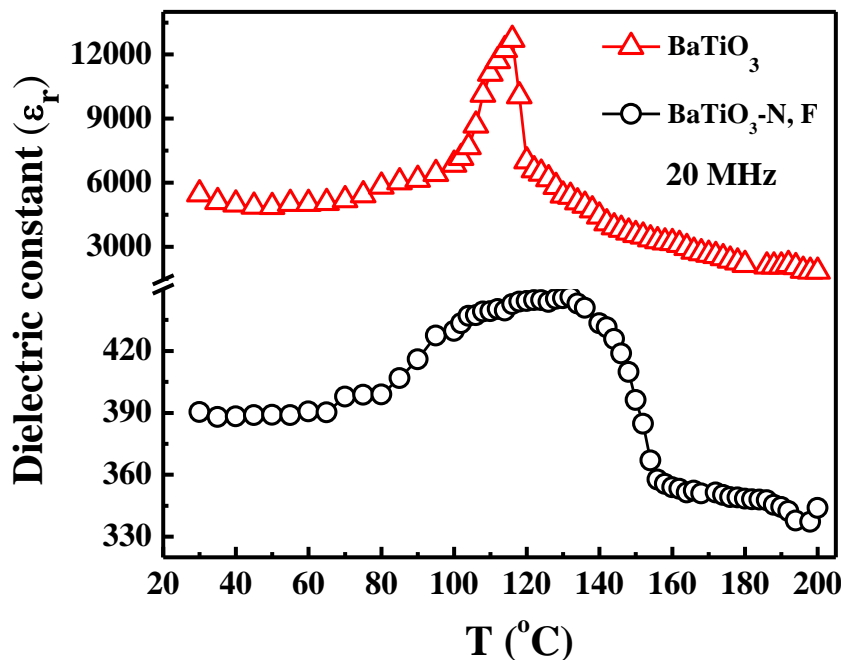


Figure 5 Ferroelectric loops of undoped and N, F doped BaTiO<sub>3</sub> at 1 kHz and 300 K

temperature employed. According to First-principles calculations, local distortions due to the random distribution of N and F, give a vanishing polarization. In contrast, structural distortions involving Ti off-centering give rise to an overall polarization similar to undoped BaTiO<sub>3</sub>. These lead to changes in the F-Ti-N bond angle to 173° and O-Ti-O angles that range from 167° to 173°. The Ti-O bond lengths range from 1.93 to 2.1 Å. Interestingly, the Ba-F bond is shorter than Ba-O and Ba-N bonds which are about 2.83 Å. In the ferroelectric phase of pure BaTiO<sub>3</sub>, off-centering of Ti atoms is uniform throughout the crystal and gives a macroscopic polarization. In the N, F-doped BaTiO<sub>3</sub>, off-centering of Ti exhibits inhomogeneity due to randomly oriented polarization arising from the local electric dipole

and Ti- off-centering in the  $\text{TiO}_4\text{NF}$  clusters. Thus, an overall macroscopic polarization is reduced.

In Figure 6, we show the temperature dependence of the dielectric constant of the doped and undoped samples. Pure  $\text{BaTiO}_3$  shows a sharp peak in the dielectric constant near  $120^\circ\text{C}$



**Figure 6** Variation of dielectric constant with temperature of undoped and N, F co-doped  $\text{BaTiO}_3$  at 20 kHz

whereas, N, F co-doped  $\text{BaTiO}_3$  shows a broad transition extending from  $80^\circ\text{C}$  to  $150^\circ\text{C}$ . The centre of the broad peak is at a temperature higher than  $120^\circ\text{C}$ . The dielectric constant of the co-substituted  $\text{BaTiO}_3$  is considerably lower than that of pure  $\text{BaTiO}_3$ . At  $115^\circ\text{C}$  and 20 MHz, the values of dielectric constant are 12200 and 440 for pure and N, F co-substituted  $\text{BaTiO}_3$  respectively. The first-order transition in undoped  $\text{BaTiO}_3$  transforms to a diffuse transition (somewhat relaxor-like) on N, F co-substitution.

The structural changes induced by N and F co-substitution can be described in terms of (a) local distortions that arise from different charge and chemistry of N, F and O and (b) a long-range (uniform) ferroelectric distortion dominated by off-centering of Ti (also present in pure  $\text{BaTiO}_3$ ). The local structural distortions involve formation of short Ti-N bonds ( $1.83 \text{ \AA}$ ) and long Ti-F bonds ( $2.15 \text{ \AA}$ ) (Figure 7(a) and (b)). The Ti-O bond-length in the cubic structure is average of the two,  $2 \text{ \AA}$ . Based on this, it appears that the effect of N and F on Ti is like that

of a negative and a positive charge respectively (Figure 7(b)). As a result, there is a strong local electric dipole moment associated with N-Ti-F cluster that is expected to naturally couple with ferroelectricity, much the same way as Pb-O-vacancy pair influences ferroelectricity in  $\text{PbTiO}_3$ <sup>30</sup> and causes relaxor or diffuse ferroelectric behavior.

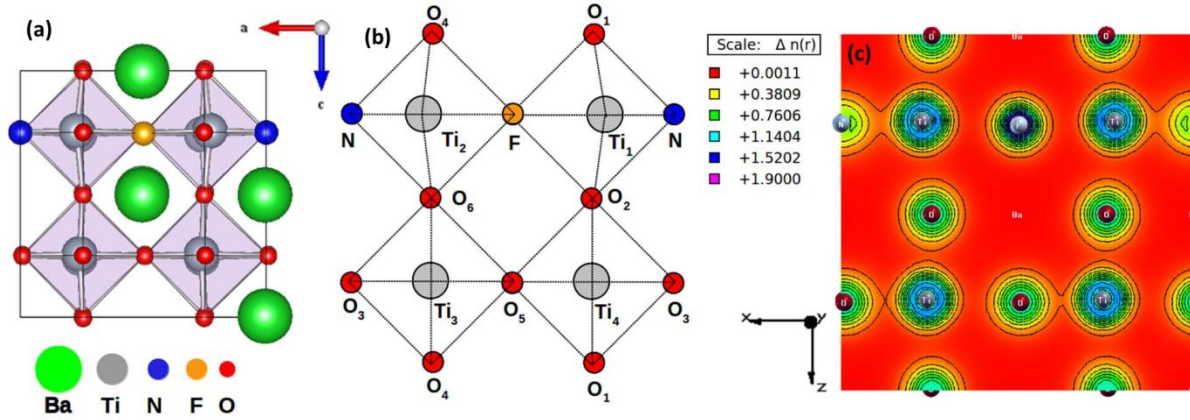


**Figure 7 (a) Distortion of the structure of  $\text{BaTiO}_3$  upon F and N substitution, (b) schematic showing displacement of Ti (here  $\text{Ti}_1$  and  $\text{Ti}_2$ ) atom towards N and also away from F, (c) contour plot of charge density of N and F doped  $\text{BaTiO}_3$  in the (010) plane**

## 5. Conclusions

We have co-substituted nitrogen and fluorine in  $\text{BaTiO}_3$  by solid state method. Co-substituted  $\text{BaTiO}_3$  is less tetragonal than the pure  $\text{BaTiO}_3$ . On doping,  $\text{BaTiO}_3$  turns light green with absorption in the visible region. It still remains ferroelectric with saturating P-E loop but value of polarization reduces compared to undoped- $\text{BaTiO}_3$ . Ferroelectric transition near 120 °C becomes diffused unlike a sharp first order transition in pure  $\text{BaTiO}_3$ . First-principles calculations show that linear N-Ti-F is the most stable arrangement. Local distortions in the structure due to co-doping reduce the overall macroscopic polarization. Local electric dipole moment associated with N-Ti-F cluster naturally couples with ferroelectricity to result in diffused ferroelectric behavior.

## 6. References

1. R. Asahi, T. Morikawa, T. Ohwaki, K. Aoki and Y. Taga, *science* **2001**, 293, 269-271.
2. Y. Cong, J. Zhang, F. Chen and M. Anpo, *J. Phys. Chem. C* **2007**, 111, 6976-6982.
3. N. Kumar, U. Maitra, V. I. Hegde, U. V. Waghmare, A. Sundaresan and C. N. R. Rao, *Inorg. Chem.* **2013**, 52, 10512-10519.
4. D. Li, H. Haneda, S. Hishita and N. Ohashi, *Chem. Mater.* **2005**, 17, 2596-2602.
5. G. Liu, H. G. Yang, X. Wang, L. Cheng, J. Pan, G. Q. Lu and H.-M. Cheng, *J. Am. Chem. Soc.* **2009**, 131, 12868-12869.
6. B. Chavillon, L. Cario, A. Renaud, F. Tessier, F. o. Cheviré, M. Boujtita, Y. Pellegrin, E. Blart, A. Smeigh and L. Hammarström, *J. Am. Chem. Soc.* **2011**, 134, 464-470.
7. M. Mapa and C. S. Gopinath, *Chem. Mater.* **2008**, 21, 351-359.
8. R. Saha, S. Revoju, V. I. Hegde, U. V. Waghmare, A. Sundaresan and C. N. R. Rao, *ChemPhysChem* **2013**, 14, 2672-2677.
9. Q. Wang, Q. Sun and P. Jena, *New J. Phys.* **2009**, 11, 063035.
10. G. Drera, M. C. Mozzati, P. Galinetto, Y. Diaz-Fernandez, L. Malavasi, F. Bondino, M. Malvestuto and L. Sangaletti, *Appl. Phys. Lett.* **2010**, 97, 012506-012506-3.
11. T. Müller, T. Großmann and H.-P. Abicht, *J. Phys. Chem. Solids* **2009**, 70, 1093-1097.
12. X. Tan, C. Chen, K. Jin and B. Luo, *J. Alloys Compd.* **2011**, 509, L311-L313.
13. M. Kahn, *J. Am. Ceram. Soc.* **1971**, 54, 455-457.
14. M. Kahn, *J. Am. Ceram. Soc.* **1971**, 54, 452-454.
15. R. Vivekanandan and T. R. N. Kutty, *Ceram. Int.* **1988**, 14, 207-216.
16. V. V. Shvartsman, W. Kleemann, J. Dec, Z. K. Xu and S. G. Lu, *J. Appl. Phys.* **2006**, 99, 124111.
17. J. W. Liou and B. S. Chiou, *Mater. Chem. Phys.* **1997**, 51, 59-63.
18. F. D. Morrison, D. C. Sinclair and A. R. West, *J. Appl. Phys.* **1999**, 86, 6355-6366.
19. F. D. Morrison, D. C. Sinclair, J. Skakle and A. R. West, *J. Am. Ceram. Soc.* **1998**, 81, 1957-1960.
20. F. D. Morrison, D. C. Sinclair and A. R. West, *J. Am. Ceram. Soc.* **2001**, 84, 474-76.



21. D. Hennings, A. Schnell and G. Simon, *J. Am. Ceram. Soc.* **1982**, 65, 539-544.
22. D. Makovec and D. Kolar, *J. Am. Ceram. Soc.* **1997**, 80, 45-52.
23. D. F. K. Hennings, B. Schreinemacher and H. Schreinemacher, *J. Eur. Ceram. Soc.* **1994**, 13, 81-88.
24. A. Chen, Y. Zhi, J. Zhi, P. M. Vilarinho and J. L. Baptista, *J. Eur. Ceram. Soc.* **1997**, 17, 1217-1221.
25. Y. H. Han, J. B. Appleby and D. M. Smyth, *J. Am. Ceram. Soc.* **1987**, 70, 96-100.
26. J. Zhi, A. Chen, Y. Zhi, P. M. Vilarinho and J. L. Baptista, *J. Am. Ceram. Soc.* **1999**, 82, 1345-1348.
27. Z. Jing, C. Ang, Z. Yu, P. M. Vilarinho and J. L. Baptista, *J. Appl. Phys.* **1998**, 84, 983-986.
28. P. Giannozzi, S. Baroni, N. Bonini, M. Calandra, R. Car, C. Cavazzoni, D. Ceresoli, G. L. Chiarotti, M. Cococcioni and I. Dabo, *J. Phys.: Condens. Matter* **2009**, 21, 395502.
29. J. P. Perdew and A. Zunger, *Phys. Rev. B* **1981**, 23, 5048.
30. B. P. Burton, E. Cockayne, S. Tinte and U. V. Waghmare, *Phys. Rev. B* **2008**, 77, 144114.



***Part III***  
*Investigations*  
*of nitrides*

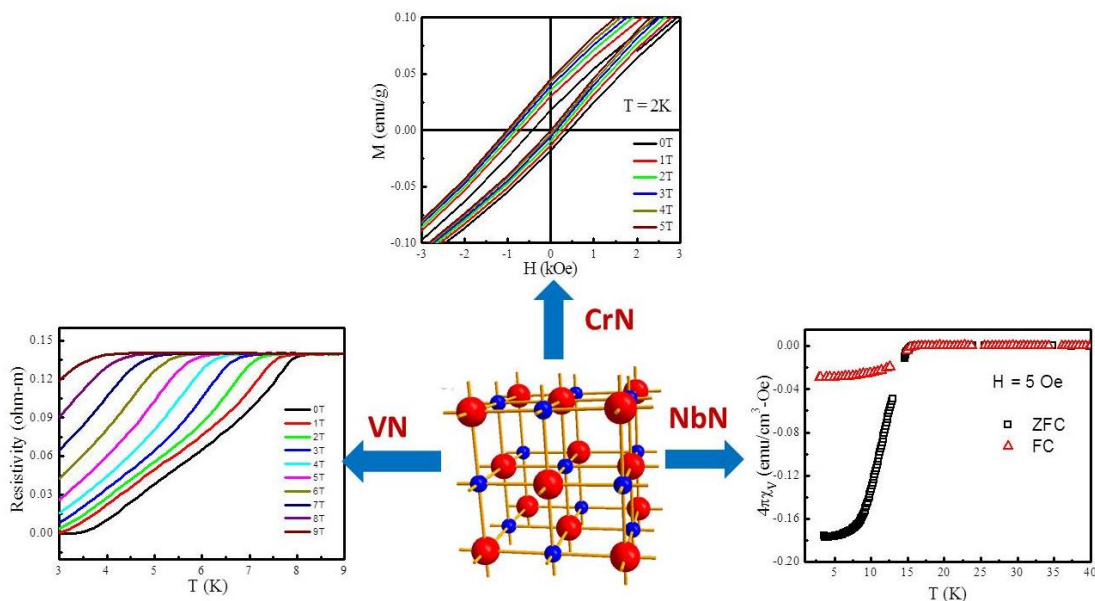


# Chapter III.1

## Rock salt-type transition metal nitrides: Urea based synthesis and superconducting, magnetic & photocatalytic properties\*

### Summary

Nanoparticles of rock salt-type VN, CrN and NbN are prepared by urea based method. We study the superconducting properties of VN and NbN nanoparticles at different synthesis conditions. Best of the samples of these two compounds show superconducting transition temperature of 8 and 15 K respectively. Superconducting transition is also observed in these materials in the electrical resistivity measurement of cold pressed powders. CrN nanoparticles exhibit antiferromagnetism with a Néel's temperature of 275 K. Below this temperature, nanoparticles of CrN show exchange bias effect. Metallic TiN and VN are used as catalysts for reduction of water.



\* A paper based on this work has appeared in *Mater. Chem. Phys.*, 2013

## 1. Introduction

Transition metal nitrides constitute an important class of materials which find many technological applications.<sup>1</sup> These are vastly known for their great strength and hardness, wear resistance, high melting temperature and good chemical inertness.<sup>2-3</sup> Hence, they are the choice of materials at extreme temperature and pressure conditions for examples in rocket nozzles and drill bits. Because of their excellent hardness they are used in cutting tools, shoe spikes and snow tires. They are also employed as thin protective coating to increase the edge retention and corrosion resistance of the cutting tools and their machining performance. Because of the golden color of metallic TiN, it is used in coating in costume jewelry. Biostability of TiN makes it useful for making electrodes in bioelectronics devices for example *in-vivo* biosensors that have to withstand severe corrosion caused by body fluid.<sup>4</sup>

Earlier transition metal nitrides in all the three rows are known to crystallize in rock salt structure while the rest of them exist as interstitial compounds with low oxidation states of transition metal. Scandium nitride (ScN), apart from its superior physical properties is a wide band gap semiconductor (2-2.4 eV).<sup>5</sup> It has a rock salt type structure with lattice constant 2.50 Å which is a good lattice match with zinc-blend GaN and therefore it is used as a buffer layer to grow high quality GaN single crystals and GaN/ScN heterostructures. VN is metallic and becomes superconductor at 2-9 K depending on the nitrogen content.<sup>6-7</sup> Considering high electron-phonon coupling in this compound a high  $T_C$  of 32 K was predicted.<sup>8</sup> The difference between the experimental and theoretical  $T_C$  was explained by spin fluctuation due to the high value of spin susceptibility. Because of the metallic conductivity, VN nanostructures are also studied for supercapacitor applications.<sup>9</sup> TiN also exhibits superconductivity with further smaller  $T_C$  (3.5-3.9 K). Its optical properties resemble to that of gold yet maintaining significance hardness comparable to diamond and a very high melting point (3000 °C). CrN is known to undergo a transition from high temperature cubic paramagnetic phase to a low temperature orthorhombic antiferromagnetic phase at 280 K.<sup>10</sup> Resistivity measurements on epitaxially grown CrN show a semiconductor to metal transition at the magnetic transition temperature with a significant hysteresis.<sup>11</sup> NbN holds the record of highest superconducting transition temperature,  $T_C \sim 17.3$  K, among rock salt type binary compounds and has a high critical current density ( $J_C \sim 10^{10}$  A/m<sup>2</sup> for thin films at 4.2 K).<sup>12</sup>  $T_C$  in the bulk phase is

sensitive to the nitrogen contents, hence, the investigation is more focused on epitaxial thin films.

Bulk transition metal nitrides are prepared by the ammonolysis of metal or corresponding metal oxides at high temperatures. Carbothermal reduction technique where the metal oxide is mixed with graphite and heated in nitrogen at very high temperature (up to 1800 °C) has also been used to prepare bulk metal nitrides.<sup>13</sup> Nanoparticles of the transition metal nitrides are made conventionally using ammonia as the nitrogen source but recently many other nitrogen sources have been employed such as urea, sodium azide, melamine,  $\text{Li}_3\text{N}$  etc.<sup>14-16</sup> Gomathi *et al.* synthesized nanoparticles of transition metal nitrides of Ti and Nb by treating  $\text{TiCl}_4$  and  $\text{NbCl}_5$  respectively with excess of urea.<sup>17</sup> They also obtained nanotubes under the similar conditions by adding gold nanoparticles as the catalyst. Giordano *et al.* prepared several transition metal nitrides nanoparticles by heating a gel formed by metal salt and urea.<sup>18</sup> By a similar method, Yao *et al.* synthesized metal nitride nanoparticles and used them as alkylation catalysis.<sup>19</sup> Zhao *et al.* started with metal oxide nanoparticles and melamine as the nitrogen source to make corresponding nitride at 600 °C in vacuum.<sup>20</sup> They argued the importance of both carbon and hydrogen in aiding the nitriding process.  $\text{Li}_3\text{N}$  has not yet been used to prepare transition metal nitrides, however its use to prepare GaN has been demonstrated in the literature.<sup>21-22</sup>

## 2. Scope of the present investigation

Research on the transition metal nitride nanoparticles has mainly been limited to their synthesis and characterization. There are only a few reports of their magnetic and electrical properties. Superconducting properties of VN and NbN nanoparticles have been studied earlier but the transition temperature reported are considerable low. There is no report on the magnetic properties of nanocrystalline CrN. Herein, we synthesize transition metal nitrides nanoparticles by heating metal ion precursors with excess of urea. Superconducting properties of VN and NbN with superior transition temperature have been studied. We have observed the exchange bias properties of CrN nanoparticles for the first time. VN obtained by urea method and TiN nanoparticles by direct ammonolysis have been tested for hydrogen evolution reaction.

### 3. Experimental section

#### 3.1 Synthesis of transition metal nitride nanoparticles

To make VN nanoparticles, ammonium metavanadate was mixed with excess of urea (5 and 10 times by weight) and ground to make a homogenous mixture. The mixture was then heated at 750-850 °C for 2 h in the nitrogen atmosphere. CrN nanoparticles were prepared by heating a mixture of chromium acetyl acetonate and urea (10 times by weight) at 800 °C for 2h in nitrogen atmosphere. NbN nanoparticles were synthesized by mixing NbCl<sub>5</sub> and urea (12 times by moles) inside the glove box and subsequently heating the mixture at 700-900 °C for 2h in nitrogen atmosphere. TiN nanoparticles were prepared heating sol-gel derived TiO<sub>2</sub> (procedure is mentioned in Chapter II.1) at 800 °C for 2h in ammonia.

#### 3.2 Characterization

X-ray diffraction patterns were recorded in Bruker D8 Discover Diffractometer and Rigaku-99 diffractometer using Cu K $\alpha$  radiation. X-ray photoelectron (XP) spectra were recorded in an Omicron Nanotechnology Spectrometer with the Mg K $\alpha$  as x-ray source. Transmission electron microscopy studies were carried out in JEOL JEM 3010, fitted with Gatan CCD camera operating at an accelerating voltage of 300 kV. Field Emission Scanning Electron Microscopy (FESEM) images were carried out using NOVA NANOSEM 600 (FEI, The Netherlands). Magnetic measurements were carried out in SQUID VSM (Quantum Design, USA) and Physical Property Measurement System (PPMS, Quantum Design, USA). DC electrical transport measurements were performed using the conventional four-point probe technique in PPMS on cold pressed powder sample.

### 4. Results and discussion

#### 4.1 VN nanoparticles

Figure 1 shows XRD patterns of VN nanoparticles prepared at different temperatures and urea ratios. VN crystallizes in cubic rock-salt type structure (space group, *Fm-3m*). Samples prepared at 750 °C at both the ratios (1:5 and 1:10) contain small amount of V<sub>2</sub>O<sub>3</sub> as a secondary phase. In conventional ammonolysis reactions such kind of secondary phases can be removed by extending the duration of the reaction but in the present reaction conditions



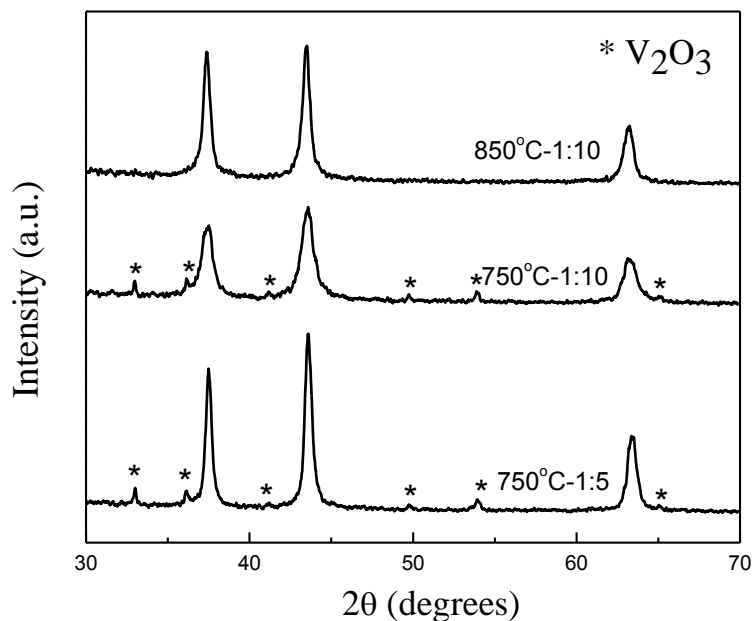


**Figure 1 XRD patterns of VN nanoparticles prepared at different temperatures and precursor-urea ratios**

the extent of ammonolysis is limited by factors like the amount of urea used and the low temperature decomposition of urea to supply  $\text{NH}_3$  during the reaction. In order to obtain an appreciable amount of product, the amount of urea cannot be increased above a certain limit. The other way to get rid of this problem is to increase the reaction

temperature. At 850 °C, we obtain a pure phase of vanadium nitride. We obtain crystallite size of 28, 16 and 23 nm for samples: VN-750-5, VN-750-10 and VN-850-10 respectively. Figure 2 shows FESEM images of VN-750-5 and VN-850-10. Nanoparticles are seen in the agglomerated form for both these compounds. Formation of nanoparticles at such high temperatures is not very common in the literature because of the sintering effect. However, several reports of nanoparticles formation in urea assisted synthesis can be found.

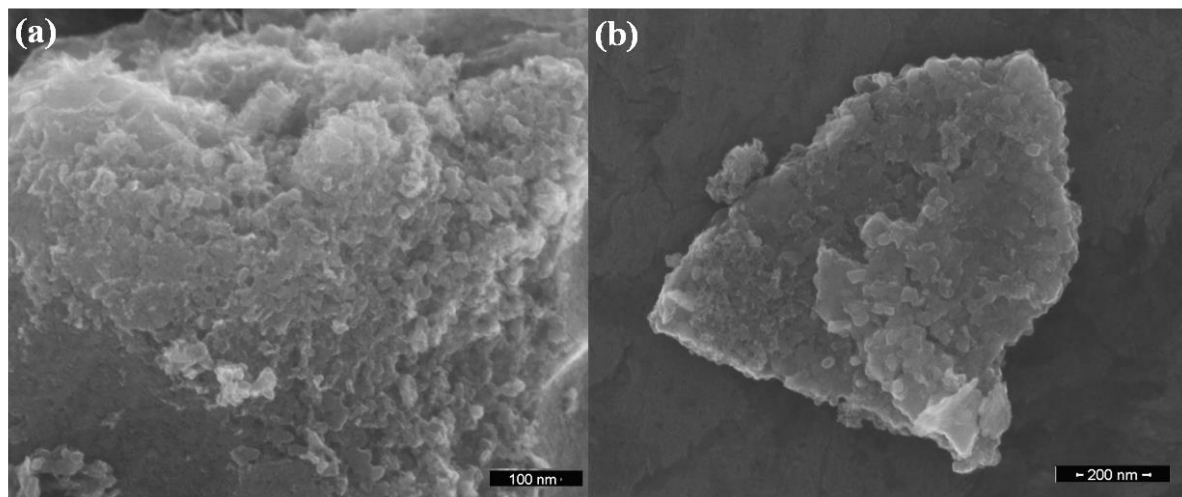


**Figure 2 FESEM images of (a) VN-750-5 and (b) VN-850-10**

Figure 3 shows the magnetization under ZFC conditions at 5 Oe field. All the three samples show superconducting state at low temperature. Superconducting  $T_C$  for VN-750-5 and VN-750-10 is found to be 7.5 K while it is 8.8 K for VN-850-10. These values are comparable

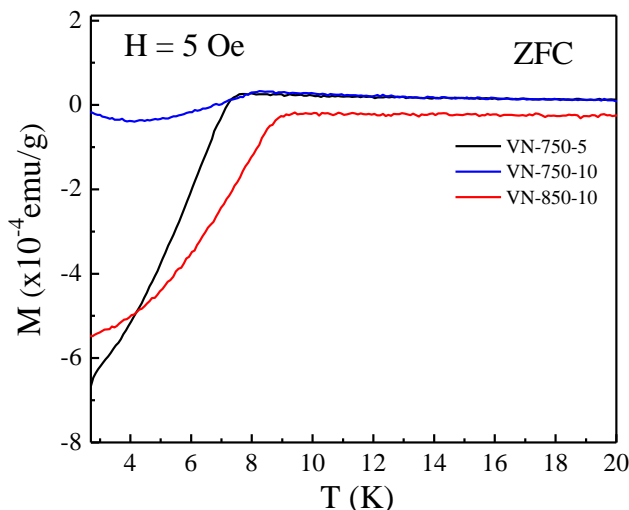


**Figure 3** ZFC magnetization of the three VN samples at 5 Oe

and even better than some of the bulk VN (9.2 K, highest value) reported in the literature. Slight difference in the transition temperatures is probably due to the difference in the nitrogen content in these samples. Superconducting volume fraction of VN-750-10 is considerable less than the other two samples. This is due to the nonstoichiometry at the surface of the nanoparticles. This is consistent

with the XRD analysis which shows that it is more amorphous compared to the other two samples as evident from the large full width at the half maxima (FWHM) of the reflections. Figure 4(a) shows the resistivity data of VN-750-5 at different magnetic fields. At zero field, an onset is observed at 8 K and reaches the superconducting state at 3.5 K. This huge difference might be due to the poor connectivity between the individual superconducting

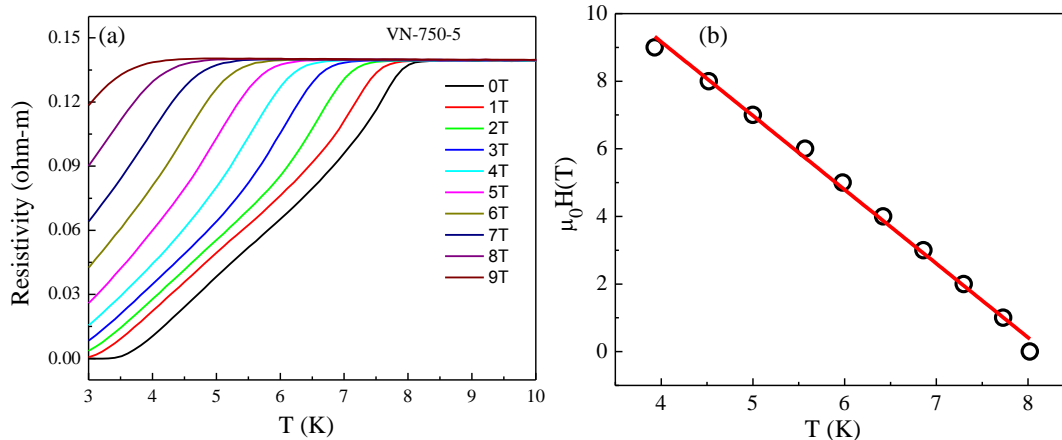


**Figure 4** (a) Resistivity of VN-750-5 as a function of temperature at different fields, (b) the upper critical field as a function of temperature

grains. At a field as small as 2 T, the material ceases to attain the superconducting state whereas the onset of the transition could be observed even at a field as large as 9 T. The upper critical field as a function of temperature is plotted in Figure 4(b) by inverting the  $T_C(H)$  data. We calculate the upper critical field ( $B_{c2}$ ) and Ginzburg-Landau coherence length ( $\xi_{GL}$ ) by using Werthamer-Helfand-Hohenberg (WHH) relationship for a dirty type-II superconductor by the following relations:  $H_{c2}(0) = 0.69T_C(dH_{c2}/dT) \Big|_{T=T_C}$  and  $\xi_{GL} = [2.07 \times 10^{-7}/(2\pi/H_{c2})]^{1/2}$ . The calculated values of upper critical field and coherence length are 12.1 T and 7.38 nm respectively.

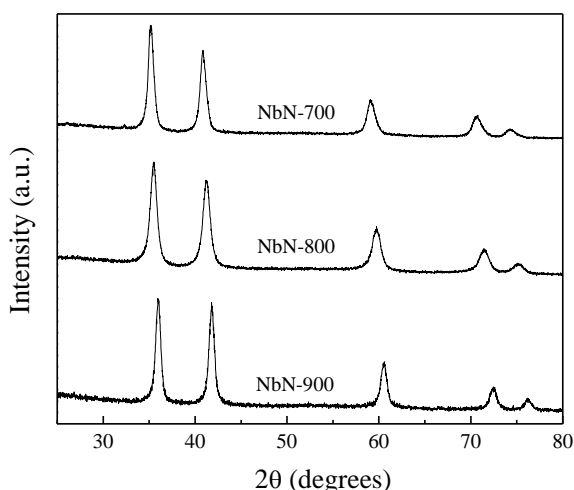


**Figure 5 XRD patterns of NbN nanoparticles prepared at different temperatures**

#### 4.2 NbN nanoparticles

Like VN, NbN also forms NaCl-type cubic lattice. We have prepared NbN nanoparticles at three different temperatures, i.e. at 700, 800 and 900 °C. Figure 5 shows XRD patterns of these samples. Average calculated crystallite size for NbN-700, NbN-800 and NbN-900 samples are 20, 21 and 27 nm respectively. Figure 6(a) shows the TEM image of NbN-700 where it can be seen

that the grains are less agglomerated with distinguishable grain boundaries. The average particles size varied between 15 - 20 nm. The sample synthesized at 900 °C (NbN-900) is more agglomerated compared to NbN-700 (Figure 6(b)). The average particle size is 23 nm as can be observed in the histogram of Figure 6(b). Rings in the selected area electron diffraction (SAED) pattern confirm the polycrystalline nature of both the samples (inset of Figure 6(a) and (b)). HRTEM image of NbN-700 (Figure 6(c)) reveals lattice fringes corresponding to (111) planes. Figure 6(d) shows HRTEM image of NbN-900 where lattice fringes corresponding to the (200) planes can be seen clearly. Figure 7(a) shows the ZFC-FC data of NbN-900 at an applied field of 5 Oe. Superconducting state sets in at 15 K below

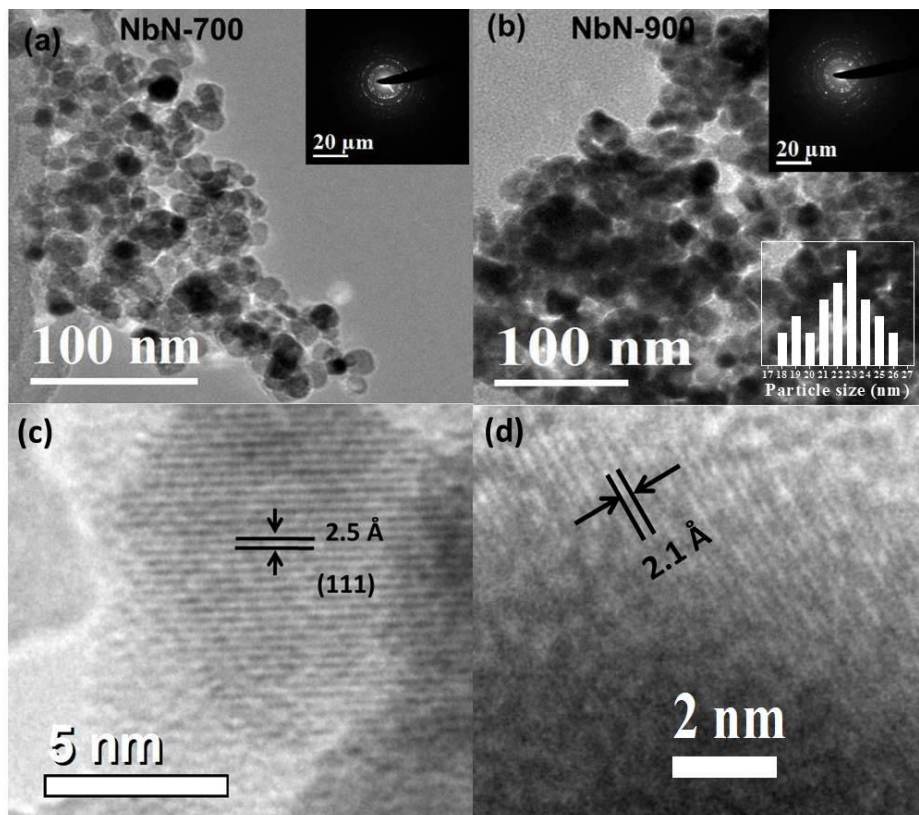
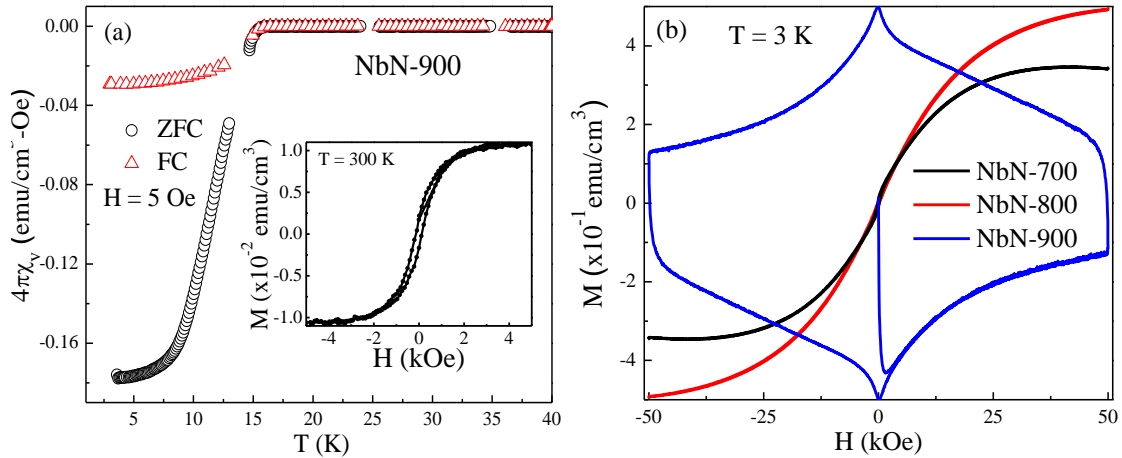
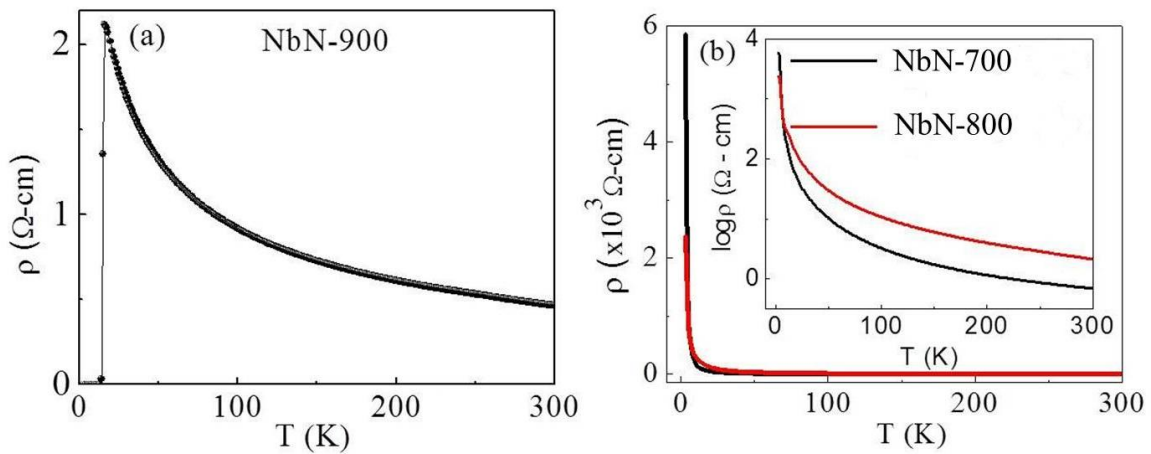


Figure 6(a) TEM image of NbN-700 with ED pattern in the inset, (b) TEM image of NbN-900 with ED pattern and particle size distribution in the inset and HRTEM image of (c) NbN-700 and (d) NbN-900

which strong diamagnetic behavior is observed. Irreversibility between the ZFC-FC curves at a low field (5 Oe) indicates the presence of flux pinning. The sample prepared at 800 °C shows a very small diamagnetic response in the ZFC data with a  $T_C$  at around 10 K, while no trace of superconductivity was observed in the sample prepared at 700 °C. Isothermal magnetization curve in the inset of Figure 7(a) shows the presence of surface ferromagnetism in the nanoparticles prepared at 900 °C, a phenomenon which has been reported earlier for the same material prepared under slightly different conditions, where a lower  $T_C$  (6-12 K) was observed.<sup>23</sup> Surface ferromagnetism has been suggested to be a universal feature of almost all nanoparticles of otherwise nonmagnetic inorganic materials and arises due to surface cation or anion vacancies resulting in ferromagnetic spin polarizations<sup>24</sup>. At  $T = 3$  K in Figure 7(b), the sample prepared at 900 °C shows hysteresis curve typical of a type II



**Figure 7(a) ZFC and FC magnetization of NbN-900 at 5 Oe with inset showing the room temperature hysteresis loop, (b) isothermal magnetization of NbN-700, NbN-800 and NbN-900 at 3 K**



**Figure 8(a) Resistivity versus temperature plot of (b) NbN-900 and (b) NbN-700 and NbN-800 with the inset showing the resistivity in the log scale**

superconductor, whereas in other samples surface ferromagnetism continue to influence the magnetization loop whereas in other samples surface ferromagnetism continue to influence the magnetization loop.

As the nanoparticles are agglomerated, we found it interesting to perform the resistivity measurements on the cold pressed rectangular bar. Figure 8(a) shows the temperature dependence of zero field resistivity. As expected for cold pressed nanoparticles which form a granular system, the temperature dependent resistivity profile above  $T_C$  shows a negative temperature coefficient for the entire temperature range. However, at  $T = 16.2$  K, a sharp

drop in resistivity is observed and it becomes zero at 14.4 K with a narrow transition width,  $\Delta T_c = 1.8$  K. Resistivity ( $\rho$ ) versus temperature (T) plots for samples NbN-700 and NbN-800 show semiconductor behavior throughout the temperature range with a sharp divergence at very low temperatures ( $T < 25$  K) as shown in Figure 8(b).

### 4.3 CrN nanoparticles

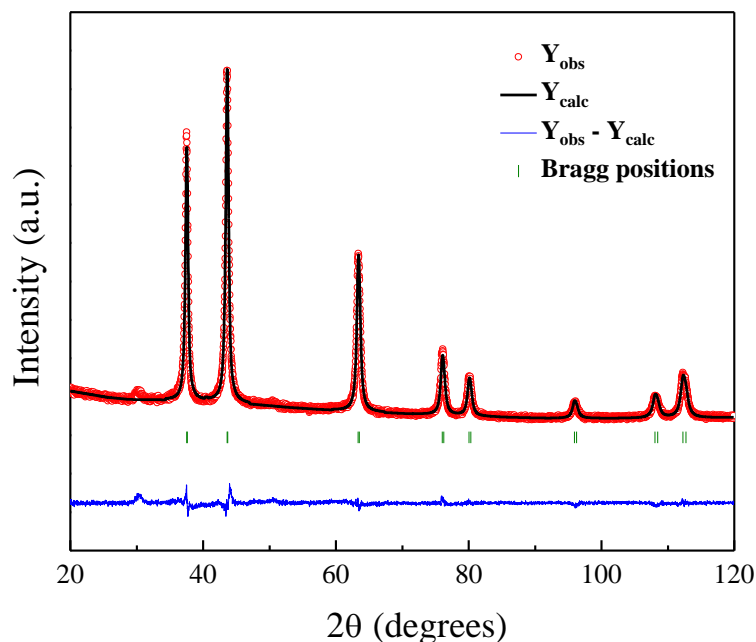
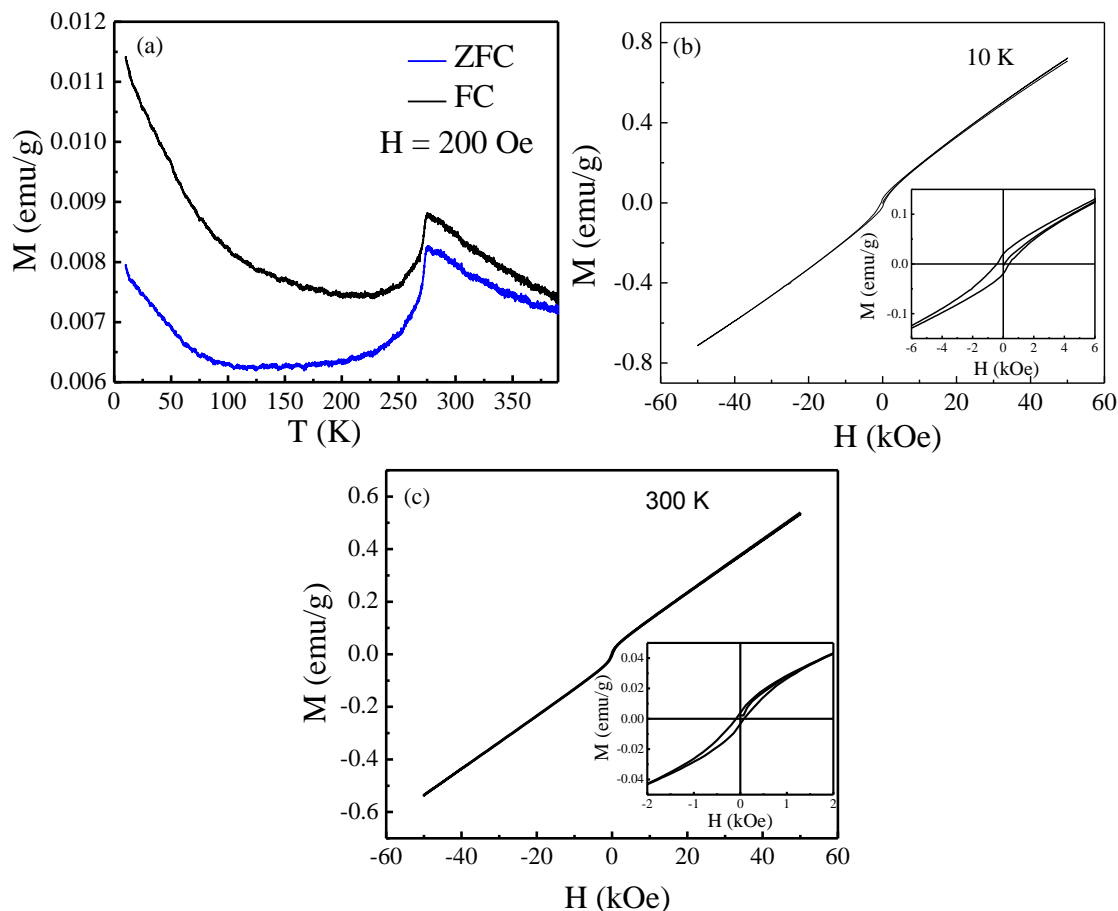


Figure 9 XRD pattern of CrN nanoparticles with Le Bail fitting

temperature with Le Bail fitting. At room temperature, it crystallizes in rock salt-type cubic structure (space group,  $Fm-3m$ ) with lattice constant of 4.1485(1) Å. The calculated crystallite size as obtained from the Scherrer's formula is 32 nm.

Figure 10(a) shows ZFC-FC magnetizations of CrN nanoparticles at 200 Oe. A clear transition at 275 K is observed in both ZFC and FC magnetization data below which it becomes antiferromagnetic coupled with a structural transition to an orthorhombic phase. It is interesting to note that Ney *et al.* do not observe any anomaly around this temperature in a CrN thin film prepared by rf-plasma-assisted molecular beam epitaxy method.<sup>25</sup> In the case of our CrN nanoparticles just below the transition temperature the magnetization starts

According to Filippetti *et al.*<sup>10</sup> CrN is an antiferromagnet in its orthorhombic ( $Pnma$ ) phase composed of ferromagnetic (1-10) layers with alternate layers antiferromagnetically arranged. We obtain CrN nanoparticles by heating ammonium metavanadate with excess of urea in nitrogen atmosphere. Figure 9 shows the XRD pattern of CrN nanoparticles at room



**Figure 10(a)** ZFC-FC magnetizations of CrN nanoparticles at 200 Oe, **(b)** magnetic hysteresis loop at 10 K with inset showing the enlarged view near the origin, **(c)** magnetic hysteresis loop at room temperature with inset showing the enlarged view near the origin.

decreasing as expected in an antiferromagnetic system but unlike the bulk counterpart we observe a rise in the magnetization at low temperature. This can be explained on the basis of some uncompensated spins on the surface of the nanoparticles which can constitute a net magnetization in the direction of the applied magnetic field. We expect no divergence between ZFC and FC magnetizations above the transition temperature for an ideal antiferromagnetic system in the paramagnetic state. In contrast, we do observe such divergence in CrN nanoparticles. We attribute this to defect related spins on the surface of the nanoparticles. In Figure 10(b) and (c) we show the magnetic hysteresis loops at 10 and 300 K respectively. Insets show enlarged view of the magnetization near the origin. The observed coercivity is attributed to the above mentioned surface defects.

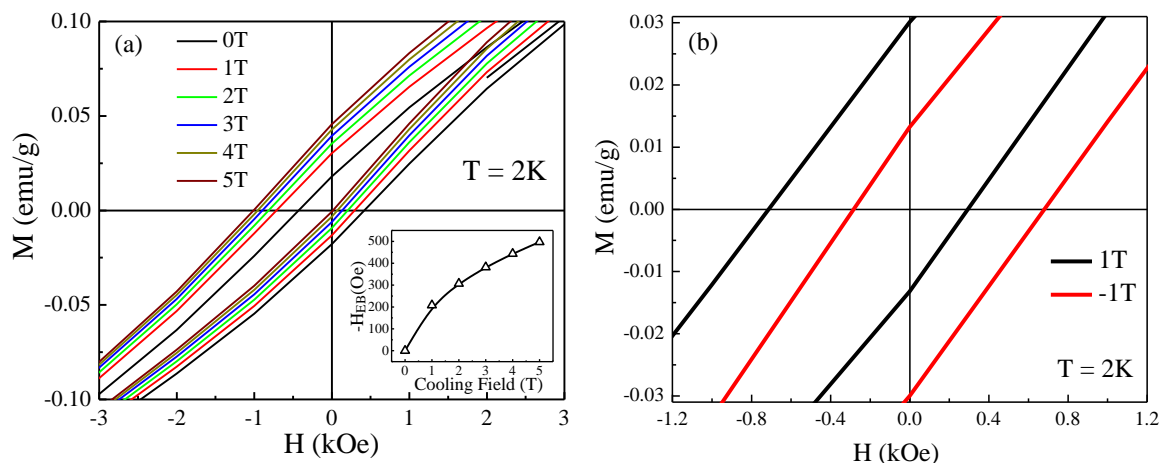


**Figure 11(a) Magnetic hysteresis at different positive biasing fields, (b) magnetic hysteresis loops under two biasing fields with different polarity**

Figure 11(a) shows the exchange bias effect studied under different cooling fields at 2 K. It is observed that when a positive field is applied while cooling the sample, the magnetization loop shifts towards the negative field side hence, exhibiting a negative exchange bias effect. Exchange bias effect increases with increasing cooling field and does not saturate even at 5 T field. The effect of cooling field on the exchange bias effect is shown in the inset of Figure 11(a). At the cooling field of 5 T, a shift of  $\sim 500$  Oe is observed in the negative field direction. In order to verify that the exchange bias is not due to any artifact we perform the experiment under fields of different polarity (-1 and +1 T) at 2 K and find that on changing the polarity the exchange bias also changes its sign (Figure 11(b)). The phenomenon of exchange bias in this system can be explained by considering the individual nanoparticle to be composed of core of antiferromagnetic CrN with a shell of uncompensated disordered spins which acts as the ferromagnetic component. At the interface of these two components spins of ferromagnetic component are pinned by the more anisotropic spins of antiferromagnetic component and thus exhibiting the exchange bias effect. Such an effect also contributes to the overall magnetic anisotropy thus increasing the coercivity of the magnetic hysteresis loops. We also see an increase in the coercive field ( $H_c$ ) on recording the magnetization under biasing field. For example,  $H_c$  in the absence of any biasing field is 0.43 kOe which increases to a value of 0.5 kOe under a biasing field of 1 T. We also observe a decrease in the exchange bias effect as we approach the Néel's temperature of CrN as shown in Figure 12.



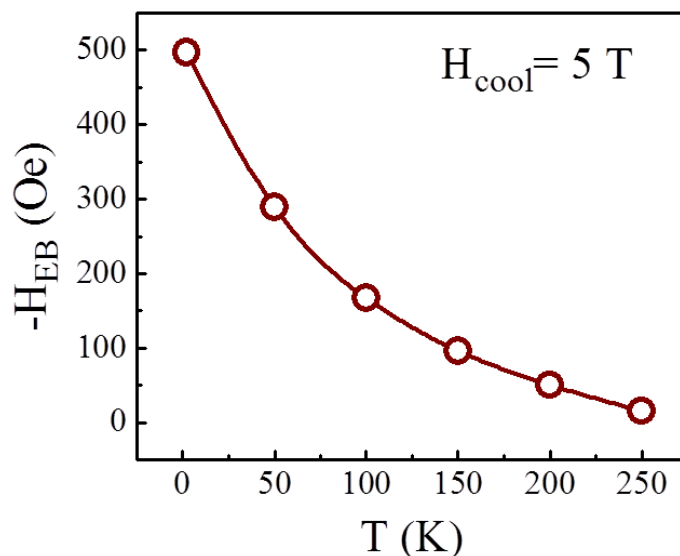


Figure 12 Variation in exchange bias effect with respect to temperature in CrN nanoparticles

#### 4.4 Photocatalytic water splitting by TiN and VN nanoparticles

TiN and VN are metallic and show superconductivity at low temperatures. Metallic properties of VN have been exploited for supercapacitor applications. A metallic component, which could accept/donate electron or hole from/to the light absorbing semiconductor thus preventing the electron-hole recombination, is desirable in a system for efficient water

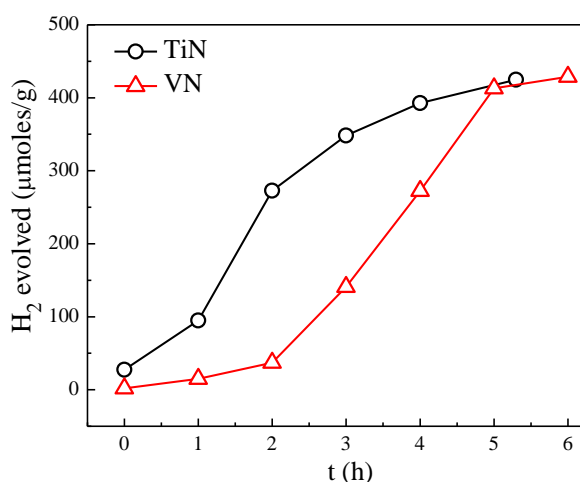


Figure 13 Hydrogen evolution with time for VN and TiN nanoparticles

used here is prepared by heating TiO<sub>2</sub> nanoparticles in ammonia atmosphere at 800 °C for 2h. Figure 13 shows the profile of hydrogen evolution reaction using TiN and VN nanoparticles

splitting. Noble metals are often used for this purpose. Recently, hydrogen evolution properties of TiN have been studied in which it is proposed to be acting as a gapped semiconductor which absorbs light and being a low electrical resistance material does not require any use of noble metal.<sup>26</sup> Herein, we show that metallic TiN and VN nanoparticles

along with a light harvesting dye can be used as a hydrogen evolving system. TiN

as catalyst along with eosin Y (EY) dye for light harvesting and triethanol amine as sacrificial electron donor. Both the catalysts show an overall activity of  $\sim 400 \mu\text{moles/g}$  with at a rate of  $\sim 70 \mu\text{moles/g/h}$ . As TiN and VN are gap less metallic materials they must be used along with a light harvesting dye. On absorption of visible light, EY goes to a triplet excited state which by accepting electron from triethanol amine becomes  $\text{EY}^-$ . This EY anion is a highly reductive species and therefore donates an electron to the catalyst. We believe that the catalyst being metallic can accept electrons easily from  $\text{EY}^-$  and thereby reduce water. The catalyst must therefore have its Fermi level more positive than  $\text{EY}^-$  and more negative than water reduction potential.

## **5. Conclusions**

We obtained nanoparticles of rock salt-type VN, NbN and CrN by urea method. VN and NbN nanoparticles show superconducting properties with transition temperatures comparable to the corresponding bulk phase. CrN nanoparticles show exchange bias effect at low temperatures because of the formation of an interface between antiferromagnetic core and spin disordered shell. Metallic TiN and VN along with a photosensitizer are used as catalysts for water reduction reaction.

## 6. References

1. L. Toth, *Transition metal carbides and nitrides*. Academic press: 1971.
2. F. Lévy, P. Hones, P. E. Schmid, R. Sanjinés, M. Diserens and C. Wiemer, *Surf. Coat. Technol.* **1999**, 120–121, 284-290.
3. S.-H. Jhi, S. G. Louie, M. L. Cohen and J. Ihm, *Phys. Rev. Lett.* **2001**, 86, 3348-3351.
4. M. Birkholz, K. E. Ehwald, D. Wolansky, I. Costina, C. Baristiran-Kaynak, M. Fröhlich, H. Beyer, A. Kapp and F. Lisdat, *Surf. Coat. Technol.* **2010**, 204, 2055-2059.
5. D. Gall, M. Städele, K. Järrendahl, I. Petrov, P. Desjardins, R. T. Haasch, T. Y. Lee and J. E. Greene, *Phys. Rev. B* **2001**, 63, 125119.
6. L. E. Toth, C. P. Wang and G. M. Yen, *Acta Metall.* **1966**, 14, 1403-1408.
7. F. I. Ajami and R. K. MacCrone, *J. Phys. Chem. Solids* **1975**, 36, 7-15.
8. H. Rietschel, H. Winter and W. Reichardt, *Phys. Rev. B* **1980**, 22, 4284-4292.
9. D. Choi, G. E. Blomgren and P. N. Kumta, *Adv. Mater.* **2006**, 18, 1178-1182.
10. A. Filippetti and N. A. Hill, *Phys. Rev. Lett.* **2000**, 85, 5166-5169.
11. C. Constantin, M. B. Haider, D. Ingram and A. R. Smith, *Appl. Phys. Lett.* **2004**, 85, 6371-6373.
12. J. Gavaler, A. Santhanam, A. Braginski, M. Ashkin and M. Janocko, *Magnetics, IEEE Transactions on* **1981**, 17, 573-576.
13. P. K. Tripathy, J. C. Sehra and A. V. Kulkarni, *J. Mater. Chem.* **2001**, 11, 691-695.
14. R. Marchand, F. Tessier and F. J. DiSalvo, *J. Mater. Chem.* **1999**, 9, 297-304.
15. R. Niewa and F. J. DiSalvo, *Chem. Mater.* **1998**, 10, 2733-2752.
16. D. H. Gregory, *J. Chem. Soc., Dalton Trans.* **1999**, 259-270.
17. A. Gomathi and C. N. R. Rao, *Mater. Res. Bull.* **2006**, 41, 941-947.
18. C. Giordano, C. Erpen, W. Yao, B. Milke and M. Antonietti, *Chem. Mater.* **2009**, 21, 5136-5144.
19. W. Yao, P. Makowski, C. Giordano and F. Goettmann, *Chem. Eur. J.* **2009**, 15, 11999-12004.
20. H. Zhao, M. Lei, X. Chen and W. Tang, *J. Mater. Chem.* **2006**, 16, 4407-4412.
21. Y. Xie, Y. Qian, W. Wang, S. Zhang and Y. Zhang, *Science* **1996**, 272, 1926.
22. K. Sardar and C. N. R. Rao, *Adv. Mater.* **2004**, 16, 425-429.

23. Shipra, A. Gomathi, A. Sundaresan and C. N. R. Rao, *Solid State Commun.* **2007**, *142*, 685-688.
24. A. Sundaresan and C. N. R. Rao, *Nano Today* **2009**, *4*, 96-106.
25. A. Ney, R. Rajaram, S. S. P. Parkin, T. Kammermeier and S. Dhar, *Appl. Phys. Lett.* **2006**, *89*, 112504-112504-3.
26. G. Li, P. Zhang, Z. Bian, J. Zhu, L. Wu and H. Li, *ChemSusChem* **2013**, *6*, 1461-1466.

## Appendix A

### Gas phase synthesis of CrN and Fe<sub>3</sub>N

We have also carried out gas phase synthesis of CrN and Fe<sub>3</sub>N by using volatile metal precursors. For this synthesis metal-acetyl acetonate was taken in an alumina boat and

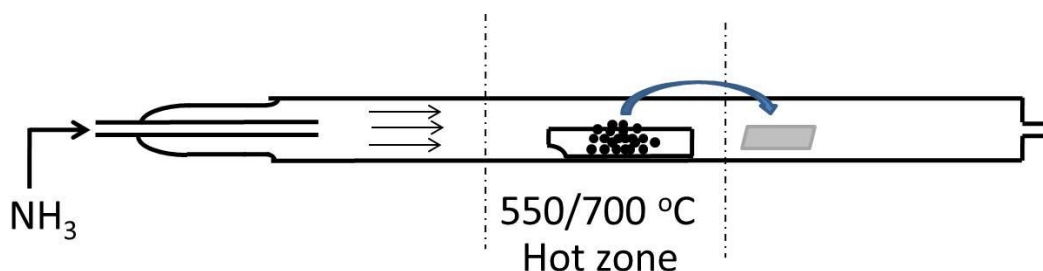


**Figure 1** Experimental set up for the gas phase synthesis of CrN and Fe<sub>3</sub>N

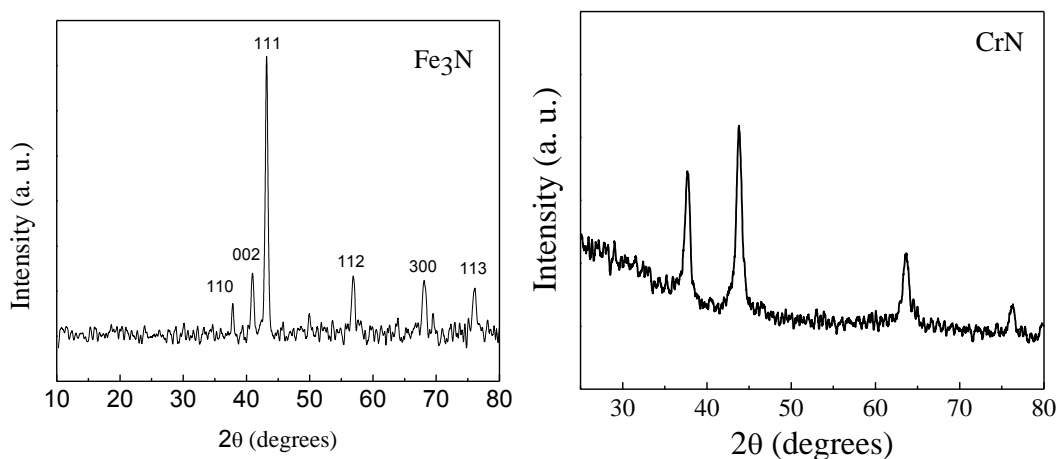


**Figure 2** XRD patterns of Fe<sub>3</sub>N and CrN nanoparticles obtained by gas phase synthesis

adjacent to it at a distance of 5 cm a quartz substrate was kept for collecting the product in a quartz tube. The tube was flushed with ammonia while keeping the reactant and the substrate at room temperature. After 30 minutes of ammonia flow (200 mL/min) the reactant was pushed to the hot zone of the furnace maintained high temperature (700 and 550 °C for CrN and Fe<sub>3</sub>N respectively). The experimental set up is shown in Figure 1. XRD patterns of Fe<sub>3</sub>N and CrN are shown in Figure 2. Fe<sub>3</sub>N crystallizes in hexagonal structure (space group, *P312*).

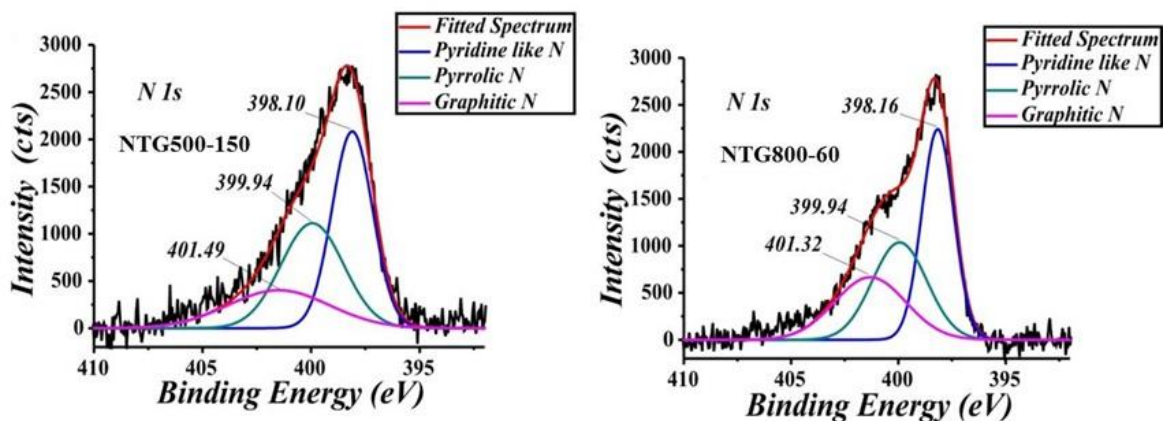


## Chapter III.2

### Synthesis and characterization of N-doped graphene\*

#### Summary

Ammonolysis of graphene oxide in pure ammonia is used for the synthesis of nitrogen doped graphene. The amount of nitrogen doping depends on various factors like temperature, ammonia flow rate and duration of ammonolysis. Nitrogen content decreases with increase in ammonolysis temperature. Remaining two factors have lesser effects on N-content. The presence of nitrogen within the structure of reduced graphene oxide results in a remarkable increase in the thermal stability against oxidation by air. The thermal stability is closely related with the temperature of synthesis and the nitrogen content. The combustion reaction of nitrogen in different coordination environments (pyridine, pyrrole and graphitic) is analyzed against a graphene fragment (undoped) from a thermodynamic point of view. In agreement with the experimental observations, the combustion of undoped graphene turns out to be more spontaneous than when nitrogen atoms are present.



\* A paper based on these studies has been submitted to *Chem. Eur. J.*

## 1. Introduction

Graphene is a two dimensional hexagonal network of  $sp^2$  hybridized carbon atoms. It can be considered as the building block of the three dimensional graphite. Since its discovery in 2004,<sup>1</sup> graphene has been one of the most exciting materials attracting the attention of chemists, physicists and materials scientists all over the world. Graphene exhibits extraordinary physical properties, for example high surface area (theoretical value  $\sim 2630 \text{ m}^2\text{g}^{-1}$ ), high chemical stability, excellent conductivity ( $106 \text{ Scm}^{-1}$ ) and electron mobility ( $1-20 \times 10^3 \text{ cm}^2\text{V}^{-1}\text{s}^{-1}$  depending on the degree of disorder). Graphene exhibits a unique electronic band structure with a linear dispersion relation close to the charge neutrality point (or Dirac point). Perfect two dimensional quantum confinement along with electron-hole degeneracy and the vanishing carrier mass near the point of charge neutrality cause graphene to exhibit quantum Hall effect. Easiness of functionalization and production pose interesting opportunities to chemists. These unique physical and chemical properties lead graphene as an ideal material for applications in electric device<sup>2</sup>, biosensors<sup>3-4</sup>, field effect transistors<sup>5</sup>, supercapacitors<sup>6</sup>, lithium secondary batteries<sup>7</sup>, and fuel cells<sup>8-11</sup>. Graphene in its purest form is gapless which limits its use in many device applications. According to recent theoretical predictions, in-plane substitution of nitrogen in carbon sites can modulate the electronic properties of graphene to an n-type semiconductor with a result of electron and hole transport features being asymmetric relative to the Dirac point.

Nitrogen doping can be achieved either during the synthesis of graphene via chemical vapor deposition (CVD)<sup>12-14</sup>, arc discharge<sup>15</sup> and solvothermal synthesis<sup>16</sup> or through a post synthesis modification of graphene, graphene oxide (GO) or reduced graphene oxide (RGO) with thermal<sup>17</sup>, hydrothermal<sup>18</sup>, plasma<sup>19-20</sup>, and hydrazine treatments<sup>21</sup>. The nitrogen content depends on both, the method and the starting material employed, but it is typically in the range of 2-5 at. % and rarely exceeds 9 at. %. Only few recent examples have achieved higher N contents. Sheng *et al.* reported 10.1 at. % nitrogen doping using GO as a starting material and melamine as a nitrogen source.<sup>22</sup> Deng *et al.* achieved 13 wt. % doping (16.4% N/C) with solvothermal synthesis using tetrachloromethane and lithium nitride as carbon and nitrogen source respectively.<sup>16</sup> Rao *et al.* recently reported 18 wt. % via microwave treatment of GO with urea (nitrogen source).<sup>23</sup> Simple heating of GO and urea in inert atmosphere



gives rise to 8.5 wt. % doping.<sup>23</sup> Nitrogen doping of graphene was reported by Dai *et al.* in 2009 that used a mixture of Ar and ammonia allowing the simultaneous nitridation and reduction of GO.<sup>24</sup> Several works have followed employing ammonia under thermal,<sup>17, 25</sup> microwave<sup>26</sup> and hydrothermal conditions, the latter leading to a higher degree of doping (7.2 at. %).<sup>27</sup>

## 2. Scope of the present investigation

Direct ammonolysis has always resulted in low amount of nitrogen in graphene. From the available literature of nitrogen doping in graphene it is clear that oxygen functionalities are important for high nitrogen doping concentrations. 100 % ammonia gas has rarely been used as a nitrogen source and most often 5-10 % ammonia gas diluted with argon or nitrogen is used for this purpose. Herein, we report the highest nitrogen content achieved so far by ammonia treatment (13 wt. %) starting with GO and 100 % ammonia as the nitrogen source. We study the effect of temperature, duration of ammonia treatment and flow rate on nitrogen doping and the influence that nitrogen has on the thermal oxidation stability of the sheets. A remarkable increase of 137 °C in the oxidation temperature in air is observed for the N-doped RGO in comparison to undoped-RGO. Thermally stable graphene is of interest for instance as reinforcing material in components exposed at elevated temperatures and friction and to prepare catalysts with applications in fuel cells. It has been reported that N-doping reduces the presence of easily oxidizable defects, which are unstable under fuel cell operation.<sup>26, 28</sup> To the best of our knowledge, this is the first time that the thermal oxidation stability of N-doped graphene samples is investigated.

## 3. Experimental section

### 3.1 Synthesis of GO

5 g graphite in 115 mL of conc. H<sub>2</sub>SO<sub>4</sub> was cooled down to 0 °C. 2.5 g NaNO<sub>3</sub> was added slowly. After 30 min, KMnO<sub>4</sub> was added slowly in order to maintain the temperature below 20 °C. The mixture was warmed to 35 °C and stirred for 30 min. 230 mL of water was added slowly and the temperature was maintained at 98 °C for 2 h. After that 700 mL water and 5 mL H<sub>2</sub>O<sub>2</sub> solution (25 %) were added slowly. The content was air cooled, centrifuged and washed several times with distilled water till the pH of the solution became ~ 7.

### 3.2 Synthesis of nitrogen doped graphene

GO was heated in the presence of ammonia in different conditions in order to vary the doping level.

#### 3.2.1 *Effect of temperature*

GO was heated in ammonia atmosphere at a temperature range of 20 °C (room temperature) to 800 °C for 60 min with a flow rate of 300 mL/min. For all the reactions the final temperature was achieved in 3 h except for the reaction at 100 °C where the temperature was achieved in 1 h. Heating above 800 °C was not carried out in order to avoid the formation of HCN gas in the presence of ammonia. For each synthesis 100 mg of GO was spread in the ceramic boat and heated in the quartz tube keeping the sample exactly above the thermocouple. Before switching on the heater, the quartz tube was evacuated by passing N<sub>2</sub> for 15 min followed by ammonia for 30 min. After the reaction, once the temperature reached below 100 °C the quartz tube was evacuated by passing N<sub>2</sub> for 30 min before removing the sample.

Samples name were kept as follows:

NG500-60: GO heated at 500 °C for 60 min.

Similarly, all other samples were named as: NG100-60, NG220-60, NG300-60, NG400-60, NG600-60, NG700-60, NG800-60.

The sample which was kept in ammonia at room temperature for 60 min was named as NGRT-60

#### 3.2.2 *Effect of duration of ammonolysis*

GO was heated at 500 °C for 10 min, 60 min, 150 min and 300 min at a flow rate of 300 mL/min in order to see the effect of the duration of ammonolysis on the doping level. The heating rate was kept as mentioned earlier. Samples name were kept as follows:

NG500-300: GO heated at 500 °C for 300 min. Similarly, other samples were named as: NG500-10, NG500-600 and NG500-150.

### 3.2.3 Effect of flow rate of ammonia

In order to see the effect of flow rate, GO was heated at 800 °C for 60 min with flow rates of 60, 300 and 600 mL/min.

### 3.3 Preparation of dispersion

A dispersion of nitrogen doped graphene was prepared by bath sonicating 5 mg powder in a mixture of 5 mL water and 5 mL ethanol for 30 min. followed by centrifuging the content at a speed of 4000 rpm for 30 min. A clear liquid was carefully collected by a dropper from the top and rest of the content was discarded.

### 3.4 Characterization

Elemental analyses data were recorded on a Thermo Scientific™ FLASH 2000 Series CHNS Analyzer using a Metler Toledo MX5 microbalance. SEM images were obtained using a Quanta FEI 200 ESEM FEG microscope, operating at 10.0 kV. Samples were sonicated and dispersed in hexane and placed dropwise onto a lacey carbon support grid. Thermogravimetric analysis was performed on a Netzsch instrument, model STA 449 F1 Jupiter®, under flowing air at a heating rate of 10 °C/min. X-ray photoelectron (XP) spectra were recorded in an Omicron Nanotechnology Spectrometer with the Mg K $\alpha$  as X-ray source. Samples were dispersed in alcohol followed by drop casting onto a silicon substrate. Infrared spectra were recorded with a Bruker IFS 66v/S spectrometer. Raman spectra were recorded with a LabRAM HR with a 633 nm line from a HeNe laser. UV-visible spectra were recorded in Perkin Elmer Lambda 900 UV/Vis/NIR spectrometer. X-ray diffraction data were collected in Siemens D5000 using Cu K $\alpha$  radiation ( $\lambda = 1.5418 \text{ \AA}$ ).

## 4. Results and discussion

GO is brown powder which on treatment under ammonia at high temperature becomes black in color. XRD patterns of starting graphite powder, GO, ammonia treated GO at 500 °C for 10 min and 150 min are shown in Figure 1. Graphite used for the synthesis exhibits very high crystallinity which is clear from the extremely sharp (002) reflection. The interlayer separation obtained from the position of this reflection is 3.354 Å which matches

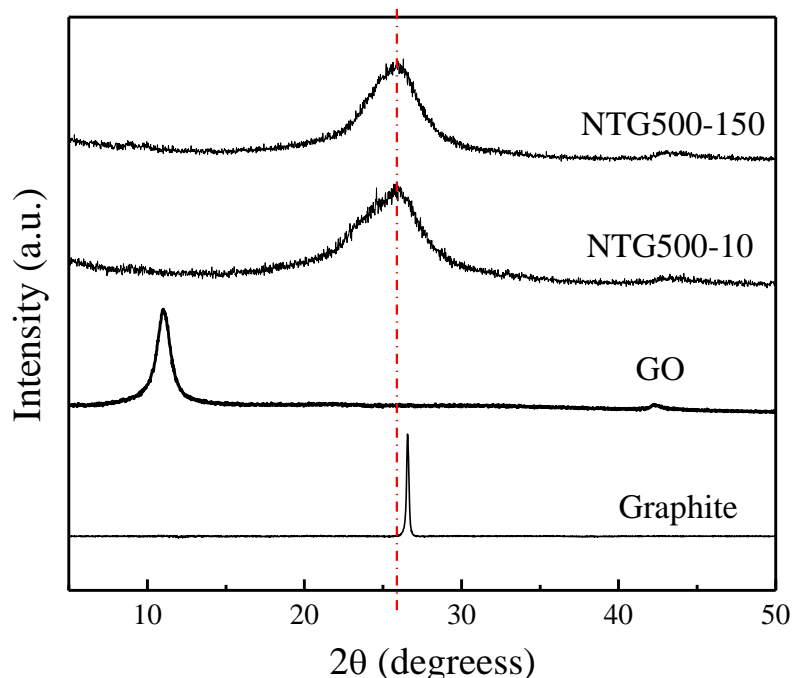


**Figure 1** XRD patterns of graphite, GO and ammonia treated GO at 500 °C for 10 and 150 min.

to the bulk graphite powder (3.35 Å). Upon oxidation, the (002) reflection shifts significantly to a lower  $2\theta$  of  $11.04^\circ$  with a corresponding interlayer separation of 8.018 Å. This distance is more than twice that of the van der Waals distance between two graphitic layers and in GO they are believed to be held together by hydrogen bonding between functional groups of the adjacent layers. On treatment with  $\text{NH}_3$  at 500 °C for 10 and 150 min. (002) reflections come back to  $2\theta = 25.898^\circ$  which corresponds to an interlayer separation of 3.440 Å. This value is slightly higher than that of the graphite powder (3.354 Å). This increase is due to small amount of carboxylic acid and hydroxyl functional groups present even after reduction. Ripples and bending induced by defects in the basal plane might also contribute to the increase in interlayer separation.

We have carried out ammonolysis of GO by varying different reaction parameters to optimize the ammonolysis condition. The amount of nitrogen and oxygen are obtained from combustion based elemental analysis. Figure 2(a) shows the variation of nitrogen content with respect to ammonolysis temperature at a flow rate of 300 mL/min and duration of 60

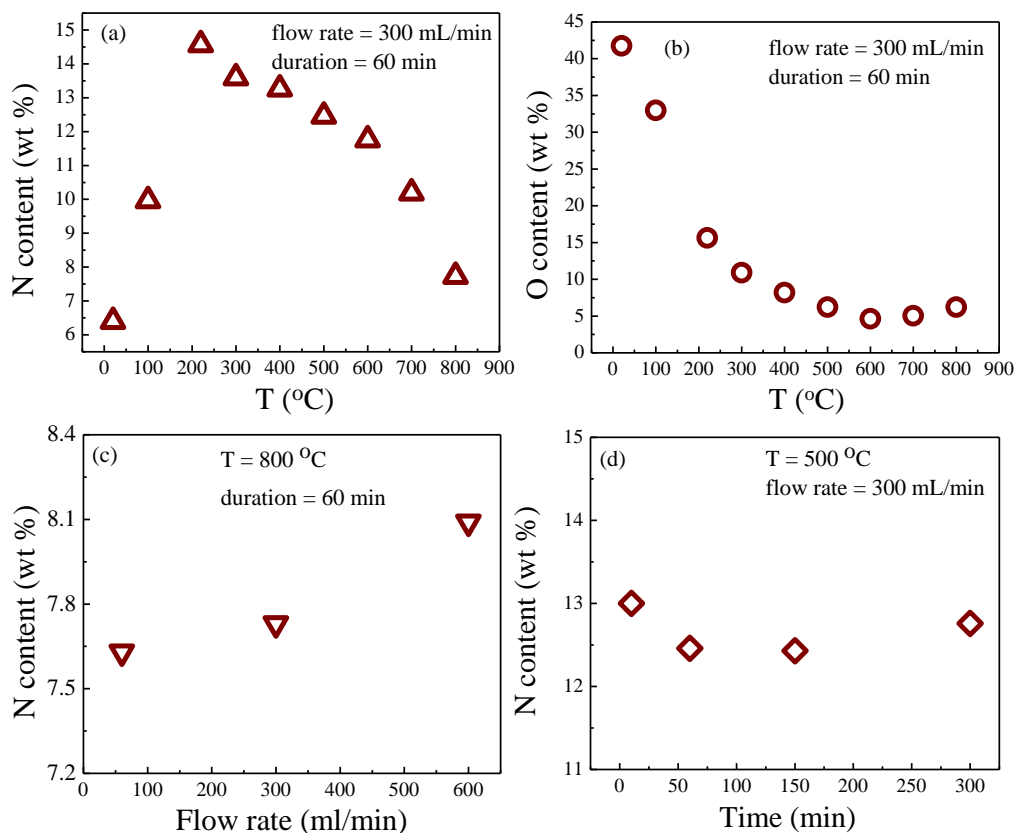


**Figure 2** Effect of ammonolysis temperature on (a) nitrogen and (b) oxygen content, (c) effect of duration of ammonolysis and (d) effect of flow rate of ammonia on nitrogen content

min. To our surprise, we observe 6.5 wt. % nitrogen at room temperature which increases till 220 °C to where we obtain the highest nitrogen content of 14.6 wt. %. After 220 °C, N content decreases gradually resulting in the minimum value (7.7 wt. %) at 800 °C. Oxygen content decreases with increase in temperature with a sudden jump at 220 °C (Figure 2(b)). After 220 °C it decreases more gradually with a minimum value (4.6 wt. %) at 600 °C above which it increases slightly. We propose that below 220 °C, N in the sample is mainly as functional groups like amine, amide *etc.* Above this temperature, nitrogen starts occupying sites at the basal plane of graphene. A sudden decrease in oxygen content at 220 °C is because of the decomposition of carboxylic group at this temperature. From the profiles of nitrogen and oxygen contents it can be concluded that 500-600 °C is the optimum temperature range for ammonolysis because after this temperature  $\text{NH}_3$  decomposes to form  $\text{N}_2$  and  $\text{H}_2$  thus inhibiting the ammonolysis process. This is also supported by the fact that on

**Table 1 Amount of N, C and H in different N-RGO samples obtained from elemental analysis**

SAMPLE	%N	%C	%H
NG500-10	13.0	80.1	0.6
NG500-60	12.5	80.9	0.5
NG500-150	12.4	80.8	0.5
NG600-60	11.8	83.3	0.4
NG700-60	10.2	84.5	0.4
NG800-60	7.7	85.7	0.4

increasing ammonia flow rate which reduces the effect of  $\text{NH}_3$  decomposition, nitrogen content increases gradually (Figure 2(c)). Moreover, at higher temperatures due to thermal effects, oxygen functionalities are decomposed resulting in lower concentrations of nitrogen as we know that oxygen functionalities favor nitridation. In order to demonstrate that oxygen functionalities are important for N-doping, we carried out ammonolysis starting with exfoliated graphene (prepared by heating GO in Ar at 1050 °C) and found that the nitrogen content in the resulting sample was below 0.2 wt. %. We do not observe any significant effect of duration of ammonolysis at 500 °C at a flow rate of 300 mL/min. It also implies that 10 min of ammonolysis reaction is enough to achieve a high concentration of N. Such a fast kinetics of ammonolysis could be attributed to the high surface area of graphene oxide.

To investigate the thermal oxidation stability of nitrogen doped RGO, we focused on samples that showed the highest (500 °C) and lowest (800 °C) nitrogen contents while retaining the same amount of oxygen and prepared two additional samples by annealing GO under flowing Ar at the same temperatures (called G500-Ar and G800-Ar) and treatment time. Thermogravimetric analyses (TGA) of the four samples are shown in Figure 3 and the onsets of the combustion temperature are summarized in Table 2. Let us first focus on the samples prepared under Ar (solid lines). It is well established that annealing GO under an inert atmosphere results in the decomposition of functional groups leading to the formation of reduced graphene oxide. The higher the annealing temperature, lower is the degree of oxygen-bearing functionalities present in the reduced material,<sup>17, 29</sup> which in turn should confer the sample a higher stability against air oxidation. This is in agreement with our

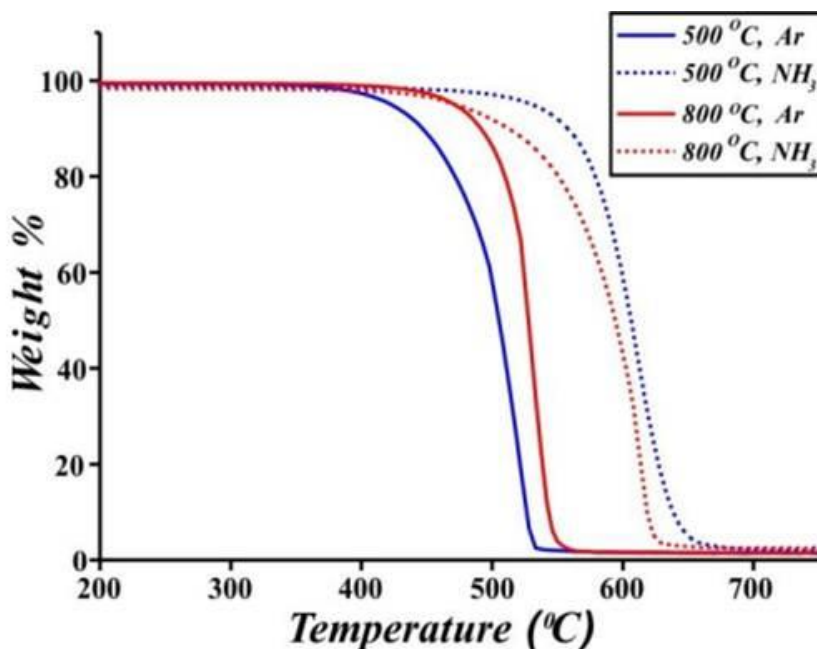


Figure 3 Thermogravimetric analyses of G500-Ar, G800-Ar, NG500-60 and NG800-60 in flowing air at a heating rate of 10 °C/min

Table 2 Onset of combustion temperature of GO Samples treated in Ar and NH<sub>3</sub> at 500 and 800 °C

Sample	Onset of combustion (°C)
G500-Ar	432
NG500-60	569
G800-Ar	493
NG800-60	520

TGA data. G800-Ar shows a higher onset of combustion temperature (493 °C) than G500-Ar (blue solid line; onset: 432 °C). Remarkably, the opposite trend is observed in the nitrogen doped samples (dashed lines) where NG500-60 (blue dashed line) shows a higher (onset: 569 °C) than NG800-60 (red dashed line; onset: 520 °C). This is an interesting phenomenon since thermal annealing is typically employed to increase the crystallinity of the samples and to reduce the concentration of functional groups.

The higher stability of the NG500-60 must arise from the larger amount of nitrogen (12.5 wt. % N) compared to NG800-60 (7.7 wt. % N). The ~5 wt. % difference in nitrogen content

seems to prevail and be responsible for the different observed thermal oxidation stabilities. A remarkable increase of 137 °C is observed in NG500-60 (blue solid line) compared to G500-Ar (blue dashed line). This corresponds to more than 30% increase in thermal stability. The same trend, although to a lesser degree, is observed between NG800-60 and G800-Ar. Nitrogen doped samples are markedly more stable (against thermal oxidation in air) than their non-doped counterparts.

We have performed X-ray photoelectron spectroscopy measurements over the N 1s region to determine the nature of the nitrogen present in NG500-60 and NG800-60. The experimental XPS data along with the fitted deconvolution to pyridinic-N, pyrrolic-N and graphitic-N are shown in Figure 4. The highest intensity in both XP spectra is observed at about 398.1 eV, which can originate from either pyridine-N or amines/amides present in the structure. The absence of any weight loss below 400 °C in the TGA analysis allows us to disregard the presence of amines, amides or derivative species in the N-RGO samples, which contribute

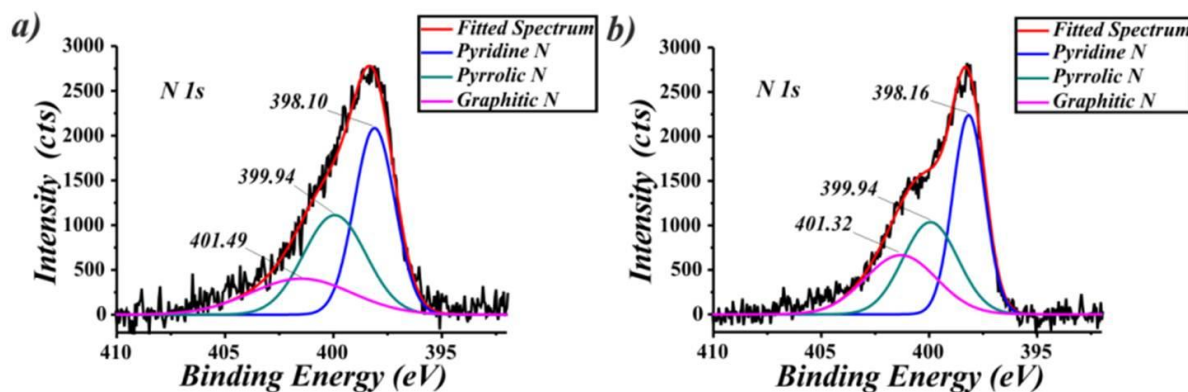


**Figure 4** Core-level XP spectra of (a) NG-500-60 and (b) NG-800-60

in the range of 399-400 eV.<sup>30-31</sup> Organic moieties are expected to thermally decompose at lower temperatures. Therefore, we can assign the peak at 398.1 eV to pyridinic-N. A shoulder at higher binding energies (above 400 eV) becomes patent in the sample prepared at 800 °C, which arises from pyrrolic and graphitic type nitrogen, the latter having a major effect. Actually, a higher intensity of the fitted graphitic-N peak (~ 401.4 eV) is observed in the sample prepared at 800 °C.



**Table 3** Amounts of different types of nitrogen in NG500-60 and NG800-60 obtained from XPS and elemental analysis

Sample		Total N (elemental- analysis)	Pyridinic-N	Pyrrolic-N (XPS analysis)	Graphitic-N
NG500-60	N (wt.%)	12.5	5.4	4.5	2.6
	%	100	43.4	35.7	20.9
NG800-60	N (wt.%)	7.7	3.2	2.5	2.1
	%	100	40.8	32.3	26.9

Table 3 summarizes the content of each type of nitrogen. Since the total amount of nitrogen present in NG800-60 (7.7 wt. %) is much lower than NG500-60 (12.5 wt. %), the total weight percent of the three types of nitrogen is also lower in NG800-60 (1<sup>st</sup> & 3<sup>rd</sup> rows; wt. %). Interestingly though, is the fact that the weight percent of both pyridine and pyrrole decreases by about 42.5 % (40.7 % for pyridinic-N, from 5.4 to 3.2 wt. %; 44.4 % for pyrrolic-N, from 4.5 to 2.5 wt. %) whereas, the total amount of graphitic-N decreases by only 19.2 % (from 2.6 to 2.1 wt. %). It is also worth to compare the relative percentage (2<sup>nd</sup> & 4<sup>th</sup> rows) to appreciate the effect that temperature has on relative fraction of each type of nitrogen. It becomes patent that treatment of GO in NH<sub>3</sub> at higher temperatures favors the formation of the graphitic nitrogen. A ~ 6 % increase in the graphitic-N content is observed for NG800-60 with respect to NG500-60 (26.9 relative % graphitic-N at 800 °C; 20.9% at 500 °C). Accordingly, both pyridinic- and pyrrolic-N suffer a ~ 3 % relative decrease. From such analysis it is difficult to attribute the enhanced thermal stability of N-doped RGO to the presence of a particular type of nitrogen. To get further insights on the stability that N doping confers to the samples, we next looked at the thermodynamics of the combustion reaction for each type of N, and C for undoped RGO, considering the fragments depicted in the reactions (1-4). We first worked out the enthalpy of combustion for each type of N, which can be estimated from the mean bond enthalpies (averages of bond enthalpies over a related series of compounds) for the gas-phase reaction.<sup>32</sup> We must consider the enthalpy changes accompanying the breaking of C-C(C=C), C-N(C=N) and O=O bonds in a typical reaction of combustion and the subsequent formation of the products of oxidation (CO<sub>2</sub> and N<sub>2</sub> in this

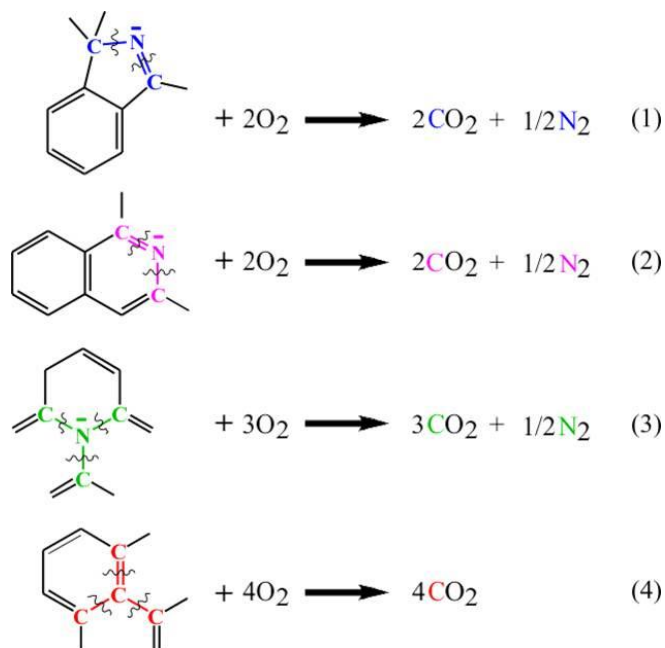


**Table 4. Mean bond enthalpies involved in the combustion reaction of RGO and N-RGO samples.<sup>32</sup>**

Bond	$\Delta H$ (kJmol <sup>-1</sup> )
C-C	345.6
C=C	602
C-N	304.6
C=N	615
O=O	493.6
C=O (CO <sub>2</sub> )	799
N≡N	941.7

case).<sup>33</sup> The estimated enthalpy of combustion for the NC<sub>2</sub> (pyrrolic- and pyridinic-N), NC<sub>3</sub> (graphitic-N) and CC<sub>3</sub> (graphene) fragments is -1760 kJmol<sup>-1</sup>, -2870 kJmol<sup>-1</sup> and -3470 kJmol<sup>-1</sup> respectively. Comparison between the combustion of N-containing moieties reveals that whereas both pyrrolic- and pyridinic-N have the same enthalpy of combustion, the oxidation of N in a graphitic environment leads to a much higher release of energy. Furthermore, the combustion of a graphene fragment (with no N) is more exothermic than an N-doped structure. The enthalpy of a transition can be determined from differential scanning

calorimetry (DSC) measurements. Figure 5 presents DSC analyses of the samples of RGO and N-RGO prepared at 500 °C. A more exothermic process is observed for the combustion

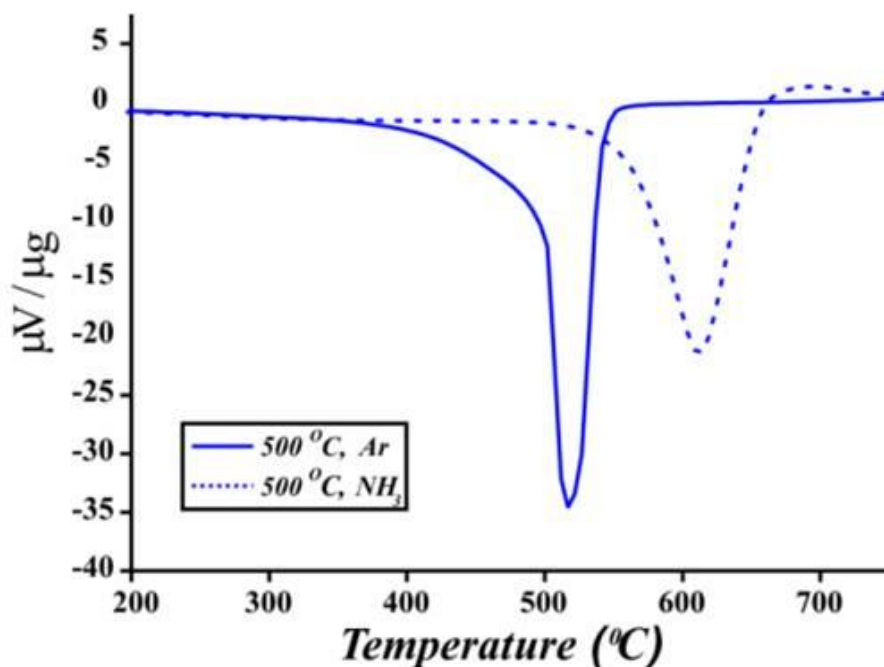


**Figure 5** DSC curves of undoped RGO (from Ar annealed GO) and N-doped RGO (NH<sub>3</sub> treated GO) prepared at 500 °C. DSC was performed under flowing air at a heating rate of 10 °C/min

of undoped RGO compared to the N-doped RGO. The enthalpy of the process is proportional to the integrated area of the associated peaks, which have a value of  $|1544| \mu\text{V}^2\mu\text{g}^{-2}$  for the undoped RGO (Ar treated) and  $|1370| \mu\text{V}^2\mu\text{g}^{-2}$  for the N-doped RGO (NH<sub>3</sub> treated). This is in good agreement with our thermodynamic calculations that predict a higher energy release for the combustion of undoped samples. Finally, the Gibbs energy ( $\Delta G$ ) has been calculated to estimate the spontaneity of the combustion reaction for each of the considered fragments (1-4). For ease of comparison and taking into account that the combustion of all the samples starts to occur in the range 432 – 569 °C, the temperature was fixed at the mean value of 500 °C for the calculation of both  $\Delta S$  and  $\Delta G$ . Estimated values of  $\Delta G_{500}$  of  $-1870 \text{ kJmol}^{-1}$ ,  $-2992 \text{ kJmol}^{-1}$  and  $-3521 \text{ kJmol}^{-1}$  have been obtained for NC<sub>2</sub>, NC<sub>3</sub> and CC<sub>3</sub> systems respectively. From the obtained values both pyridinic-N and pyrrolic-N are expected to confer a higher thermal stability to the system than graphitic-N. The calculated  $\Delta G$  further supports our experimental observation since from a thermodynamic point of view the reaction of undoped samples with oxygen is more spontaneous than when N is present. The entropy changes for

the reactions of oxidation of reduced graphene oxide and N-doped reduced graphene oxide at 500 °C (773 K,  $T_2$ ) are calculated using the tabulated data for the entropy values of the compounds involved in the combustion at 298 K ( $T_1$ ) and the heat capacity,  $\Delta C_p$  (assumed to be constant) at the initial temperature.<sup>34</sup> Thus,

$$\Delta S_{(T_2)} = \Delta S_{(T_1)} + \Delta C_p \ln\left(\frac{T_2}{T_1}\right)$$

Finally, in order to estimate the spontaneity of the oxidation processes, and considering the *Enthalpy* and the *Entropy* changes of the combustion reactions, the *Gibbs Energy* is calculated

**Table 5 Changes in the Gibbs Energy ( $\Delta G$ ) for the combustion reactions of RGO and N-doped RGO**

REACTION	$\Delta C_p$ (kJK <sup>-1</sup> mol <sup>-1</sup> )	$\Delta S_{298}$ (kJK <sup>-1</sup> mol <sup>-1</sup> )	$\Delta S_{773}$ (kJK <sup>-1</sup> mol <sup>-1</sup> )	$\Delta G$ (kJmol <sup>-1</sup> )
(1-2)	30.1	113.1	141.8	-1869.6
(3)	37.8	121.7	157.8	-2992.3
(4)	31.0	34.6	66.2	-3521.2

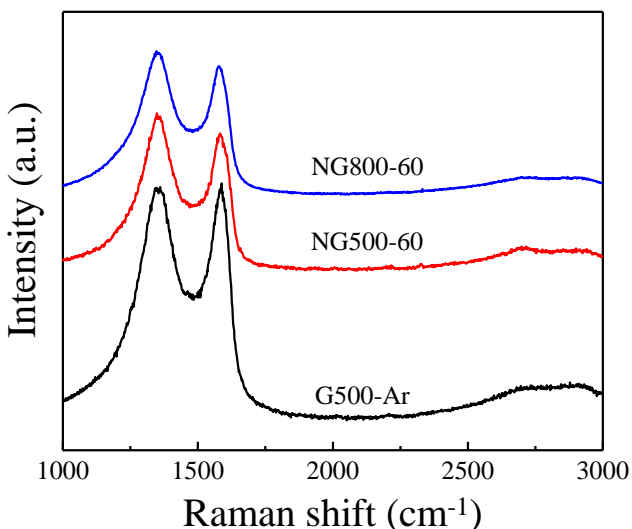


**Figure 6 Raman spectra of undoped (G500-Ar) and N-doped graphene (NG500-60 and NG800-60)**

Figure 6 shows the Raman spectra of undoped (G500-Ar) and nitrogen doped (NG500-60 and NG800-60) samples. We observe two main bands as shown in Figure 6. The one with lower energy near 1350 cm<sup>-1</sup> is called 2D band and is related to the defects in graphene (departure from the sp<sup>2</sup> hybridization of carbon) while the band with higher energy near 1580 cm<sup>-1</sup> is because of the first order scattering of

$E_{2g}$  mode  $sp^2$  carbon domain. Both the nitrogen doped samples exhibit higher  $I_D/I_G$  ratio compared to the undoped graphene. This is expected as nitrogen doping increases defects in the structure at the edges as well as in the basal plane of graphene. We observe a slight

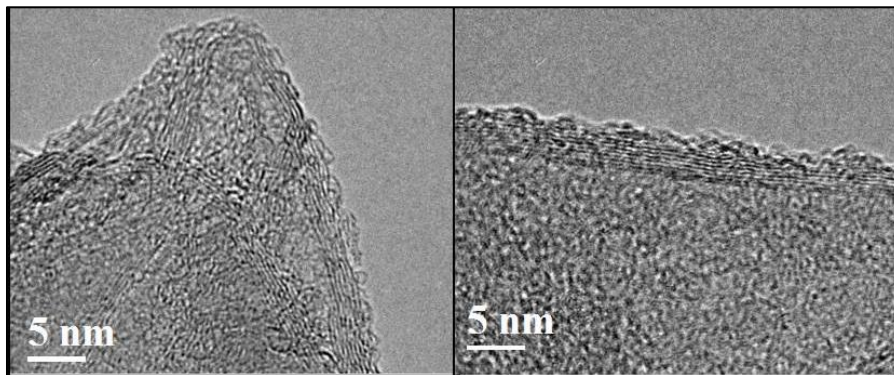


Figure 7 TEM images of NG500-60

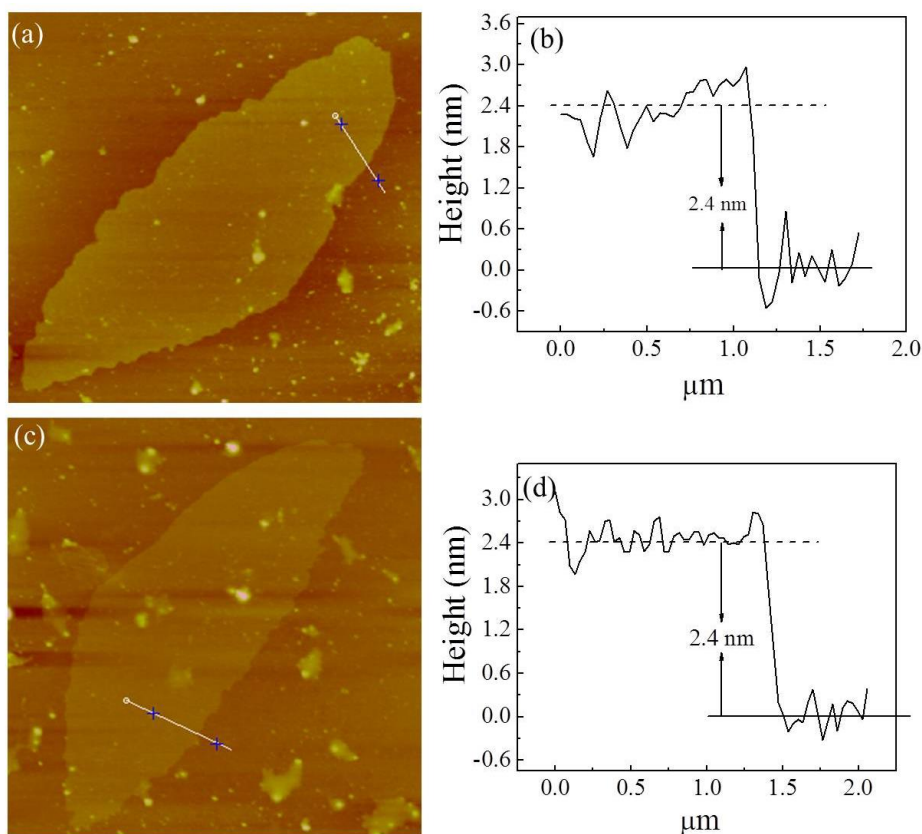


Figure 8 AFM images and corresponding height profiles of NG500-60

softening of the G band as also reported in N-graphene earlier.<sup>22</sup> The samples obtained after ammonolysis of GO at high temperatures consist of many layers. These cannot be used in

device applications. Few-layers N-doped graphene has been demonstrated to be a good material for field effect transistors. In order to obtain few-layers highly doped graphene, we bath sonicated the bulk material in a mixture of 1:1 water-ethanol mixture. The clear supernatant after centrifugation consists of few layers graphene. This method was recently used for obtaining few-layer graphene analogues (MoS<sub>2</sub>, WS<sub>2</sub> and BN) from their corresponding bulk materials.<sup>35</sup> Figure 7 shows the TEM images of few-layer NG500-60. It consists of 4-6 layers with interlayer separation 0.34 nm which is close to that in the graphite. AFM images reveal large lateral dimensions of the samples obtained after sonication (Figure 8). Corresponding height profiles account for 5-6 layers.

## **5. Conclusions**

We obtain highly nitrogen doped reduced graphene oxide by heating graphene oxide at different reaction conditions. We see that with increasing content of temperature graphitic-N increases with respect to pyrrolic- and pyridinic-N. N-doped RGOs are thermally more stable towards combustion in air compared to their undoped counterparts. By DTA analysis and calculations of Gibb's free energy of combustion it appears that with increase in the graphitic-N content thermal stability decreases. We could obtain few-layer N-graphene by sonicating the bulk material in water-ethanol mixture.

## 6. References

1. K. S. Novoselov, A. K. Geim, S. V. Morozov, D. Jiang, Y. Zhang, S. V. Dubonos, I. V. Grigorieva and A. A. Firsov, *Science* **2004**, *306*, 666-669.
2. N. Levy, S. A. Burke, K. L. Meaker, M. Panlasigui, A. Zettl, F. Guinea, A. H. C. Neto and M. F. Crommie, *Science* **2010**, *329*, 544-547.
3. M. Zhou, Y. Zhai and S. Dong, *Anal. Chem.* **2009**, *81*, 5603-5613.
4. C. Shan, H. Yang, J. Song, D. Han, A. Ivaska and L. Niu, *Anal. Chem.* **2009**, *81*, 2378-2382.
5. F. Xia, D. B. Farmer, Y.-m. Lin and P. Avouris, *Nano Lett.* **2010**, *10*, 715-718.
6. L. L. Zhang, R. Zhou and X. S. Zhao, *J. Mater. Chem.* **2010**, *20*, 5983-5992.
7. E. Yoo, J. Kim, E. Hosono, H.-s. Zhou, T. Kudo and I. Honma, *Nano Lett.* **2008**, *8*, 2277-2282.
8. D. R. Kauffman and A. Star, *Analyst* **2010**, *135*, 2790-2797.
9. B. Seger and P. V. Kamat, *J. Phys. Chem. C* **2009**, *113*, 7990-7995.
10. L. Qu, Y. Liu, J.-B. Baek and L. Dai, *ACS nano* **2010**, *4*, 1321-1326.
11. Y. Shao, S. Zhang, C. Wang, Z. Nie, J. Liu, Y. Wang and Y. Lin, *J. Power Sources* **2010**, *195*, 4600-4605.
12. D. Wei, Y. Liu, Y. Wang, H. Zhang, L. Huang and G. Yu, *Nano Lett.* **2009**, *9*, 1752-1758.
13. Z. Jin, J. Yao, C. Kittrell and J. M. Tour, *ACS nano* **2011**, *5*, 4112-4117.
14. Y. Xue, B. Wu, L. Jiang, Y. Guo, L. Huang, J. Chen, J. Tan, D. Geng, B. Luo and W. Hu, *J. Am. Chem. Soc.* **2012**, *134*, 11060-11063.
15. L. S. Panchakarla, K. S. Subrahmanyam, S. K. Saha, A. Govindaraj, H. R. Krishnamurthy, U. V. Waghmare and C. N. R. Rao, *Adv. Mater.* **2009**, *21*, 4726-4730.
16. D. Deng, X. Pan, L. Yu, Y. Cui, Y. Jiang, J. Qi, W.-X. Li, Q. Fu, X. Ma and Q. Xue, *Chem. Mater.* **2011**, *23*, 1188-1193.
17. X. Li, H. Wang, J. T. Robinson, H. Sanchez, G. Diankov and H. Dai, *J. Am. Chem. Soc.* **2009**, *131*, 15939-15944.
18. D. Long, W. Li, L. Ling, J. Miyawaki, I. Mochida and S.-H. Yoon, *Langmuir* **2010**, *26*, 16096-16102.

19. H. M. Jeong, J. W. Lee, W. H. Shin, Y. J. Choi, H. J. Shin, J. K. Kang and J. W. Choi, *Nano Lett.* **2011**, *11*, 2472-2477.
20. Y.-C. Lin, C.-Y. Lin and P.-W. Chiu, *Appl. Phys. Lett.* **2010**, *96*, 133110-133110-3.
21. S. Park, Y. Hu, J. O. Hwang, E.-S. Lee, L. B. Casabianca, W. Cai, J. R. Potts, H.-W. Ha, S. Chen and J. Oh, *Nat. Commun.* **2012**, *3*, 638.
22. Z.-H. Sheng, L. Shao, J.-J. Chen, W.-J. Bao, F.-B. Wang and X.-H. Xia, *ACS nano* **2011**, *5*, 4350-4358.
23. K. Gopalakrishnan, K. Moses, A. Govindaraj and C. N. R. Rao, *Solid State Commun.* **2013**, *175–176*, 43-50.
24. X. Wang, X. Li, L. Zhang, Y. Yoon, P. K. Weber, H. Wang, J. Guo and H. Dai, *Science* **2009**, *324*, 768-771.
25. H. Wang, C. Zhang, Z. Liu, L. Wang, P. Han, H. Xu, K. Zhang, S. Dong, J. Yao and G. Cui, *J. Mater. Chem.* **2011**, *21*, 5430-5434.
26. Y. Xin, J.-g. Liu, X. Jie, W. Liu, F. Liu, Y. Yin, J. Gu and Z. Zou, *Electrochim. Acta* **2012**, *60*, 354-358.
27. B. Jiang, C. Tian, L. Wang, L. Sun, C. Chen, X. Nong, Y. Qiao and H. Fu, *Appl. Surf. Sci.* **2012**, *258*, 3438-3443.
28. B. Xiong, Y. Zhou, R. O'Hayre and Z. Shao, *Appl. Surf. Sci.* **2013**, *266*, 433-439.
29. G. E. Romanos, V. Likodimos, R. R. N. Marques, T. A. Steriotis, S. K. Papageorgiou, J. L. Faria, J. L. Figueiredo, A. n. M. T. Silva and P. Falaras, *J. Phys. Chem. C* **2011**, *115*, 8534-8546.
30. S. R. Kelemen, M. Afeworki, M. L. Gorbaty, P. J. Kwiatek, M. S. Solum, J. Z. Hu and R. J. Pugmire, *Energy Fuels* **2002**, *16*, 1507-1515.
31. R. Pietrzak, *Fuel* **2009**, *88*, 1871-1877.
32. J. E. Huheey, R. L. Keiter and E. A. Keiter, *Inorganic Chemistry, Principles of Structure and Reactivity*. Fourth Edition. ed.; New York, 1993.
33. P. Atkins and J. d. Paula, *Physical Chemistry for the Life Sciences*. Second ed.; Oxford University Press.: Oxford, U. K., 2009.
34. R. G. Mortimer, *Physical Chemistry*. Third ed.; Elsevier Academic Press: Canada, 2008.



35. K.-G. Zhou, N.-N. Mao, H.-X. Wang, Y. Peng and H.-L. Zhang, *Angew. Chem. Int. Ed.* **2011**, *50*, 10839-10842.



*Part IV*

*Borocarbonitrides*

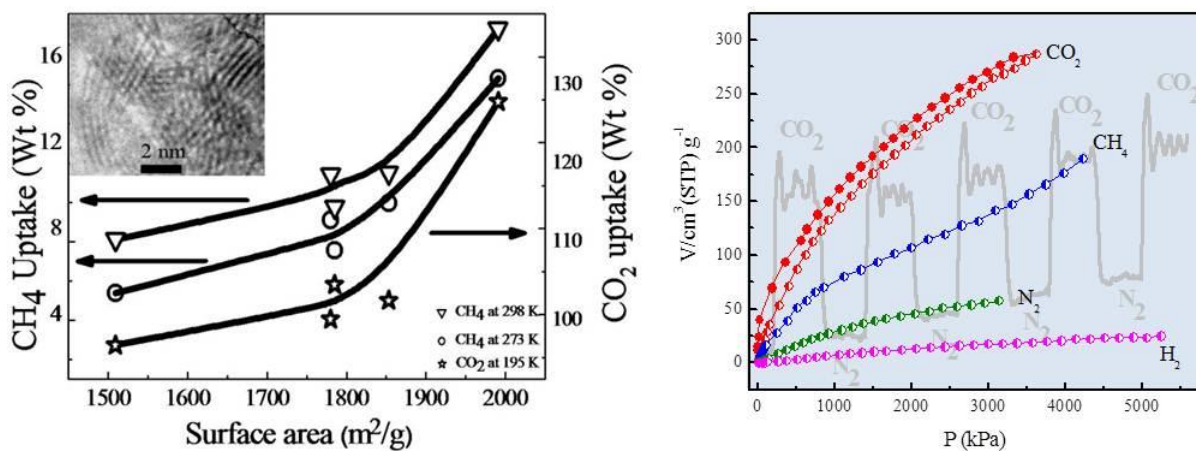


# Chapter IV.1

## Synthesis and gas adsorption studies of high surface area borocarbonitrides\*

### Summary

Borocarbonitrides ( $B_xC_yN_z$ ) prepared using high surface area activated charcoal, urea and boric acid by solid state method exhibit surface areas in the range 1500-1990  $m^2/g$ , with the uptake values of  $CO_2$  and  $CH_4$  being in the ranges 97-128 wt % (at 195 K, 1 atm) and 7.5-17.3 wt % respectively. The uptake of these gases varies exponentially with the surface area of  $B_xC_yN_z$  and the uptake of  $CH_4$  generally varies proportionally with that of  $CO_2$ . The  $CO_2$  uptake in the case of the best  $BC_{1.9}N$  sample was 64 wt % at 298 K. The large uptake of both  $CO_2$  and  $CH_4$  by  $BC_{1.9}N$  bettering the performance of graphenes and activated charcoal, is indeed noteworthy. First-principles calculations show how the adsorption of  $CO_2$  and  $CH_4$  is much more favored on BCN compared to graphene. High surface area borocarbonitrides not only exhibit large uptakes of  $CO_2$  and  $CH_4$  but also good selectivity for  $CO_2$ , the interaction energies with  $CO_2$  and other gases being in the desirable range. The comparison between absorption of  $CO_2$  and  $N_2$  at 293 K and 1 atm shows that  $CO_2$  is more selectively adsorbed than  $N_2$  for a sample of composition  $BC_{1.7}N_{0.6}$ .



\* Papers based on this work have appeared in *ChemSusChem*, 2011 and *J. Mater. Chem. A*, 2013

## 1. Introduction

Apart from water vapor, carbon dioxide and methane are main greenhouse gases. Greenhouse effect refers to the entrapment of heat radiation by infrared absorbing gases, which is in other words difference in energy that escapes to space and the energy emitted from the earth's surface. In the last few decades there has been an unprecedented increase in the CO<sub>2</sub> emission in the atmosphere. Main sources of this increment are deforestation, factory exhausts, vehicular emission *etc.* Role of CO<sub>2</sub> in climate change over other natural variability is a much debated topic. However, some recent studies have suggested increased amount of CO<sub>2</sub> to be an important contributor towards global warming. According to a study, (1) energy related CO<sub>2</sub> emission over a period of 2005-2030 would cause CO<sub>2</sub> emission jump of 57 %, (2) fossil fuel will still be the most important energy source covering 83 % of the total increase in the demand and (3) considering that the policies by governments around the world to stabilize global emissions achieve their goals there would still be an increase of 3 % in average global temperature by 2030. One way to tackle this problem is to convert CO<sub>2</sub> into fuels and various other useful products by chemical reactions also known as chemical fixation. CO<sub>2</sub> has been converted into methanol, formic acid, dimethyl carbonate, methyl formate, higher hydrocarbons, pharmaceutical products *etc.* Another strategy to capture excess CO<sub>2</sub> in the environment is to capture it in porous materials like activated carbon, zeolites, metal-organic frameworks (MOFs) *etc.* by physical adsorption. Recently, varieties of metal-organic frameworks (MOFs) have been studied which can selectively adsorb CO<sub>2</sub> inside the pores. One main advantage of these materials is that the pore size can easily be tuned by proper modifications of linkers. For example, Yaghi *et al.* showed huge CO<sub>2</sub> uptake in MOF-210 which is based on Zn<sub>4</sub>O(CO<sub>2</sub>)<sub>6</sub> units.<sup>1</sup> More recently, polyethyleneimine incorporated MIL-101 which is a chromium based MOF, is tested with an unprecedented CO<sub>2</sub> uptake selectivity of 770 over N<sub>2</sub> at room temperature and 1200 at 50 °C.<sup>2</sup> Despite such outstanding performances, factors like very high cost and poor thermal stability limit the large scale use of MOFs to trap CO<sub>2</sub>. A class of carbon based materials, activated carbon and carbon nanotubes in particular are potential candidates for CO<sub>2</sub> sequestration. There are several reports of CO<sub>2</sub> adsorption on the ammine functionalized carbon nanotubes. Lu and co-workers<sup>3-5</sup> compared the adsorption properties of pure and 3-aminopropyl-triethoxysilane

(APTS) functionalized Multiwalled carbon nanotubes (MWNTs) at a temperature range of 293 to 373 K. They showed an increase of more than 40 % of CO<sub>2</sub> adsorption at 293 K and influent flow of 50 mg/L. They also showed that the adsorption and physiochemical properties of APTS modified MWNT remain preserved even after 100 adsorption-desorption cycles. The water vapor content also influenced the adsorption properties with a maximum adsorption of 2.4 mmol/g at 2.4 % water vapour and 323 K. Dillon *et al.*<sup>6</sup> studied the effect of polyethyleneimine (PEI) functionalization on fluorinated SWNTs (FSWNTs). A maximum adsorption of 9.2 wt % could be achieved at 27 K and 1 atm of CO<sub>2</sub>. Single-walled carbon nanohorns (SWNH) and MWNTs are also explored for CH<sub>4</sub> storage. Bekyarova *et al.*<sup>7</sup> showed that single walled nanohorns (SWNH) with interconnected network structure could store 160 v/v methane at 3.5 MPa and 303 K. Murata *et al.*<sup>8</sup> reported the enhancement of adsorption of methane on SWNH by dispersing lanthanide nitrate on it. By mixed acid treatment, alkali treatment and mechanical shearing, Yulong *et al.*<sup>9</sup> showed that the optimal uptake of methane in MWNTs can be enhanced to a value as high as 11.7 wt % at room temperature and 10.5 MPa. Mishra *et al.*<sup>10</sup> studied adsorption of CO<sub>2</sub> on magnetite decorated graphite nanoflakes prepared by acid intercalation followed by thermal exfoliation. They could see a large enhancement of 90 % in the uptake of CO<sub>2</sub> on decorating graphite nanoflakes with magnetite nanoparticles at 298 K and 11.5 bar. The enhancement was attributed to the chemical interaction of CO<sub>2</sub> with magnetite nanoparticles. Rao *et al.* studied uptake of CO<sub>2</sub> by the graphenes and compared them with that of activated charcoal.<sup>11</sup> Activated charcoal showed 64 wt % uptake of CO<sub>2</sub> at 195 K and 1 atm while uptake of CO<sub>2</sub> by EG at 298 K and 50 bar was 51 %. Uptake values varied between 5 and 45 wt % in the case of graphene samples, with EG exhibiting the highest uptake. EG and RGO samples with relatively high CO<sub>2</sub> uptake capacity contain oxygen functionalities on the surface while HG with relatively clean surface did not show considerable uptake. Graphenes were also studied for CH<sub>4</sub> adsorption where the uptake varied between 0 and 3 wt % at 273 K and 5MPa. EG and RGO with relatively high methane uptakes contain oxygen functionalities on the surface while in the case of HG with little or no uptake of methane, the surface of HG was clean with negligible oxygen functionalities.

## 2. Scope of the present investigation

In view of the earlier studies of few-layer BN exhibiting high surface area and remarkably huge theoretical surface area of graphene, we considered it to be of significance to study the gas adsorption properties of  $B_xC_yN_z$ . The main focus is to achieve bulk amount of  $B_xC_yN_z$  from cheap starting materials. High surface area activated charcoal, urea and boric acid which are used here as starting materials are all readily available at low cost unlike expensive ligands used in the synthesis of MOFs. By employing first-principles calculations we have identified the potential binding sites of  $CO_2$  and  $CH_4$  on  $B_xC_yN_z$ . Considering the importance of separation of gases, we have also compared uptakes of different gases at normal temperature and pressure as well as at high pressure conditions.

## 3. Experimental Section

$B_xC_yN_z$  samples were prepared by the high-temperature reaction of boric acid and urea with high-surface area activated charcoal ( $1250 \text{ m}^2/\text{g}$ ).<sup>12</sup> The ratio of boric acid to urea was varied between 1:6 and 1:24 while keeping the amount of activated charcoal fixed (0.5 g). For BCN-1, BCN-4 and BCN-5 the molar ratio of boric acid to urea was 1:24 (0.1 g  $H_3BO_3$  and 2.4 g urea) while it was 1:12 and 1:6 for BCN-2 and BCN-3 respectively. The aqueous mixture of  $H_3BO_3$ , urea and activated carbon was sonicated for 30 minutes followed by evaporation of water at  $70^\circ\text{C}$  to get viscous slurry. The slurry was transferred to a quartz boat and heated at different temperatures under  $N_2$  flow. To obtain BCN-1 and BCN-2 samples, the mixture was heated at  $900^\circ\text{C}$  for 18 hours. To obtain BCN-3, BCN-4 and BCN-5, the mixture was heated at  $950$ ,  $1000$  and  $900^\circ\text{C}$  respectively for 12 h. The products were cooled to room temperature and subsequently heated in an ammonia atmosphere at  $930^\circ\text{C}$  for 3 hours to obtain black-coloured  $B_xC_yN_z$ . These samples were subjected to elemental analysis and other techniques of characterization.

The morphology of the samples was examined by a transmission electron microscope (TEM) with a Tecnai T20 instrument (FEI) operated at an accelerating voltage of 200 kV. Atomic force microscopy (AFM) measurements were performed using innova atomic force microscope with tapping mode. X-ray photoelectron spectroscopy (XPS) measurements were carried out using an Omicron spectrometer employing  $AlK\alpha$  ( $1486.6 \text{ eV}$ ). Raman spectra



were recorded employing a LabRAM HR with a 633 nm line from a HeNe laser. FTIR spectra were recorded using a Bruker IFS 66v/S spectrometer. Powder XRD patterns of the products were recorded with a Bruker-D8 X-ray diffractometer using Cu K $\alpha$  radiation. Nitrogen adsorption (surface area) measurements and CO<sub>2</sub> uptake experiments were carried out in a Quanta Chrome Autosorb-1 instrument. CH<sub>4</sub> uptake experiments were carried out by using a BELSORP-aqua3 analyzer.

#### 4. Results and discussion

The five B<sub>x</sub>C<sub>y</sub>N<sub>z</sub> samples prepared by us possess graphene-like layered structures. The reactions involved in the formation of B<sub>x</sub>C<sub>y</sub>N<sub>z</sub> by our method of synthesis are given below. The composition of B<sub>x</sub>C<sub>y</sub>N<sub>z</sub> depends on the relative proportion of carbon, but in practice both reactions (3) and (4) may occur simultaneously to different extents. It appears reaction (4) is more predominant than reaction (3) under the conditions of the experiments carried out by us.

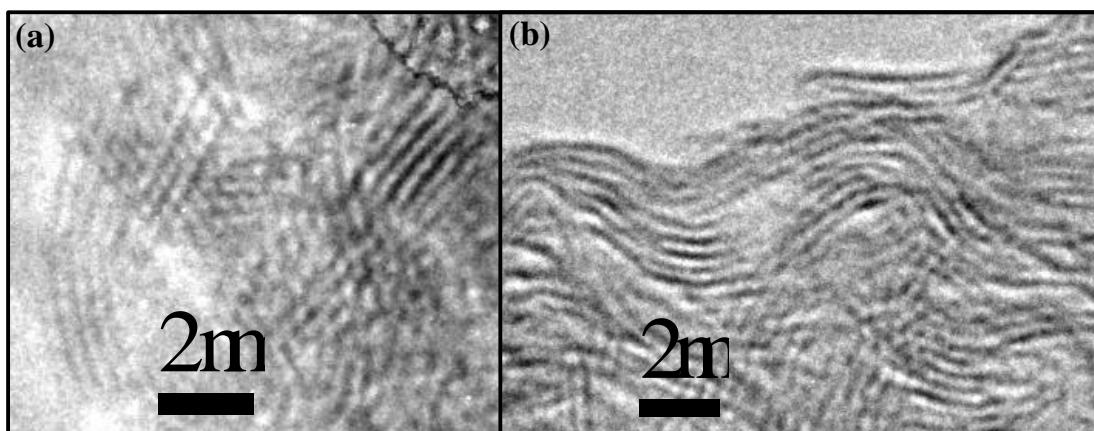
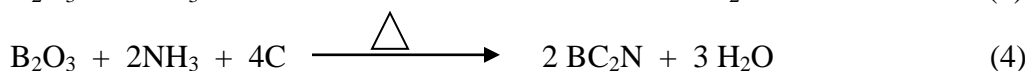
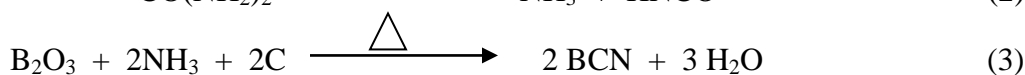
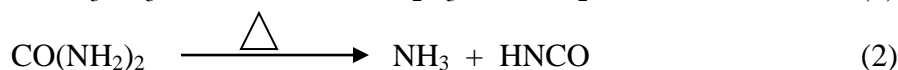
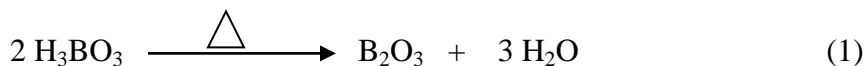


Figure 1 TEM images of BCN-5 and BCN-1

While preparing the slurry it should be noted that the evaporation temperature should be as less as possible so that there is no decomposition of urea in this step. We have carried out the evaporation at 70 °C. The viscous slurry obtained after the evaporation should immediately be transferred to a boat followed by heating in the tube furnace at high temperature. We observe that this step is very important to avoid unreacted products. The starting material should not contain high amount of boric acid which results in unreacted  $B_2O_3$  in the final product. The second heating in ammonia at high temperature is very important. Ammonia decomposes into nitrogen and hydrogen at high temperatures. At 930 °C, hydrogen obtained from decomposition removes amorphous carbon from the final product and a finite vapour pressure of ammonia ensures no loss of nitrogen from the system. Figures 1(a) and (b) show representative high resolution transmission electron microscopic (HRTEM) images of BCN-5 and BCN-1 respectively showing the presence of two to six layers with an interlayer separation of  $\sim 3.42$  Å, a value somewhat higher than in hexagonal BN (3.36 Å) and graphite (3.33 Å). This increase might be due to the presence of some functional groups like OH-group in the material. The observed layers in the TEM images are not flat like their bulk counterparts and such wrinkles in  $B_xC_yN_z$  can give rise to an increase in the interlayer distances.

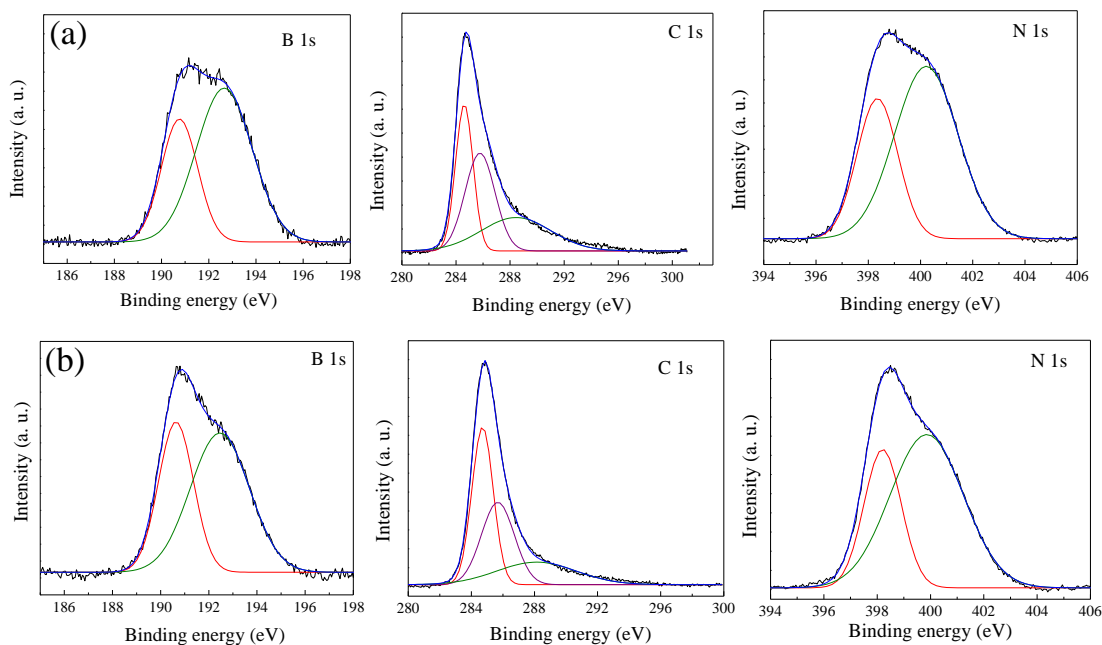
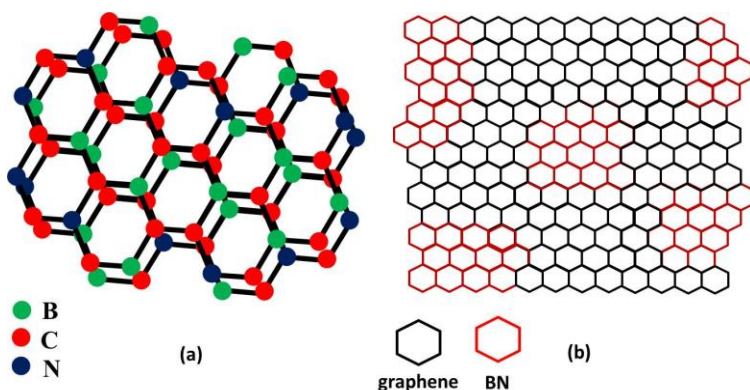


Figure 2 XPS core level spectra of B, C and N of (a) BCN-5 and (b) BCN-1

Compositions of  $B_xC_yN_z$  samples were examined by X-ray photoelectron spectroscopy and we show typical core-level spectra of BCN-5 and BCN-1 in Figures 2(a) and (b) respectively. The 1s spectra of boron, carbon and nitrogen are centred at around 190, 284 and 399 eV respectively.<sup>12-13</sup> We have estimated the compositions of BCN-5 and BCN-1 from the areas under the spectra by taking the capture cross sections into account to be  $BC_{1.9}N$  and  $BC_{1.6}N$  respectively. The B 1s feature of these compositions can be deconvoluted into two peaks arising from the contribution from B-N and B-C bonds. C 1s feature can be deconvoluted into three peaks because of contributions from C-B, C-C and C-N bonds while N1s feature can be deconvoluted into two peaks arising

**Table 1 Binding energies of B, C and N for different bonding considerations obtained from XPS analysis of  $BC_{1.9}N$  and  $BC_{1.6}N$**

	Binding energies (eV)	
	$BC_{1.9}N$	$BC_{1.6}N$
B-C	190.8	190.6
B-N	192.6	192.5
C-B	284.6	284.7
C-C	285.7	285.7
C-N	288.4	288.1
N-B	398.4	398.2
N-C	400.2	399.9



**Figure 3 (a) Schematic of BCN containing (a) random arrangement of B, C and (b) domains of BN and graphene**

from N-B and N-C bonds. Binding energies corresponding to all these contributions are listed in Table 1. XPS analysis thus suggests the presence of different bonding environments of B, C and N atoms and hence the presence of random BCN networks. There might even be some separate domains of BN and graphene present in the system along with these random networks. Both the arrangements, random as well as domains of BN and graphene are shown in Figure 3. Typical AFM images of BCN-5 and BCN-1 along with the height profiles are shown in Figure 4 revealing the presence of 2-3 layers. Our AFM investigation indicates that

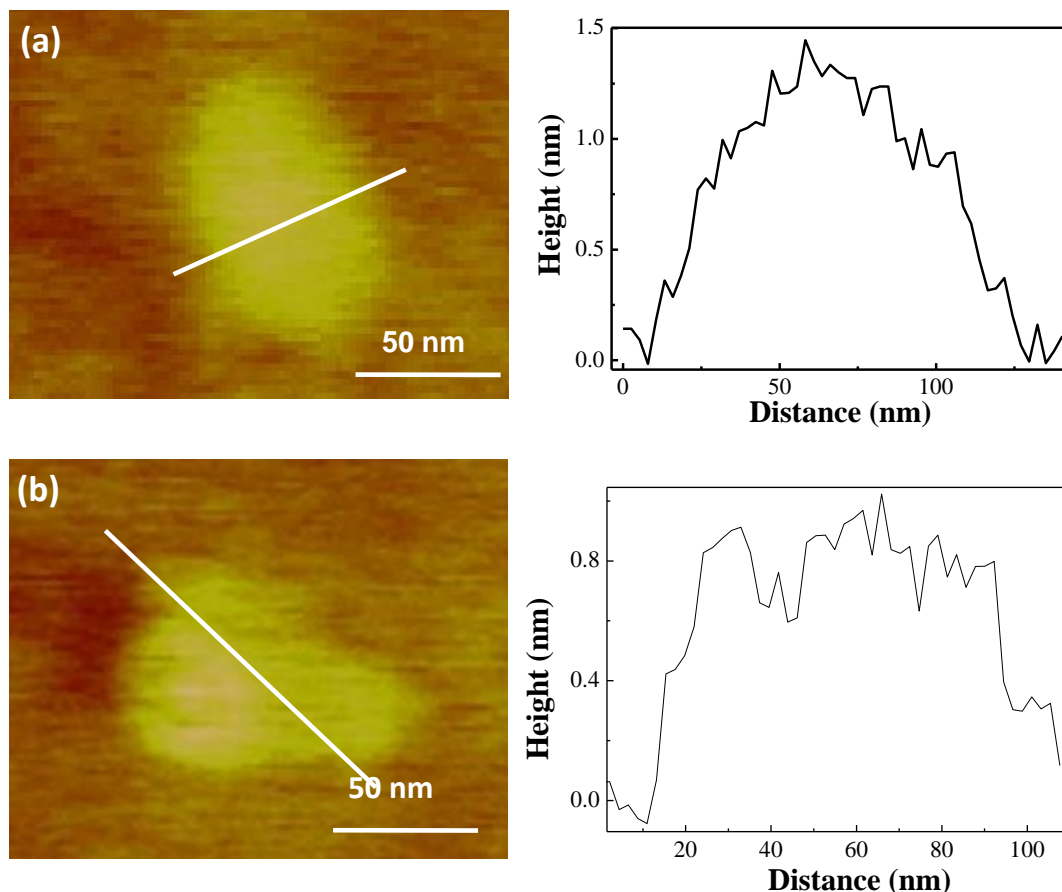


**Figure 4 AFM images of (a) BCN-5 and (b) BCN-1 along with their height profiles**

a majority of  $B_xC_yN_z$  flakes contain 2 to 6 layers as found from HRTEM images as well. Lateral dimensions are in the range of 70-140 nm. We have measured the BET surface areas of the  $B_xC_yN_z$  samples and shown typical  $N_2$  adsorption-desorption isotherms in the case of BCN-5 and BCN-1 at 77 K and 1 atm in Figures 5(a) and (b) respectively. Both the compositions show Type IV isotherm. The most important feature of the Type IV isotherm is its hysteresis loop, which is associated with capillary condensation taking place in mesopores, and the limiting uptake over a range of high  $P/P^\circ$ . The initial part of the Type IV isotherm is attributed to monolayer-multilayer adsorption since it follows the same path as the corresponding part of a Type II isotherm obtained with the given adsorptive on the same surface area of the adsorbent in a non-porous form. BCN-5 and BCN-1 gave the highest and the lowest values of surface area, the actual values being  $1990 \text{ m}^2/\text{g}$  and  $1509 \text{ m}^2/\text{g}$  respectively. Activated charcoal has a surface area of  $1250 \text{ m}^2/\text{g}$ . The BET surface areas of the  $B_xC_yN_z$  samples are listed in Table-2. The values of surface areas reported here are

significantly higher than different types of the graphene samples investigated by us and in the literature.

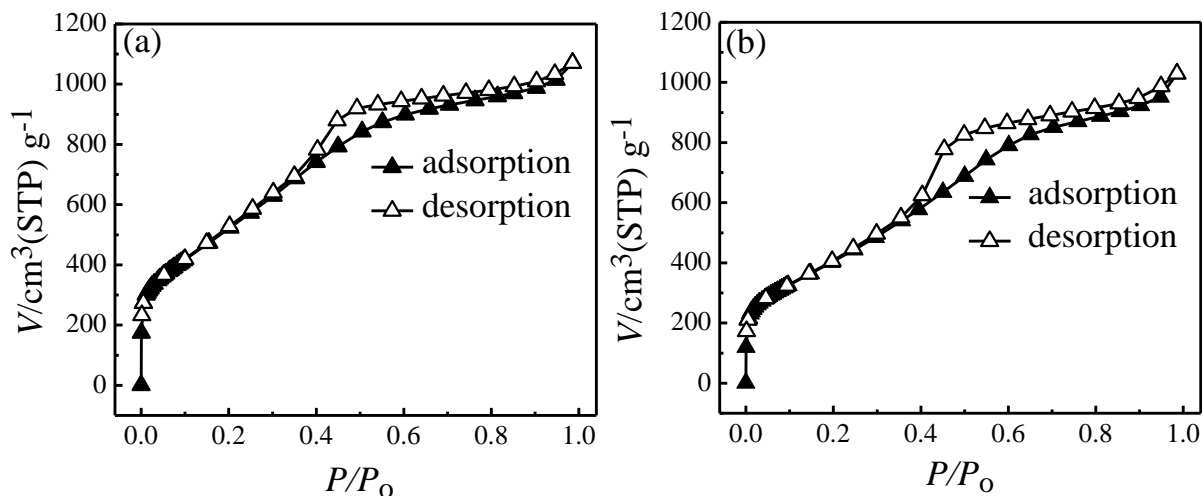


Figure 5 Nitrogen adsorption-desorption isotherms of (a) BCN-5 and (b) BCN-1 at 77 K and 1 atm

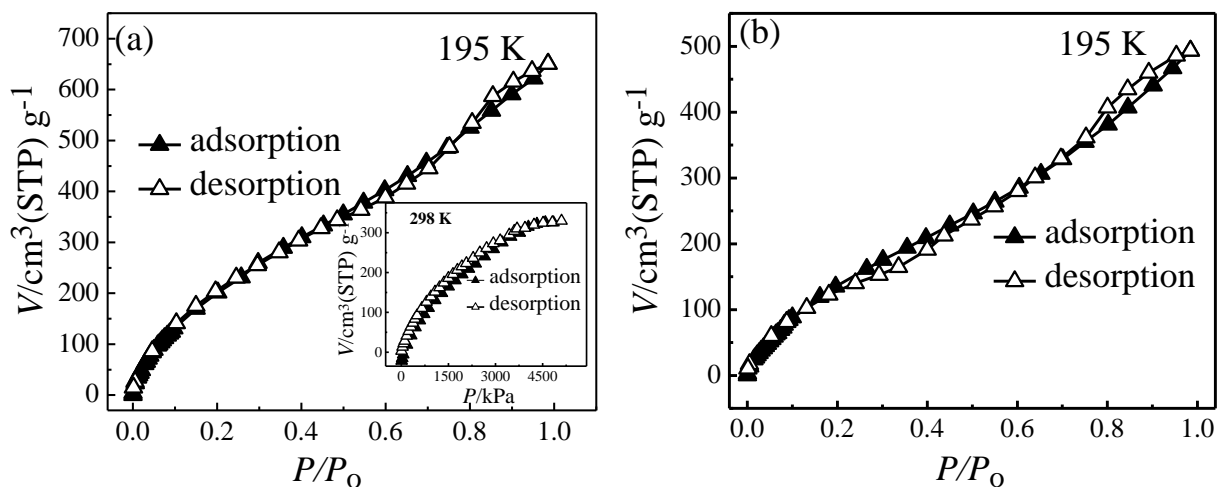


Figure 6 CO<sub>2</sub> adsorption-desorption isotherms (a) BCN-5 and (b) BCN-1 at 195 K and 1 atm. Inset of (a) shows the corresponding isotherms of BCN-5 at 298 K and 5 MPa

The CO<sub>2</sub> uptake of the B<sub>x</sub>C<sub>y</sub>N<sub>z</sub> samples were measured at 195 K and 1 atm. Typical CO<sub>2</sub> adsorption-desorption isotherms for two B<sub>x</sub>C<sub>y</sub>N<sub>z</sub> samples are shown in Figure 6. The highest CO<sub>2</sub> uptake was found in the case of BCN-5 with a value of 127 wt % which also has the highest surface area. Activated charcoal shows 64 wt % uptake of CO<sub>2</sub> at 195 K and 1 atm.

We have also measured the CO<sub>2</sub> uptake at 298 K and 50 bar for BCN-5 and found it to be 64 %. The uptake of 64 % CO<sub>2</sub> at room temperature is truly remarkable.

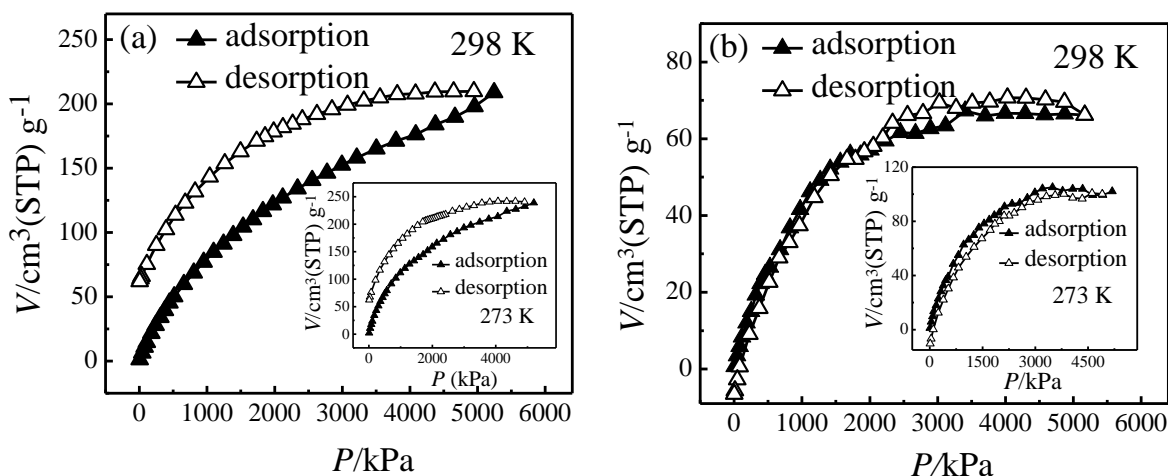
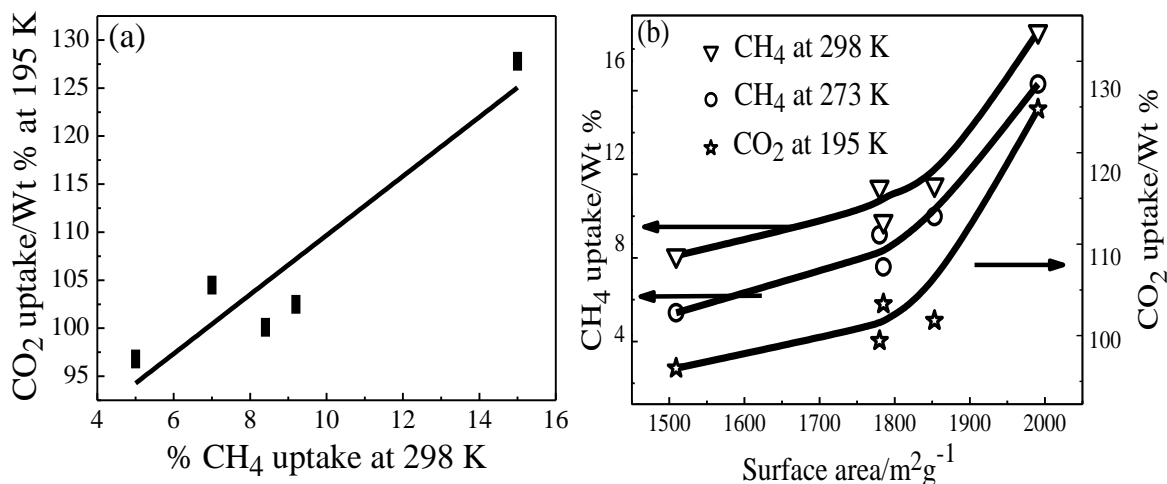


Figure 7 CH<sub>4</sub> adsorption-desorption isotherms (a) BCN-5 and (b) BCN-1 at 298 K and 5 MPa. Insets show corresponding isotherms at 273 K and 5 MPa

Table 2 Surface area, CO<sub>2</sub> and CH<sub>4</sub> uptakes for activated carbon and different BCN samples

Sample	Surface area (m <sup>2</sup> /g)	CO <sub>2</sub> (wt % uptake) 195 K	CH <sub>4</sub> (wt % uptake)	
			273 K	298 K
Activated charcoal	1250	64	6.0	7.0
BCN-1	1509	97	7.5	5.0
BCN-2	1780	100	10.5	8.4
BCN-3	1795	105	9.0	7.0
BCN-4	1853	103	10.6	9.2
BCN-5	1991	128	17.3	15.0

Figure 7 shows typical adsorption data of CH<sub>4</sub> at 298 and 273 K. The CH<sub>4</sub> uptake value varies from 7.5 to 17 % CH<sub>4</sub> at 273 K. At 298 K, it is 5 wt % for BCN-1 and 15 wt % for BCN-5. Uptake of 15 and 17 wt % at 273 and 298 K by BCN-5 is comparable to the highest



**Figure 8(a) Variation of CO<sub>2</sub> uptake in different BCN samples with respect to CH<sub>4</sub> uptake, (b) Variation of uptakes of CO<sub>2</sub> and CH<sub>4</sub> for different BCN samples with respect to surface area**

values of CH<sub>4</sub> uptake reported in the literature.<sup>14-17</sup> The CH<sub>4</sub> uptake varies linearly with the CO<sub>2</sub> (Figure 8(a)). In Figure 8(b), we have shown the variation of the uptake of CO<sub>2</sub> and CH<sub>4</sub> by the B<sub>x</sub>C<sub>y</sub>N<sub>z</sub> samples with the surface area. The uptake of both the gases increases with the surface area. This observation may be taken to indicate that these gases may have specific interaction with high surface area B<sub>x</sub>C<sub>y</sub>N<sub>z</sub> samples, possibly due to the presence of specific structure entities unique for these compositions.

A composition of BC<sub>1.7</sub>N<sub>0.6</sub> with a surface area of 1760 is selected in order to study the selectivity of gas adsorption. We compare the adsorption of CO<sub>2</sub> and N<sub>2</sub> of this compound at 195 K and 1 atm as shown in Figure 9(a). The amount of CO<sub>2</sub> and N<sub>2</sub> adsorbed are 10 wt. % (2.23 mmol/g) and 1.0 wt. % (0.32 mmol/g) respectively. This comparison shows that CO<sub>2</sub> is more selectively adsorbed than N<sub>2</sub> with the ratio of selectivity of CO<sub>2</sub> over N<sub>2</sub> being 10 in terms of weight percentage. We have determined the CO<sub>2</sub> selectivity over CH<sub>4</sub>, N<sub>2</sub> and H<sub>2</sub> at high pressures, this being necessitated by the insignificant adsorption of CH<sub>4</sub> and H<sub>2</sub> at low pressures. In Figure 9(b) we show the adsorption of the different gases at room temperature and high pressures. The uptake of CO<sub>2</sub> is 57 wt. % (13 mmol/g), of CH<sub>4</sub> 14 wt% (8 mmol/g), of N<sub>2</sub> 7 wt. % (3 mmol/g) and of H<sub>2</sub> 2 wt. % (1 mmol/g). The ratio of selectivity of CO<sub>2</sub> over other gases is as follows: CO<sub>2</sub>/H<sub>2</sub> 28:1, CO<sub>2</sub>/N<sub>2</sub> 8:1, CO<sub>2</sub>/CH<sub>4</sub> 4:1.

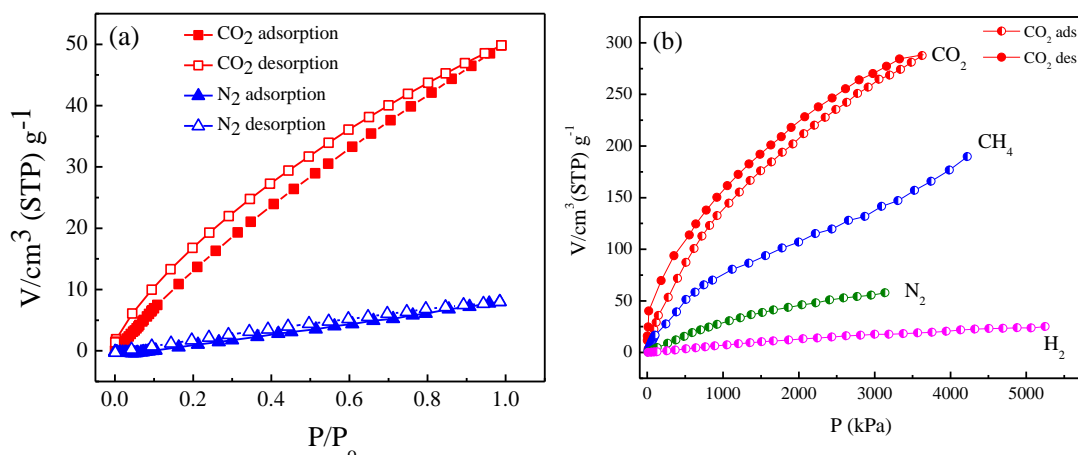


Figure 9(a) Adsorption-desorption isotherms of  $N_2$  and  $CO_2$  at 195 K and 1 atm for BCN sample of surface area  $1760 \text{ m}^2/\text{g}$ , (b) isotherms of different gases at room temperature and high pressures

The isosteric heats of adsorption ( $Q_{st}$ ) for  $CO_2$  for  $BC_{1.7}N_{0.6}$  are obtained by using the Clausius-Clapeyron equation for adsorption isotherm data at 273 and 293 K and 1 atm. As

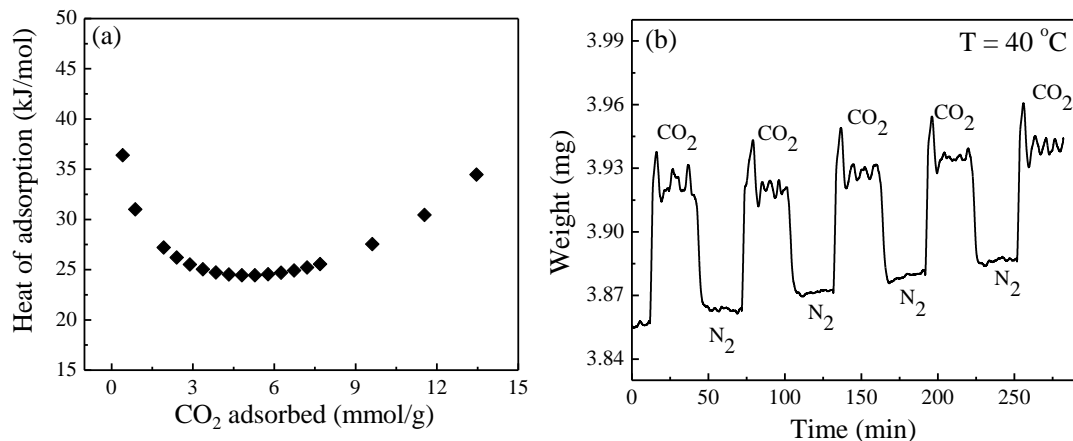


Figure 10(a) Variation of heat of adsorption of  $CO_2$  with respect to amount of  $CO_2$  adsorbed, (b) stepwise variation in weight with alternate exposure to  $N_2$  and  $CO_2$  at room temperature and 1 atm

shown in Figure 10(a), the onset value of  $Q_{st}$  is  $-36.4 \text{ kJ/mol}$  which decreases with increase in  $CO_2$  loading and again reaches a high value. This isosteric heat of adsorption is comparable to that reported in some of the MOFs. Thermogravimetric analysis of  $BC_{1.7}N_{0.6}$  at  $40^\circ\text{C}$  in



alternate N<sub>2</sub> and CO<sub>2</sub> atmospheres is shown in Figure 10(b). This experiment reveals an increase in the weight of BC<sub>1.7</sub>N<sub>0.6</sub> in CO<sub>2</sub> atmosphere and retention of the original weight by switching to N<sub>2</sub> atmosphere. Hence, the cyclability of the material in selective uptake of CO<sub>2</sub> is clearly demonstrated.

Prof. Waghmare and co-workers employed first-principles calculations to understand the interaction of CH<sub>4</sub> and CO<sub>2</sub> with BCN. For CH<sub>4</sub> the following atomic sites in BCN are found to be strongly adsorbing sites: (a) boron bonded with at least one carbon atom which is likely to be a weakly negative ion, (b) hexagonal ring consisting of at least two carbon atoms along with B and nitrogen, and (c) carbon bonded with two boron atoms, which would develop a slightly negative charge to attract the molecule. However, adsorption of CH<sub>4</sub> at the boron-carbon bond is found to be stronger than that at atomic site or pore sites (Figure 11).

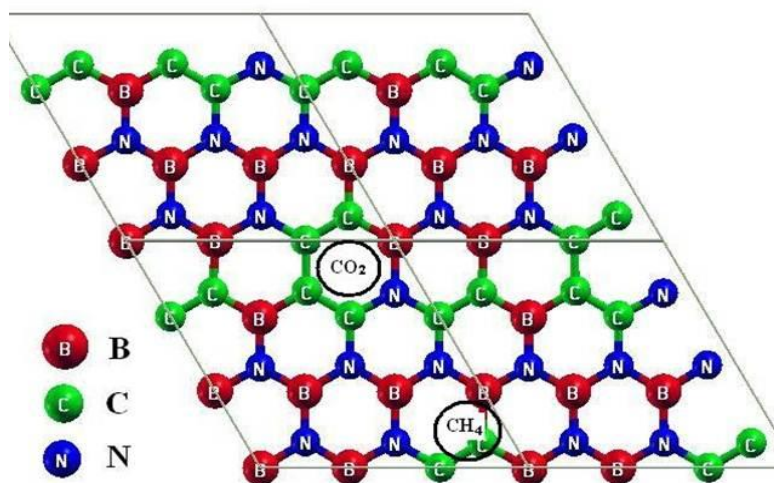


**Figure 11 Preferred sites of adsorption for CO<sub>2</sub> and CH<sub>4</sub>**

The lowest energy configuration, energy of adsorption of CH<sub>4</sub> with 7 wt % on BCN is -2.08 kJ/mol (stronger than -1.97 kJ/mol for graphene). At higher coverage of 13 wt % (two CH<sub>4</sub> molecules per supercell used here), interactions between nearby CH<sub>4</sub> molecules become important. Our estimate of adsorption energy at this coverage on BCN is -2.72 kJ/mol, compared to -2.27 kJ/mol energy of adsorption on graphene.

CO<sub>2</sub> adsorption occurs strongly at the following atomic sites in BCN<sup>12</sup>: (a) nitrogen bonded with at least one carbon atom which is likely to be a weakly negative ion, (b) boron bonded

with one nitrogen atom, and one carbon atom, which would attract negatively charged oxygen of the molecule, and (c) a hexagonal ring with 4 carbon atoms forming the hexagonal ring and a boron and a nitrogen atom (Figure 11).

They estimate an adsorption energy of  $-2.79 \text{ kJmol}^{-1}$  at 20 wt. % coverage and  $\sim 3.67 \text{ kJmol}^{-1}$  at 40 wt. % coverage of  $\text{CO}_2$  on BCN. On graphene it is  $-1 \text{ kJmol}^{-1}$  at 40 wt. % coverage. At 60 wt % coverage the adsorption energy is  $-3.73 \text{ kJmol}^{-1}$  on BCN compared to  $2.04 \text{ kJmol}^{-1}$  for graphene. Furthermore, the distance between  $\text{CO}_2$  molecules and BCN plane is shorter by 3% than in the case of graphene. The distance between  $\text{CO}_2$  molecule and BCN plane at 40 and 60 wt % coverage are 3.74 and 3.89 Å respectively.

## 5. Conclusions

High surface area  $\text{B}_x\text{C}_y\text{N}_z$  are obtained by solid state method wherein boric acid, high surface area activated carbon and urea are mixed and heated in nitrogen and ammonia at high temperatures. The obtained graphene-like  $\text{B}_x\text{C}_y\text{N}_z$  samples show large surface areas and very high uptake of both  $\text{CO}_2$  and  $\text{CH}_4$ . Uptake values of  $\text{CO}_2$  and  $\text{CH}_4$  increase exponentially with the surface area of the  $\text{B}_x\text{C}_y\text{N}_z$  samples.  $\text{CO}_2$  adsorbs selectively over  $\text{N}_2$  in these materials. Isothermic heat of adsorption ( $Q_{st}$ ) of  $\text{CO}_2$  over  $\text{B}_x\text{C}_y\text{N}_z$  surface is found to be  $-36.4 \text{ kJ/mol}$ . In general, the uptake of  $\text{CH}_4$  varies linearly with that of  $\text{CO}_2$ . The experimental results along with our theoretical calculations reveal that the high uptake of  $\text{CO}_2$  and  $\text{CH}_4$  by BCN could arise from the greater surface area which may be related to the weaker rippling strength than graphene and the presence of fewer defects.

## 6. References

1. H. Furukawa, N. Ko, Y. B. Go, N. Aratani, S. B. Choi, E. Choi, A. Ö. Yazaydin, R. Q. Snurr, M. O’Keeffe, J. Kim and O. M. Yaghi, *Science* **2010**, 329, 424-428.
2. Y. Lin, Q. Yan, C. Kong and L. Chen, *Sci. Rep.* **2013**, 3.
3. F. Su, C. Lu, W. Cnen, H. Bai and J. F. Hwang, *Sci. Total Environ.* **2009**, 407, 3017-3023.
4. S.-C. Hsu, C. Lu, F. Su, W. Zeng and W. Chen, *Chem. Eng. Sci.* 65, 1354-1361.
5. F. Su, C. Lu and H.-S. Chen, *Langmuir* 27, 8090-8098.
6. E. P. Dillon, C. A. Crouse and A. R. Barron, *ACS Nano* **2008**, 2, 156-164.
7. E. Bekyarova, K. Murata, M. Yudasaka, D. Kasuya, S. Iijima, H. Tanaka, H. Kahoh and K. Kaneko, *J. Phys. Chem. B* **2003**, 107, 4681-4684.
8. K. Murata, A. Hashimoto, M. Yudasaka, D. Kasuya, K. Kaneko and S. Iijima, *Adv. Mater.* **2004**, 16, 1520-1522.
9. W. Yulong, W. Fei, L. Guohua, N. Guoqing and Y. Mingde, *Mater. Res. Bull.* **2008**, 43, 1431-1439.
10. A. K. Mishra and S. Ramaprabhu, *J. Mater. Chem.* **2011**, 21, 7467-7471.
11. N. Kumar, K. S. Subrahmanyam, P. Chaturbedy, K. Raidongia, A. Govindaraj, K. P. S. S. Hembram, A. K. Mishra, U. V. Waghmare and C. N. R. Rao, *ChemSusChem* **2011**, 4, 1662-1670.
12. K. Raidongia, A. Nag, K. P. S. S. Hembram, U. V. Waghmare, R. Datta and C. N. R. Rao, *Chem. Eur. J.* **2010**, 16, 149-157.
13. S. Y. Kim, J. Park, H. C. Choi, J. P. Ahn, J. Q. Hou and H. S. Kang, *J. Am. Chem. Soc.* **2007**, 129, 1705-1716.
14. M. Eddaoudi, J. Kim, N. Rosi, D. Vodak, J. Wachter, M. O’Keeffe and O. M. Yaghi, *Science* **2002**, 295, 469-472.
15. S. Ma, D. Sun, J. M. Simmons, C. D. Collier, D. Yuan and H.-C. Zhou, *J. Am. Chem. Soc.* **2008**, 130, 1012-1016.
16. H. Wu, W. Zhou and T. Yildirim, *J. Am. Chem. Soc.* **2009**, 131, 4995-5000.
17. H. Wu, J. M. Simmons, Y. Liu, C. M. Brown, X. S. Wang, S. Ma, V. K. Peterson, P. D. Southon, C. J. Kepert and H. C. Zhou, *Chem. Eur. J.* **2010**, 16, 5205-5214.

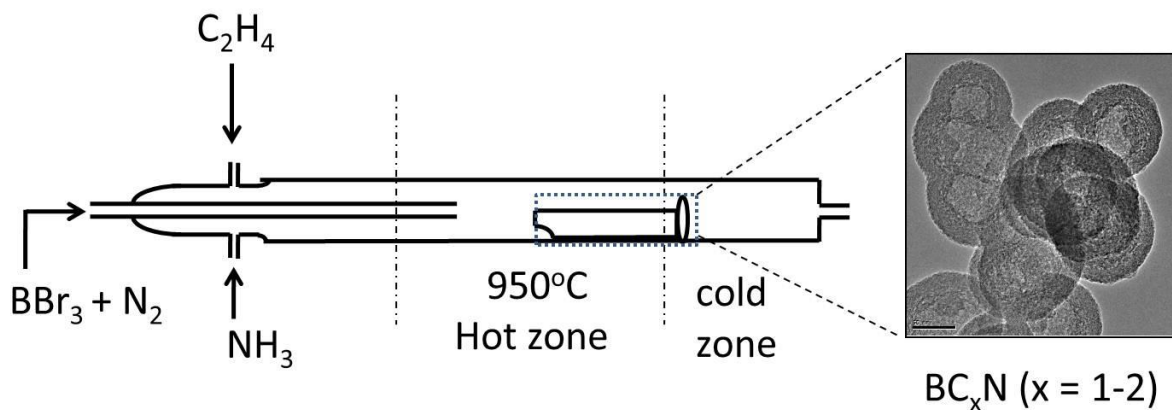


## Chapter IV.2

### Gas phase synthesis of $\text{BC}_x\text{N}$ ( $x = 1-2$ ) and their characterization\*

#### Summary

In order to synthesize borocarbonitrides of the general formula  $\text{BC}_x\text{N}$  where  $x$  varies between 1 and 2, we have carried out high-temperature gas phase reaction of  $\text{BBr}_3$  with a mixture of ethylene and ammonia. The composition of the product is close to  $\text{BC}_{1.6}\text{N}$  as shown by x-ray photon spectroscopy (XPS) and electron energy loss spectroscopy (EELS). The products are further characterized by infra-red, Raman and other spectroscopic techniques. The borocarbonitrides obtained from the gas phase reaction have low surface areas, in contrast to those of similar compositions prepared by the urea method. In line to the surface area, we observe the magnetic properties of the borocarbonitrides prepared by gas phase synthesis to be inferior to that of high surface area borocarbonitride prepared by urea method.



\* A paper based on this work has appeared in *J. Solid State Chem.*, 2011

## 1. Introduction

Emergence of graphene as an exciting two-dimensional material has propelled research on analogous layered inorganic materials. Thus, recently graphene-like MoS<sub>2</sub> and BN have been synthesized and characterized.<sup>1-2</sup> Hexagonal borocarbonitrides of the general formula B<sub>x</sub>C<sub>y</sub>N<sub>z</sub> have attracted interest recently. B<sub>x</sub>C<sub>y</sub>N<sub>z</sub> is expected to possess properties intermediate between graphene and BN which can be tuned by varying the carbon content as well as by changing the structural characteristics.<sup>3-6</sup> There are a few reports on the synthesis of B<sub>x</sub>C<sub>y</sub>N<sub>z</sub> type materials in the form of nanotubes by chemical vapor deposition (CVD), using transition metal nanoparticles as catalysts and also by methods such as arc-discharge and laser ablation.<sup>7-13</sup> Dai *et al.* recently prepared vertically aligned B<sub>0.11</sub>C<sub>0.85</sub>N<sub>0.04</sub> and B<sub>0.26</sub>C<sub>0.57</sub>N<sub>0.17</sub> by CVD method on a Ni-Fe-coated SiO<sub>2</sub>/Si substrate from melamine diborate precursor.<sup>14</sup> Kawaguchi *et al.* synthesized BCN(H) and BC<sub>3</sub>N(H) by CVD using acetonitrile and BCl<sub>3</sub> in hydrogen and nitrogen atmosphere respectively.<sup>15</sup> They also prepared BC<sub>3</sub>N by treating poly(acrylonitrile) powder with BCl<sub>3</sub> at 400 °C followed by heating the product in nitrogen at 1000 °C.<sup>16</sup> Jansen and co-workers<sup>17-18</sup> have synthesized Si-B-N-C ceramics using molecular precursors. There is, however, limited information available on the borocarbonitrides, B<sub>x</sub>C<sub>y</sub>N<sub>z</sub>, with well-defined compositions. Vinu *et al.*<sup>19</sup> reported mesoporous BCN obtained by the reaction of B<sub>2</sub>O<sub>3</sub> and mesoporous carbon at very high temperatures under flowing nitrogen. Dai *et al.* carried out heavy doping of boron and nitrogen in graphene oxide by boric acid and ammonia to obtain various compositions of B<sub>x</sub>C<sub>y</sub>N<sub>z</sub>.<sup>20</sup> Raidongia *et al.*<sup>21</sup> prepared a borocarbonitride of the composition BC<sub>1.5</sub>N<sub>1.1</sub> by heating urea, boric acid and high-surface area activated charcoal in an inert atmosphere. Ci *et al.*<sup>22</sup> synthesized layers of B<sub>x</sub>C<sub>y</sub>N<sub>z</sub> with separated graphene and BN domains by the reaction between NH<sub>3</sub>-BH<sub>3</sub> complex and methane.

## 2. Scope of the present investigation

In view of the marginal success in synthesizing B<sub>x</sub>C<sub>y</sub>N<sub>z</sub> materials and the potential uses of these materials, we have carried out vapor phase synthesis of B<sub>x</sub>C<sub>y</sub>N<sub>z</sub> by taking BBr<sub>3</sub>, ethylene and ammonia as the sources of boron, carbon and nitrogen respectively. Our interest has been to synthesize borocarbonitrides with compositions in the vicinity of BCN or BC<sub>2</sub>N.

A vapor phase synthesis of BCN was carried out by Kaner *et al.*<sup>23</sup> some years ago by the reaction of acetylene, BCl<sub>3</sub> and NH<sub>3</sub>. These authors could not characterize the product adequately. We have prepared BC<sub>x</sub>N (x = 1-2) compositions by the gas phase reaction of ethylene, BBr<sub>3</sub> and NH<sub>3</sub> and compared their characteristics with those of similar compositions obtained by the reaction of activated carbon, boric acid and urea.

### 3. Experimental section

Gas phase synthesis of composition BC<sub>x</sub>N was carried out by using liquid BBr<sub>3</sub>, high purity ammonia gas and 20 % ethylene gas mixed with nitrogen as the sources of boron, nitrogen and carbon respectively. The experimental set up for the reaction is shown in Figure 1. In this set-up, nitrogen gas which acts as the carrier gas bubbles through liquid BBr<sub>3</sub> and carries its vapor into the hot zone of the tube furnace. In the hot zone, BBr<sub>3</sub> reacts with the mixture of ammonia and ethylene gas coming from the other two inlets. A quartz boat present in the hot zone was used to collect the deposited product. At the end of the boat, we keep a circular glass slide in order to keep the gaseous reactants in the hot zone. Before starting the reaction, the quartz tube was purged with ammonia for 30 minutes. The furnace temperature was set to 950 °C at the rate of 7 °C/min. When the temperature reached to 850 °C, nitrogen gas was allowed to bubble through the liquid BBr<sub>3</sub> and the flow of ethylene also started at this temperature. The furnace was maintained at 950 °C for 1 hour with the reactants. The supply of BBr<sub>3</sub> and ethylene was stopped, but the ammonia gas flow was continued till the furnace attained room temperature. The product deposited in the quartz boat was heated at 750 °C in an inert atmosphere for 5 hours in order to remove traces of NH<sub>4</sub>Br in the product.

X-ray diffraction of the samples was carried out by Bruker-D8 X-ray diffractometer using Cu K $\alpha$  radiation. FESEM images were obtained using FEI Nova-Nano SEM-600, Netherlands. TEM and HRTEM analysis were carried out by FEI TITAN3 80-300 kV aberration corrected transmission electron microscope. Quantification of the electron energy loss spectra (EELS) was possible with a Gun monochromator (resolution better than 0.3 eV), camera length 73 mm and GIF aperture 1 mm, which gives collection angle ~ 3.336 mrad. AFM measurements

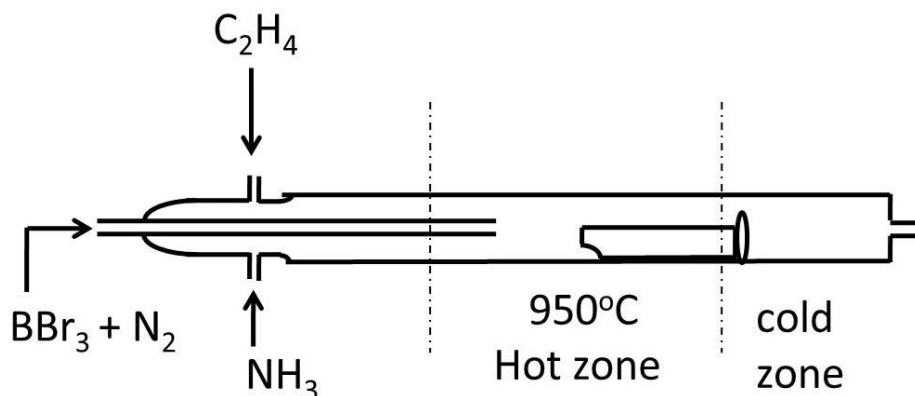


Figure 1 Experimental setup for the gas phase synthesis of borocarbonitride

were performed using NanoMan instrument in the tapping mode. XPS was performed in ESCALAB MKIV spectrometer employing Al K $\alpha$  (1486.6 eV) as photon source. IR spectra were recorded by a Bruker IFS 66v/S spectrometer. Raman spectroscopy was carried out in a LabRAM HR with a 633 nm line from a HeNe laser. TGA was performed in Mettler Toledo Star system. Nitrogen adsorption-desorption measurements were carried out in a QUANTACHROME AUTOSORB-1C instrument.

#### 4. Results and discussion

For the gas phase synthesis of BC<sub>x</sub>N, we have employed the reaction of BBr<sub>3</sub> with a mixture of CH<sub>4</sub> and NH<sub>3</sub> at high temperatures. The product of the reaction was analyzed by x-ray photoelectron spectroscopy (XPS) to determine the elemental composition. We show typical

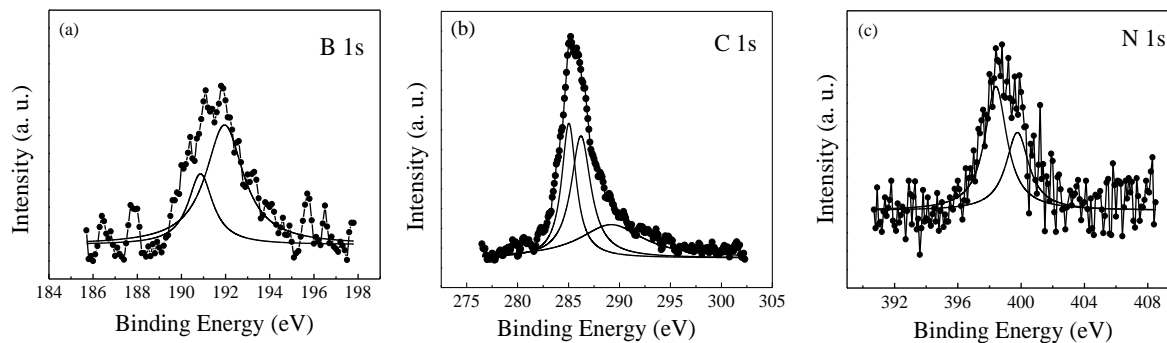
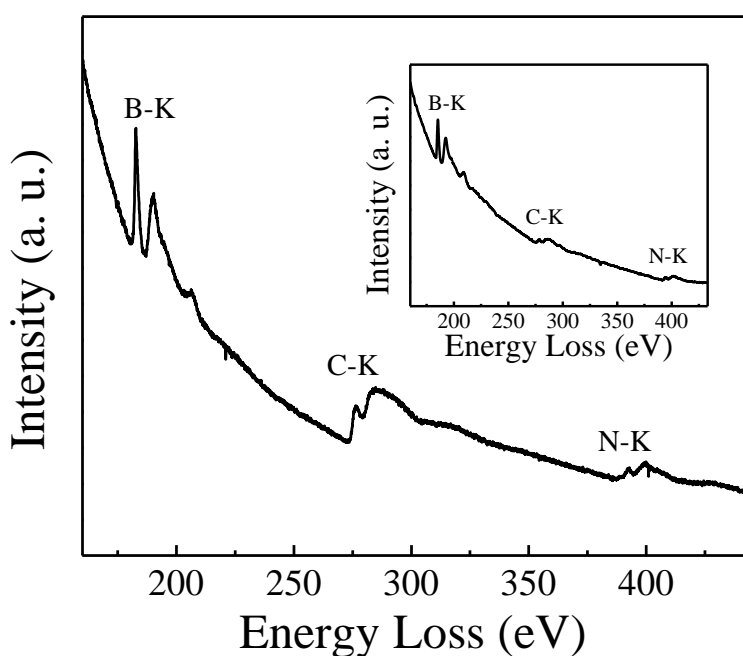


Figure 2 XP core-level spectra of (a) B, (b) C and (c) N of borocarbonitride by gas phase synthesis



core-level spectra of B, C and N in Figure 2, with peaks centred at 191.5, 284 and 399 eV respectively. The B 1s signal can be deconvoluted into two peaks at 190.5 and 192 eV corresponding to boron atoms bonded to carbon and nitrogen respectively. The C 1s signal can be deconvoluted to three peaks centred at ~ 284, 286 and 290 eV corresponding to carbon atoms bonded to boron, carbon and nitrogen respectively. The N 1s signal can be deconvoluted into two peaks at 397.5 and 400 eV corresponding to nitrogen atoms bonded to boron and carbon respectively. From the areas under the 1s features, we obtained the elemental composition B:C:N to be 1:1.6:1 after taking the relevant capture cross sections

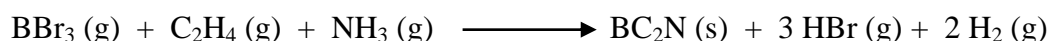
into account.



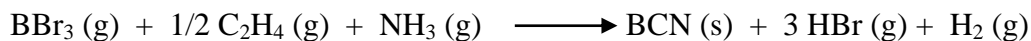
**Figure 3 EELS of a sample of composition BC<sub>1.6</sub>N. The inset shows the corresponding spectrum for a different region of the same sample with composition BCN**

In order to ensure the compositions of the B<sub>x</sub>C<sub>y</sub>N<sub>z</sub> products obtained by the gas phase reaction, electron energy loss spectroscopy (EELS) was carried out in several regions of the sample. In Figure 3, we show the spectrum of one of the samples showing K shell ionization edges. The EELS peaks are split into two peaks corresponding to the  $\pi^*$  and  $\sigma^*$  bands showing

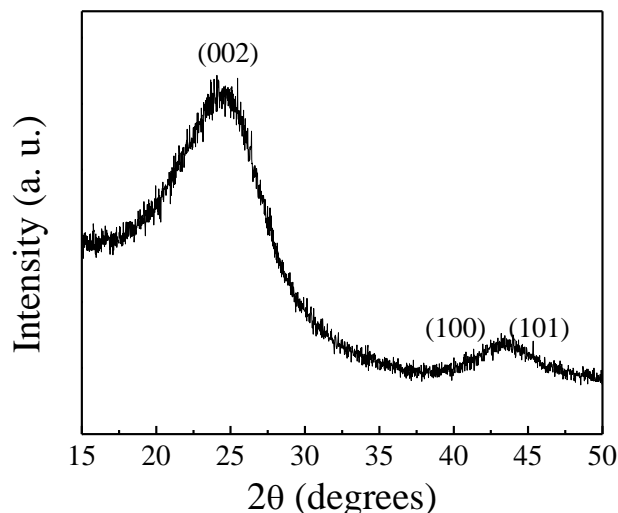
thereby that boron, carbon and nitrogen atoms are all in the sp<sup>2</sup> hybridized state. Based on the EELS data, the composition was estimated to be B:C:N as 1:2:1. Some regions of the samples gave compositions close to 1:1:1. A spectrum corresponding to this composition is shown in the inset of Figure 3. The composition obtained by XPS corresponding more to an average composition is between the above two compositions obtained by EELS. If we take the composition of the product to be BC<sub>2</sub>N, we can write the reaction for the formation as,



If we take the composition as BCN, the reaction will be,

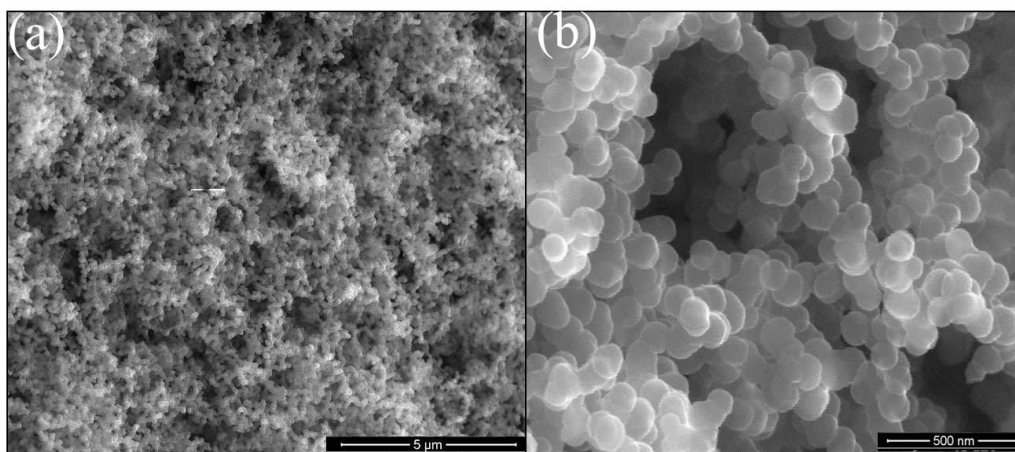


For purpose of convenience we shall describe the product as BCN in the remaining of the chapter.



**Figure 4 XRD pattern of BC<sub>2</sub>N sample prepared by gas phase reaction**

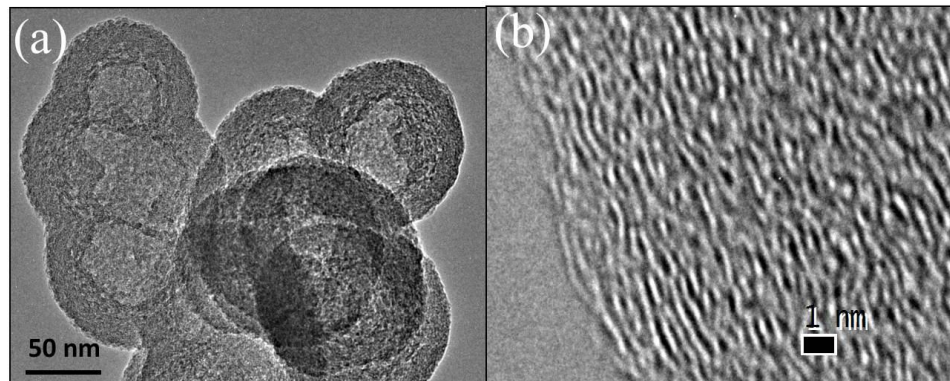
BCN obtained from the gas phase reaction gives a broad x-ray diffraction (XRD) pattern as shown in Figure 4. The (002) and (100) reflections respectively correspond to the interlayer separation and the in-plane parameter of hexagonal structure. The (002) peak is at a slightly lower  $2\theta$  value than bulk BN indicating a larger interlayer separation. From the broadening of the (100) peak, we estimate the average particle size to be  $\sim 30$  nm.



**Figure 5 FESEM images of the samples prepared by gas phase reaction**

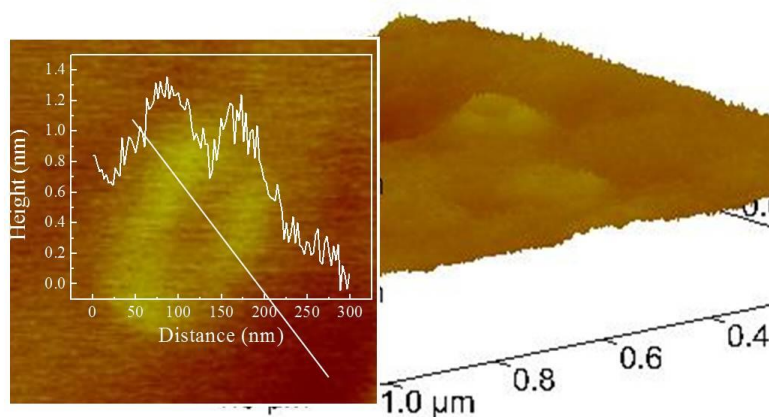
In Figure 5, we show field emission scanning electron microscope (FESEM) images of BCN showing spherical shaped particles with an average diameter of 100 nm. A transmission

electron microscope (TEM) image of BCN is shown in Figure 6. We see that the real shape of the BCN particles corresponds to that of nanopans with inner and outer diameters of approximately 50 and 100 nm respectively. The high-resolution TEM (HRTEM) image in



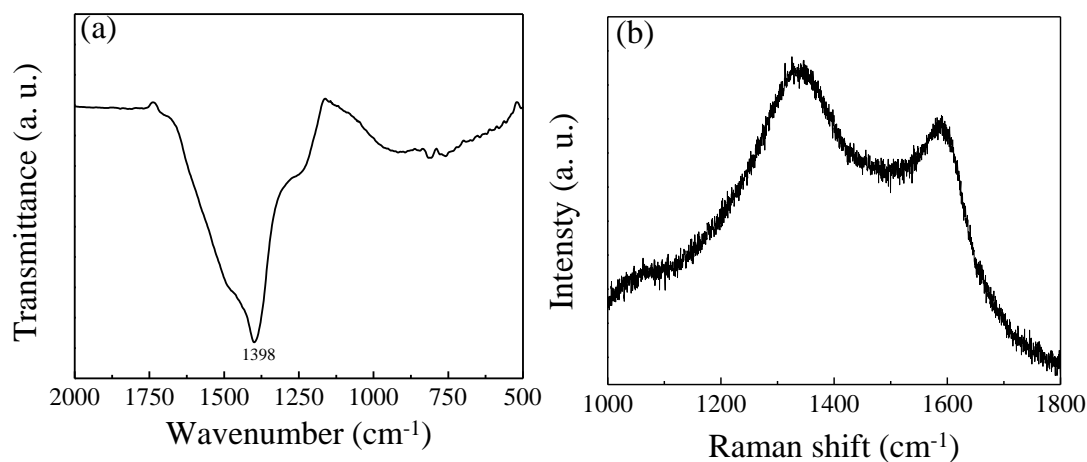
**Figure 6** TEM image of BC<sub>2</sub>N prepared by gas phase reaction. (b) HRTEM of the corresponding sample

Figure 6(b) at the rim of the particle shows presence of layers. The interlayer separation is  $\sim 3.4 \text{ \AA}$  which is slightly larger than in hexagonal BN. In Figure 7, we show an atomic force microscope (AFM) image of one of the nanopans along with the height profile. It shows a dip at the centre as expected of a pan, the thickness of the central region corresponds to a monolayer. The rim portion shows a height of  $\sim 7 \text{ \AA}$  corresponding to two layers of BCN. We do not fully understand the mechanism of the formation of round shape nanoparticles in



**Figure 7** AFM image of a BC<sub>2</sub>N nano-pan prepared by gas phase reaction along with the height profile

our synthesis. However, curling of the basal planes is observed in the past in graphite-like structures.<sup>24-26</sup> Curling occurs in the carbon systems due to the formation of five-member rings but in BN, because five member ring requires B-B and N-N bonds, four member rings may be involved in curling.<sup>26</sup> In the compositions obtained by us curling might happen due to combined effect of both. The infra-red spectrum of BCN in Figure 8(a) shows a band around  $1400\text{ cm}^{-1}$  due to the in-plane bond stretching. A broad peak centred around  $750\text{ cm}^{-1}$  may correspond to the out of plane bending mode. The Raman spectrum of BCN in Figure 8(b)



**Figure 8 (a) IR and (b) Raman spectra of borocarbonitride prepared by gas phase reaction**

shows bands at  $1300$  and  $1600\text{ cm}^{-1}$ , the latter being similar to the G band of  $\text{sp}^2$  carbon systems.

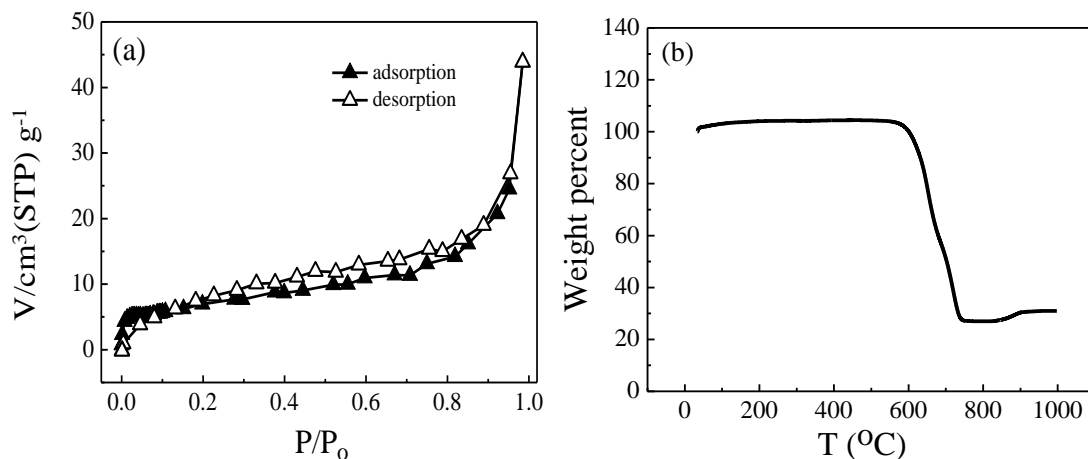


**Figure 9(a) Nitrogen adsorption-desorption isotherms of BCN at 77 K and 1 atm, (b) TGA curve of BCN in oxygen atmosphere**

Nitrogen adsorption-desorption curves of BCN are shown in Figure 9(a). It shows a *Type-II* behavior typical of nonporous or macroporous adsorbents. It has a limited nitrogen uptake with a BET surface area of 25 m<sup>2</sup>/g. Thermogravimetric analysis (TGA) of BCN shows it to have a slightly higher thermal stability than graphene or activated charcoal (Figure 9(b)). In Chapter III.2 we have shown that RGO has an onset of decomposition at 420 °C. BCN decomposes fully at ~ 740 °C in air compared to activated charcoal which decomposes at 690 °C. Greater stability of BCN than graphene supports the fact that it consists of random network of B, C and N atoms rather than containing domains of graphene and BN.

Graphene shows magnetic hysteresis at room temperature. Such high temperature ferromagnetism in graphene and in many inorganic nanomaterials<sup>27-28</sup> has been of much interest in the last few years. Several investigations of graphene have shown that magnetism

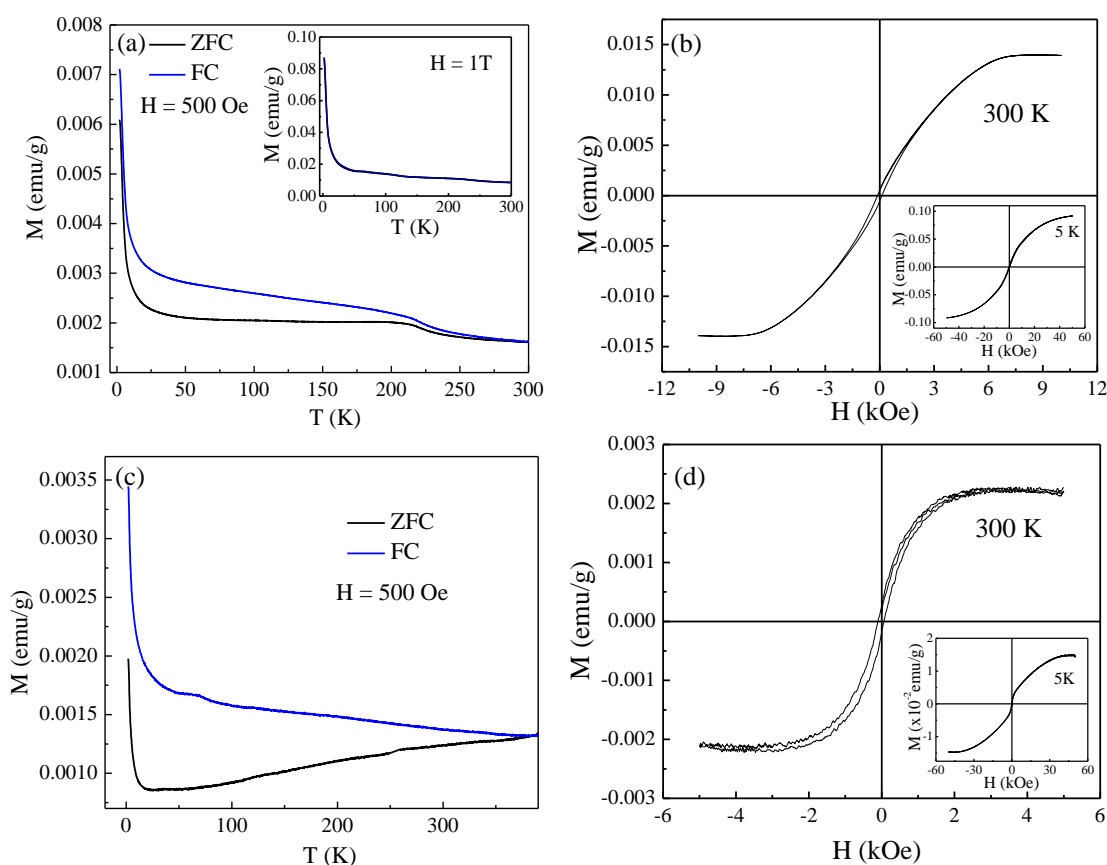


**Figure 10 (a) ZFC-FC magnetization curves for high surface area borocarbonitride (BC<sub>1.9</sub>N) at 500 Oe with the inset showing the same at 1 T. (b) Room temperature magnetic hysteresis loop of BC<sub>1.9</sub>N; inset shows the loop at 5 K. (c) ZFC-FC magnetization curves of gas synthesized borocarbonitride at 500 Oe. (d) Room temperature hysteresis with inset showing hysteresis at 5 K.**

is not due to impurities. Thus, interaction with electron donor and acceptor molecules as well as hydrogenation, affect the magnetic properties. Graphene-like BN sheets exhibit magnetic hysteresis with the saturation magnetization increasing with the decreasing number of layers.<sup>28</sup> It would, therefore, be not surprising to find room-temperature ferromagnetism in borocarbonitrides. We have studied magnetic properties of a borocarbonitride with the composition BC<sub>1.9</sub>N prepared by urea route with a BET surface area of 1990 m<sup>2</sup>/g. Figure 10(a) shows magnetization data under zero field cooled (ZFC) and field cooled conditions (FC) at 500 Oe. The data clearly show divergence between the ZFC and FC curves up to room temperature. The curves overlap at a higher field of 1 tesla as shown in the inset of Figure 10(a). The behavior resembles that of magnetically frustrated systems. Room temperature hysteresis data in Figure 10(b) give saturation magnetization (M<sub>S</sub>) of 0.014 emu/g and a coercive field (H<sub>c</sub>) of ~ 120 Oe. The inset of Figure 10(b) shows the hysteresis loop at 5 K with M<sub>S</sub> and H<sub>c</sub> values of 0.092 emu/g and 300 Oe respectively. Borocarbonitride prepared by the gas phase route with composition BC<sub>1.6</sub>N also shows similar behavior with a lower magnetization. The ZFC and ZF curves of the same at 500 Oe are shown in Figure 10(c). Divergence between the two curves prevails until 390 K. The room temperature hysteresis loop (Figure 10(d)) gives a M<sub>S</sub> of 2.2 x 10<sup>-3</sup> emu/g and a H<sub>c</sub> of 65 Oe. The inset of Figure 10(d) shows the hysteresis loop at 5 K.

## 5. Conclusions

We obtain BC<sub>x</sub>N (x = 1-2) by gas phase reaction of BBr<sub>3</sub>, methane and NH<sub>3</sub> at 950 °C. XPS and EELS spectroscopy reveal an average composition of BC<sub>1.6</sub>N. By FESEM, TEM and AFM images we observe pan-like morphology of BC<sub>1.6</sub>N. XRD and TEM analysis confirm layered structure. It shows characteristic bands in Raman and IR spectra. It has a very low BET surface area (25 m<sup>2</sup>/g) with nonporous *Type II* isotherms. TGA analysis indicates towards a random arrangement of B, C and N atoms in individual layers. It exhibits defect related ferromagnetism at room temperature.

## 6. References

1. H. S. S. Ramakrishna Matte, A. Gomathi, A. K. Manna, D. J. Late, R. Datta, S. K. Pati and C. N. R. Rao, *Angew. Chem. Int. Ed.* 2010, *49*, 4059-4062.
2. A. Nag, K. Raidongia, K. P. S. S. Hembram, R. Datta, U. V. Waghmare and C. N. R. Rao, *ACS nano* 2010, *4*, 1539-1544.
3. S. Y. Kim, J. Park, H. C. Choi, J. P. Ahn, J. Q. Hou and H. S. Kang, *J. Am. Chem. Soc.* 2007, *129*, 1705-1716.
4. L.-W. Yin, Y. Bando, D. Golberg, A. Gloter, M.-S. Li, X. Yuan and T. Sekiguchi, *J. Am. Chem. Soc.* 2005, *127*, 16354-16355.
5. M. O. Watanabe, S. Itoh, T. Sasaki and K. Mizushima, *Phys. Rev. Lett.* 1996, *77*, 187.
6. Y. Chen, J. C. Barnard, R. E. Palmer, M. O. Watanabe and T. Sasaki, *Phys. Rev. Lett.* 1999, *83*, 2406.
7. W. L. Wang, X. D. Bai, K. H. Liu, Z. Xu, D. Golberg, Y. Bando and E. G. Wang, *J. Am. Chem. Soc.* 2006, *128*, 6530-6531.
8. R. Ma, D. Golberg, Y. Bando and T. Sasaki, *Philosophical Transactions of the Royal Society of London. Series A: Mathematical, Physical and Engineering Sciences* 2004, *362*, 2161-2186.
9. R. Sen, B. C. Satishkumar, A. Govindaraj, K. R. Harikumar, G. Raina, J.-P. Zhang, A. K. Cheetham and C. N. R. Rao, *Chem. Phys. Lett.* 1998, *287*, 671-676.
10. O. Stephan, P. M. Ajayan, C. Colliex, P. Redlich, J. M. Lambert, P. Bernier and P. Lefin, *Science* 1994, *266*, 1683-1685.
11. Z. Weng-Sieh, K. Cherrey, N. G. Chopra, X. Blase, Y. Miyamoto, A. Rubio, M. L. Cohen, S. G. Louie, A. Zettl and R. Gronsky, *Phys. Rev. B* 1995, *51*, 11229.
12. P. Redlich, J. Loeffler, P. M. Ajayan, J. Bill, F. Aldinger and M. Rühle, *Chem. Phys. Lett.* 1996, *260*, 465-470.
13. M. Terrones, N. Grobert and H. Terrones, *Carbon* 2002, *40*, 1665-1684.
14. E. Iyyamperumal, S. Wang and L. Dai, *ACS nano* 2012, *6*, 5259-5265.
15. M. Kawaguchi, T. Kawashima and T. Nakajima, *Chem. Mater.* 1996, *8*, 1197-1201.
16. M. Kawaguchi and T. Kawashima, *J. Chem. Soc., Chem. Commun.* 1993, 1133-1134.
17. H. P. Baldus and M. Jansen, *Angew. Chem. Int. Ed.* 1997, *36*, 328-343.

18. L. van Wüllen and M. Jansen, *Solid State Nucl. Magn. Reson.* 2005, 27, 90-98.
19. A. Vinu, M. Terrones, D. Golberg, S. Hishita, K. Ariga and T. Mori, *Chem. Mater.* 2005, 17, 5887-5890.
20. S. Wang, L. Zhang, Z. Xia, A. Roy, D. W. Chang, J. B. Baek and L. Dai, *Angew. Chem. Int. Ed.* 2012, 51, 4209-4212.
21. K. Raidongia, A. Nag, K. P. S. S. Hembram, U. V. Waghmare, R. Datta and C. N. R. Rao, *Chem. Eur. J.* 2010, 16, 149-157.
22. L. Ci, L. Song, C. Jin, D. Jariwala, D. Wu, Y. Li, A. Srivastava, Z. F. Wang, K. Storr and L. Balicas, *Nature Materials* 2010, 9, 430-435.
23. R. B. Kaner, J. Kouvetakis, C. E. Warble, M. L. Sattler and N. Bartlett, *Mater. Res. Bull.* 1987, 22, 399-404.
24. F. Banhart, M. Zwanger and H.-J. Muhr, *Chem. Phys. Lett.* 1994, 231, 98-104.
25. O. Stephan, Y. Bando, A. Loiseau, F. Willaime, N. Shramchenko, T. Tamiya and T. Sato, *Applied Physics A: Materials Science & Processing* 1998, 67, 107-111.
26. F. Xu, Y. Xie, X. Zhang, S. Zhang, X. Liu and X. Tian, *Inorg. Chem.* 2004, 43, 822-829.
27. A. Sundaresan and C. N. R. Rao, *Nano Today* 2009, 4, 96-106.
28. C. N. R. Rao, H. S. S. R. Matte, K. S. Subrahmanyam and U. Maitra, *Chem. Sci.* 2012, 3, 45-52.



*Part V*

*Other studies*

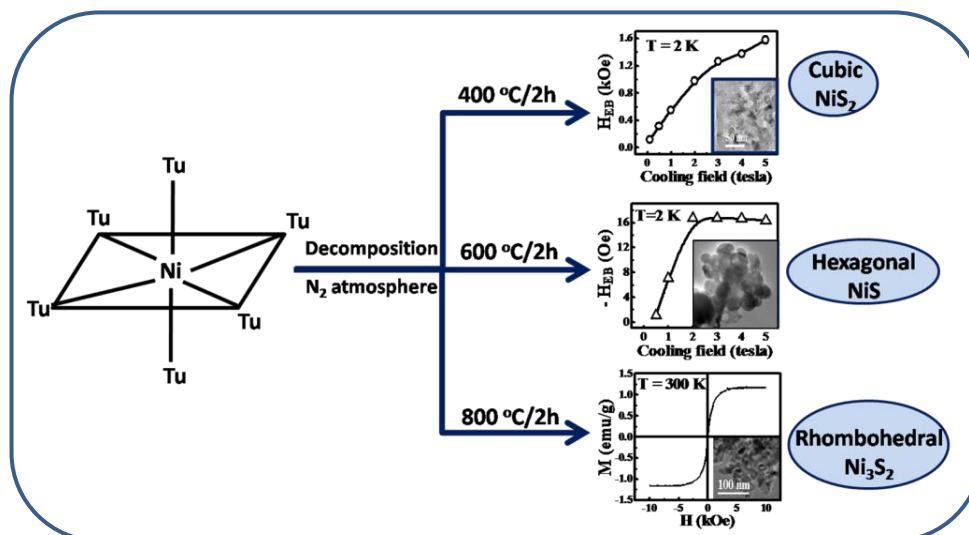


# Chapter V.1

## Temperature evolution of nickel sulphide phases: Their electrical and magnetic properties\*

### Summary

Considering the very complex phase diagram of nickel sulphide, it is quite challenging to stabilize pure phases from single precursor. Here, we obtain nanoparticles of various phases of nickel sulphide by decomposing nickel-thiourea complex at different temperatures. The first phase in the evolution is the one with the maximum sulphur content, namely, NiS<sub>2</sub> nanoparticles obtained at 400 °C. As the temperature is increased, nanoparticles of phases with lesser sulphur content, NiS (600 °C) and Ni<sub>3</sub>S<sub>2</sub> (800 °C) are formed. NiS<sub>2</sub> nanoparticles exhibit weak ferromagnetic transition at 30 K and show a large exchange bias at 2 K. NiS nanoparticles are antiferromagnetic and show relatively smaller exchange bias effect. On the other hand, Ni<sub>3</sub>S<sub>2</sub> nanoparticles exhibit very weak temperature dependent magnetization. Electrical measurements showed that both NiS<sub>2</sub> and NiS are semiconductors whereas Ni<sub>3</sub>S<sub>2</sub> is a metal. The present synthesis method can also be extended to other sulphides, for example, CoS<sub>2</sub> nanoparticles.



\* A paper based on this work has appeared in *J. Solid State Chem.*, 2013

## 1. Introduction

Diverse magnetic and electrical properties of transition metal sulphides make them one of the most desired compounds to study apart from oxides. One of the remarkable properties is the recently discovered superconductivity in several iron chalcogenides.<sup>2</sup> The difference in transport properties compared to their oxide counterparts arises due to the covalent character of metal to sulphur bond which affects the electronic properties of these materials.<sup>3</sup> Transition metal sulphides provide an opportunity to study the effect of covalency on the electronic structure, electrical transport and magnetic properties which is otherwise not possible in corresponding halides and in some sense oxides. As discussed by Rao *et al.*, the greater covalency screens the Coulomb interaction between the electrons and the nuclear charge of the transition metal. This results in smaller electrostatic energy,  $U$ , which means that lesser transfer energy is required for the formation of itinerant electrons. Some of the other differences between oxides and sulphides which are also related to the above mentioned covalency are:<sup>3</sup> (a) hybridization of anion 3s and 3p orbitals with the anion 3d orbitals could stabilize six nearest-neighbor cations in a trigonal-pyramid configuration; (b) sulfur-sulfur bonding may give rise to molecular anions; (c) larger covalency reduces the effective charges on the ions, and (d) the large polarizability of the anions favor formation of layer structures with van der Waals forces between layers.

Among the sulphides of the same structure, variations are seen in the electronic structure and thereby in the electrical and magnetic properties. One good example is the class of 3d transition metal disulphides with pyrite structure. In this

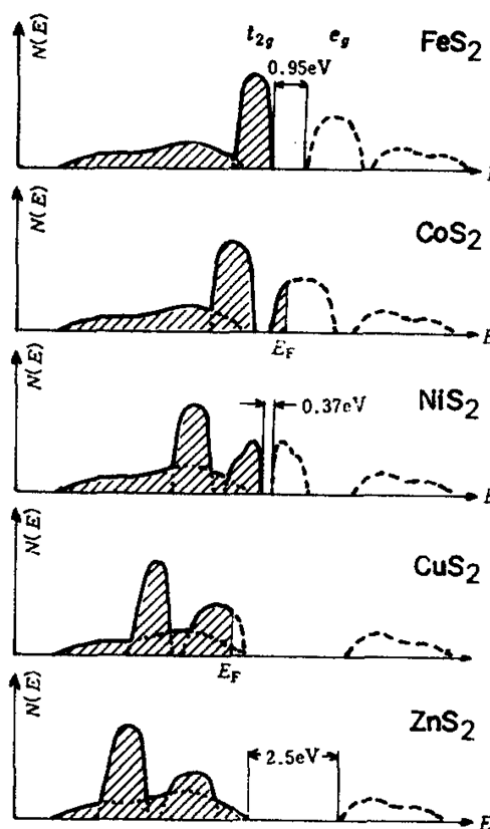


Figure 1 Schematic of the density of states of 3d transition metal disulphides in pyrite structure<sup>1</sup> [reproduced from ref. 1 with permission]

structure the transition metal ion is octahedrally coordinated with six sulphide ions. The octahedral crystal field removes the five-fold degeneracy of 3d orbitals of metal ion and split into orbitals of  $t_{2g}$  and  $e_g$  symmetry, giving rise to  $t_{2g}$ , and  $e_g$ , bands in the solid. Because the  $t_{2g}$  orbitals point away from the negatively charged anions, the  $t_{2g}$  band lies below the  $e_g$  band. It has been shown experimentally by electrical, magnetic, optical, XPS and UPS measurements that in this structure, metal ions remain in low spin state.<sup>4-7</sup> Band model correctly predicts the semiconducting and the metallic behavior of the  $FeS_2$  and  $CoS_2$  respectively. The highest occupied level of valence electrons in  $FeS_2$  is localized and  $t_{2g}$  band while the lowest unoccupied level is the antibonding  $e_g$  band. In the case of  $CoS_2$ , one extra electron occupies the antibonding  $e_g$  band, which leads to metallic conductivity. In  $NiS_2$ , the band model predicts it to be metallic because the antibonding  $e_g$  band is half filled but it turns out to be a semiconductor. In order to resolve this discrepancy, it has been suggested that  $NiS_2$ , is a Mott insulator and the  $e_g$  band is split into spin-up and spin-down bands by electron-electron correlations. The metallic and semiconducting behavior of  $CuS_2$  and  $ZnS_2$  respectively can again be explained by the band theory. It is important to note that, while  $NiS_2$  is a Mott-insulator,  $NiSe_2$  with the same pyrite structure is metallic.

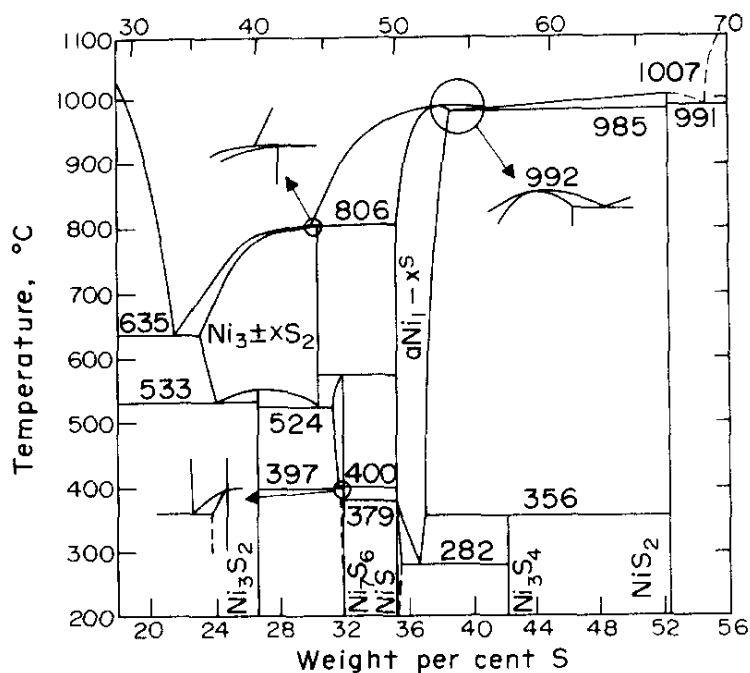


Figure 2 Phase diagram of Ni-S system above 200 °C and from 18 to 56 % of sulphur<sup>3</sup> [reproduced from ref. 3 with permission]

Among all the transition metal sulphides, nickel sulphide is known to have a complex phase diagram containing binary phases like  $\text{Ni}_{3+x}\text{S}_2$ ,  $\text{Ni}_3\text{S}_2$ ,  $\text{Ni}_4\text{S}_{3+x}$ ,  $\text{Ni}_6\text{S}_5$ ,  $\text{Ni}_7\text{S}_6$ ,  $\text{Ni}_9\text{S}_8$ ,  $\text{NiS}$ ,  $\text{Ni}_3\text{S}_4$  and  $\text{NiS}_2$  (Figure 2).<sup>8</sup> Only some of the phases have been studied in detail like  $\text{NiS}_2$  and  $\text{NiS}$  owing to their interesting transport properties.  $\text{NiS}_2$  has pyrite structure with Ni atoms arranged in fcc lattice. Triangular arrangement of Ni in the fcc lattice imparts magnetic frustration in the system.  $\text{NiS}$  has high temperature hexagonal ( $\alpha$ - $\text{NiS}$ ) and low temperature rhombohedral ( $\beta$ - $\text{NiS}$ ) phase.<sup>8</sup>  $\text{Ni}_3\text{S}_2$  has sulphur atoms positioned in body centered cubic structure with Ni atoms in some of the pseudotetrahedral holes.<sup>9</sup> At high temperature, it converts into  $\text{Ni}_{3+x}\text{S}_2$  with face centered cubic structure.  $\text{Ni}_7\text{S}_6$  is believed to form from  $\text{Ni}_9\text{S}_8$  and  $\text{Ni}_3\text{S}_2$  eutectoidally and structurally related to the high temperature  $\text{Ni}_{7\pm x}\text{S}_6$  phase.<sup>10</sup>

Magnetic properties of nickel sulphide nanoparticles have rarely been investigated. Magnetization and neutron scattering studies on  $\text{NiS}_2$  bulk single crystal reveal that it goes from paramagnetic (PM) state to collinear antiferromagnetic (AFM) state at  $T_{N2} \sim 40$  K and changes to a spin canted or weak ferromagnetic state below  $T_{N1} \sim 30$  K.<sup>11</sup> Bulk hexagonal  $\text{NiS}$  is collinear antiferromagnetic below 265 K.<sup>12</sup> Magnetic measurements on single crystalline and polycrystalline  $\text{Ni}_3\text{S}_2$  show temperature independent Pauli paramagnetic behavior.<sup>13</sup> Research on nanostructured nickel sulphide has been mainly concentrated on obtaining different phases and morphologies. Barry *et al.* conducted magnetic measurements on  $\text{NiS}$  nanoparticles.<sup>14</sup> They found unusual magnetic properties like superparamagnetism at low temperature while spin freezing phenomenon at higher temperature without any anomaly corresponding to the paramagnetic to antiferromagnetic transition.

## 2. Scope of the present investigation

Considering the very complex phase diagram of nickel sulphide, it is difficult to obtain pure phases of nickel sulphide. In most of the cases, a mixture of two or more phases is obtained.<sup>15-17</sup> Nanostructures of nickel sulphides have been mainly prepared in hydrothermal or solvothermal conditions but the method suffers from the co-occurrence of impurity phases. Yu and Yashimura prepared  $\text{Ni}_3\text{S}_2$  thin films,  $\text{NiS}$  nanowhiskers and  $\text{NiS}_2$  single crystals in ethylenediamine in solvothermal conditions.<sup>15</sup> Zhang *et al.* synthesized oriented nanostructured films of  $\text{NiS}$  and  $\text{Ni}_3\text{S}_2$  hydrothermally using Ni foil and sulphur powder.<sup>18</sup>

Layer-rolled NiS nanostructures were made from nickel chloride and  $\text{NH}_3\text{-H}_2\text{O-CS}_2$  system at temperature as low as  $60\text{ }^\circ\text{C}$ .<sup>19</sup> Other morphologies of nickel sulphides like nanorods and nanoprism,<sup>20</sup> hollow spheres,<sup>21</sup> nanosheets and nanoneedles,<sup>22</sup> peapods-nanochain,<sup>23</sup> flowers,<sup>17</sup> urchin<sup>16</sup> etc. have also been reported. Ramasamy *et al.* prepared thin films of various phases of nickel sulphide by aerosol assisted chemical vapor deposition by decomposition of thio- and dithiobiuret complexes.<sup>9</sup>

In this work, we adapted a new procedure for the preparation of pure nanocrystalline  $\text{NiS}_2$ , NiS and  $\text{Ni}_3\text{S}_2$  phases by thermal decomposition of nickel-thiourea complex at high temperature and studied their magnetic and electrical properties. The interesting finding is the temperature evolution of nickel sulphide phases and a large exchange bias effect in  $\text{NiS}_2$  nanoparticles.

### 3. Experimental section

#### 3.1 Synthesis of hexakis(thiourea)nickel(II) nitrate

Hexakis(thiourea)nickel(II) complex was synthesized according to an earlier reported method.<sup>24</sup> In a typical synthesis, 1.16 g  $\text{Ni}(\text{NO}_3)_2 \cdot 6\text{H}_2\text{O}$  in n-butyl alcohol and 1.82 g thiourea in n-butyl alcohol were mixed together and sonicated for 10 min. The fine light green colored crystals were precipitated. Precipitate was filtered and washed with diethylether several times and dried at  $80\text{ }^\circ\text{C}$  in an oven.

#### 3.2 Synthesis of nickel sulphide particles

Hexakis(thiourea)nickel(II) complex was taken in a ceramic boat and heated in nitrogen atmosphere in a tube furnace at different temperatures for 2 h to get pure phases of nickel sulphide. Single phases of  $\text{NiS}_2$ , NiS and  $\text{Ni}_3\text{S}_2$  were obtained at temperatures 400, 600 and  $800\text{ }^\circ\text{C}$  respectively.

#### 3.3 Characterization

X-ray diffraction (XRD) of hexakis(thiourea)nickel(II) complex and different phases of nickel sulphide particles were carried out in Bruker D8 Discover diffractometer. Cell parameters were obtained by Le Bail fitting carried out on overnight collected XRD data

using *FullProf* programme.<sup>25</sup> Analysis of particle size and morphology were carried out by Field Emission Scanning Electron Microscopy (FESEM) using NOVA NANOSEM 600 (FEI, The Netherlands). Transmission electron microscopy (TEM) images were obtained by Tecnai T20 instrument (FEI) operated at an accelerating voltage of 200 kV. Magnetic measurements were carried out in SQUID VSM, Quantum Design, USA and electrical transport measurements were done with Physical Property Measurement System (PPMS, Quantum Design, USA).

#### 4. Results and discussion

In the hexakis(thiourea)nickel(II) complex, which decomposes to form nickel sulphide nanoparticles, there are three thiourea molecules in the asymmetric unit with six sulphur atoms directly bonded to the nickel(II). This increases the possibility of the formation of nickel sulphide phase without any oxide or nitride impurity phases.

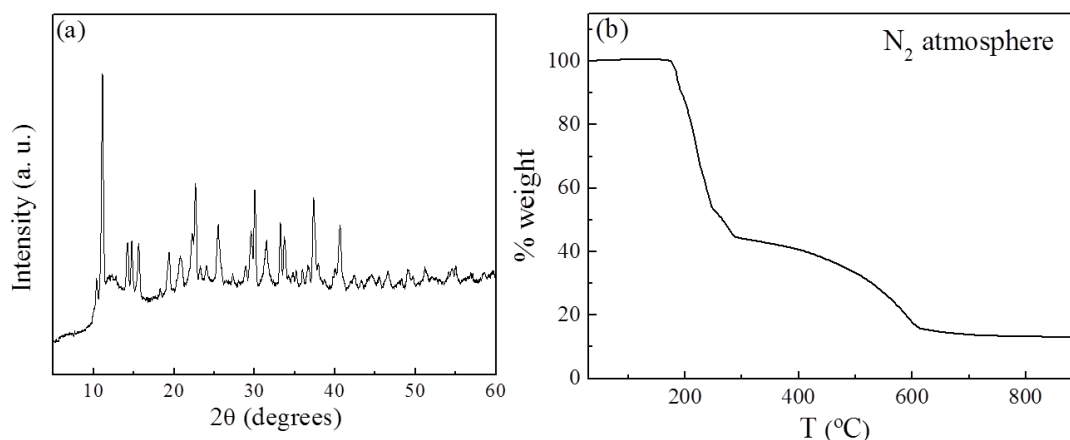


**Figure 3(a) XRD and (b) TGA of hexakis(thiourea)nickel(II) complex**

The XRD data of the hexakis(thiourea)nickel(II) complex is shown in Figure 3(a). It belongs to the monoclinic system with space group *C2/c*. Thermogravimetric analysis (TGA) curve in Figure 3(b) shows a sudden change in weight starting at 200 °C which continues till 300 °C owing to the removal of volatile substances such as ammonia, nitrogen oxide and sulphur oxide. From 300 °C onwards, the change in weight is gradual which might be attributed to the loss of sulphur from already formed one or a mixture of nickel sulphide phases. After 600



°C the curve shows a more gradual change in weight which continues till the highest temperature measured (900 °C).

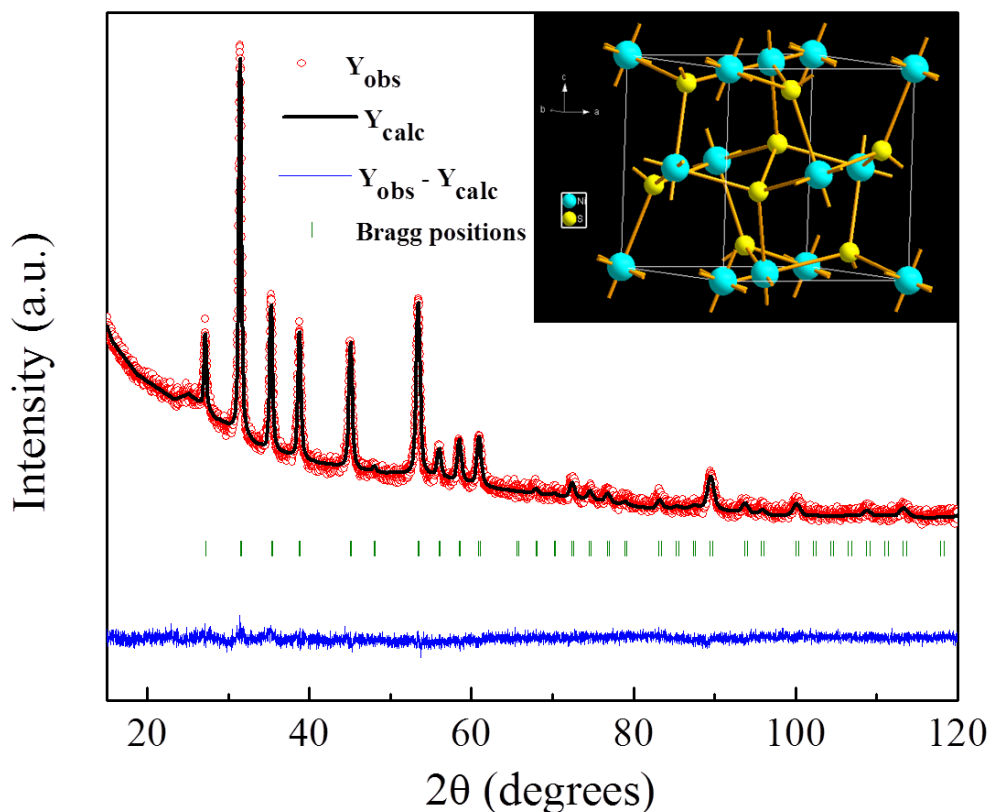


**Figure 4 Rietveld refined XRD pattern of NiS<sub>2</sub> nanoparticles with inset showing the crystal structure**

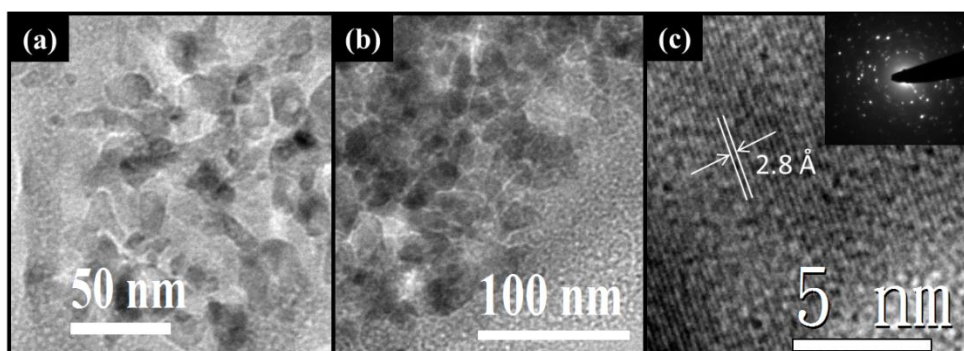
Figure 4 shows the XRD pattern of the NiS<sub>2</sub> nanoparticles prepared at 400 °C which is the first phase to come out in the temperature evolution of nickel sulphide. It is important to note here that the oxidation state of Ni is +2 and S<sub>2</sub><sup>2-</sup> acts as anion. Formation of such anion is possible due to higher covalency of sulphur compared to oxygen. NiS<sub>2</sub> crystallizes in cubic pyrite type structure with space group *Pa-3* (Figure 4). The cell parameter obtained by Rietveld refinement of the room temperature X-ray data using *FullProf* is 5.6485(4) Å. This value is smaller than that of the single crystal of stoichiometric NiS<sub>2</sub> (5.688 Å) which indicates that the sulphur content in our sample is less than the stoichiometric one. The  $\chi^2$  value of the refinement is 1.33 whereas the  $R_{Bragg}$  parameter is 13.8. The high value of  $\chi^2$  can be attributed to the poor statistics because of the nanocrystalline nature of the sample. All the refinement parameters are presented in Table 1.

**Table 1 Crystallographic data of NiS<sub>2</sub> nanoparticles at 300 K**

Atom	Wyck. position	Oxidation state	x	y	z	B <sub>iso</sub>	Occ.
Ni	4a	+2	0.0000	0.0000	0.0000	1.714(49)	0.167
S	8c	-1	0.3955(1)	0.3955(1)	0.3955(1)	1.019(50)	0.327(84)

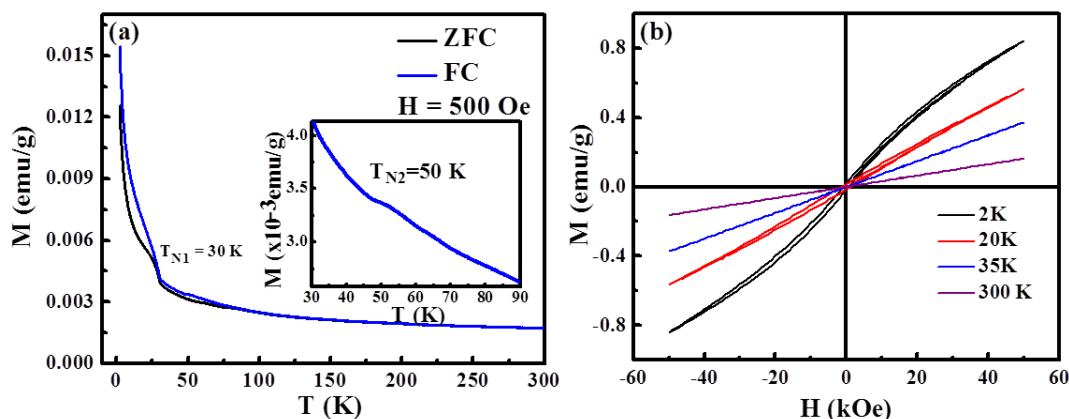
Space group = *Pa*-3, a = b = c = 5.6485(4) Å,  $\chi^2 = 1.33$ ,  $R_{Bragg} = 13.8$

Figure 5(a) and (b) show TEM images of NiS<sub>2</sub> nanoparticles. The average particle size is about 20 nm. Figure 5(c) shows the high resolution TEM image of NiS<sub>2</sub> nanoparticles. The observed fringes correspond to the interlayer separation between (200) planes. The electron diffraction pattern consists of individual dots instead of continuous rings indicating the single crystalline nature of the particles as can be seen in the inset.



**Figure 5 (a) and (b) TEM images of NiS<sub>2</sub> nanoparticles, (c) high resolution TEM image with ED pattern in the inset**

Figure 6(a) shows zero field cooled (ZFC) and field cooled (FC) magnetization of NiS<sub>2</sub> nanoparticles at an applied field of 500 Oe. An anomaly at 30 K is seen, which can be attributed to a transition from canted antiferromagnetic state or a weak ferromagnetic state (low temperature phase) to a collinear antiferromagnetic ( $T_{N1}$ ). According to the neutron diffraction studies carried out by Tineke *et al.*, canting angle of  $\sim 0.1^\circ$  was found in the z direction.<sup>11</sup> This canting imparts weak ferromagnetism in the system below 30 K. Inset of Figure 6(a) shows second anomaly in the (FC) magnetization near 50 K which corresponds to the transition from a collinear AFM to paramagnetic state ( $T_{N2}$ ). Magnetic measurement on the single crystal of stoichiometric NiS<sub>2</sub> showed that this transition is at 39 K. However,



**Figure 6 (a) Zero field cooled (ZFC) and field cooled (FC) magnetizations of NiS<sub>2</sub> nanoparticles, inset shows T<sub>N2</sub> in the FC curve, (b) magnetic hysteresis loops at different temperatures**

Gautier *et al.* have shown that non-stoichiometry of sulphur has great influence on the magnetic properties of NiS<sub>2</sub>.<sup>26</sup> They studied the magnetic properties of NiS<sub>x</sub> ( $1.91 \leq x \leq 2.09$ ) and concluded that although T<sub>N1</sub> did not vary much with x but T<sub>N2</sub> reached as high as 170 K for a sample of composition NiS<sub>2.09</sub>. For the composition of NiS<sub>1.91</sub>, they observed maxima at 50 K. Hence, we suggest that our sample contains sulphur vacancies, which is also supported by the smaller value of cell parameter for the nanoparticles compared to the single crystal of NiS<sub>2</sub>. We could not determine the exact stoichiometry of our compound as it contains some amorphous unreacted material confirmed by elemental analysis and X-ray measurements. Figure 6(b) shows magnetization versus magnetic field data at different temperatures. Hysteresis loop obtained at 2 K has a coercive field (H<sub>C</sub>) value of 824 Oe and remanent magnetization M<sub>R</sub> of 21.2 memu/g. The observed hysteresis in the magnetization arises due to spin canting. The remanent magnetization at 20 K is smaller than that at 2 K. The magnetization is linear with field both in the collinear antiferromagnetic and paramagnetic states.

Nanoparticles impart an additional property of exchange bias to an antiferromagnetic material which the bulk counterpart does not entail. Exchange bias effect is an interface phenomenon between the layers of antiferromagnetic and ferromagnetically aligned

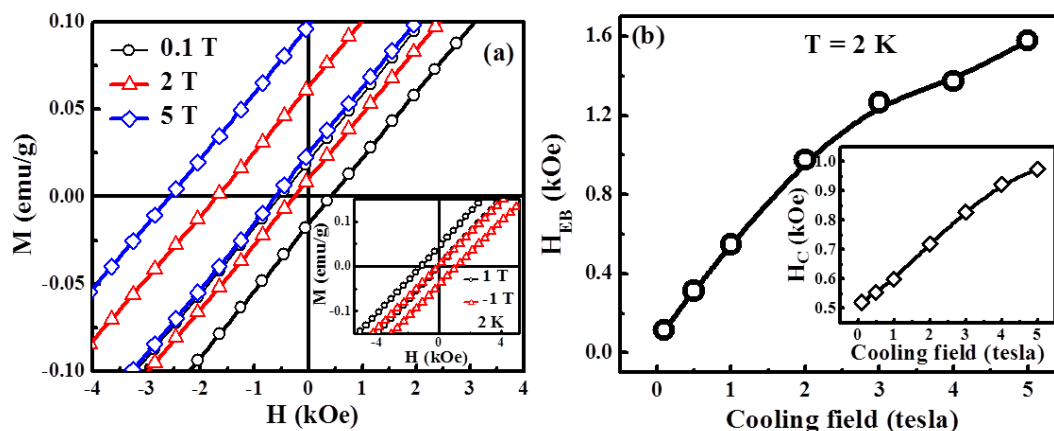


**Figure 7 (a) Exchange bias (EB) effect in NiS<sub>2</sub> nanoparticles with different biasing field at 2 K and inset shows comparison of EB with biasing field of 1 and -1 T. (b) Change in EB with cooling field and inset shows the change of coercive field with cooling field.**

spins.<sup>27-28</sup> It causes the magnetization hysteresis loop to shift to either positive or negative field direction depending on the polarity of the field in which the sample is cooled. It should be noticed that the NiS<sub>2</sub> nanoparticles show such exchange bias effect as shown in Figure 7(a). The sample is cooled in the presence of applied magnetic field of 0.1, 2 and 5 T field and the hysteresis loops are obtained at 2 K. It is clearly seen that as the magnetic field is increased exchange bias ( $H_{EB}$ ) also increases.  $H_{EB}$  is calculated according to the formula  $H_{EB} = (H_{C1} - H_{C2})/2$ , where  $H_{C1}$  and  $H_{C2}$  are negative and positive coercive fields respectively. An  $H_{EB}$  value of 1.57 kOe is observed when the cooling field is 5 T. Inset of the Figure 7(a) shows the effect of polarity of applied magnetic field on exchange bias. When the sample is cooled in the presence of -1 T field, hysteresis loop shifts towards positive field direction. Figure 7(b) shows the effect of cooling field on  $H_{EB}$  indicating that it doesn't saturate even at the highest cooling field of 5 T.  $H_C$  also increases gradually with the increase of cooling field as shown in the inset of Figure 7(b). This is due to the increase in the overall anisotropy in the system in the direction of applied magnetic field. At 35 K, which corresponds to the collinear AFM state, a weak exchange bias value of 180 Oe is observed at 2 K and a cooling field of 1 T. Exchange bias in this system can be explained by considering the core of nanoparticles to be made of highly anisotropic canted AFM component while the shell acting like a less anisotropic ferromagnetic (FM) component with uncompensated spins at the

surface of the nanoparticles. Such systems have been shown to exhibit exchange bias effect considering the fact that the  $T_N$  of the AFM component is lower than the  $T_C$  of the FM component.

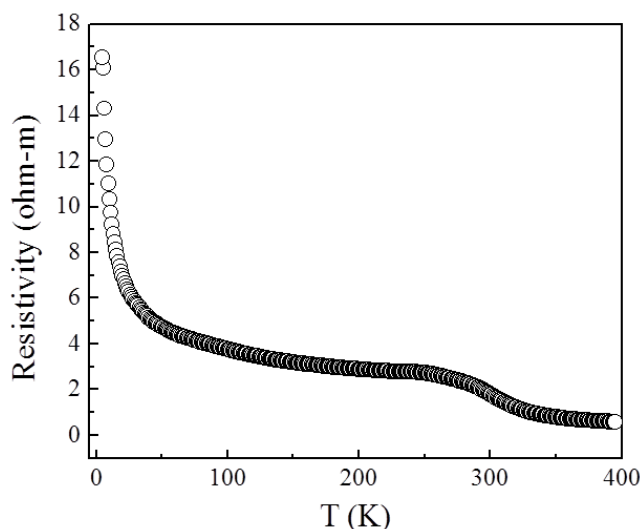


**Figure 8 Electrical resistivity of NiS<sub>2</sub> nanoparticles**

NiS<sub>2</sub> contains exactly half filled  $e_g$  band and hence metallic properties can be predicted but experimentally it is found to be semiconducting. On this basis, NiS<sub>2</sub> is considered to be Mott insulator. Temperature dependence of resistivity of cold pressed NiS<sub>2</sub> nanoparticles showed semiconducting behavior (Figure 8). The value of resistivity (1.8  $\Omega$ -m at room temperature) is a few orders higher than the value reported for single crystals.<sup>29-30</sup> This might be due to the fact that the measurements are carried out on the cold-pressed NiS<sub>2</sub> nanocrystals.

NiS has hexagonal NiAs-type structure with space group  $P6_3/mmc$ . The structure can be generated by creating a hexagonal close packed structure of sulphur atoms and subsequently filling all the octahedral holes with nickel atoms. Rietveld refined pattern of the material obtained by decomposing nickel-thiourea complex at 600 °C in nitrogen atmosphere is shown in Figure 9. The obtained values of cell parameters are  $a = 3.4373(1)$  Å and  $c = 5.3456(2)$  Å. Refined parameters for this phase are listed in Table 2.

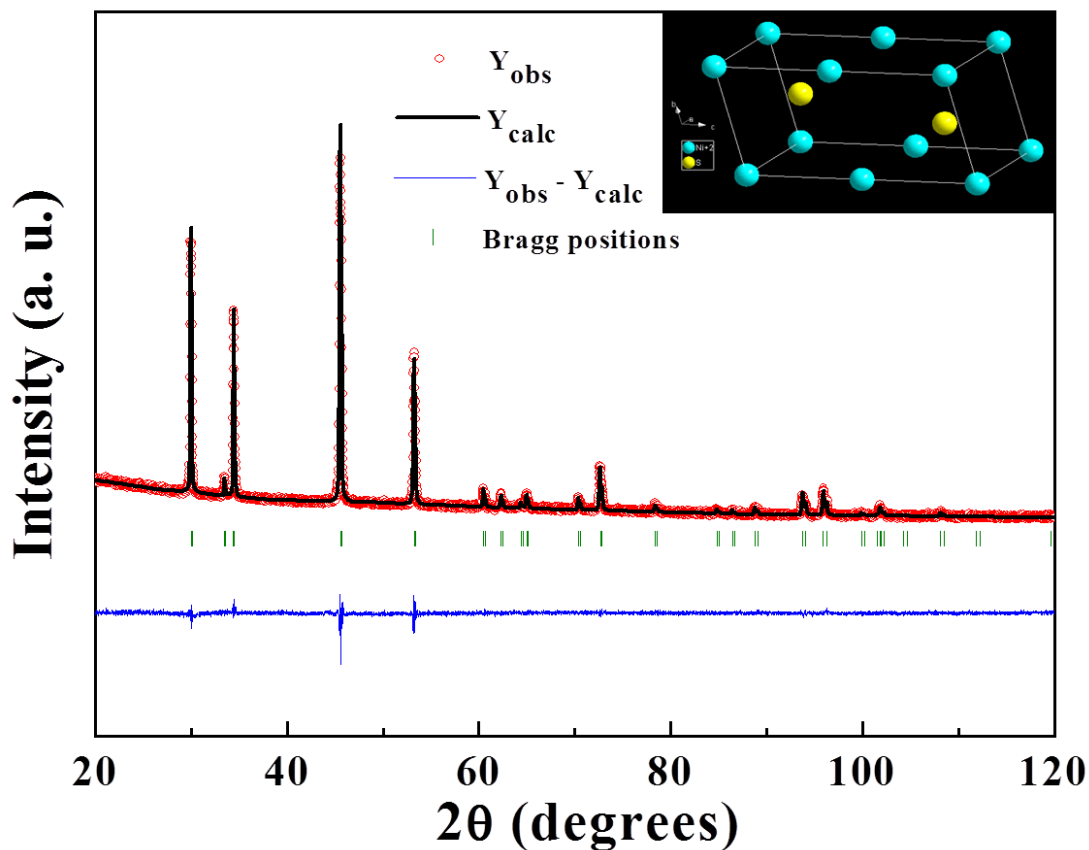


Figure 9 Rietveld refined XRD pattern of NiS nanoparticles with inset showing the crystal structure

Table 2 Crystallographic data of NiS nanoparticles at 300 K

Atom	Wyck. position	Oxidation state	x	y	z	$B_{iso}$	Occ.
Ni	2a	+2	0.0000	0.0000	0.0000	2.271(44)	0.084(19)
S	2c	-2	0.3333	0.6667	0.2500	1.344(47)	0.083

Space group =  $P6_3/mmc$ ,  $a = b = 3.4373(1) \text{ \AA}$ ,  $c = 5.3456(2) \text{ \AA}$ ,  $\chi^2 = 1.78$ ,  $R_{Bragg} = 6.56$

TEM images of NiS nanoparticles are shown in Figure 10(a). The sample contains nanoparticles of with an average dimension of  $\sim 60 \text{ nm}$ . ED pattern in Figure 10(b) consists of continuous rings implying the polycrystalline nature of the nanoparticles.

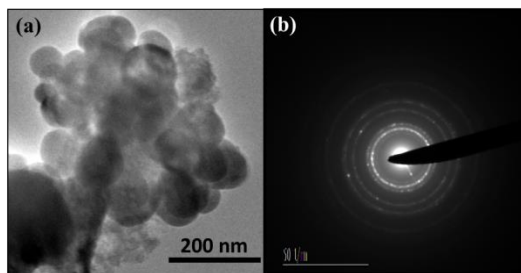


Figure 10 (a) TEM image and (b) ED pattern of NiS particles

Magnetic studies on NiS nanoparticles are carried out in detail. Figure 11(a) shows the FC magnetization data at 1000 Oe applied magnetic field. An anomaly corresponding to a transition from PM state to collinear AFM state is observed at  $\sim 200$  K. In this AFM state,

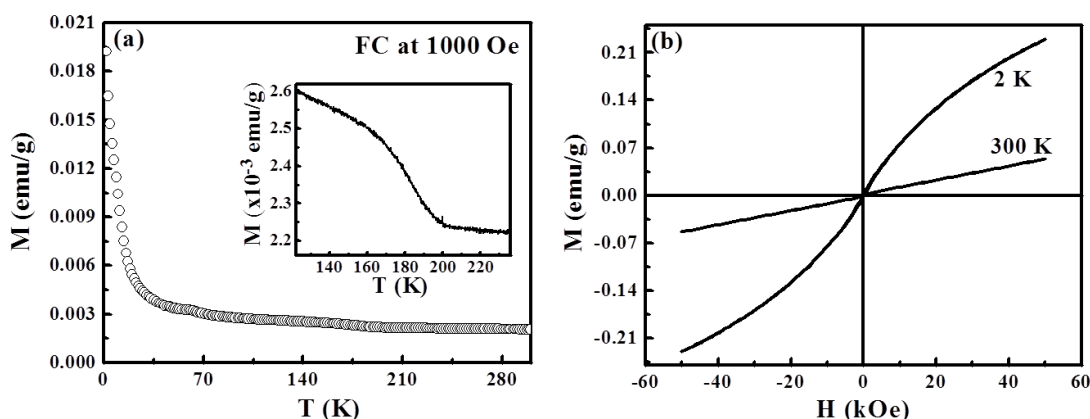
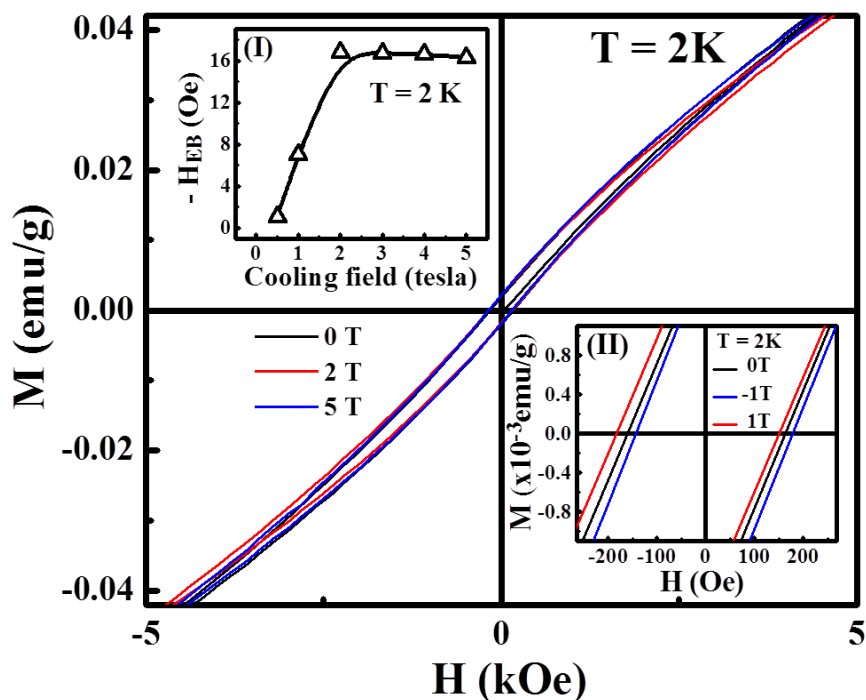


Figure 11 (a) FC magnetization with enlarged view near the transition temperature (inset), (b) isothermal magnetization at 2 and 300 K of NiS particles.

spins in the (001) planes have ferromagnetic interactions while the neighboring (001) planes are antiferromagnetically coupled.<sup>12</sup> For a stoichiometric single crystal of NiS, this transition is found to be at  $\sim 265$  K. However, it has been found that this transition is very sensitive to the composition with  $T_N$  for samples with various Ni contents.<sup>12</sup> We found the composition to be  $Ni_{1.05}S$  from elemental analysis by combustion method. Magnetization at 100 Oe also reveals divergent nature of ZFC and FC till 380 K which indicates that at 200 K the sample does not achieve pure paramagnetic state and the net magnetic interaction can come from uncompensated spins at the surface of the nanoparticles. Inset of Figure 11(a) shows the enlarged view of the anomaly at  $\sim 200$  K under FC conditions at 1000 Oe of applied magnetic field. When magnetization is measured against field at 300 K, as shown in Figure

11(b), a very weak hysteresis loop with small value of  $H_C$  (40 Oe) is observed supporting the magnetic interactions in this material above 200 K. Hysteresis loop at 2 K is also shown in Figure 11(b) with a coercivity of 185 Oe and a remanent magnetization of 1.8 memu/g. At this temperature the sample is in the collinear AFM state and should not show any coercivity. The observed coercivity can again be explained on the basis of uncompensated spins at the surface of the nanoparticles.



**Figure 12** magnetic hysteresis loops of NiS at 2 K at different biasing fields. Inset (I) shows the effect of biasing field and Inset (II) shows the effect of polarity of the biasing field on exchange bias properties.

Unlike NiS<sub>2</sub>, NiS nanoparticles show very small exchange bias effect as shown in Figure 12. The maximum shift in the magnetization curve is 16.75 Oe at 2 K when the sample is cooled in the presence of 2 T field. Variation of exchange bias with cooling field is shown in the inset I of Figure 12. After achieving the maximum value of 16.75 Oe at 2 T, it decreases thereafter. Inset II shows the effect of change of polarity of cooling field on the exchange bias property.



Figure 13 shows the electrical resistivity of NiS nanoparticles against temperature. In order to compare to the corresponding magnetic properties, the resistivity data are plotted along with the magnetization data. The resistivity shows an anomaly at the magnetic transition.

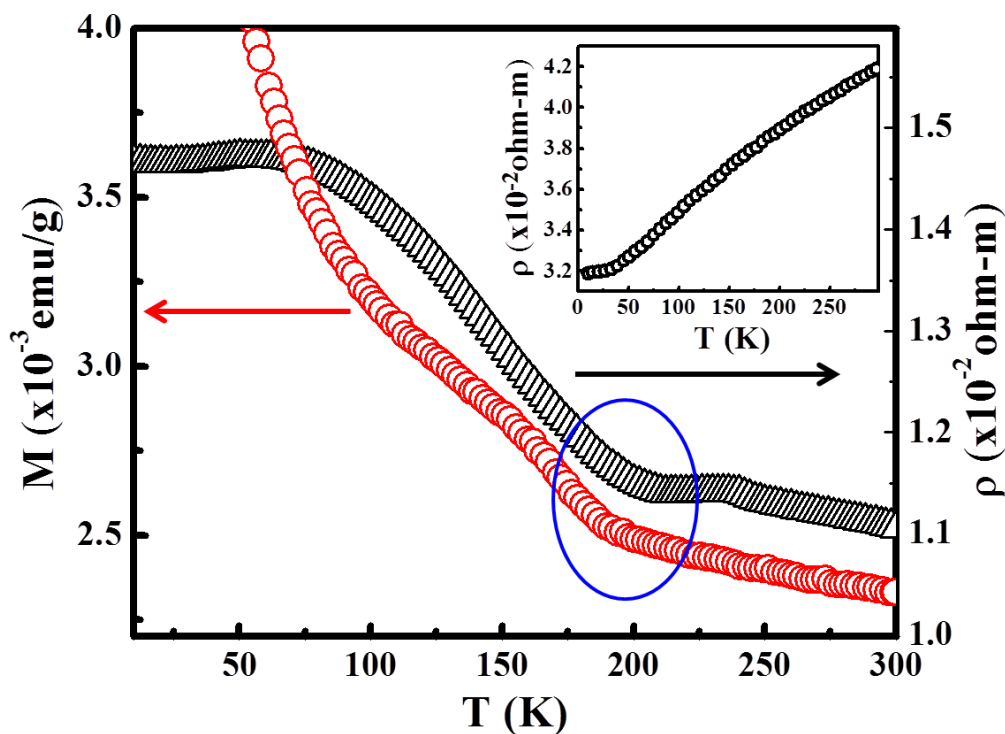


**Figure 13** Electrical resistivity as a function of temperature of NiS nanoparticles prepared at 600 °C along with the magnetization data for comparison. Inset shows the electrical resistivity of Ni<sub>0.96</sub>S nanoparticles prepared at 500 °C

Unlike in the single crystal reported earlier, we do not observe a vast change in the resistivity value at the magnetic transition temperature. It is interesting to note from the inset of Figure 13 that the resistivity of NiS nanoparticles sample prepared at 500 °C (Ni<sub>0.96</sub>S) shows a metallic behavior. Such a behavior can arise from the deficiency of Ni as found in bulk polycrystalline Ni<sub>0.95</sub>S.<sup>31</sup> The origin of this metallic conductivity in Ni-deficient phase is not yet understood.

When the nickel-thiourea complex is heated at 800 °C for 2 h in nitrogen atmosphere, rhombohedral Ni<sub>3</sub>S<sub>2</sub> (space group, *R*32) is obtained. This has a slightly distorted body-centered cubic arrangement of sulphur atoms with nickel atoms occupying some of the pseudo-tetrahedral holes. Rietveld refined pattern of Ni<sub>3</sub>S<sub>2</sub> particles is show in Figure 14. The

obtained values of cell parameters are  $a = 5.7444(1)$  and  $c = 7.1353(2)$  Å. Refined parameters for this phase is listed in Table 3.

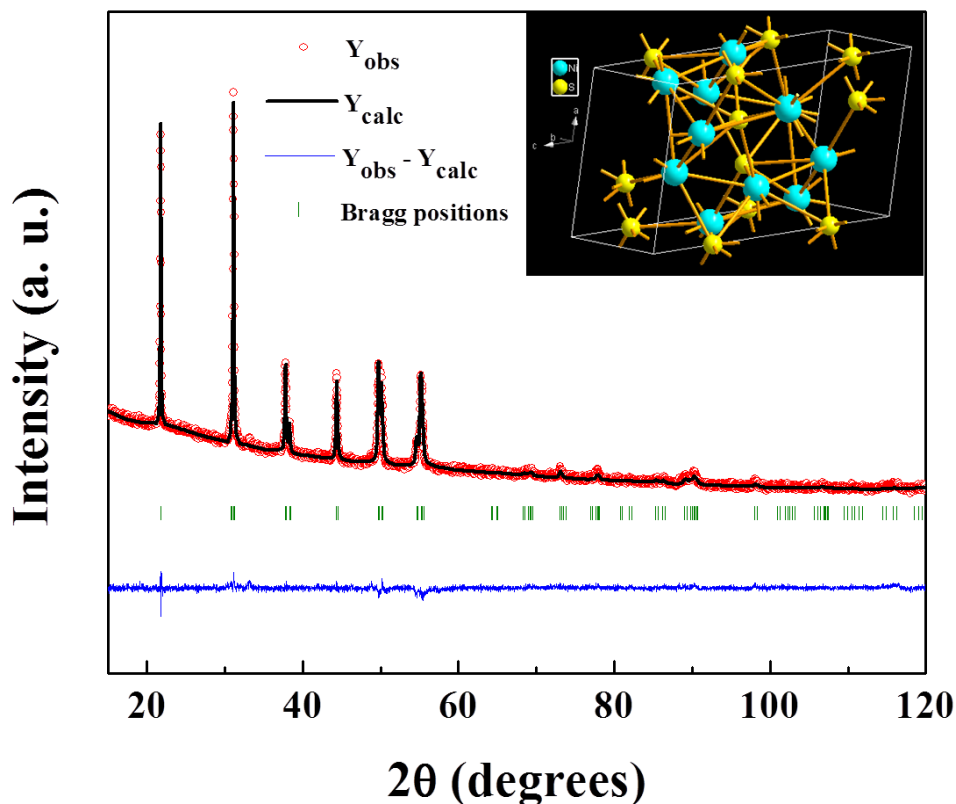


Figure 14 Rietveld refined XRD pattern of NiS nanoparticles with inset showing the crystal structure

Table 3: Crystallographic data of Ni<sub>3</sub>S<sub>2</sub> nanoparticles at 300 K

Atom	Wyck. position	Oxidation state	x	y	z	$B_{iso}$	Occ.
Ni	9e	+1.33	0.7455(3)	0.0000	0.5000	3.241(78)	0.500
S	6c	-2	0.0000	0.0000	0.2589(5)	1.808(95)	0.333

Space group =  $R32$ ,  $a = b = 5.7444(1)$  Å,  $c = 7.1353(2)$  Å,  $\chi^2 = 1.83$ ,  $R_{Bragg} = 17.4$

Figure 15(a) shows TEM image of Ni<sub>3</sub>S<sub>2</sub> nanoparticles. The average size is found to be  $\sim 20$  nm. ZFC and FC curves at 100 Oe are shown in Figure 15(b). It shows a rise in magnetic susceptibility at low temperature. It is known in the literature that pure stoichiometric Ni<sub>3</sub>S<sub>2</sub> shows temperature independent Pauli paramagnetic behaviour.<sup>13</sup> The rise in the magnetization value might occur due to the non-stoichiometry related paramagnetic centres

at the surface of the nanoparticles often called as Curie tail in the literature. The magnetization value is a few orders higher than the earlier reported values.<sup>13</sup>

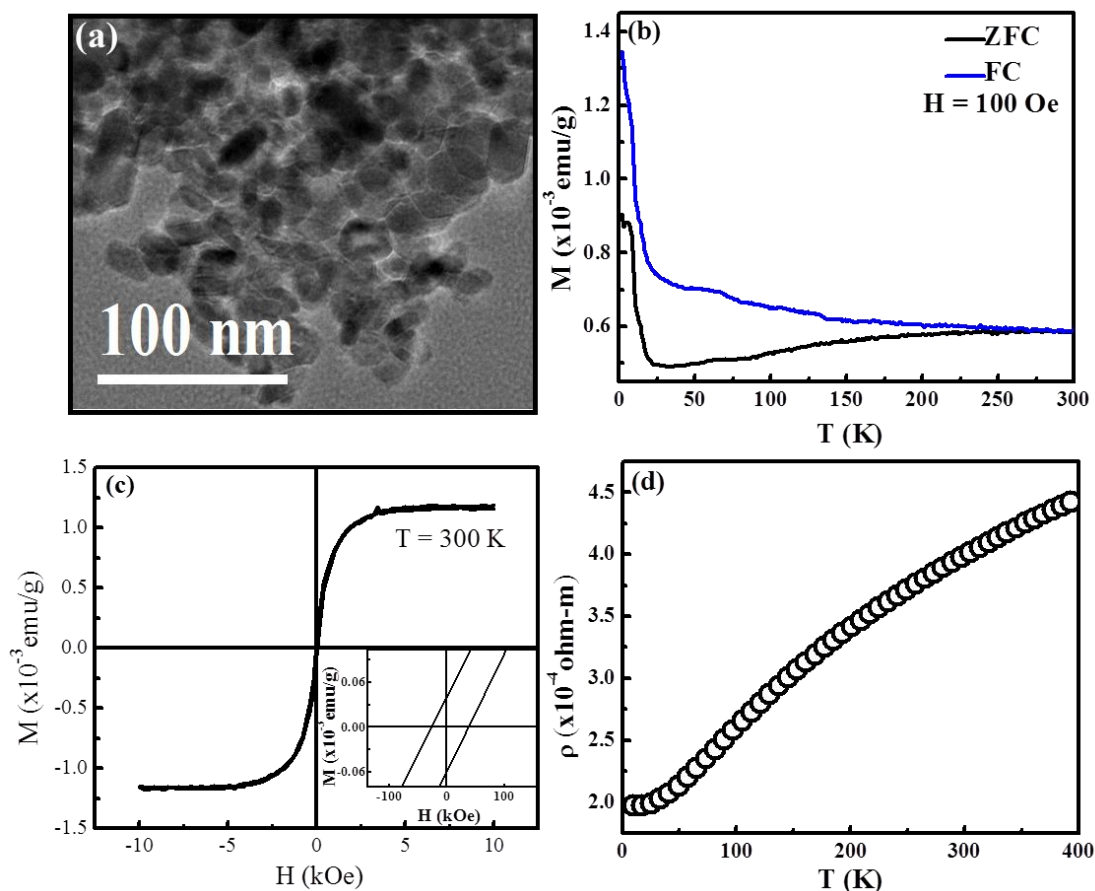


**Figure 15 (a) TEM image of  $\text{Ni}_3\text{S}_2$  nanoparticles, (b) ZFC and FC curves of  $\text{Ni}_3\text{S}_2$  at 100 Oe, (c) Magnetic hysteresis loop of  $\text{Ni}_3\text{S}_2$  at 300 K with inset showing enlarged view near origin, (d) Electrical resistivity of  $\text{Ni}_3\text{S}_2$  nanoparticles as a function of temperature**

The divergence in the ZFC and FC curves indicates the magnetic interactions throughout the temperature range. Figure 15(c) shows magnetic hysteresis loop at 300 K with a small  $H_C$  of 37 Oe and  $M_S$  of  $1.2 \times 10^{-3}$  emu/g. The value of  $M_S$  is of the same order as that observed in the samples containing defect related ferromagnetism in nanoparticles of otherwise nonmagnetic materials.<sup>32</sup> It shows metallic behaviour throughout the temperature range as also shown in the literature earlier.<sup>13</sup> The resistivity measurements carried out on the cold pressed  $\text{Ni}_3\text{S}_2$  nanoparticles are shown in Figure 15(d). It can be seen that it exhibits a metallic behaviour despite poor connectivity between the grains.

## **5. Conclusions**

Temperature evolution of different phases of nickel sulphide nanoparticles has been achieved by decomposing nickel-thiourea complex at various temperatures. NiS<sub>2</sub> nanoparticle, which is low temperature sulphur-rich phase, shows remarkable exchange bias effect at 2 K. The value of exchange bias as well as the coercivity increase with increasing cooling field. The intermediate NiS phase is collinear antiferromagnetic and shows very less exchange bias compared to the weak ferromagnetic NiS<sub>2</sub> at 2 K. Electrical resistivity of NiS nanoparticles shows semiconducting behaviour with an anomaly corresponding to the antiferromagnetic to paramagnetic transition. Nanoparticles of high temperature phase Ni<sub>3</sub>S<sub>2</sub> show a weak temperature dependent magnetization with a hysteresis loop at the room temperature. Electrical resistivity measurements reveal metallic behaviour of the nanoparticles.

## 6. References

1. S. Ogawa, *J. Appl. Phys.* **1979**, *50*, 2308-2311.
2. F. C. Hsu, J. Y. Luo, K. W. Yeh, T. K. Chen, T. W. Huang, P. M. Wu, Y. C. Lee, Y. L. Huang, Y. Y. Chu, D. C. Yan and M. K. Wu, *Proc. Natl. Acad. Sci.* **2008**, *105*, 14262-14264.
3. C. N. R. Rao and K. P. R. Pisharody, *Prog. Solid State Chem.* **1976**, *10*, 207-270.
4. H. S. Jarrett, W. H. Cloud, R. J. Bouchard, S. R. Butler, C. G. Frederick and J. L. Gillson, *Phys. Rev. Lett.* **1968**, *21*, 617-620.
5. K. Adachi, K. Sato and M. Takeda, *J Phys Soc Japan* **1969**, *26*, 631-638.
6. E. K. Li, K. H. Johnson, D. E. Eastman and J. L. Freeouf, *Phys. Rev. Lett.* **1974**, *32*, 470-472.
7. A. Ohsawa, H. Yamamoto and H. Watanabe, *J. Phys. Soc. Jpn.* **1974**, *37*, 568.
8. G. Kullerud and R. A. Yund, *J. Petrol.* **1962**, *3*, 126.
9. K. Ramasamy, M. A. Malik, P. O'Brien, J. Raftery and M. Helliwell, *Chem. Mater.* **2010**, *22*, 6328-6340.
10. H. Seim, H. Fjellvåg, F. Grønvold and S. Stølen, *J. Solid State Chem.* **1996**, *121*, 400-407.
11. T. Thio, J. W. Bennett and T. R. Thurston, *Phys. Rev. B* **1995**, *52*, 3555-3560.
12. J. T. Sparks and T. E. D. Komoto, *Rev. Mod. Phys.* **1968**, *40*, 752-754.
13. P. A. Metcalf, B. C. Crooker, M. McElfresh, Z. Kąkol and J. M. Honig, *Phys. Rev. B* **1994**, *50*, 2055-2060.
14. L. Barry, J. D. Holmes, D. J. Otway, M. P. Copley, O. Kazakova and M. A. Morris, *J. Phys.: Condens. Matter* **2010**, *22*, 076001.
15. S. H. Yu and M. Yoshimura, *Adv. Funct. Mater.* **2002**, *12*, 277-285.
16. X. Shen, J. Sun, G. Wang, J. Park and K. Chen, *Mater. Res. Bull.* **2010**, *45*, 766-771.
17. Q. Pan, K. Huang, S. Ni, F. Yang and D. He, *Mater. Res. Bull.* **2008**, *43*, 1440-1447.
18. L. Zhang, J. C. Yu, M. Mo, L. Wu, Q. Li and K. W. Kwong, *J. Am. Chem. Soc.* **2004**, *126*, 8116-8117.
19. X. Jiang, Y. Xie, J. Lu, L. Zhu, W. He and Y. Qian, *Adv. Mater.* **2001**, *13*, 1278-1281.
20. A. Ghezelbash, M. B. Sigman and B. A. Korgel, *Nano Lett.* **2004**, *4*, 537-542.

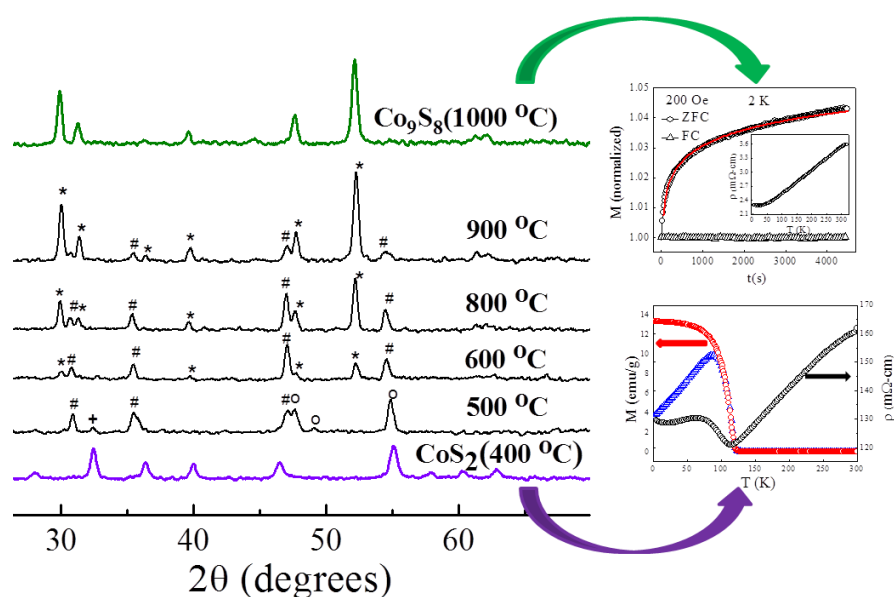
21. Y. Hu, J. Chen, W. Chen, X. Lin and X. Li, *Adv. Mater.* **2003**, *15*, 726.
22. D. Chen, L. Gao and P. Zhang, *Chem. Lett.* **2003**, *32*, 996-997.
23. W. Zhou, W. Chen, J. Nai, P. Yin, C. Chen and L. Guo, *Adv. Funct. Mater.* **2010**, *20*, 3678-3683.
24. K. Muthu and S. P. Meenakashisundaram, *J. Cryst. Growth* **2012**, *352*, 158-162.
25. J. Rodríguez-Carvajal, *Physica B* **1993**, *192*, 55-69.
26. F. Gautier, G. Krill, M. F. Lapierre and C. Robert, *J. Phys. C Solid State Phys.* **1973**, *6*, L320.
27. W. H. Meiklejohn and C. P. Bean, *Phys. Rev.* **1957**, *105*, 904-913.
28. W. H. Meiklejohn, *J. Appl. Phys.* **1962**, *33*, 1328-1335.
29. R. L. Kautz, M. S. Dresselhaus, D. Adler and A. Linz, *Phys. Rev. B* **1972**, *6*, 2078-2082.
30. P. Kwizera, M. S. Dresselhaus and D. Adler, *Phys. Rev. B* **1980**, *21*, 2328-2335.
31. T. Ohtani, *J. Phys. Soc. Jpn.* **1974**, *37*, 10.
32. A. Sundaresan and C. N. R. Rao, *Nano Today* **2009**, *4*, 96-106.

## Chapter V.2

### Synthesis, electrical and magnetic properties of cobalt sulphides: $\text{CoS}_2$ and $\text{Co}_9\text{S}_8$ \*

#### Summary

Single phase cobalt disulphide ( $\text{CoS}_2$ ) nanoparticles have been prepared by thermal decomposition of cobalt-thiourea complex at a low temperature ( $400\text{ }^\circ\text{C}$ ).  $\text{CoS}_2$  nanoparticles exhibit ferromagnetic ordering at  $122\text{ K}$  below which the temperature dependent resistivity of cold pressed nanoparticles deviates from metallic behaviour and shows a broad maximum. Just below  $T_c$ , it also exhibits a large magnetoresistance effect ( $6.5\%$ ). A mixture of  $\text{CoS}$  and  $\text{Co}_9\text{S}_8$  phases were obtained between the temperature interval  $400\text{ }^\circ\text{C} < T < 1000\text{ }^\circ\text{C}$ . At  $1000\text{ }^\circ\text{C}$ , a pure bulk  $\text{Co}_9\text{S}_8$  phase was obtained. It exhibits magnetic hysteresis typical of a ferromagnet at room temperature and a peak in magnetization at low temperature with a strong relaxation indicating possible spin glass state.



\* A paper based on these studies has appeared in *Z. Anorg. Allg. Chem.*, **2014**

## 1. Introduction

Transition metal sulphides are very important class of materials known for their rich structural diversities along with interesting and technologically relevant electronic and magnetic properties. One additional advantage is that they are cheap and abundant, many of which are found in nature in the form of minerals such as heazlewoodite ( $\text{Ni}_3\text{S}_2$ ), chalcocite ( $\text{Cu}_2\text{S}$ ), pyrite ( $\text{FeS}_2$ ) *etc.* Among all, sulphides which crystallize in pyrite structure ( $\text{FeS}_2$ ,  $\text{CoS}_2$ ,  $\text{NiS}_2$ ,  $\text{CuS}_2$  and  $\text{ZnS}_2$ ) show great variation in electronic properties by changing transition metal ion and also by substituting Se or Te in the anion site. According to the band theory,  $\text{FeS}_2$  and  $\text{ZnS}_2$  are semiconducting while  $\text{CoS}_2$  and  $\text{CuS}_2$  are metallic.  $\text{NiS}_2$  is a Mott insulator. In  $\text{CoS}_2$ ,  $\text{Co}^{2+}$  remains in the low spin state with one electron in the  $e_g$  sub-band. Because of the intermediate strength of the  $e_g$  electron correlation, ferromagnetic transition temperature (Curie temperature,  $T_C$ ) is found to be less (120 K) with fractional magnetic moment (0.85 B.M.). The electrons which are responsible for ferromagnetic interaction also give rise to electronic conduction in  $\text{CoS}_2$ .

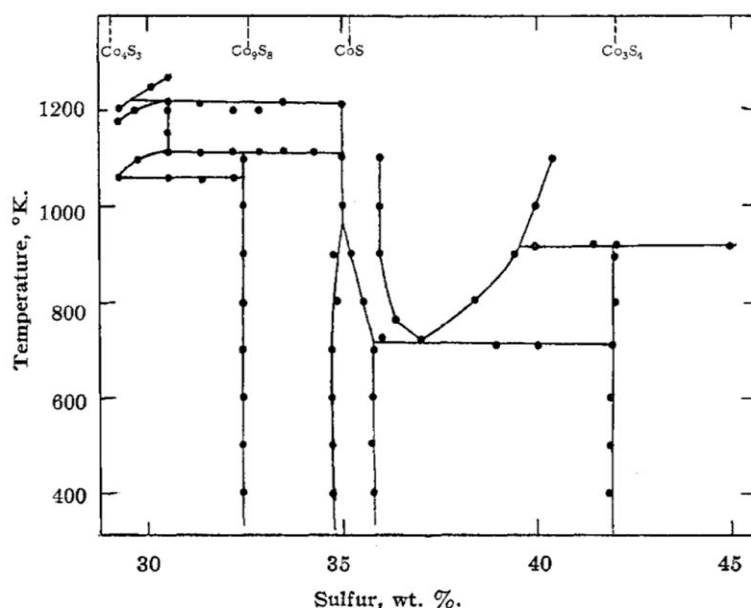


**Figure 1** Phase diagram of Co-S system based on magnetic susceptibility data<sup>1</sup> [reproduced from ref. 1 with permission]

The phase diagram of cobalt sulphide is fairly complex containing  $\text{Co}_4\text{S}_3$ ,  $\text{Co}_9\text{S}_8$ ,  $\text{CoS}$ ,  $\text{Co}_3\text{S}_4$ ,  $\text{Co}_2\text{S}_3$  and  $\text{CoS}_2$  phases (Figure 1).  $\text{Co}_4\text{S}_3$  is the high temperature phase stable between 1065 K



and 1106 K. It has a very weak temperature dependence of magnetic susceptibility which increases slightly with temperature. Crystal structure and other properties are not known.

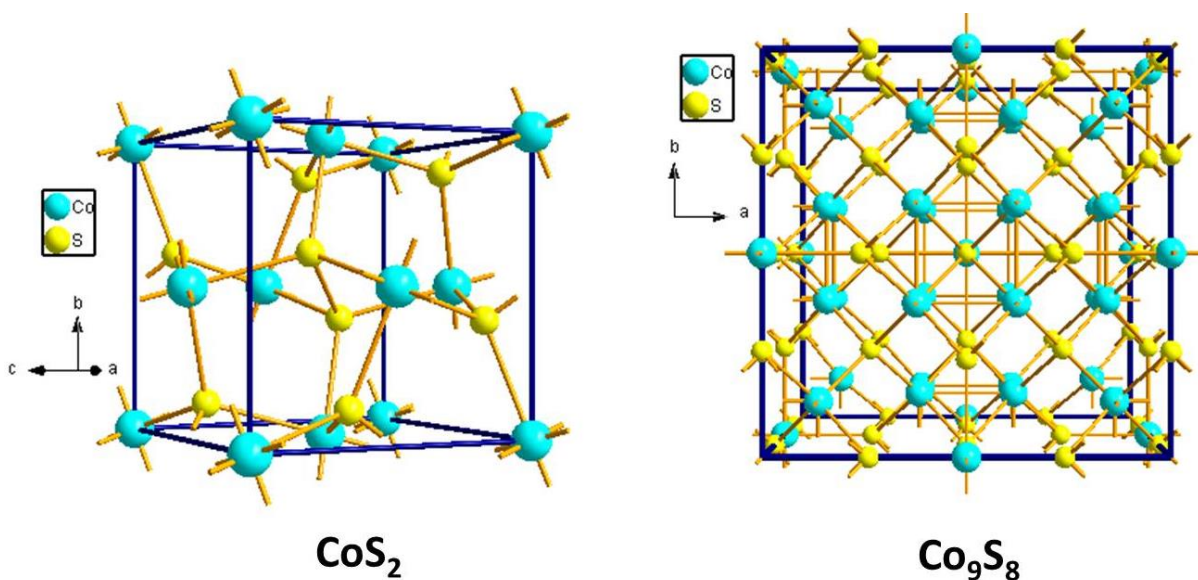


**Figure 2** Crystal structure of  $\text{CoS}_2$  and  $\text{Co}_9\text{S}_8$

$\text{Co}_9\text{S}_8$  is peritectically formed at 1108 K with a narrow homogeneity range. It crystallizes in the cubic structure. There has been some work on the magnetic properties of this compound. Lotgering has showed it to follow Curie-Weiss law between 150 and 300 K. He concludes that the compound is an antiferromagnet with  $\theta = -50$  K. Heidelberg *et al.* observes the material to exhibit Néel temperature near 300 K above which it follows Curie-Weiss law.<sup>1</sup> Stoichiometric CoS is difficult to achieve but there has been studies on  $\text{Co}_{1-x}\text{S}$  which exists in NiAs-type structure as well as NiAs superlattice.<sup>1-2</sup> Below 748 K, it disproportionates into  $\text{Co}_9\text{S}_8$  and  $\text{Co}_4\text{S}_3$ . It exhibits nearly temperature independent paramagnetism consisting of itinerant  $\sigma^*$ -electrons.  $\text{Co}_3\text{S}_4$  has spinel structure with  $\text{Co}^{2+}$  in the tetrahedral sites according to NMR studies.<sup>3</sup> It is Pauli paramagnetic with metallic conduction ( $3 \times 10^{-4}$  ohm-cm at 300 K).<sup>4</sup>  $\text{CoS}_2$ , as already mentioned, has the pyrite-type structure. It exhibits ferromagnetic properties below 120 K and is metallic.

Bulk polycrystalline materials of these phases are synthesized by heating elemental sulphur and cobalt together in silica ampoules. Corresponding single crystals are prepared by adding flux such as  $\text{CoBr}_2$  in addition to elemental reactants. Recently, chemical synthesis of nanoparticles and submicron sized particles of phases like  $\text{CoS}_2$ , CoS and  $\text{Co}_9\text{S}_8$  are carried out hydrothermally

at relatively lower temperatures (120-230 K). Bao *et al.* demonstrated bio-assisted CoS nanowires synthesis hydrothermally by using cysteine as the sulphur source.<sup>5</sup> The same sulphur source is used to synthesized  $\text{CoS}_2$  nanoparticles on graphene surface.<sup>6</sup> CoS nanocrystals are grown on graphene hydrothermally starting with thioacetamide as the sulphur source for supercapacitor applications.<sup>7</sup> Other sulphur sources used for the synthesis of cobalt sulphide nanostructures are thiourea,<sup>8</sup>  $\text{H}_2\text{S}$ ,<sup>8</sup>  $\text{Na}_2\text{S}$ ,<sup>9-10</sup>  $\text{Na}_2\text{S}_2\text{O}_3$ ,<sup>11</sup> *etc.*

## 2. Scope of the present investigation

Pyrite type  $\text{CoS}_2$  is particularly interesting in the cobalt-sulphur phase diagram for its interesting magnetic and electronic properties. Properties of bulk polycrystals and single crystals have been extensively studied but the studies of corresponding properties of nanocrystalline  $\text{CoS}_2$  are scarce in the literature. Herein, we have demonstrated the single precursor synthesis of  $\text{CoS}_2$  nanoparticles by the decomposition of cobalt-thiourea complex yet retaining the bulk-like transport properties. We have also investigated electrical and magnetic properties of bulk  $\text{Co}_9\text{S}_8$  prepared by heating the complex at 1000 °C.

## 3. Experimental section

### 3.1 Synthesis of $[\text{Co}(\text{tu})_4(\text{NO}_3)_2]$

Synthesis of  $[\text{Co}(\text{tu})_4(\text{NO}_3)_2]$  was carried out following a previously reported procedure.<sup>12</sup> In a typical synthesis,  $\text{Co}(\text{NO}_3)_2 \cdot 6\text{H}_2\text{O}$  (2.91 g, 0.01 mol) was dissolved in 25 mL of red hot butanol. 3.04 g (9.04 mol) of thiourea was added and the mixture was heated to boiling, until all solid had dissolved. The color of the solution changed from red to blue. On cooling, a blue solid separated. This was suction filtered, washed with ether, dried under vacuum and then recrystallised from ethyl acetate. This produced large green-blue crystals which were dried under vacuum at 100 °C.

### 3.2 Synthesis of cobalt sulphide phases

Cobalt-thiourea complex was heated at different temperatures in the nitrogen flow in a tubular furnace. The complex was heated at different temperatures between 400 and 1000 °C for 2 h in nitrogen atmosphere to obtain several phases of cobalt sulphide.

### 3.3 Characterization

X-ray diffraction patterns were obtained from Bruker D8 Discover and Rigaku 99 diffractometers. Rietveld refinement was carried out using *FullProf* software. Transmission electron microscopy images were taken from JEOL JEM 3010 fitted with Gatan CCD camera operating at accelerating voltage of 300 kV. Magnetic properties were studied using SQUID VSM, Quantum Design, USA. DC electrical resistivity measurements were carried out in Physical Property Measurement System (PPMS), Quantum design, USA. Experiment for thermogravimetric analysis (TGA) was conducted in Mettler Toledo Star system.

## 4. Results and discussion

Several thiourea complexes of cobalt are known. Cotton *et al.* carried out detailed synthesis and characterization of  $\text{Co}(\text{CH}_4\text{N}_2\text{S})_2\text{Cl}_2$ ,  $\text{Co}(\text{CH}_4\text{N}_2\text{S})_2\text{Br}_2$ ,  $\text{Co}(\text{CH}_4\text{N}_2\text{S})_4(\text{NO}_3)_2$ ,  $\text{Co}(\text{CH}_4\text{N}_2\text{S})_3\text{SO}_4$  and  $\text{Co}(\text{CH}_4\text{N}_2\text{S})_4(\text{ClO}_4)_2$ .<sup>13</sup> Here, we choose the most volatile of them,  $\text{Co}(\text{CH}_4\text{N}_2\text{S})_4(\text{NO}_3)_2$ , (b.p. 127 °C) for thermal decomposition in order to obtain different phases of cobalt sulphide.

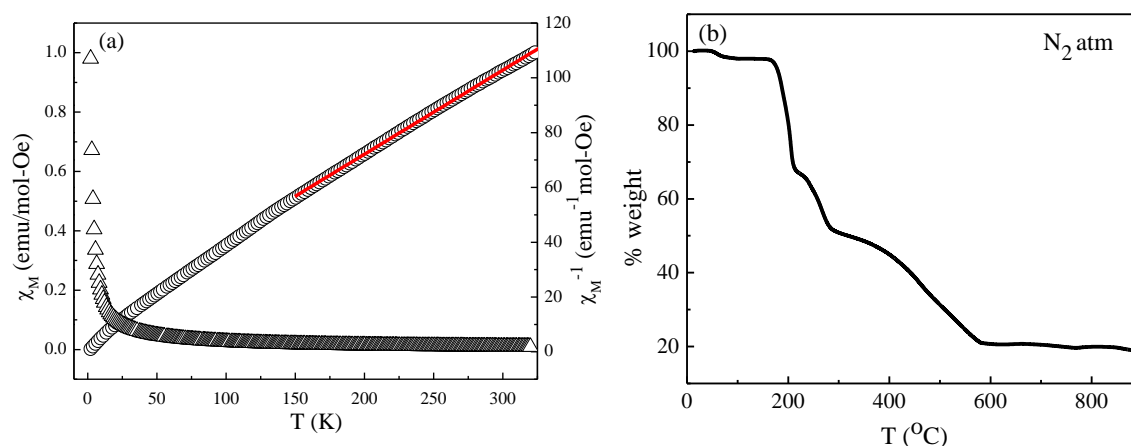


**Figure 3 (a) Magnetic susceptibility and (b) TGA plot of Co-thiourea complex**

The complex exhibits paramagnetic behavior down to the lowest measured temperature (2 K). The susceptibility and inverse susceptibility plots are shown in Figure 3(a). The effective paramagnetic moment per formula unit is calculated at 300 K by using the relation:  $\mu_{\text{eff}} = 2.83(\chi_M \cdot T)^{1/2}$ . The observed  $\mu_{\text{eff}}$  is 4.84 B.M. which is close to the earlier report of 4.75 B.M for

high spin  $\text{Co}^{2+}$ .<sup>12</sup> This confirms the absence of any magnetic impurity as well as the unreacted starting material.

Figure 3(b) shows the TGA data of  $\text{Co}(\text{CH}_4\text{N}_2\text{S})_4(\text{NO}_3)_2$  in nitrogen atmosphere obtained by ramping the temperature at a speed of  $10\text{ }^\circ\text{C}/\text{min}$ . Till  $200\text{ }^\circ\text{C}$  the complex is almost stable apart from a small weight loss because of removal of absorbed water and/or alcohol. Near  $200\text{ }^\circ\text{C}$  there is a sudden weight loss because of the decomposition of the complex with the evolution of gases containing nitrogen and sulphur. This is continued till  $280\text{ }^\circ\text{C}$  after which the weight loss becomes gradual. The region between  $280\text{ }^\circ\text{C}$  and  $580\text{ }^\circ\text{C}$  is perhaps due to the removal of sulphur from already formed cobalt sulphide phases. After  $600\text{ }^\circ\text{C}$ , the weight loss is very slow which implies that low sulphur content phases like  $\text{CoS}$  and  $\text{Co}_9\text{S}_8$  would be stable for wide range of temperature. In contrast, high sulphur containing phase like  $\text{CoS}_2$  could be stabilized for a narrow range of temperature because of the steeper change in the weight loss at low temperature.

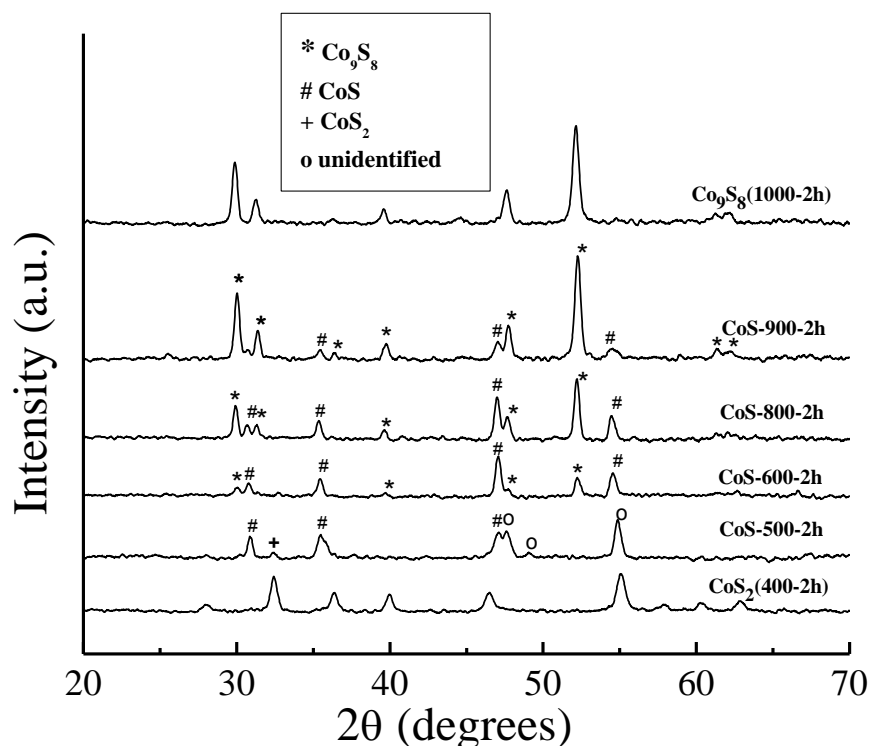


**Figure 4 XRD patterns of cobalt sulphide phases obtained at different temperatures**

The thermal decomposition of the Co-thiourea complex is carried out at different temperatures in order to obtain different phases of cobalt sulphide (Figure 4). Such strategy to obtain metal

sulphides which involves single precursor solution-free approach is not very well explored in the literature. We have demonstrated phase evolution of different nickel sulphide phases using this strategy in Chapter V.1.<sup>14</sup> When the complex is heated at 400 °C for 2 h in nitrogen atmosphere, nanocrystalline pyrite-type cubic  $\text{CoS}_2$  (space group,  $Pa-3$ ) is obtained. The XRD pattern of  $\text{CoS}_2$  nanoparticles is shown in Figure 5(a). Crystallite size of the  $\text{CoS}_2$  nanoparticles is obtained to be 23 nm using Scherrer's formula. For making other phases of cobalt sulphide, we heated the complex at higher temperatures till 1000 °C. Figure 4 shows XRD patterns of samples obtained at different temperatures. At 500 °C,  $\text{CoS}_2$  phase almost disappears with major contributions from an unknown phase and NiAs-type hexagonal  $\text{CoS}$ . This unknown phase does not match to any of the reported phase in the Co-S phase diagram and could be attributed to a nonstoichiometric composition.  $\text{CoS}$  is the only major phase with a small amount of  $\text{Co}_9\text{S}_8$  at 600 °C.  $\text{CoS}$  is present at temperatures as high as 900 °C although in small amount along with  $\text{Co}_9\text{S}_8$  (major phase). At 1000 °C, pure phase of  $\text{Co}_9\text{S}_8$  is obtained.

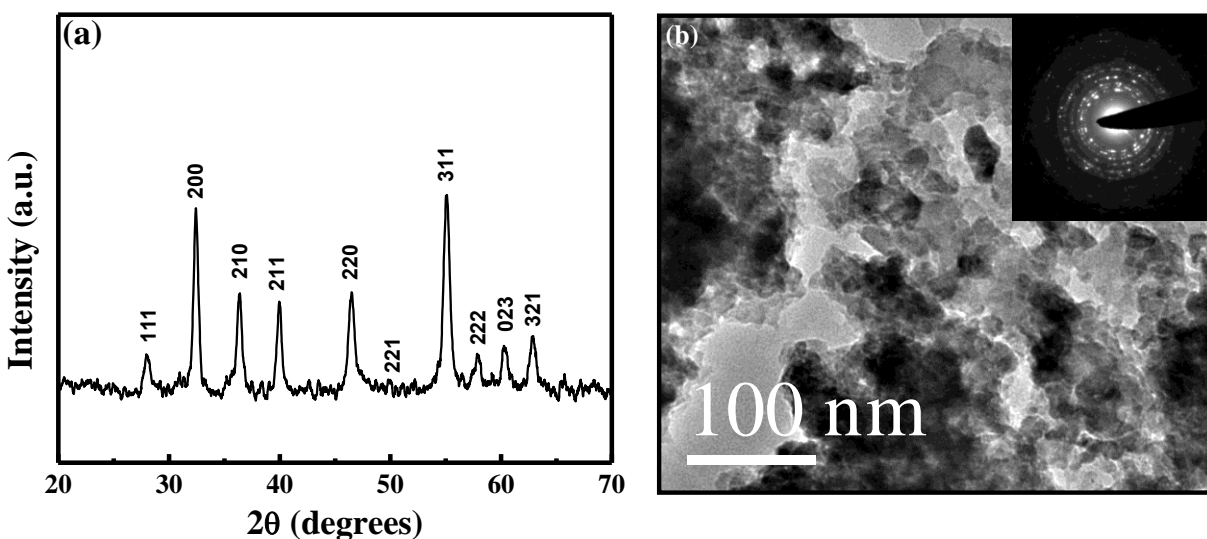


Figure 5(a) XRD pattern and (b) TEM image of  $\text{CoS}_2$  nanoparticles with electron diffraction pattern in the inset

TEM image of  $\text{CoS}_2$  nanoparticles is shown in Figure 5(b). The average size of the particles is  $\sim 20$  nm with no defined morphology. Dots in the electron diffraction pattern reveal the crystalline nature of the particles. Figure 6(a) shows the zero field cooled (ZFC) and field cooled (FC) magnetizations of  $\text{CoS}_2$  nanoparticles obtained at an applied magnetic field of 100 Oe. It undergoes a ferromagnetic transition at 121.5 K ( $T_C$ ) which is consistent with the previous

studies of bulk  $\text{CoS}_2$  phases. Surprisingly, Lei *et al.* reported a  $T_C$  of 140 K for a composition  $\text{CoS}_{1.93}$  and attributed the increase in the  $T_C$  due to the sulphur vacancies as compared to the bulk  $\text{CoS}_2$ . There are no further reports on the magnetic properties of  $\text{CoS}_2$  nanoparticles. Near-120 K  $T_C$  in our nanocrystalline material rules out the possibility of nonstoichiometry. Another main feature of the ZFC-FC magnetizations is the large divergence at low temperature compared to the bulk material which can be attributed to the surface anisotropy of the nanoparticles. According to Coey and coworkers,<sup>15</sup> due to the competition between surface and bulk magnetocrystalline anisotropy the spins at the surface tend to orient normal to the surface while the spins inside the bulk remain parallel to each other. The effect of surface anisotropy is also observed in the magnetic hysteresis of nanocrystalline  $\text{CoS}_2$  as shown in Figure 6(b). Inset of Figure 6(b) shows the enlarged view of the magnetization near the origin. The value of coercive field ( $H_C$ ) is  $\sim 100$  Oe at 2 K which is otherwise non hysteretic in the bulk form. The value of  $H_C$  decreases as the temperature is increased and almost vanishes near  $T_C$ . Unlike the bulk phase where the saturation magnetization ( $M_S$ ) is  $\sim 0.84$  B.M.,  $\text{CoS}_2$  nanocrystals exhibit a value of 0.61 B.M., which is

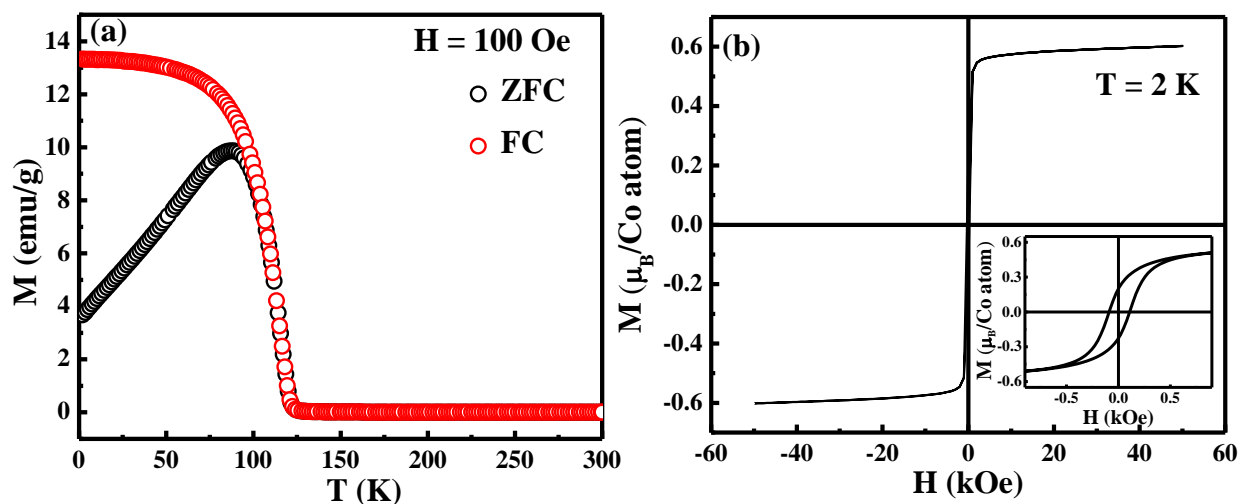


Figure 6(a) ZFC-FC magnetization and (b) isothermal magnetization of  $\text{CoS}_2$  nanoparticles at 2 K with inset showing the enlarged view of magnetization near the origin

around 25 % less. Such a decrease in the magnetization is often observed in the ferromagnetic nanoparticles because of the surface disorder.

$\text{CoS}_2$  is a metallic ferromagnet. Figure 7(a) shows the resistivity of  $\text{CoS}_2$  nanoparticles as a function of temperature in the cold pressed form using four probe technique. Interestingly,

connectivity among the nanoparticles is sufficient enough to exhibit metallic behavior down to the magnetic transition temperature. Such a behavior is rare in the bulk electrical resistivity measurements of otherwise intrinsically conducting nanoparticles and they are often observed to be showing semiconducting property because of electron hopping between loosely connected grains. We observe an anomaly in the resistivity corresponding to the ferromagnetic transition ( $\sim 120$  K). A broad hump is observed because of the increase in the resistivity below the transition temperature which again decreases at low temperature. A similar but much sharper hump is observed in bulk  $\text{CoS}_2$ . The origin of this anomaly is because of a very interesting property of  $\text{CoS}_2$ , which is its transformation to a half metal below  $T_C$ . Turning to a half metal implies that due to exchange splitting the density of states for minority spins near the Fermi level decreases drastically which therefore increases the resistivity. Effect of magnetic field on resistivity of bulk  $\text{CoS}_2$  has been studied in detail but the same has not been explored in nanoparticles.<sup>16-19</sup> Figure 7(b) shows magnetoresistance of cold pressed  $\text{CoS}_2$  nanoparticles in a configuration where the magnetic field is applied perpendicular to the current direction. Magnetoresistance of 6.5 % is observed at 115 K and 5 T which varies almost linearly with respect to field. At 70 K there is a negative contribution at low field but as the field is increased positive contribution takes over. At a temperature significantly higher than the  $T_C$ , resistivity does not depend on the magnetic field. The negative contribution is due to the spin orientation effect of H while the positive

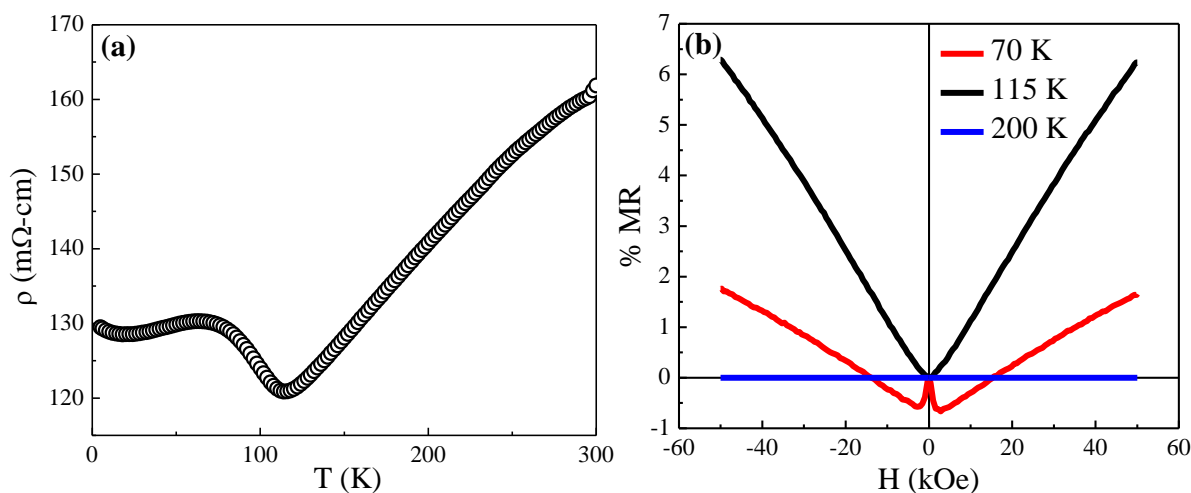
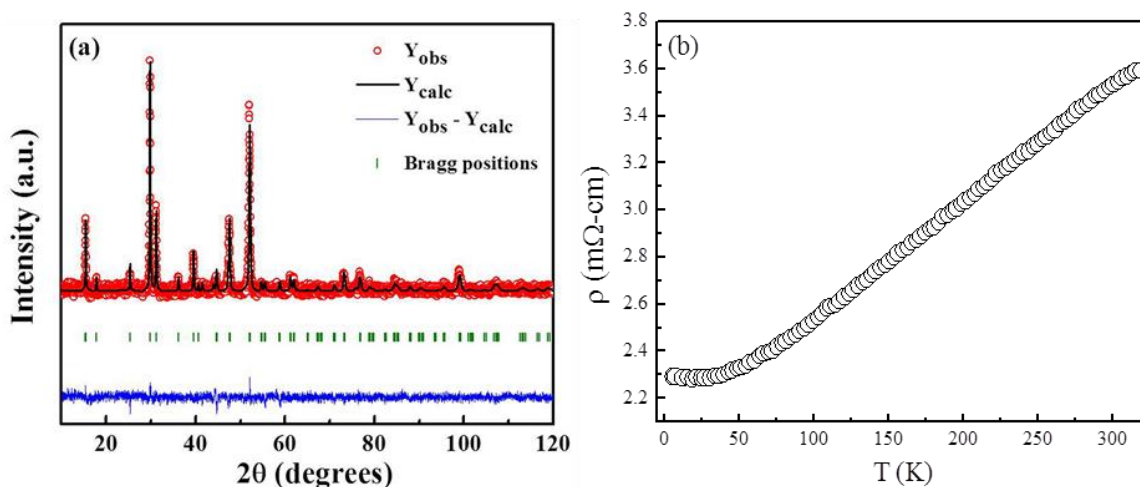


Figure 7(a) Resistivity of  $\text{CoS}_2$  nanoparticles as a function of temperature and (b) magnetoresistance at fixed temperatures

contribution can be explained by the Lorentz force magnetoresistance. It has also been shown that magnetoresistance diverges near the transition temperature.<sup>19</sup>



**Figure 8(a) XRD pattern and (b) temperature dependent resistivity of  $\text{Co}_9\text{S}_8$**

$\text{Co}_9\text{S}_8$  is the high temperature phase in the Co-S phase diagram which forms peritectically at 835 °C. We obtain a pure phase of  $\text{Co}_9\text{S}_8$  on decomposing the Co-thiourea complex at 1000 °C.  $\text{Co}_9\text{S}_8$  crystallizes in a face centred cubic structure (space group,  $Fm-3m$ ). It consists of cubic closed packed sulphur atoms with one cobalt atom in each of the tetrahedral holes and the ninth cobalt atom occupies an octahedral hole. Figure 8(a) shows the XRD pattern of  $\text{Co}_9\text{S}_8$  at room temperature. Cell parameter of  $\text{Co}_9\text{S}_8$  as obtained from Le Bail fitting is 9.9282(9) Å. Scherrer's formula is used to obtain the crystallite size which is found to be ~ 70 nm. We cold-press the powder and measure the resistivity as a function of temperature by employing four probe technique. It shows a metallic behavior throughout the temperature range with a resistivity value of 3.5 mohm-cm at 300 K as shown in Figure 8(b). Figure 9(a) shows ZFC-FC magnetizations of  $\text{Co}_9\text{S}_8$  at 100 Oe applied field. Unlike the finding of Lotgering *et al.* wherein Curie-Weiss law is observed between 150 and 300 K, we find an entirely different behaviour. There is a strong irreversibility between ZFC-FC curves and hysteresis at room temperature (inset of Figure 9(a)) indicating ferromagnetism at room temperature. The observation of high magnetic ordering temperature in transition metal sulphides is uncommon. Therefore, the observed ferromagnetism could be due to cobalt metal. However, we do not see any impurity peak in X-ray diffraction pattern. Moreover, the obtained saturation magnetization at room temperature is ~ 10% of cobalt metal. Such a high amount of cobalt metal should be seen in x-ray diffraction.



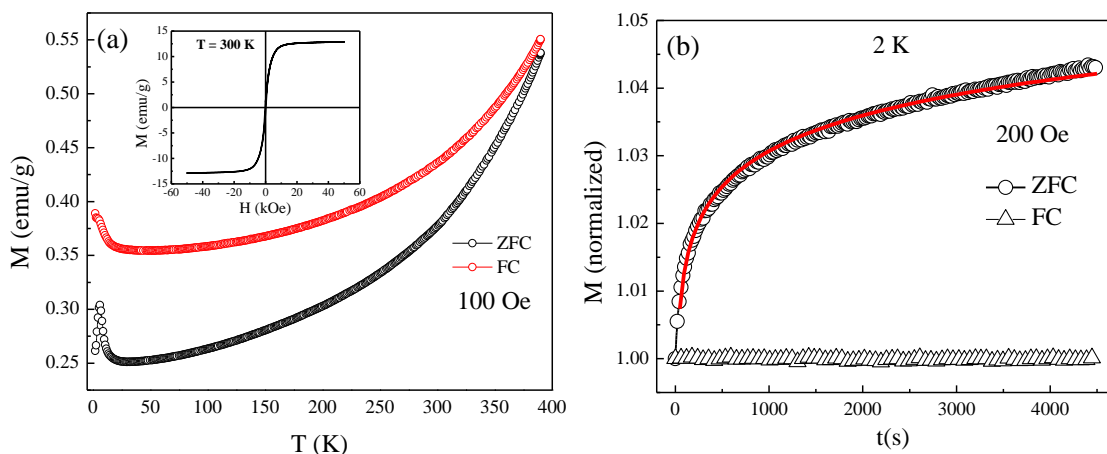


**Figure 9 (a) ZFC-FC magnetization of  $\text{Co}_9\text{S}_8$  at 100 Oe with inset showing room temperature hysteresis and (b) magnetization versus time plot in ZFC and FC conditions at 2 K and 200 Oe**

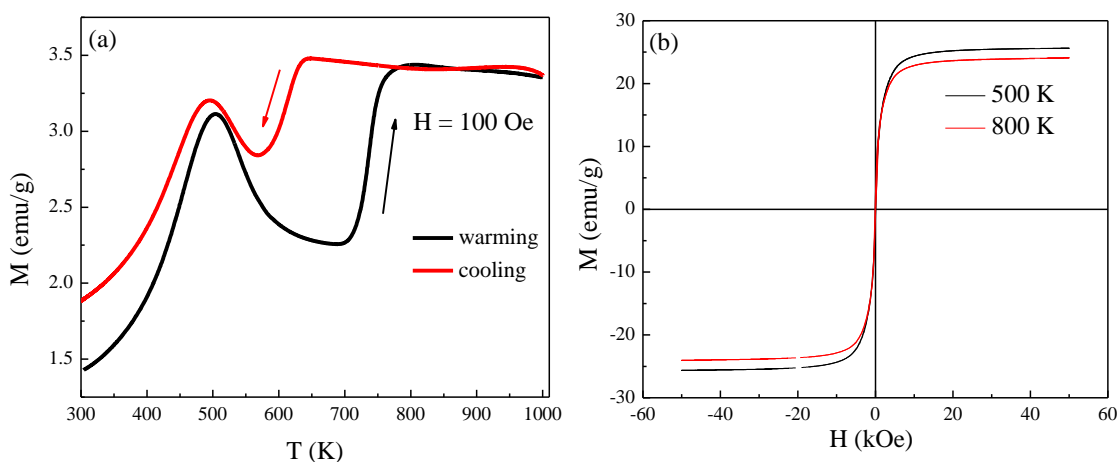


**Figure 10 High temperature magnetization of  $\text{Co}_9\text{S}_8$  while cooling and warming, (b) magnetic hysteresis loops at 500 and 800 K**

At low temperature ( $\sim 5$  K), a peak in the ZFC magnetization is observed. To verify whether this peak indicates a spin glass state, we have performed relaxation measurements. At 2 K and under ZFC conditions, a strong relaxation is observed in the magnetization versus time plot while under FC conditions there is almost no relaxation (Figure 9(b)). The relaxation behaviour under ZFC conditions is fitted with the equation  $M = -1 + 2t^\gamma$  where  $\gamma$  signifies the extent of relaxation. We obtain a  $\gamma$  value of 0.0037 which is comparable to alloys like  $\text{Au}_{82}\text{Fe}_{18}$  known for exhibiting strong relaxation behaviour.<sup>20</sup> At 30 K, we do not observe any relaxation under ZFC conditions which confirms the low temperature peak ( $\sim 5$  K) to be due to spin freezing. We have performed

high temperature magnetization of Co<sub>9</sub>S<sub>8</sub> while cooling and warming till 1000 K (Figure 10(a)). In both the conditions magnetization increases until 500 K where it peaks followed by a sharp increase at high temperature. On warming, this transition takes place just above 700 K while on cooling it shifts to 600 K. It requires further investigation in order to understand the above magnetic transitions. We observe ferromagnetic-like hysteresis loop at 500 and 800 K (Figure 10(b)).

## **5. Conclusions**

Decomposition of Co-thiourea complex at 400 °C leads to the formation of pyrite type cubic CoS<sub>2</sub> nanoparticles. It exhibits metallic behaviour with a ferromagnetic transition at 122 K. Near this transition, a magnetoresistance of 6.5 % is observed which might have contributions from both intrinsic as well as extrinsic effects. At moderate temperatures a mixture of CoS and Co<sub>9</sub>S<sub>8</sub> phases is obtained. Bulk Co<sub>9</sub>S<sub>8</sub> obtained at 1000 °C exhibits metallic behaviour and ferromagnetic ordering at room temperature. It shows spin glass behaviour below 5 K with strong relaxation.

## 6. References

1. R. F. Heidelberg, A. H. Luxem, S. Talhouk and J. J. Banewicz, *Inorg. Chem.* **1966**, *5*, 194-197.
2. C. N. R. Rao and K. P. R. Pisharody, *Prog. Solid State Chem.* **1976**, *10*, 207-270.
3. P. Locher, *Z. Angew. Phys.* **1968**, *24*, 277-280.
4. R. J. Bouchard, P. A. Russo and A. Wold, *Inorg. Chem.* **1965**, *4*, 685-688.
5. S.-J. Bao, C. M. Li, C.-X. Guo and Y. Qiao, *J. Power Sources* **2008**, *180*, 676-681.
6. B. Wang, J. Park, D. Su, C. Wang, H. Ahn and G. Wang, *J. Mater. Chem.* **2012**, *22*, 15750-15756.
7. B. Qu, Y. Chen, M. Zhang, L. Hu, D. Lei, B. Lu, Q. Li, Y. Wang, L. Chen and T. Wang, *Nanoscale* **2012**, *4*, 7810-7816.
8. M. Lei, X. L. Fu, H. J. Yang, Y. G. Wang, Y. B. Zhang and P. G. Li, *J. Nanosci. Nanotechnol.* **2012**, *12*, 2586-2590.
9. G. H. Yue, P. X. Yan, X. Y. Fan, M. X. Wang, D. M. Qu, Z. G. Wu, C. Li and D. Yan, *Electrochem. Solid-State Lett.* **2007**, *10*, D29-D31.
10. Q. Wang, L. Jiao, H. Du, Y. Si, Y. Wang and H. Yuan, *J. Mater. Chem.* **2012**, *22*, 21387-21391.
11. J. S. Jirkovský, A. Björling and E. Ahlberg, *J. Phys. Chem. C* **2012**, *116*, 24436-24444.
12. F. A. Cotton, O. D. Faut and J. T. Mague, *Inorg. Chem.* **1964**, *3*, 17-21.
13. F. A. Cotton, O. D. Faut and J. T. Mague, *Inorg. Chem.* **1964**, *3*, 17-21.
14. N. Kumar, N. Raman and A. Sundaresan, *J. Solid State Chem.* **2013**, *208*, 103-108.
15. Y. Labaye, O. Crisan, L. Berger, J. Greneche and J. Coey, *J. Appl. Phys.* **2002**, *91*, 8715-8717.
16. S. Hebert, E. Guilmeau, D. Berthebaud, O. I. Lebedev, V. Roddatis and A. Maignan, *J. Appl. Phys.* **2013**, *114*, 103703-103703-6.
17. L. Wang, T. Y. Chen and C. Leighton, *Phys. Rev. B* **2004**, *69*, 094412.
18. L. Wang, T. Y. Chen, C. L. Chien and C. Leighton, *Appl. Phys. Lett.* **2006**, *88*, 232509-232509-3.
19. S. Yomo, *J. Phys. Soc. Jpn.* **1979**, *47*, 1486-1494.
20. S. B. Roy and M. K. Chattopadhyay, *Phys. Rev. B* **2009**, *79*, 052407.

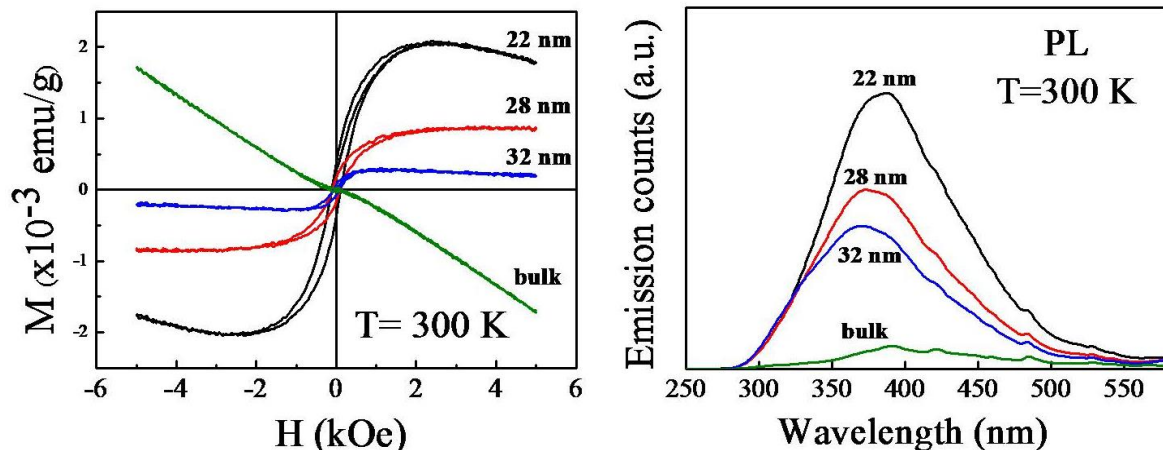


## Chapter V.3

### Investigation of ferromagnetism in MgO nanoparticles\*

#### Summary

Positron annihilation spectroscopy has been used to explore the nature of defects and to estimate the defect concentrations in ferromagnetic MgO nanoparticles. Our experimental results show that Mg vacancies are present at the concentration of  $3.4 \times 10^{16} \text{ cm}^{-3}$  in the nanocrystalline MgO which is halved in the bulk sample. This is in correlation with the decrease of the intensity of blue luminescence and the saturation magnetic moment with increasing particle size. These results clearly demonstrate that the ferromagnetism in MgO nanoparticles arises from Mg vacancies at the surface of the particles. In addition, effect of Li doping on the magnetic properties of MgO nanoparticles have been studied. The results show that 10 % Li doping in MgO nanoparticles almost doubles the value of saturation magnetization at room temperature.



\* A paper based on this work has appeared in *Chem. Phys. Lett.*, 2009

## 1. Introduction

Very many oxide systems have been reported to show ferromagnetism in nanoscale in recent past. Among them, investigation of ferromagnetism in MgO nanoparticles is particularly interesting because of its very simple rock salt type structure. Moreover MgO is very ionic. Due to the same reason many theoretical work based on first principle calculations have been carried out in order to explain ferromagnetism in alkaline earth metal oxides like MgO and CaO.<sup>1-5</sup> In fact ferromagnetism in CaO with cation vacancies was predicted much earlier than its experimental verification.<sup>1</sup> It has been shown that ferromagnetism in MgO appears due to neutral Mg vacancies. One advantage in working with MgO nanoparticles is, unlike other alkaline earth metal oxides it does not absorb atmospheric CO<sub>2</sub>. Synthesis and characterization of MgO nanoparticles are hence not troublesome. In addition to the defects arising at the surface of the nanoparticles naturally, doping d<sup>0</sup> cations of different valency can further increase the amount of defects. Effect of such doping on the ferromagnetic properties of MgO will improve our understanding of magnetism in otherwise nonmagnetic inorganic materials.

MgO crystallizes in rock salt type structure with one Mg surrounded by six O atoms and vice-versa. Generally, there are two kinds of point defects in MgO, which are O vacancy (V<sub>O</sub>) and Mg vacancy (V<sub>Mg</sub>).<sup>3-4</sup> Effects of both the defect types have been studied in the literature by first-principles calculations. As expected, density of states (DOS) of pure MgO where spin up and spin down bands are same give net zero moment where the valence band is composed of 2p orbital of oxygen, which is completely filled and the conduction band is formed mainly by 3s orbital of Mg, which is completely empty. Similarly, V<sub>O</sub> results in zero polarization. Unlike V<sub>O</sub>, V<sub>Mg</sub> leads to spin polarization where Fermi level moves to lower energy with empty states at the top of the valence band. Asymmetry in the spin up and spin down DOS results in local magnetic moments coming mainly from spin polarization of O 2p orbitals.

## 2. Scope of the present investigation

In the present work we further attempt to understand the ferromagnetism in MgO nanoparticles. Nature and concentration of defects can give an insight to look at this problem

in deeper a sense. For this regard, we have chosen two of the most potent tools namely photoluminescence and positron annihilation spectroscopy in order to investigate the nature and the concentration of defects.

### **3. Experimental section**

MgO nanoparticles were synthesized using high purity (99.99%) magnesium acetate tetrahydrate  $(\text{CH}_3\text{COO})_2\text{Mg}\cdot 4\text{H}_2\text{O}$ , polyvinyl pyrrolidone (PVP) and ethylctene glycol (EG, 99.5%) as starting materials as reported earlier.<sup>6</sup> A simple scheme for the synthesis of MgO 0.05 mol of magnesium acetate tetrahydrate and 0.3 mmol of PVP as capping agent were dissolved in EG in a round bottom flask connected to condenser. The solution was refluxed at 200 °C with constant stirring for 2 h to get a white flocculate. The reaction mixture was allowed to cool down to room temperature. The flocculate was collected by centrifuging the reaction mixture at 6000 rpm followed by washing with distilled water and then ethanol to remove remaining PVP and EG. Final drying of the flocculate was done at 80 °C in an oven to get magnesium oxide precursor. Precursor was calcined at 650, 750 and 850 °C for 2 h in oxygen atmosphere to form magnesium oxide nanoparticles of different sizes in a tube furnace. Bulk magnesium oxide was prepared by palletizing the nanoparticles followed by sintering at 1450 °C in air in a box furnace. All the heat treatments of precursor were done in alumina boat. Precautions were taken to avoid any metallic contacts with the sample in order to avoid extrinsic magnetic contamination. For the study of Li doping in MgO, the samples were prepared as follows: 6.4102 g of  $\text{Mg}(\text{NO}_3)_2\cdot 6\text{H}_2\text{O}$  was dissolved in 20 ml ethanol. A dilute aqueous solution of KOH (0.001 M) was added drop-wise with constant stirring in order to precipitate magnesium nitrate. A thick gel was obtained which was centrifuged at 4000 rpm followed by several cycles of washing first with distilled water and then with ethanol. The white product (precursor) was dried at 80 °C for 4 h. Precursor was divided into two parts. The first part of which was mixed with stoichiometric amount (10 %) of  $\text{LiNO}_3$  followed by heating at 650 °C in oxygen atmosphere for 4 h to obtain Li-doped MgO nanoparticles. The second part was directly heated at 650 °C in oxygen atmosphere for 4 h to obtain undoped MgO nanoparticles.

## 4. Results and discussion

### 4.1 Undoped MgO nanoparticles

XRD patterns of MgO nanoparticles annealed at different temperatures, as shown in Figure 1, confirm that the sample is single phase with cubic structure. Peaks become broader with the increase in size of nanoparticles. Scherrer's formula was used to calculate crystallite size from peak broadening which comes about 22 nm for the sample annealed at 650 °C. The average particle size increases to 28, 32 nm for the sample annealed at 850 and 950 °C respectively. The sample sintered at 1450 °C shows sharp lines in XRD pattern which is typical of bulk crystalline sample.

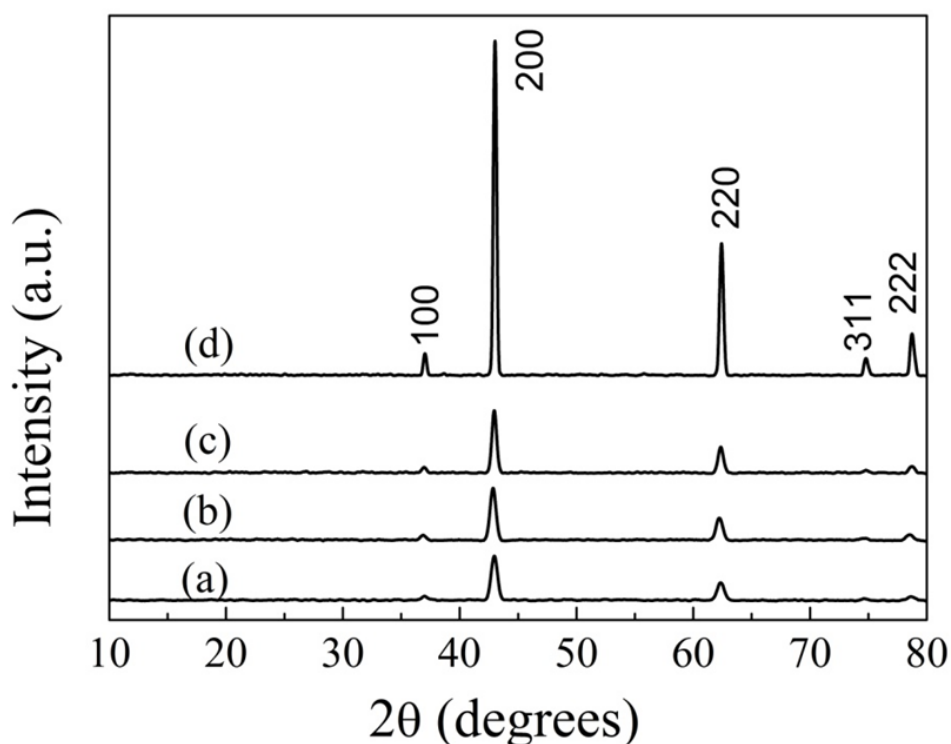


**Figure 1** XRD patterns of MgO nanoparticles and bulk

These results are in agreement with FESEM images as shown in Figure 2. FESEM images show that nanoparticles are agglomerated which is due to the annealing the precursor at high temperature. As the annealing temperature is increased agglomeration in the sample also increases (Figures 2(a)-(c)). The bulk sample which is formed by heating the nanoparticles sample at 1450 °C for 24 hours is micron sized (Figure 2(d)). The particle sizes observed



from the FESEM images agree well with the calculated value as obtained from the Scherrer's formula.

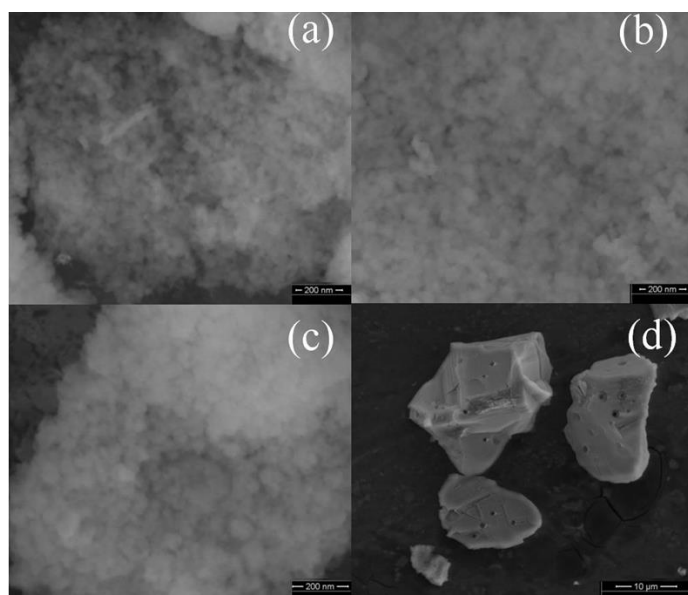


Figure 2 FESEM images of MgO nanoparticles and bulk

The results of magnetization measurements performed at 300 K on the three nanoparticles and bulk MgO are shown in Figure 3(a). All the nanoparticles show ferromagnetic hysteresis at room temperature. The saturation magnetization ( $2.04 \times 10^{-3}$  emu/g) is higher for the 22 nm sample. As the average particle size increases, the value of saturation magnetization decreases which is consistent with the earlier suggestion that magnetism comes from surface defects which decreases with increase of particles size due to decrease in surface to volume ratio.<sup>7</sup>

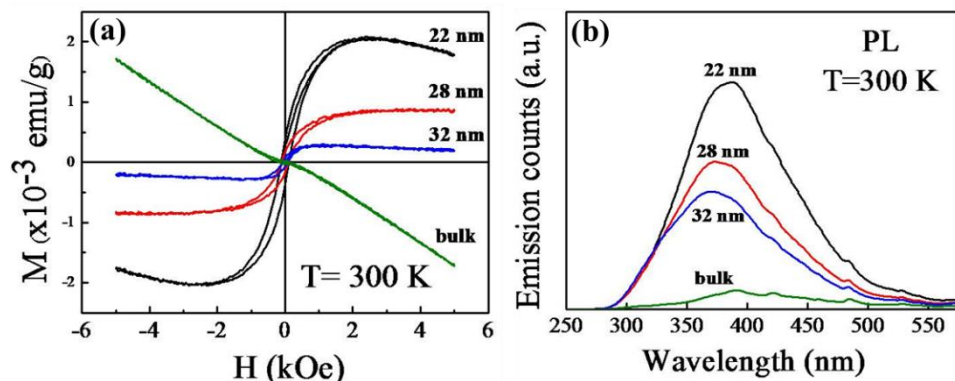


Figure 3(a) Magnetic hysteresis loops, (b) PL spectra of nanoparticles and bulk

The bulk sample which was heated at 1450 °C shows diamagnetic behaviour as expected. In all the curves for nanoparticles samples diamagnetic contribution is subtracted. Diamagnetic contribution essentially comes from the bulk of the nanoparticles, brown tape and sample holder. Diamagnetic correction can be made by subtracting the bulk sample magnetic contribution performed with almost equal amount of brown tape.

Optical properties of nanomaterials provide important information about the surface states. It is known that nanocrystals of MgO show a broad photoluminescence (PL) spectrum in the blue region due to low coordinated surface ions or defects.<sup>8-11</sup> It should be noted that bulk MgO does not show such luminescence spectrum consistent with relatively low concentration of surface defects. Figure 3(b) shows PL spectra of the three nanoparticles and the bulk sample excited at the wavelength 225 nm. It can be seen that there is a broad peak centered around 370 nm whose intensity decreases with increase of particle size. Such a broad PL peak has already been reported in the literature and has been attributed to defects. In the present work, the observation that the peak intensity decreases with increase of particle size suggests that the concentration of surface defect decreases with increasing particle size.

In order to find the nature of defect and estimate its concentration, positron annihilation spectroscopy has been used. Table 1 shows the value of positron lifetimes, their corresponding intensities and finally the defect concentrations of 22 nm particles and bulk sample. The free fitting of all the positron lifetime spectra for both the samples (bulk and sample annealed at 650 °C) are found to be best fitted (variance of fit is less than 1 per channel) with three lifetime components yielding a very long lifetime component ( $\tau_3$ ) with intensity ( $I_3$ ) of  $5 \pm 0.2$  %. This component is due to the formation of orthopositronium and its subsequent decay as parapositronium by pick-off annihilation processes.

Positronium formation is always favourable in polycrystalline samples due to the presence of microvoids. The short lifetime component ( $\tau_1$ ) of  $161 \pm 4$  ps and  $168 \pm 4$  ps for bulk and the 22 nm MgO sample respectively is generally attributed to the free annihilation of positrons. Theoretically calculated free positron lifetime in bulk MgO is 166 ps which is in agreement with the presently observed values. The most important lifetime component is the intermediate one,  $\tau_2$ , which arises from the annihilation of positrons at defect sites. In the

present case  $\tau_2$  is found to be  $\sim 385$  ps and 400 ps for the bulk and nanocrystalline MgO, respectively, which is coming from the annihilation of positron in the Mg vacancy type defect or Mg vacancy clusters.

**Table 1 Positron lifetimes and corresponding intensities of 22 nm particles and bulk MgO**

Sample MgO	$t_1$ (ps)	$I_1$ (%)	$t_2$ (ps)	$I_2$ (%)	$t_3$ (ps)	$I_3$ (%)	$V_{Mg}$ (cm <sup>-3</sup> )
Bulk	161±4	70±1	385±10	25±1	1610±50	5±0.2	$1.6 \times 10^{16}$
22 nm	168±4	38±1	400±10	57±1	1730±50	5±0.2	$3.4 \times 10^{16}$

One can have an idea about the defect concentration from  $I_2$ , the intensity of the intermediate lifetime component. It obvious from Table 1, that  $I_2$  which is a measure of defect concentration is higher in nanoparticles (57 %) than that in the bulk sample (25 %). As the grain size decreases more positrons diffuse towards the grain surfaces and trapped in the defect sites present on the surface. Assuming a specific trapping coefficient of  $\mu_v \sim 3 \times 10^{15}$  sec<sup>-1</sup> at 300 K, similar to the Ga vacancy in GaN , the Mg vacancy in MgO has been calculated by the relation  $[V_{Mg}] = N_{at}\mu_v^{-1}\tau_B^{-1}(\tau_{ave} - \tau_B) / (\tau_2 - \tau_{ave})$ , where  $\tau_B$  = bulk positron lifetime,  $\tau_{ave}$  = average positron lifetime,  $\tau_2$  = positron lifetime at defect site,  $N_{at}$  is the atomic density, in case of MgO it is  $\sim 5 \times 10^{22}$  cm<sup>-3</sup>.<sup>12</sup> The Mg vacancy in bulk MgO and nanocrystalline MgO comes out to be  $(V_{Mg})_{Bulk} \sim 1.6 \times 10^{16}$  cm<sup>-3</sup>;  $(V_{Mg})_{Nano} \sim 3.4 \times 10^{16}$  cm<sup>-3</sup>, respectively. Therefore, the suppression of magnetization with increase of particle size is in agreement with the decrease of defect concentration, since  $(V_{Mg})_{Nano} / (V_{Mg})_{Bulk} \sim 2$ .

Figure 4(a) shows the area normalized ratio curve of bulk and nanocrystalline MgO CDBAR spectra with respect to CDBAR spectrum of defects free 99.9999% purity Al sample.<sup>13-16</sup> Both the ratio curves (Figure 4(a)) show a major peak at  $\sim 11 \times 10^{-3}$  m<sub>0</sub>c, which is extended upto  $30 \times 10^{-3}$  m<sub>0</sub>c.

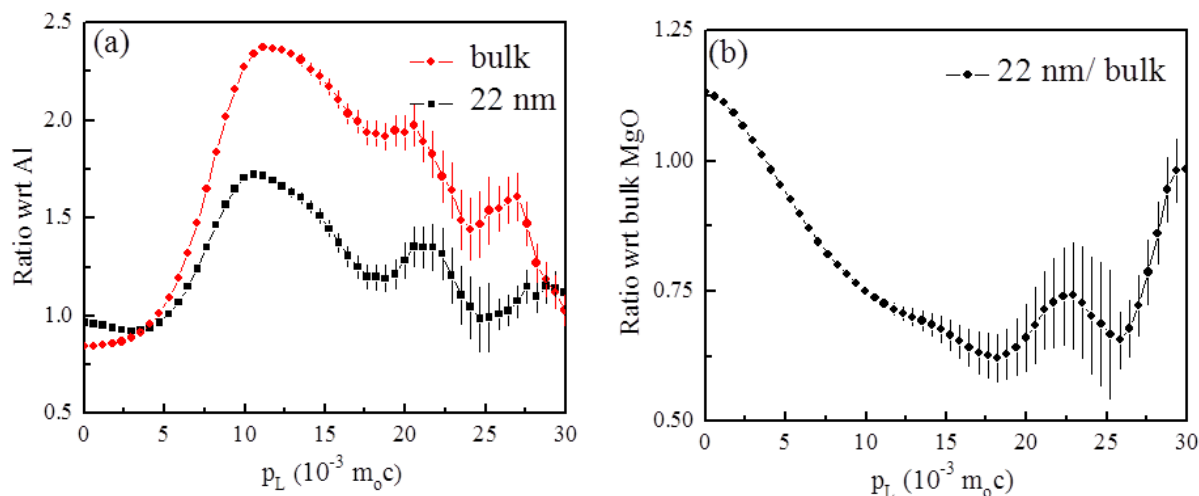


**Figure 4(a)** Area normalized ratio curves of 22 nm and bulk MgO CDBAR spectra with respect to defects free 99.9999 % purity Al CDBAR spectrum. **(b)** Area normalized ratio curve of 22 nm MgO CDBAR spectrum with respect to bulk MgO CDBAR spectrum.

In general, the peak at momentum value  $\sim 11 \times 10^{-3} m_0c$  in the ratio-curve with respect to Al is mainly coming from the annihilation of positrons with the 2p electrons of Oxygen and some contributions coming from the annihilations of core electrons of Mg while the higher momentum region solely represents the annihilation of positrons with the core electrons of Mg.<sup>14</sup> The most significant part of the Figure 4(a) is that throughout the momentum range ( $5 \times 10^{-3} m_0c$  to  $30 \times 10^{-3} m_0c$ ) the ratio-curve for the nano-crystalline MgO is significantly less than that for bulk MgO. This picture is much clear in Figure 4(b) where a ratio curve has been constructed between the CDBAR spectrum of nanocrystalline MgO with respect to the CDBAR spectrum of bulk MgO. Figure 4(b) shows a prominent dip in the momentum value  $17 \times 10^{-3} m_0c$ , which indicates less annihilation of positrons with the core electrons of Mg in nano-crystalline MgO with respect to the bulk MgO. This indicates the presence of a significant amount of Mg vacancy in nanocrystalline MgO. Our results are consistent with the theoretical calculations on MgO which showed that neutral Mg vacancies induce large magnetic moment on neighboring oxygen ions similar to that reported earlier.<sup>1-5</sup> They have also suggested that above a critical concentration of Mg vacancies (6.25%) these magnetic moments results in collective ferromagnetism.

## 4.2 Effect of Li Doping in MgO Nanoparticles

Doping cation or anion of different valency creates vacancies which can be controlled by varying the amount of dopant. However, doping anion in controlled amount is tedious task for example doping nitrogen in oxide materials. In contrast, cation doping with controlled stoichiometry can be achieved easily. In this respect MgO is a good candidate as a parent material due to its simple rock salt type structure and highly ionic character. MgO is known to have cation vacancies at the surface. Ferromagnetism in MgO nanoparticles has been shown to be due to neutral metal vacancies which can create holes in the 2p orbital of oxygen. Replacing  $\text{Mg}^{2+}$  with  $\text{Li}^+$  can be an alternative way to create holes in the 2p orbital of oxygen. We have compared the magnetic properties of undoped and 10 % Li doped MgO nanoparticles.

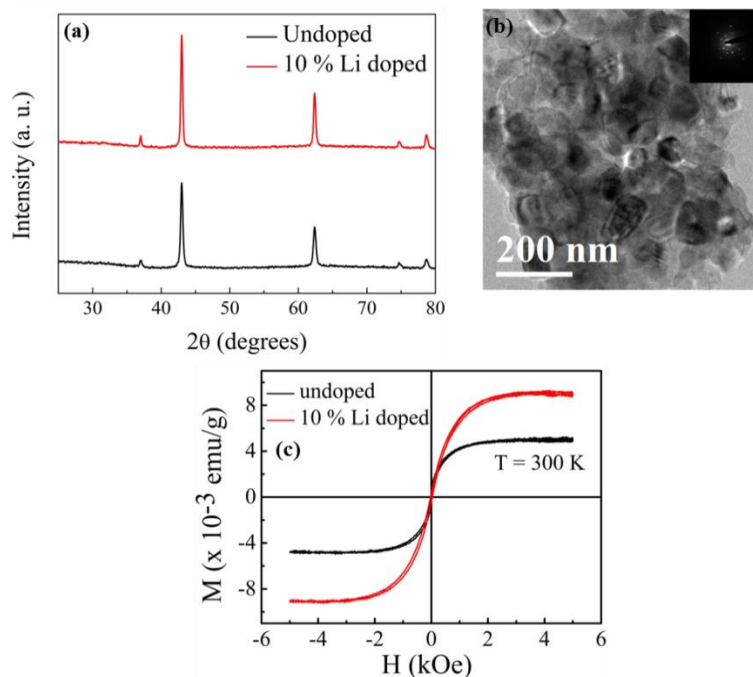


**Figure 5(a) XRD patterns of undoped and Li-doped MgO nanoparticles; (b) TEM image of Li-doped MgO nanoparticles; (c) room temperature magnetization of undoped and Li-doped MgO nanoparticles.**

Figure 5(a) shows XRD patterns of undoped and 10 % Li doped nanoparticles. Both the samples are well crystalline. No considerable shift in the peak positions due to Li doping could be seen. Peaks of undoped sample are broader which indicates that lithium doping helps in grain growth which has also been reported earlier.<sup>17</sup> Figure 5(b) shows the TEM

image of 10 % Li doped nanoparticles. Individual particles can be seen in the TEM image with average size of around 60 nm. Inset of Figure 5(b) shows continuous rings in the electron diffraction pattern which confirms the polycrystalline nature of sample. Figure 5(c) shows room temperature magnetization plots for undoped and 10 % Li doped samples. Both the samples show ferromagnetic loops with saturation magnetization of Li doped sample ( $9 \times 10^{-3}$  emu/g) being double than that of undoped sample ( $4.7 \times 10^{-3}$  emu/g). Ferromagnetism in MgO nanoparticles has been shown to be due to neutral vacancies present at the surface. These neutral vacancies create holes in oxygen 2p orbitals resulting in the spin polarization near Fermi level. Furthermore, substitution of  $\text{Li}^+$  at  $\text{Mg}^{2+}$  sites may create extra holes in oxygen 2p orbitals. Hence, the magnetization gets enhanced.

## **5. Conclusions**

We have studied the nature and concentration of defects using photoluminescence and positron annihilation spectroscopy in ferromagnetic MgO nanoparticles and compared with that of the bulk MgO. The intensity of photoluminescence which is a measure of defect concentration correlates with the decrease of saturation magnetization. Positron annihilation spectroscopy revealed the presence of Mg vacancies whose concentration decreases with increasing particle size which supports that Mg vacancies or Mg vacancy clusters are responsible for ferromagnetism in nanoparticles of MgO.

## 6. References

1. I. S. Elfimov, S. Yunoki and G. A. Sawatzky, *Phys. Rev. Lett.* **2002**, *89*, 216403.
2. J. Osorio-Guillén, S. Lany, S. V. Barabash and A. Zunger, *Phys. Rev. Lett.* **2006**, *96*, 107203.
3. F. Gao, J. Hu, C. Yang, Y. Zheng, H. Qin, L. Sun, X. Kong and M. Jiang, *Solid State Commun.* **2009**, *149*, 855-858.
4. F. Wang, Z. Pang, L. Lin, S. Fang, Y. Dai and S. Han, *Phys. Rev. B* **2009**, *80*, 144424.
5. A. Droghetti, C. D. Pemmaraju and S. Sanvito, *Phys. Rev. B* **2010**, *81*, 092403.
6. A. Subramania, G. V. Kumar, A. R. S. Priya and T. Vasudevan, *Nanotechnology* **2007**, *18*, 225601.
7. A. Sundaresan, R. Bhargavi, N. Rangarajan, U. Siddesh and C. N. R. Rao, *Phys. Rev. B* **2006**, *74*, 161306.
8. S. Stankic, M. Müller, O. Diwald, M. Sterrer, E. Knözinger and J. Bernardi, *Angew. Chem. Int. Ed.* **2005**, *44*, 4917-4920.
9. S. G. MacLean and W. W. Duley, *J. Phys. Chem. Solids* **1984**, *45*, 227-235.
10. M. Anpo, Y. Yamada, Y. Kubokawa, S. Coluccia, A. Zecchina and M. Che, *J. Chem. Soc., Faraday Trans. 1* **1988**, *84*, 751-764.
11. C. I. Chizallet, G. n. Costentin, H. I. n. Lauron-Pernot, J.-M. Krafft, M. Che, F. o. Delbecq and P. Sautet, *J. Phys. Chem. C* **2008**, *112*, 16629-16637.
12. K. Saarinen, T. Suski, I. Grzegory and D. C. Look, *Phys. Rev. B* **2001**, *64*, 233201.
13. P. Asoka-Kumar, M. Alatalo, V. J. Ghosh, A. C. Kruseman, B. Nielsen and K. G. Lynn, *Phys. Rev. Lett.* **1996**, *77*, 2097.
14. R. S. Brusa, W. Deng, G. P. Karwasz and A. Zecca, *Nucl. Instrum. Meth. B* **2002**, *194*, 519-531.
15. M. Chakrabarti, A. Sarkar, D. Sanyal, G. P. Karwasz and A. Zecca, *Phys. Lett. A* **2004**, *321*, 376-380.
16. S. Dutta, S. Chattopadhyay, A. Sarkar, M. Chakrabarti, D. Sanyal and D. Jana, *Prog. Mater Sci.* **2009**, *54*, 89-136.
17. H. Aritani, H. Yamada, T. Nishio, T. Shiono, S. Imamura, M. Kudo, S. Hasegawa, T. Tanaka and S. Yoshida, *J. Phys. Chem. B* **2000**, *104*, 10133-10143.



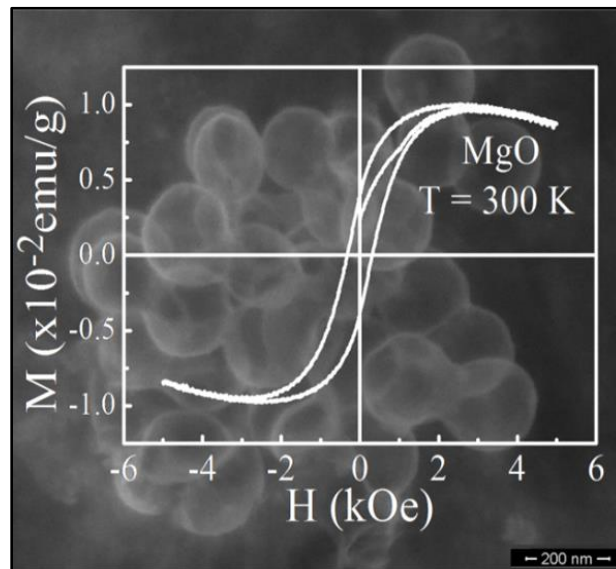


## Chapter V.4

### Room temperature ferromagnetism in thin-walled inorganic hollow spheres\*

#### Summary

In this chapter, the magnetic properties of inorganic hollow spheres of GaN, ZnAl<sub>2</sub>O<sub>4</sub> and MgO synthesized using glucose derived amorphous carbon spheres as templates are discussed. Magnetic measurements indicate the presence of ferromagnetism at room temperature in these three types of hollow spheres with especially high value of coercive field in MgO hollow spheres. Photoluminescence (PL) measurements show defect band due to magnesium vacancy in MgO and oxygen vacancy in ZnAl<sub>2</sub>O<sub>4</sub> hollow spheres which support our prediction of universal ferromagnetism in otherwise nonmagnetic inorganic nanomaterials.



\* A paper based on this work has appeared in *Chem. Phys. Lett.*, **2011**

## 1. Introduction

The fate of future technology relies on the advancement of materials science. Materials with improved properties and applicability are certainly going to fulfil this huge demand. Hollow sphere is one such kind of material which can find its applicability in many emerging fields like gas storage<sup>1</sup>, catalyst support<sup>2</sup>, and drug delivery<sup>3</sup>. Several methods have been employed in order to synthesize inorganic hollow spheres of diverse types in the past. They can broadly be divided into two types: use of hard templates like anodic alumina membrane, amorphous carbon spheres, mesoporous silica *etc.* and soft templates like non-ionic surfactant, polymers, organic ligands *etc.* to synthesize inorganic hollow spheres.<sup>4-14</sup> In addition to these two methods template free synthesis of inorganic hollow spheres is also very popular among chemists which mainly involves Ostwald ripening mechanism.<sup>2, 15-21</sup>

In recent years, use of templates is gaining popularity particularly due to the fact that different shapes and sizes of hollow morphologies can be made by choosing appropriate templates. Highly controlled synthesis of templates can be done in labs however, most of them are available commercially. Amorphous carbon spheres as template is unique in a way that after coating with desired material the core can be thermally decomposed into carbon dioxide in the presence of oxygen. The exothermic nature of this reaction provides the required thermal annealing which is very important for high crystallinity, especially for oxide materials. Owing to this fact a range of metal oxides like Fe<sub>2</sub>O<sub>3</sub>, NiO, Co<sub>3</sub>O<sub>4</sub>, CeO<sub>2</sub>, ZnO, Ga<sub>2</sub>O<sub>3</sub>, SnO<sub>2</sub>, have been prepared in recent past using carbon spheres as template.<sup>22-26</sup>

## 2. Scope of the present investigation

Surface ferromagnetism in nanoparticles and thin films of otherwise non-magnetic oxide of has been investigated in the recent past. The main disadvantage in such systems is the small value of saturation magnetization. The overall magnetization depends on the defect concentration at the surface. The problem of agglomeration is well known in crystalline oxide materials resulting in the decrease in the concentration of defect sites. In the case of conventional thin films grown on substrates only one side is agglomeration free. Hollow spheres are better option in a way that the inner as well as outer wall is free from agglomeration and thus can be considered as a thin film without any substrate support.

Magnetism of such materials will be interesting compared to thin films and nanoparticles owing to the presence of more number of defects.

### **3. Experimental section**

#### **3.1. Materials**

Anhydrous D (+) Glucose (Dextrose, Corn Sugar) and Gallium Oxide were purchased from Sigma-Aldrich. Analytical grade  $\text{Zn}(\text{NO}_3)_2 \cdot 6\text{H}_2\text{O}$ ,  $\text{Al}(\text{NO}_3)_3 \cdot 9\text{H}_2\text{O}$ ,  $\text{Mg}(\text{NO}_3)_2 \cdot 6\text{H}_2\text{O}$  and 30% aq.  $\text{NH}_3$  solution were purchased from Qualigens. All the chemicals mentioned above were used directly without further purification. The water used in the experiments was obtained from Millipore purification system and had a resistivity as high as 18 M $\Omega$ -cm. Calcination was done on an alumina boat in a muffle furnace (Elite Thermal Systems, UK). Tube furnace (Elite Thermal Systems, UK) was used for heating the sample in gaseous  $\text{NH}_3$  (99.99% purchased from Chemix gases, India).

#### **3.2. Synthesis of carbon spheres**

5 g of glucose was dissolved in 50 mL of water to form a clear solution. It was placed in a 60 mL Teflon sealed stainless steel container and heated at 180 °C for 12 h. The brown product was isolated and purified by repeated washing with ethanol after which the samples were dried at 80°C for 4 h. The as-synthesized carbon spheres were used as templates to synthesize the inorganic hollow spheres.

#### **3.3. Synthesis of $\text{ZnAl}_2\text{O}_4$ hollow spheres**

4.65 g of  $\text{Zn}(\text{NO}_3)_2 \cdot 6\text{H}_2\text{O}$  and 11.63 g of  $\text{Al}(\text{NO}_3)_3 \cdot 9\text{H}_2\text{O}$  were dissolved in 30 mL of water. The carbon spheres (0.25 g) were added to the above solution and the whole mixture was sonicated for 15 min, followed by 12 h of aging. The supernatant solution was decanted out and the black residue obtained was centrifuged five times with water and ethanol. The pH was adjusted to 8-10 by adding 30% aqueous  $\text{NH}_3$  solution. The mixture was transferred to a 20 mL teflon-lined stainless steel autoclave and maintained at 180 °C for 20 h after which it was allowed to air cool to room temperature. The supernatant was decanted out and the

residue obtained was washed with ethanol and dried at 80 °C for 3 h. The template was finally removed by heating at 600 °C for 5 h in air.

### 3.4. Synthesis of GaN hollow spheres

GaN hollow spheres were synthesized according to a reported procedure.<sup>25</sup> The precursor of gallium was GaCl<sub>3</sub> which was prepared by dissolving 0.4 g of Ga<sub>2</sub>O<sub>3</sub> in 10 mL of hot HCl. 0.25 g of carbon spheres was soaked in the HCl solution for over 12 h. This was followed by washing the sample twice in water followed by drying at 80 °C for 4 h. The gallium adsorbed carbon spheres was finally calcined at 500 °C for 5 h. The as prepared Ga<sub>2</sub>O<sub>3</sub> hollow spheres were heated in the presence of NH<sub>3</sub> at 800 °C for 3 h.

### 3.5. Synthesis of MgO hollow spheres

12.84 g of Mg(NO<sub>3</sub>)<sub>2</sub>.6H<sub>2</sub>O was dissolved in 50 mL water. 1.2 g of carbon spheres was added to this solution. The resultant mixture was sonicated for 1 h followed by 24 hours of aging. The content was centrifuged and washed with water. Final washing was done with ethanol followed by drying at 80 °C for 4 h. Magnesium adsorbed carbon spheres was heated at 500 °C for 4 h in oxygen atmosphere to get MgO hollow spheres.

## 4. Results and discussion

Figure 1(a) shows the TEM image of GaN hollow spheres. Enlarged image of an individual sphere is shown in Figure 1(b). Average diameter of GaN hollow spheres is ~ 300 nm with the wall thickness of around 20 nm. It is clear from these images that the spheres are polycrystalline in nature. Nanoparticles are actually connected in two dimensions to form hollow spheres. TEM images of ZnAl<sub>2</sub>O<sub>4</sub> hollow spheres are shown in Figure 1(c) and (d). Like GaN hollow spheres these are polycrystalline in nature but not as porous as in the case of GaN. Average diameter is ~ 120 nm while the wall thickness is around 20 nm. TEM image of MgO hollow spheres are shown in Figure 1(e). Thickness of MgO spheres is around 8 nm. Figure 1(f) shows enlarged image of an individual sphere where small grains can easily be seen. Electron diffraction pattern shown in the inset of Figure 1(f) contains continuous rings which further indicate the polycrystalline nature of MgO hollow spheres.

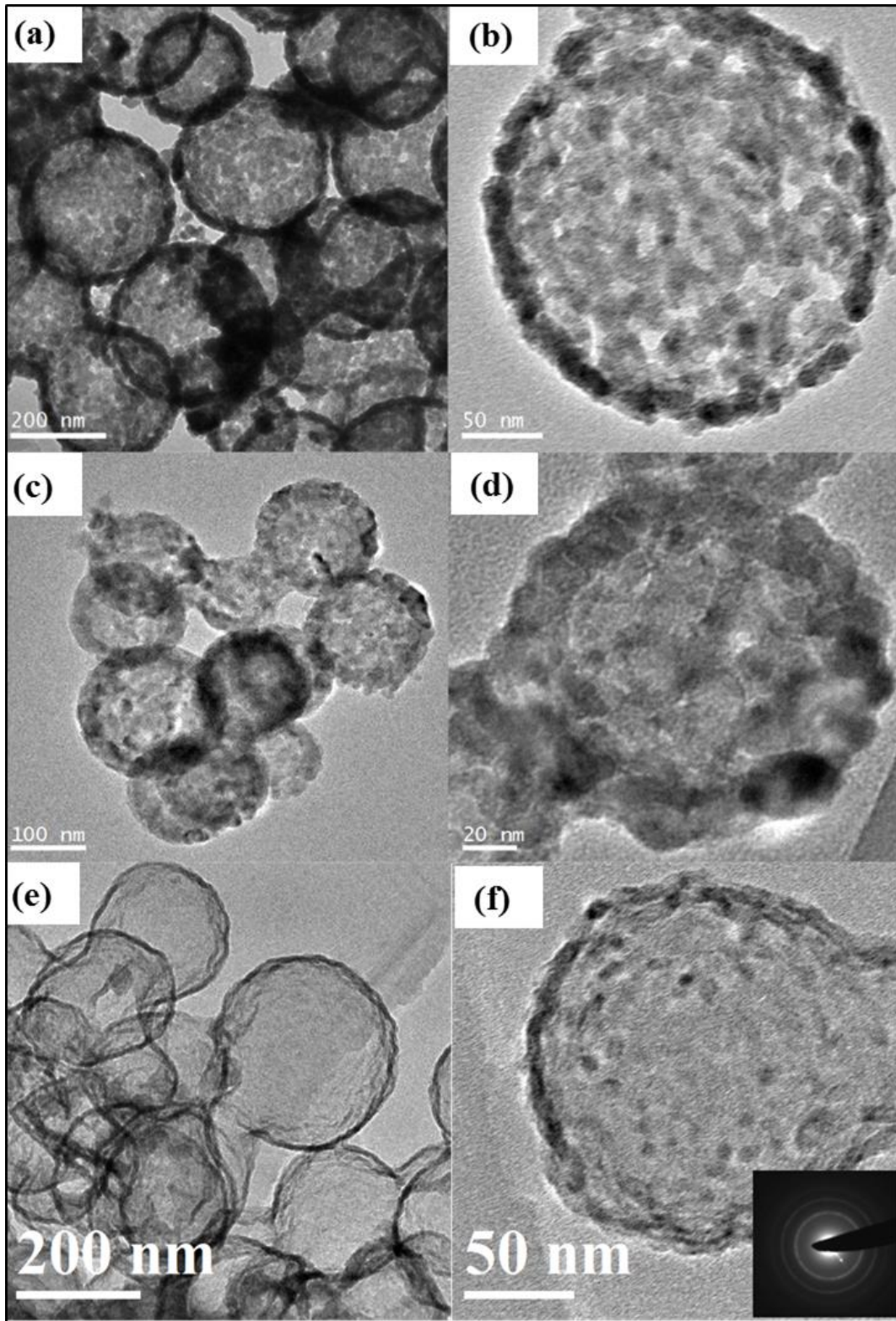
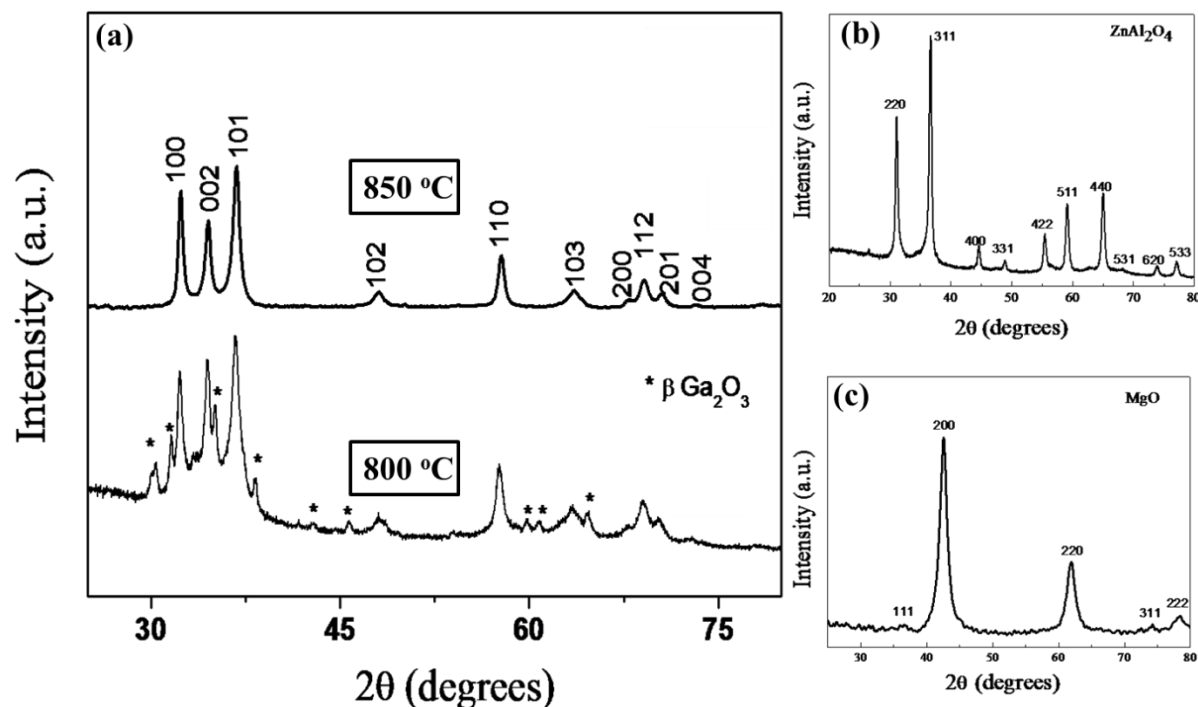


Figure 1 TEM images of (a), (b) GaN; (c), (d) ZnAl<sub>2</sub>O<sub>4</sub>; (e), (f) MgO hollow spheres



**Figure 2** XRD patterns of hollow spheres of (a) GaN prepared at different temperatures, (b)  $\text{ZnAl}_2\text{O}_4$  and (c) MgO

Figure 2(a) shows XRD image of GaN hollow spheres prepared at 800 and 850 °C. Asterisk marked peaks are of  $\beta \text{Ga}_2\text{O}_3$  impurity phase which exist along with the desired hexagonal phase of GaN. The absence of any peak due to impurity phase for the sample prepared at 850 °C indicates the fact that the formation of GaN hollow spheres is complete at this temperature. The pattern matches with the hexagonal structure (space group  $P6_3mc$ ). XRD pattern of  $\text{ZnAl}_2\text{O}_4$  as shown in Figure 2(b) is consistent with cubic phase (space group  $Fd-3m$ ) without any  $\text{Al}_2\text{O}_3$  or  $\text{ZnO}$  impurity phases.  $\text{ZnAl}_2\text{O}_4$  has normal spinel structure with  $\text{Zn}^{2+}$  being at the tetrahedral sites, while all the  $\text{Al}^{3+}$  at the octahedral sites. XRD pattern of MgO hollow spheres is shown in Figure 2(c). Broadening of the peaks can be attributed to the small crystallite size of MgO as also observed in the TEM images. It crystallizes in rock salt structure with cubic space group  $Fm-3m$ .

Figure 3(a) shows magnetization as a function of magnetic field at room temperature for GaN hollow spheres. The sample shows a ferromagnetic hysteresis loop with relatively large saturation magnetization value of 0.032 emu/g, that is one order higher than the previous report<sup>27</sup> of ferromagnetism in GaN nanoparticles. The plot has been corrected for the

diamagnetic behaviour of the core of the nanoparticles as well as for the background diamagnetism. The background diamagnetism has contributions from sample holder, sample container and adhesive tape.

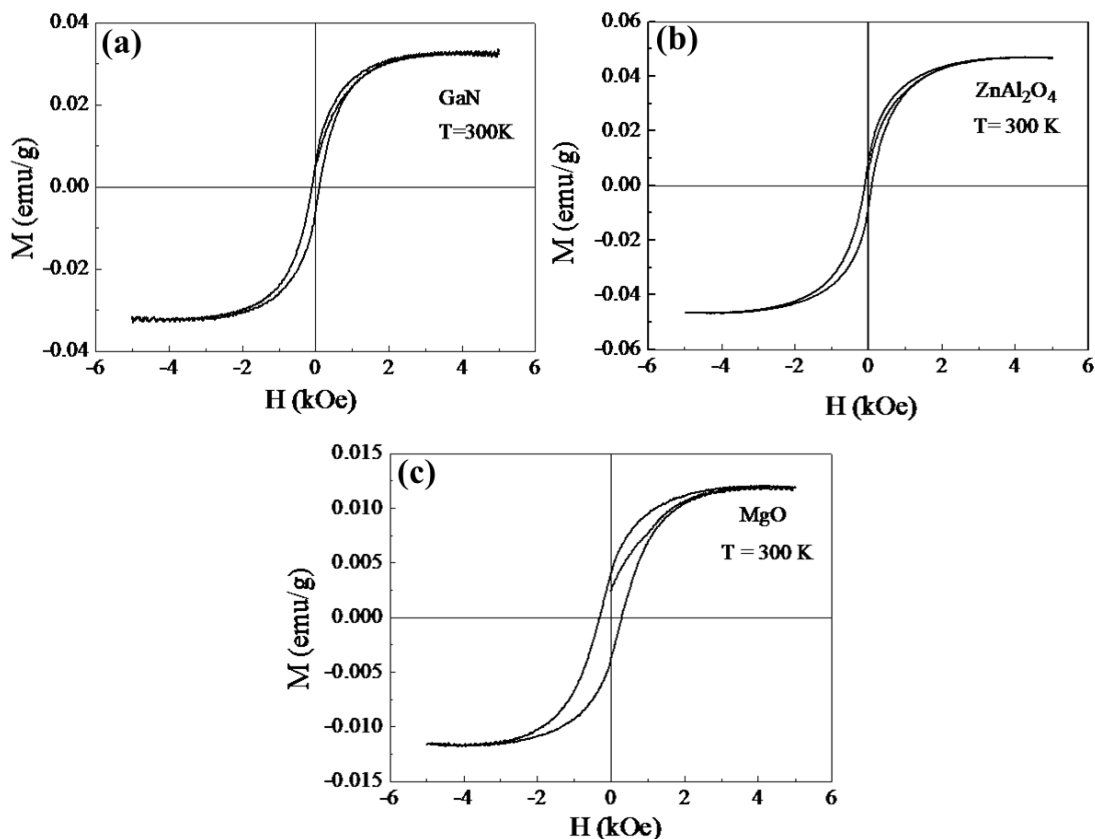


**Figure 3** Room temperature magnetization of (a) GaN, (b)  $\text{ZnAl}_2\text{O}_4$  and (c) MgO hollow spheres

This high value of saturation magnetization can be attributed to the fact that the crystallites in hollow spheres are at least not agglomerated from two sides. It has been shown earlier that agglomeration leads to the reduction of surface ferromagnetism due to the decrease in the concentration of defect sites.<sup>28</sup> The value of coercive field is more or less same as compared to the nanocrystalline GaN powder indicating the fact that there is not much interaction among grains constituting the hollow sphere. First-principles calculations have shown that Ga vacancies are actually responsible for magnetization in GaN.<sup>29</sup> The report further claims that Ga vacancies not only creates local magnetic moments but also leads to long range magnetic ordering. Figure 3(b) shows the ferromagnetic hysteresis loop of  $\text{ZnAl}_2\text{O}_4$  hollow spheres. Bulk  $\text{ZnAl}_2\text{O}_4$  is diamagnetic as there are no magnetic ions present in the compound.

Magnetic properties of  $\text{ZnAl}_2\text{O}_4$  in any form have not been reported earlier. After diamagnetic correction it shows a saturation magnetization value of 0.047 emu/g. In a very similar spinel nanoparticles system of  $\text{MgAl}_2\text{O}_4$ , it has been shown using  $^{27}\text{Al}$  NMR that the concentration of five and three fold coordinated Al at the surface increases with decrease in particle size.<sup>30</sup> A similar kind of mechanism in  $\text{ZnAl}_2\text{O}_4$  might play an important role in imparting ferromagnetism. Hysteresis loop of MgO hollow spheres at room temperature is shown in Figure 3(c). The coercive field of 300 Oe is significantly higher than the previously reported ferromagnetism in MgO nanoparticles.<sup>28</sup> The large value of coercive field may be attributed to magnetic anisotropy due to the shape of the hollow spheres. MgO vacancies at the surface of nanocrystallites give rise to ferromagnetism at room temperature. This has been supported experimentally by positron annihilation and photoluminescence spectroscopy recently.<sup>28</sup> First principle based calculations show that the magnetic moments in MgO arise from spin polarization of 2p orbitals of oxygen surrounding neutral Mg vacancies.<sup>31-32</sup>

PL spectrum of GaN hollow spheres is shown in Figure 4(a) with 325 nm excitation. The emission spectrum shows a broad peak corresponding to band edge absorption. The broadening is due to the fact that GaN crystallites are not mono-disperse and it is well known that band gap of large band gap semiconductors does depend on crystallite size. In addition to this a broad band corresponding to yellow emission ( $\sim 560$  nm) has been observed in epitaxial thin films and nanoparticles.<sup>33-34</sup> The origin of this band is not clear but there are evidences of extended defects like dislocations and stacking fault contributing towards this. On the other hand theory suggests that ferromagnetism in GaN should come from Ga vacancy. Hence in our GaN hollow spheres PL measurements do not provide any further support to the ferromagnetism observed. Figure 4(b) shows PL spectrum of  $\text{ZnAl}_2\text{O}_4$  hollow spheres. A broad peak at 500 nm is observed when excited by light of wavelength 360 nm which is less than its band gap (3.8 eV). Such kind of PL spectra for  $\text{ZnAl}_2\text{O}_4$  nanoparticles have been observed earlier and attributed to oxygen vacancies.<sup>35</sup> Photoluminescence spectroscopy is a very useful tool to identify defects. Figure 4(c) shows PL spectra of MgO hollow spheres at 240 nm and 270 nm excitation wavelengths.



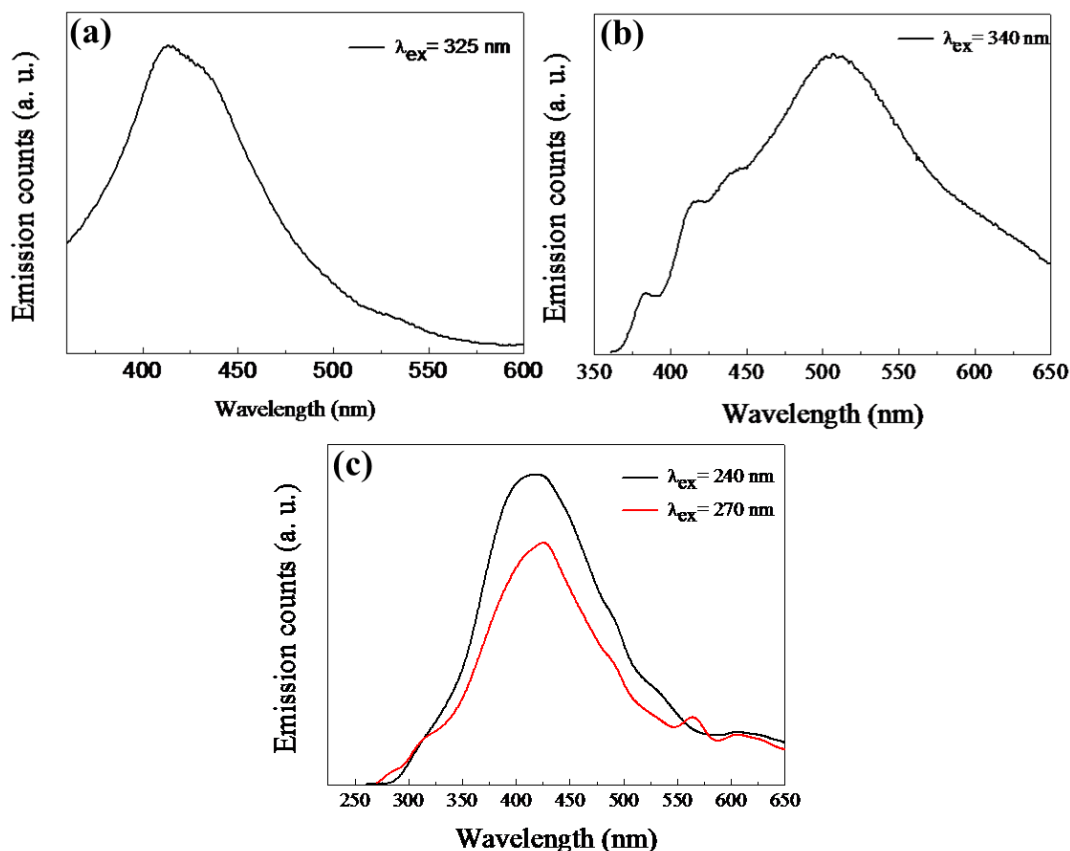


Figure 4 PL spectra of (a) GaN, (b)  $\text{ZnAl}_2\text{O}_4$  and (c) MgO hollow spheres

These are the energies much less than the band gap (7.8 eV) of MgO. Broad spectra concentrated in the blue region (around 410 nm) can then be attributed to the emission from the defect levels in MgO. In the literature peaks corresponding to 240 nm and 270 nm excitations have been attributed to four coordinated oxygen at the edge and three coordinated oxygen at the corners respectively in MgO lattice.<sup>36</sup>

## 5. Conclusions

We synthesized polycrystalline hollow spheres of GaN,  $\text{ZnAl}_2\text{O}_4$  and MgO using carbon spheres as template. TEM and XRD analysis were carried out in order to characterize the hollow spheres systematically. GaN hollow spheres show enhanced magnetic property in terms of large value of saturation magnetization when compared to the previous report in GaN nanoparticles. We attribute this property to the fact that these hollow spheres are agglomeration free from at least two sides. Hollow spheres of  $\text{ZnAl}_2\text{O}_4$  show a nice

ferromagnetic hysteresis loop with large saturation magnetization possibly due to the point defect sites at the surface. Hysteresis loop of MgO hollow spheres show a large coercive field which indicates an increase in anisotropy coming due to its shape. PL measurements support point defects related origin of ferromagnetism in MgO and ZnAl<sub>2</sub>O<sub>4</sub> hollow spheres while in the case of GaN hollow spheres PL measurements are not sufficient enough to show Ga vacancy, which has been shown to be the origin of ferromagnetism in GaN using first-principles calculations.

## 6. References

1. J. Jiang, Q. Gao, Z. Zheng, K. Xia and J. Hu, *Int. J. Hydrogen Energy* **2010**, *35*, 210-216.
2. J. Li, Y. Xu, D. Wu and Y. Sun, *Catal. Today* **2009**, *148*, 148-152.
3. W. Zhao, H. Chen, Y. Li, L. Li, M. Lang and J. Shi, *Adv. Funct. Mater.* **2008**, *18*, 2780-2788.
4. F. Caruso, R. A. Caruso and H. Möhwald, *Science* **1998**, *282*, 1111-1114.
5. S. Kobayashi, N. Hamasaki, M. Suzuki, M. Kimura, H. Shirai and K. Hanabusa, *J. Am. Chem. Soc.* **2002**, *124*, 6550-6551.
6. C. G. Göltner, *Angew. Chem. Int. Ed.* **1999**, *38*, 3155-3156.
7. C. J. Murphy, *Science* **2002**, *298*, 2139-2141.
8. Y. Sun, B. Mayers and Y. Xia, *Adv. Mater.* **2003**, *15*, 641-646.
9. T. Nakashima and N. Kimizuka, *J. Am. Chem. Soc.* **2003**, *125*, 6386-6387.
10. C.-W. Guo, Y. Cao, S.-H. Xie, W.-L. Dai and K.-N. Fan, *Chem. Commun.* **2003**, 700-701.
11. A. D. Dinsmore, M. F. Hsu, M. G. Nikolaides, M. Marquez, A. R. Bausch and D. A. Weitz, *Science* **2002**, *298*, 1006-1009.
12. R. A. Caruso, J. H. Schattka and A. Greiner, *Adv. Mater.* **2001**, *13*, 1577-1579.
13. Z. Yang, Z. Niu, Y. Lu, Z. Hu and C. C. Han, *Angew. Chem.* **2003**, *115*, 1987-1989.
14. J.-J. Zhu, S. Xu, H. Wang, J.-M. Zhu and H. Y. Chen, *Adv. Mater.* **2003**, *15*, 156-159.
15. Y. Yin, R. M. Rioux, C. K. Erdonmez, S. Hughes, G. A. Somorjai and A. P. Alivisatos, *Science* **2004**, *304*, 711-714.
16. B. Liu and H. C. Zeng, *J. Am. Chem. Soc.* **2004**, *126*, 16744-16746.
17. Y. Chang, M. L. Lye and H. C. Zeng, *Langmuir* **2005**, *21*, 3746-3748.
18. H. G. Yang and H. C. Zeng, *J. Phys. Chem. B* **2004**, *108*, 3492-3495.
19. B. Liu and H. C. Zeng, *Small* **2005**, *1*, 566-571.
20. Y. Chang, J. J. Teo and H. C. Zeng, *Langmuir* **2005**, *21*, 1074-1079.
21. J. J. Teo, Y. Chang and H. C. Zeng, *Langmuir* **2006**, *22*, 7369-7377.
22. D. Jagadeesan, U. Mansoori, P. Mandal, A. Sundaresan and M. Eswaramoorthy, *Angew. Chem.* **2008**, *120*, 7799-7802.

23. M.-M. Titirici, M. Antonietti and A. Thomas, *Chem. Mater.* **2006**, *18*, 3808-3812.
24. X. Wang, P. Hu, Y. Fangli and L. Yu, *J. Phys. Chem. C* **2007**, *111*, 6706-6712.
25. X. Sun and Y. Li, *Angew. Chem. Int. Ed.* **2004**, *43*, 3827-3831.
26. X. M. Yin, C. C. Li, M. Zhang, Q. Y. Hao, S. Liu, Q. H. Li, L. B. Chen and T. H. Wang, *Nanotechnology* **2009**, *20*, 455503.
27. C. Madhu, A. Sundaresan and C. N. R. Rao, *Phys. Rev. B* **2008**, *77*, 201306.
28. N. Kumar, D. Sanyal and A. Sundaresan, *Chem. Phys. Lett.* **2009**, *477*, 360-364.
29. P. Dev, Y. Xue and P. Zhang, *Phys. Rev. Lett.* **2008**, *100*, 117204.
30. V. Sreeja, T. S. Smitha, D. Nand, T. G. Ajithkumar and P. A. Joy, *J. Phys. Chem. C* **2008**, *112*, 14737-14744.
31. F. Gao, J. Hu, C. Yang, Y. Zheng, H. Qin, L. Sun, X. Kong and M. Jiang, *Solid State Commun.* **2009**, *149*, 855-858.
32. F. Wang, Z. Pang, L. Lin, S. Fang, Y. Dai and S. Han, *Phys. Rev. B* **2009**, *80*, 144424.
33. R. Liu, A. Bell, F. A. Ponce, C. Q. Chen, J. W. Yang and M. A. Khan, *Appl. Phys. Lett.* **2005**, *86*, 021908-021908-3.
34. F. A. Ponce, D. Cherns, W. T. Young and J. W. Steeds, *Appl. Phys. Lett.* **1996**, *69*, 770-772.
35. A. A. Da Silva, A. de Souza Gonçalves and M. R. Davolos, *J. Sol-Gel Sci. Technol.* **2009**, *49*, 101-105.
36. S. Stankic, M. Müller, O. Diwald, M. Sterrer, E. Knözinger and J. Bernardi, *Angew. Chem. Int. Ed.* **2005**, *44*, 4917-4920.